A Molecular Dynamics study of the influence of chain branching on the properties of polymer systems

Dissertation

zur Erlangung des Grades
”Doktor der Naturwissenschaften”
am Fachbereich Physik
der Johannes Gutenberg–Universität Mainz

Martin Oliver Steinhauser
geboren in Ulm

Juni, 2001

Jahr der Promotion: 2001

Jahr der Promotion: 2001

SUMMARY

This work investigates the influence of chain branching of various chain topologies on the static properties of polymers. These investigations are done with the aid of Monte-Carlo and Molecular-Dynamics simulations. Theoretical concepts and models for the description of polymer systems on mesoscopic length scales are introduced. Several important quantities that are suitable for the quantitative characterization of branched polymer structures are discussed. Different optimization techniques that were used in the implementation of the computer code are expatiated. Besides linear polymer chains we investigated various topologies: Star polymers with different number of arms, a transition from a linear chain to a star polymer, chains with a varying number of side chains, regular dendrimers and hyperbranched structures. All investigations considered the effects of different solvent qualities. At first, a thorough analysis of the used simulation model with very long linear chains is performed. The scaling properties of linear chains are investigated for a variety of different solvent qualities, ranging from an athermal good solvent to a very bad one where the chains are compact globules. An important result of this work is the confirmation of the corrections to scaling of the hydrodynamic radius which is $\propto N^{\nu-1}$ and not $\propto N^{-1/2}$, with ν being the scaling exponent of the radius of gyration and N being the degree of polymerization. We argue that this result is obtained, because of the consideration of very long chain lengths and the high quality of the obtained data. This correction to scaling is not only verified for linear chains, but also for star polymers with different arm numbers. For linear chains, the influence of polydispersity was investigated. It was shown, that a unique mapping of experimental length scales onto the simulation data is not possible, because the dimensionless quantity that is used to perform this mapping turns out to be too weekly dependent on the degree of polymerization. A comparison of simulation data with experimental data of industrial Low Density Polyethylene (LDPE) reveals that LDPE used in industry has a highly branched structure (multi-arm stars or hyperbranched polymers). This is another important result of this work. For regular dendrimer topologies it could be shown that there is a strong tendency of a back-folding of arms into the central core region.

ZUSAMMENFASSUNG

Die vorliegende Arbeit beschäftigt sich mit dem Einfluß von Kettenverzweigungen unterschiedlicher Topologien auf die statischen Eigenschaften von Polymeren. Diese Untersuchungen werden mit Hilfe von Monte-Carlo- und Molekulardynamik-Simulationen durchgeführt. Zunächst werden einige theoretische Konzepte und Modelle eingeführt, welche die Beschreibung von Polymerketten auf mesoskopen Längenskalen gestatten. Es werden wichtige Bestimmungsgrößen eingeführt und erläutert, welche zur quantitativen Charakterisierung von Verzweigungsstrukturen bei Polymeren geeignet sind. Es wird ebenso auf die verwendeten Optimierungstechniken eingegangen, die bei der Implementierung des Computerprogrammes Verwendung fanden. Untersucht werden neben linearen Polymerketten unterschiedliche Topologien – Sternpolymere mit variabler Armzahl, Übergang von Sternpolymeren zu linearen Polymeren, Ketten mit variabler Zahl von Seitenketten, reguläre Dendrimere und hyper-verzweigte Strukturen – in Abhängigkeit von der Lösungsmittelqualität. Es wird zunächst eine gründliche Analyse des verwendeten Simulationsmodells an sehr langen linearen Einzelketten vorgenommen. Die Skalierungs-Eigenschaften der linearen Ketten werden untersucht in dem gesamten Lösungsmittel-Bereich vom guten Lösungsmittel bis hin zu weitgehend kollabierten Ketten im schlechten Lösungsmittel. Ein wichtiges Ergebnis dieser Arbeit ist die Bestätigung, daß die Korrekturen zum Skalenverhalten des hydrodynamischen Radius nicht proportional zu $N^{-1/2}$, sondern zu $N^{\nu-1}$ sind, wobei ν der Skalenexponent für den Gyrationsradius und N der Polymerisationsgrad ist. Dieses Ergebnis war möglich aufgrund der großen gewählten Kettenlängen und der hohen Qualität der erhaltenen Daten in dieser Arbeit, insbesondere bei den linearen Ketten, und es steht im Widerspruch zu vielen bisherigen Simulations-Studien und experimentellen Arbeiten. Diese Korrekturen zum Skalenverhalten wurden nicht nur für die linearen Ketten, sondern auch für Sternpolymere mit unterschiedlicher Armanzahl gezeigt. Es wurde für die linearen Kettensysteme der Einfluß von Polydispersität untersucht. Hierbei konnte gezeigt werden, daß eine eindeutige Abbildung von Längenskalen zwischen Simulationsmodell und Experiment nicht möglich ist, da die zu diesem Zweck verwendete dimensionslose Größe eine zu schwache Abhängigkeit von der Polymerisation der Ketten besitzt. Der Vergleich mit industriellem Low-Density-Polyäthylen (LDPE) zeigt, das LDPE in Form von hochgradig verzweigten Ketten (Multi-Arm-Sterne oder “Hyperbranches”) vorliegt. Dies ist ein weiteres wichtiges Ergebnis dieser Arbeit. Für Dendrimere konnte ein hochgradiges Zurückfalten der Arme in die innere Kernregion nachgewiesen werden.

To Katrin and Pia

Contents

Chapter 1

Polymer Physics – An introduction

Das Schönste, was wir erleben können,
ist das Geheimnisvolle. Es ist das
Grundgefühl, das an der Wiege von
Kunst und Wissenschaft steht.

Albert Einstein [98]

A **Polymer** is a large molecule, that is composed of many small chemical *constitutional (repeating) units* which are covalently bound to each other. The largest constitutional unit contributed by a single molecule in a polymerization process is called a *monomer unit* [1].

Polyethylene (PE) ($CH_3 - (CH_2)_N - CH_3$), proteins and DNA are typical examples of such long, chain-like molecules, which are composed of a large number of single constituents.

Such macromolecular substances are naturally occurring in living organisms and are also synthetically produced, e.g. in the form of plastic or rubber. Most of the synthetic polymers are produced by repetitively connecting particular constitutional units A, such that they finally build a long sequence of units of the form $\cdots - A - A - A - A - A - \cdots$. The number of repetitive units is called *degree of polymerization* N. Usually a molecule is called a polymer, once its properties do not change anymore when continuously adding repeating units [115]. In nature there are polymers with a degree of polymerization of up to 10^9.

Due to their large masses, polymers possess an enormous variety of conformations [2] with different sizes and shapes. The study of these conformations is a key to understanding the diverse properties of macromolecules.

Branching occurs naturally in polymer systems and usually cannot be completely avoided in the commercial fabrication of polymers. Depending on the polymerization process of low molecular weight compounds to high molecular weight polymers, the synthesis of macromolecules usually leads to a broad distribution of molecular weights [104, 122].

[1] Note that the monomer unit can be quite different from the constitutional unit.

[2] In [89] a distinction between *conformations* and *configurations* is made in the sense that the latter only refers to the arrangement of electrons in their shells. In this work, however, no such distinction will be made and the two terms will be used interchangeably.

The synthesis of ***L**ow **D**ensity **P**oly**e**thylene (LDPE)* with radical polymerization is a typical example of an important polymerization process that leads to a strong, mainly uncontrollable chain branching [10, 22, 40, 49, 121, 180, 194]. On the other hand, the properties of polymer compounds are greatly influenced by this topological variety [42, 84], see Fig. 1.1.

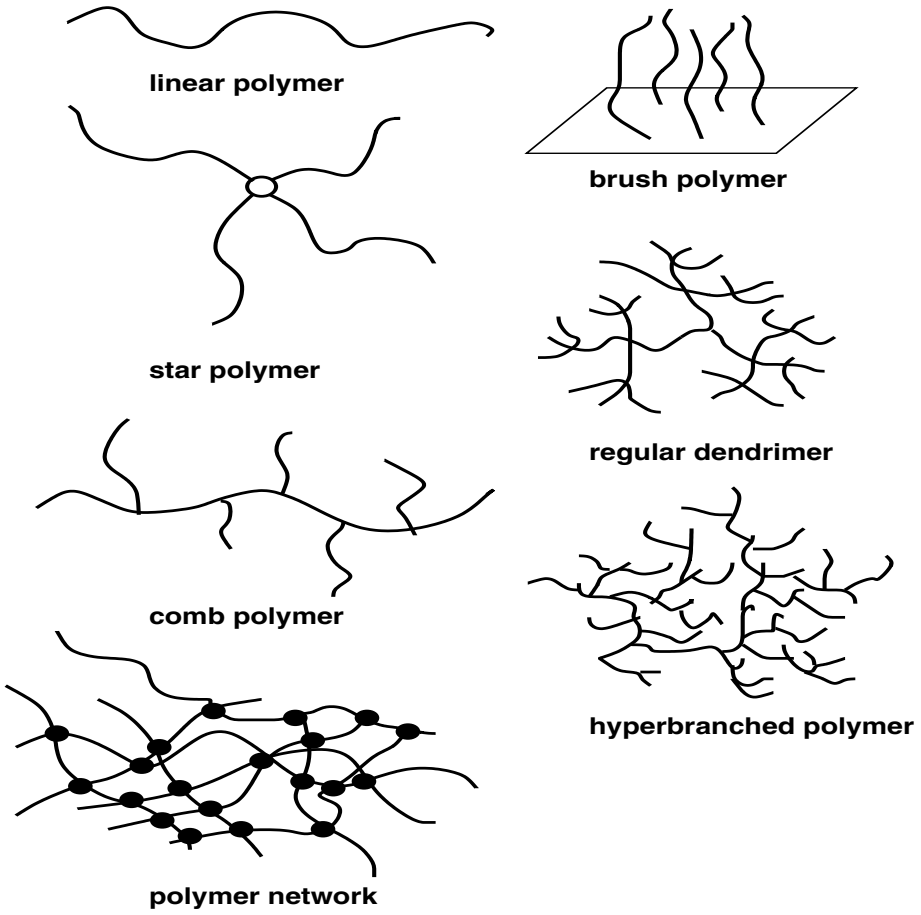

Figure 1.1: *Schematic examples of different polymer topologies.*

Further complications arise when – in addition to chain branching – monomers of different types are combined in a macromolecule and build a *copolymer* [59].

The sum of macromolecules of a polymer system constitute a complex many-particle system with a very high number of degrees of freedom. Hence, for the theoretical description of such systems one has to fall back upon the resources of statistical mechanics. By this turning away from the attempt to formulate theories that are based directly on the electronic and chemical structure, one can introduce simplified models which provide insight into macroscopic properties of polymers that depend *universally* on only a few parameters such as the chain length or interaction strength.

Usually, experiments with polymers are done in solvents of variable qualities which gives rise to solvent-polymer interactions. These interactions can be characterized by a *Flory parameter* χ [56] which depends on temperature T. For many systems (e.g. polystyrene-cyclohexane) $\chi(T)$ is a decreasing function of temperature. The phase diagram of experimental solvent-polymer systems is given in terms of concentration c and temperature T. When one introduces an effective length per monomer, a, and the volume fraction of monomers, $\Phi = ca^3$, the phase diagram assumes a *universal*

structure as described in Figure 1.2.

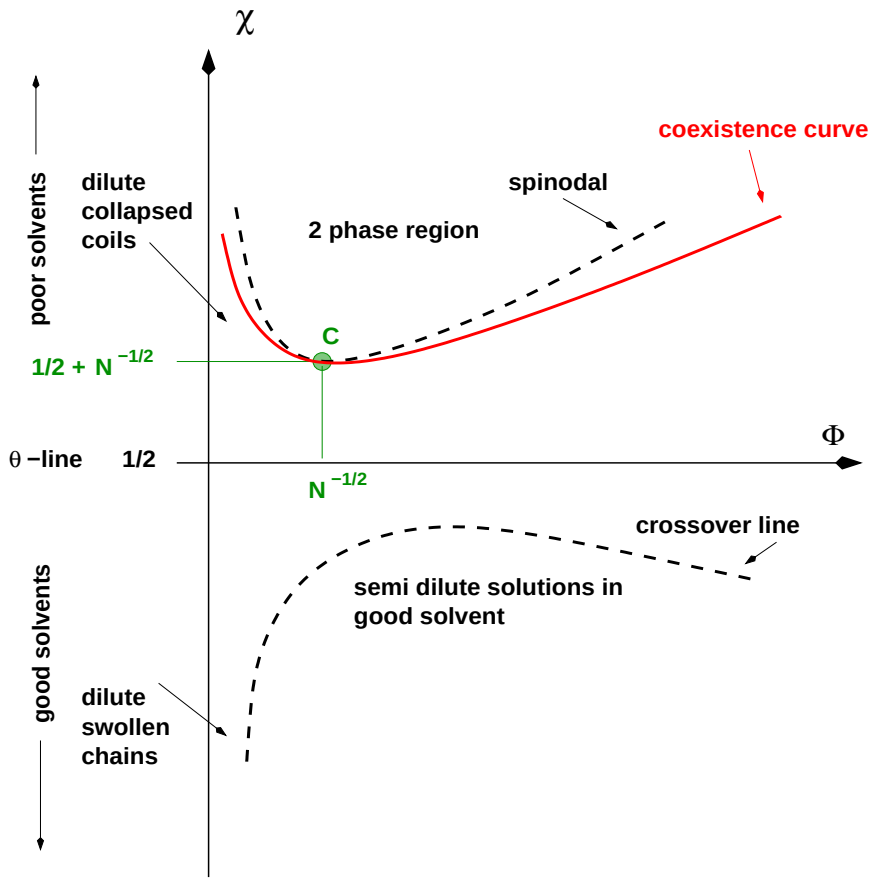

Figure 1.2: *Phase diagram of a polymer-solvent system according to [56]. A solvent is referred to as "good" if the effective interaction between chain segments is repulsive. The effective interaction is summarized in one dimensionless parameter χ in* Flory-Huggins-Theory *[56]. At lower χ-values, steric interaction dominates. The chains tend to swell. One enters this good solvent regime when one crosses a certain crossover line which defines a region of crossover between ideal and swollen chains. This crossover line is not a sharp boundary and is approximately defined by the condition $\Phi < 3(1-2\chi)$ [56]. In usual cases such as polystyrene-cyclohexane, χ is a decreasing function of temperature T; high temperatures correspond to the lower part of the figure. When $\chi > 1/2$, the solvent is referred to as being "poor" and there is a two-phase region and a critical point C as indicated in the figure. The critical point occurs at very low concentrations. Polymers and solvents segregate and the polymer chains collapse to compact coils. The condition $\chi = 1/2$ defines the "θ-condition" at "θ-temperature" $T = T_\theta$, also called "θ-point" which corresponds to an exact cancellation between steric repulsion and van der Waals attraction between monomers. At $T = T_\theta$ polymer chains possess a Gaussian conformation at all concentrations.*

The universal behavior along with the statistical nature of polymer systems is the reason why *computer simulations* are useful for the investigation of structural properties. Due to the ever increasing performance of modern computers it is possible to investigate the detailed structure of polymer models explicitly by numerical integration of the many-particle equations of motion. However, simulations test only model-systems of reality and their outcome has to be validated against both, theory and experiments. One great advantage with computer simulations is the possibility to study model systems of polymers without the typical errors and restrictions that one has to deal with when per-

forming real experiments. Instead, one can systematically alter single parameters that govern the behavior of the systems and can study the consequences thereof.

In this work, linear chains and also several differently branched polymer systems are investigated systematically with the aid of high performance computer simulations and it is revealed how various kinds of branching influence their properties. Moreover, these results are compared with experimental data and theory.

The outline of this work is as follows: In Chapter 2 many formulas and the terminology pertaining to the description of polymer systems are introduced. The following chapter discusses in detail various methods for the simulation of polymer systems. Different algorithmic optimizations that were used in the coding of this work are illustrated. It also introduces the model that was used in this work. Chapter 4 is devoted to a thorough discussion of the properties of the chosen model for linear chain systems. Finally, in Chapter 5, the model is applied to a variety of differently branched chain systems.

Chapter 2

Theoretical and experimental background

Table of Contents

This chapter provides a summary of some of the most important features of polymer systems and theoretical models of polymers insofar as they are needed for an understanding of the subsequent chapters. Also some basic definitions, formulas and terminology, that will later be used extensively, will be introduced. This chapter is finished by a short discussion of the two most important experimental techniques to obtain information on the shape and conformation of macromolecular systems.

2.1 Modeling a polymer chain on different length and time scales

The majority of most commonly used synthetic polymers, as well as all protein molecules, possess a *hydrocarbon backbone*, that is they have single covalent $\mathbf{C-C}$-bonds along their main chains. On a short length scale, flexibility is hardly noticeable, as the locations of the backbone atoms appear to be fixed. As the energy of a typical covalent bond is of the order of 1-10 eV, but the thermal energy at room temperature only is of order $kT \approx 0.03$ eV, there are only small thermal vibrations of the bond lengths l_i. Hence, these fluctuations are limited and hardly affect the overall conformation of a chain. On a larger length scale however, all different possible rotations about the $\mathbf{C-C}$-bonds add up along a chain and finally may alter the chains' shape completely. These many different *rotational*

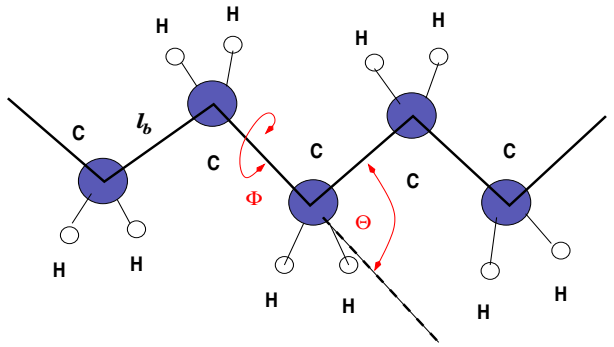

Figure 2.1: *Schematic picture of a polyethylene chain with carbon backbone of average bond length l_b, bond angle θ and torsion angle ϕ. The rotations of angle ϕ about the* $\mathbf{C}-\mathbf{C}$ *-bonds, caused by thermal motions, give rise to different rotational isomers. In the energetically most favorable* trans *state, all the* $\mathbf{C}-\mathbf{C}$ *-bonds lie in one plane whereas in the two possible meta-stable* gauche *states one bond is turned about* $\phi = \pm 120°$.

isomers are determined by Boltzmann statistics and correspond to different potential energies of the chain.

While a description of a polymer chain on this level of accuracy can be done in atomistic computer simulations by taking explicitly into account different bond angle potentials between individual atoms, the disadvantage with this kind of simulations is that one is restricted to a very small time scale of the systems. Typical $\mathbf{C}-\mathbf{C}$ -oscillations are in the infrared regime which corresponds to a time scale of the order $\delta t \approx 10^{-14}$s. Therefore, many properties that depend on a *global* relaxation of the chain, are not accessible, because this would involve time scales that are out of the scope of the atomistic description. Besides, an analytical, concise treatment, taking into account many different atomistic potentials in most cases is impossible.

When discussing structural properties of polymer chains on a lowered resolution of the order of several nanometers, polymer chains exhibit universality. This is achieved by omitting the explicit chemical details such as bond angles, or rotational potentials.

One *global aspect* of chains in such a *coarse-grained* picture is the distribution function of chain conformations. In a discussion of these properties one can make use of one of the simplest depictions of a polymer chain: The chain is modeled as a succession of rigid rods, each of length l which are fully flexible in every direction at their connection points, see Fig. 2.2. The connection points have zero volume and the segment directions are not correlated. This depiction of an *ideal chain* is called *freely jointed chain* and mathematically corresponds to a perfect *random walk (RW)* of uncorrelated steps in three dimensions.

Taking into account the eigenvolume of the connected monomer points changes the distribution function and results in a chain expansion, which was derived by *de Gennes* [56]. He noticed a fundamental equivalence between the motion of long chains and an already solved problem in the field of critical phenomena when magnetic movements undergo a phase transition. Mathematically, this situation can be modeled by considering *self avoiding walks (SAW)*.

Another depiction of a polymer chain on a coarse-grained level is that of an elastic thread. This continuous depiction of a chain is called a *worm-like chain model* [111] as displayed in Fig. 2.2.

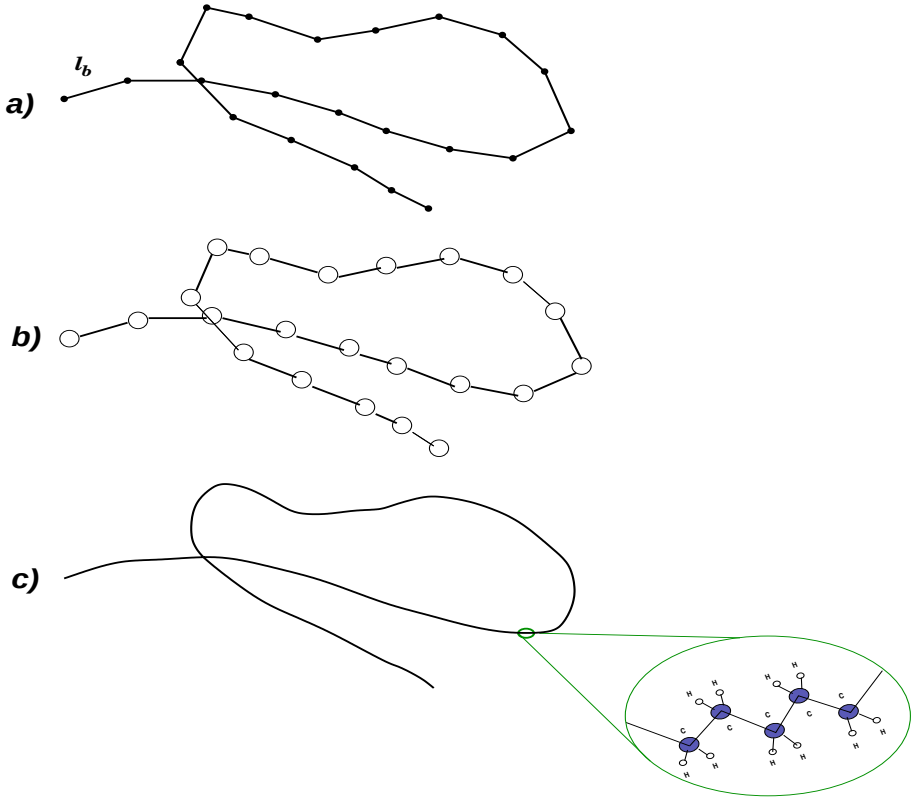

Figure 2.2: *Different stages of a coarse-grained view of a polymer chain.*

a) ideal freely jointed chain.
The chain is a sequence of rigid rods, called segments, each of length l_b, joined together with freely rotating hinges. The connection points of the segments have no eigenvolume. Such a chain corresponds to a perfect uncorrelated **random walk (RW)** *in three dimensions.*

b) excluded volume chain.
This is a more realistic chain model as it takes into account the ever present proper volume of the junction points. The excluded volume interaction leads to an expansion of a polymer chain which can be modeled by a **self-avoiding walk (SAW)** *.*

c) worm-like chain.
The polymer is modeled as a continuous elastic string which owes its flexibility to the small thermal vibrations about the equilibrium. These vibrations add up along the chain over large distances. Rotational isomers do not exist in this basic notion of a chain. However, if one zoomed in on the filament, all the chemical details would be regained.

2.2 The extension of a polymer chain

2.2.1 Linear macromolecules

When considering a *linear* chain, its overall extension is preferably discussed in terms of the **mean-square end-to-end distance** $\left\langle \vec{R}_e{}^2 \right\rangle$ or the **mean-square radius of gyration** $\left\langle \vec{R}_g{}^2 \right\rangle$ [56, 59, 72, 223]. For very long chains ($N \gg 1$) these two properties are related to each other as

$$\left\langle \vec{R}_e{}^2 \right\rangle_0 = 6 \left\langle \vec{R}_g{}^2 \right\rangle_0 , \tag{2.1}$$

where the brackets $< ... >$ indicate an ensemble average and the subscript $_0$ denotes ideal chain behavior. The simplest quantity that determines the size of a polymer chain is, see Fig. 2.3:

$$\left\langle \vec{R}_e{}^2 \right\rangle = \left\langle (\vec{r}_N - \vec{r}_1)^2 \right\rangle . \tag{2.2}$$

The dependence of $\left\langle \vec{R}_e{}^2 \right\rangle$ on N and on the bond lengths $l_i = |\vec{l}_i| = |\vec{r}_{i+1} - \vec{r}_i|$ is yielded by considering $(N+1)$ monomers of an ideal freely jointed chain (simple RW) connected by N bond vectors $\vec{l}_i$:

$$\left\langle \vec{R}_e{}^2 \right\rangle_0 = \left\langle \left(\sum_{i=0}^{N-1} \vec{l}_i \right)^2 \right\rangle = \sum_{i=0}^{N-1} \left\langle \vec{l}_i{}^2 \right\rangle + 2 \sum_{i=0}^{N-2} \sum_{j=i+1}^{N-1} \left\langle \vec{l}_i \, \vec{l}_j \right\rangle = N \left\langle |\vec{l}_i|^2 \right\rangle = N {l_b}^2. \tag{2.3}$$

There is no correlation between any bonds $\vec{l}_i$ and $\vec{l}_j$ along the chain. The term $l_b = \left\langle | \vec{l}_i |^2 \right\rangle^{1/2}$ is the average bond length of the chain.

There are many different possible configurations of a chain leading to the same value of $\left\langle \vec{R}_e{}^2 \right\rangle$. Hence, it is not possible to extract information on the actual overall shape of a chain when knowing $R_e = \left\langle \vec{R}_e{}^2 \right\rangle^{1/2}$ alone. Another crucial point is that the end-to-end distance becomes ambiguous when the macromolecule is *branched*, and it is even undefined when the macromolecule is *cyclic*. In all cases, however, the radius of gyration $R_g = \left\langle \vec{R}_g{}^2 \right\rangle^{1/2}$ remains well defined.

For a rigid set of $(N+1)$ monomers, indexed by i running from 0 to N and with particle i weighted as m_i it is defined as

$$\left\langle \vec{R}_g{}^2 \right\rangle = \left\langle \sum_{i=0}^{N} m_i \vec{s}_i{}^2 \Big/ \sum_{i=0}^{N} m_i \right\rangle , \tag{2.4}$$

where $\vec{s}_i = (\vec{r}_i - \vec{r}_{\mathrm{CM}}) = ({s_i}^x, {s_i}^y, {s_i}^z)$ and $\vec{r}_{\mathrm{CM}}$ denotes the vector to the center of mass, expressed in the same coordinate system used for the vector $\vec{r}_i$ to atom i.

The introduction of weighting factors m_i is useful in the study of *copolymers*, especially so, when the effective scattering contrast strongly differs for the various components of the macromolecule.

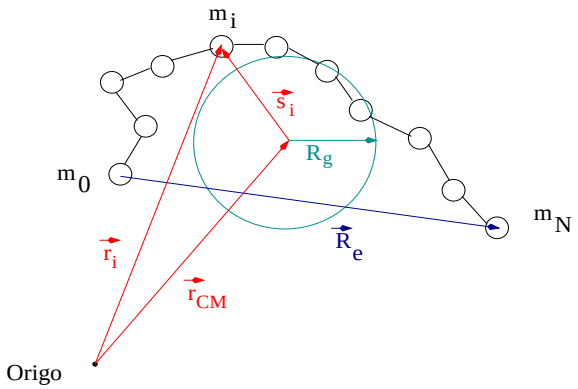

Figure 2.3: *Illustration of the end-to-end distance $\vec{R}_e$ and the radius of gyration R_g for a given chain with $(N+1)$ monomers and N segments.*

Here, however, it will be assumed that these differences are not important and thus one will adopt a simpler definition that arises when all of the m_i are identical [1]:

$$\left\langle \vec{R}_g{}^2 \right\rangle = \frac{1}{N+1} \sum_{i=0}^{N} \left\langle \vec{s}_i{}^2 \right\rangle = \frac{1}{2(N+1)} \sum \sum_{0 \le i < j \le N} \left\langle (\vec{r}_i - \vec{r}_j)^2 \right\rangle . \tag{2.5}$$

This quantity is directly available in static scattering experiments (SANS or SAXS, see Subsection 2.6.1).

By itself, $\left\langle \vec{R}_g{}^2 \right\rangle$ or $\left\langle \vec{R}_e{}^2 \right\rangle$ does not provide information about the *shape* of the distribution function. In particular it does not reveal, whether the distribution is sharp with only a few conformations populated by the chain or whether it is broad, implying that the macromolecule can take many conformations of very different extensions. This information can be obtained by considering the higher even moments.

The distribution function $P(R_e{}^2)$ of a RW chain in d dimensions is given by:

$$P(R_e{}^2) = \left(\frac{d}{2\pi N l_b{}^2} \right)^{d/2} \exp\left(-\frac{d R_e{}^2}{2 N l_b{}^2} \right) , \tag{2.6}$$

and any moment $(2m)$ is calculated by:

$$\left\langle \vec{R}_e{}^{(2m)} \right\rangle_0 = \frac{\int_0^\infty \vec{R}_e{}^{(2m)} P(R_e{}^2) d^3x}{\int_0^\infty P(R_e{}^2) d^3x} . \tag{2.7}$$

The width of the distribution function is obtained from $\left\langle \vec{R}_g{}^4 \right\rangle_0 / \left\langle \vec{R}_g{}^2 \right\rangle_0^2$. If only one single conformation is accessible, this dimensionless ratio is one. For any value of N, one yields [136]

[1] In simulations, reduced units are used in which all monomer masses $m_i = 1$ and hence the molecular weight $M = \sum_{i=1}^{N} m_i = N$. Therefore, the terms N and M will be used interchangeably in this work, unless explicitly stated otherwise.

$$\frac{\left\langle \vec{R}_g{}^4 \right\rangle_0}{\left\langle \vec{R}_g{}^2 \right\rangle_0^2} = \frac{19N^3 + 45N^2 + 32N - 6}{15N(N+1)(N+2)}. \tag{2.8}$$

Equation (2.8) yields 1 for $N = 1$ and is larger than 1 for $N \geq 2$. The limiting value for ($N \longrightarrow \infty$) is $19/15 = 1.267...$ [71].

The distribution function for the end-to-end distance is larger than the one for R_g [71]:

$$\lim_{N\to\infty} \frac{\left\langle \vec{R}_e{}^4 \right\rangle_0}{\left\langle \vec{R}_e{}^2 \right\rangle_0^2} = \lim_{N\to\infty} \frac{5N-2}{3N} = 5/3 = 1.666.... \tag{2.9}$$

Another quantity that describes the size of a polymer chain is the **hydrodynamic radius** R_h. It is experimentally determined by *dynamic light scattering* [20] and describes the equivalent radius of a polymer chain in a flow field. In computer simulations it can be measured as a static quantity. It is defined as [223]:

$$\left\langle \frac{1}{R_h} \right\rangle = \frac{1}{N^2} \sum_{i \neq j} \left\langle \frac{1}{|\vec{r}_i - \vec{r}_j|} \right\rangle. \tag{2.10}$$

De Gennes noticed a fundamental analogy between polymer statistics and the theory of critical phenomena. This analogy is obtained by taking the ($n \to 0$)-limit in the n vector model (c.f. [56]) which serves for the description of magnetic atoms on a periodic lattice. Universality in this model can be seen by all critical exponents depending only on dimension d and the number of equivalent components n. Likewise, universality of polymer chains is expressed in universal power laws of the form

$$\left\langle \vec{R}_g{}^2 \right\rangle \propto N^{2\nu}, \tag{2.11}$$

or

$$N \propto R^{d_f} \tag{2.12}$$

with the exponent d_f being the fractal dimension of the chain. Fractals and fractal behavior are abundant in nature [50, 89], with polymers being only one of many examples [4, 41, 47].

Table 2.1 gives values of ν, associated with different conformations.

2.2.2 Branched macromolecules

The average extension of the $(N + 1)$ monomers of a chain can be reduced by changing their connectivity. A common experimental means of characterizing the influence of branched molecular architectures on the mean square dimensions is designated by a branching factor g that is defined as

Conformation	ν
globule	1/3
random coil (θ-solvent)	1/2
random coil (SAW)	$\approx 3/5$
rigid rod	1
dendrimers (good solvent)	0.15-0.21

Table 2.1: *Scaling exponents ν for various conformations. The best estimate for linear random coils in good solvent according to renormalization group computations is $\nu = 0.588 \pm 0.001$ [131], [147], [154]. Monte-Carlo simulations with walks of up to $N = 80.000$ gave $\nu = 0.5877 \pm 0.0006$ [125]. The results for dendrimers are taken from Ref. [132].*

the ratio of the radii of gyration of a branched and a linear molecule at the same solvent conditions and containing the same number of monomers N [234]:

$$g = \frac{\langle {R_g}^2 \rangle_{branched}}{\langle {R_g}^2 \rangle_{linear}}. \tag{2.13}$$

In an f-functional star branched polymer, the macromolecule contains f branches ($f > 2$), each with N/f bonds that emanate from a common center. The center can be either a single atom or an extended collection of atoms that are constrained to remain close together, so that all the branches emanate from a volume much smaller than $\langle {R_g}^2 \rangle^{3/2}$, see Fig. 1.1.

The application of random flight statistics leads to a very simple expression for g [234]:

$$g = \frac{1}{N^3} \sum_{j=1}^{j=f} (3{N_j}^2 N - 2{N_j}^3), \tag{2.14}$$

with N_j indicating the number of bonds in branch j. When one assumes that each branch contains the same number N/f of bonds one yields:

$$g = \frac{3f-2}{f^2}. \tag{2.15}$$

Myake and Freed [143] performed renormalization-group calculations and obtained the branching factor g in an ε-expansion as:

$$g = \frac{3f-2}{f^2} \left\{ 1 - \varepsilon/8 \left[\frac{13(f-1)(f-2)}{2(3f-2)} - \frac{4(f-1)(3f-5)\ln 2}{3f-2} + \ln f \right] + \mathcal{O}(\varepsilon^2) \right\}. \tag{2.16}$$

As f approaches infinity, the g-value approaches zero, which implies an infinitely dense globular state. Hence, upon increasing f, at some point, the assumption of random flight statistics breaks down due to the increasing density of arms at the branch point. Deviations from the prediction of Eq. (2.15) have been seen in experiments with many-arm stars ($f > 10^2$) [171, 219]. These highly branched structures have been called *fuzzy spheres* [219], as a comparison of the hydrodynamic radii

from transport measurements with the thermodynamic radii deduced from equilibrium measurements suggests that these molecules behave like spheres with a hydrodynamically penetrable surface layer. The experimental problem of incomplete coupling of the star arms to their central vertex is discussed in [45]. For more complicated branched polymer structures, such as *comb polymers* or *randomly branched* polymers, g-factors have been calculated and can be found in [172].

2.3 The stiffness of a chain

The flexibility of a chain is not very noticeable at small scales, but it starts showing up as the scale increases. Thus, there exists an upper limit of length for the chain segments l_K at which a chain can be considered as stiff. This length is called *effective segment length* or *Kuhn length* and is accessible by experiments. A chain with total mass N and contour length L contains $N_K = L/l_K$ Kuhn segments. Since they are not correlated, one can use the freely jointed chain model with Eq. (2.3) to obtain

$$l_K = \frac{\left\langle \vec{R}_e{}^2 \right\rangle}{L} = \frac{\left\langle \vec{R}_e{}^2 \right\rangle}{(N-1)l_b}. \tag{2.17}$$

For many synthetic polymers, Kuhn lengths of about 1 nm are typical, whereas DNA's Kuhn length is 500 nm. For a perfect stiff stain $l_K = L$.

A different parameter, which cannot be measured easily in experiments, is the *persistence length* l_p of a chain, defined implicitly by the equation

$$\langle \cos\theta(s) \rangle = \exp\left(-\frac{s}{l_p}\right), \tag{2.18}$$

which is obtained from the worm-like chain model when considering consecutive unit tangent vectors which include an angle θ. The parameter s denotes the length along the chains' contour and the inverse decay constant defines the persistence length l_p. The memory of chain direction is retained on length scales shorter than l_p, but completely lost, once l_p is exceeded. Because the memory extends to both directions along a chain, the following equation holds

$$l_p/l_K = 1/2, \tag{2.19}$$

which is also approximately valid for other chain models. In the limit of large values of N one defines the *characteristic ratio* of a chain as [73]:

$$\lim_{N\to\infty} \frac{\left\langle \vec{R}_e{}^2 \right\rangle_0}{(N-1){l_b}^2} = C_\infty, \tag{2.20}$$

which is experimentally determined by viscosity measurements on polymers dissolved in θ-solvents [188]. The characteristic ratio is a measure of the effective minimum random walk step length of a chain. For an ideal freely jointed chain, $C_\infty = 1$ which is not the case with real flexible polymers

polymer	solvent	T [°C]	C_∞
polybutadiene	decalin	55	4.9
polyisobutylene (atactic)	benzene	24	6.6
polyethylene	dodecanol-1	138	6.8
polypropylene	cyclohexane	92	6.8
polymethylmethacrylate (atactic)	various solvents	4-70	6.9
polystyrene (atactic)	cyclohexane	35	10.2

Table 2.2: *Examples of characteristic ratios C_∞ for some selected polymer-solvent systems under θ-conditions. All values are taken from Ref. [42].*

under θ-conditions [2]. The restrictions in bond and rotation angles in real polymers lead to larger dimensions of the chains than expected from the random flight model. Table 2.2 includes some examples of C_∞ for different polymer-solvent systems.

2.4 The gyration tensor

When the components ${T_x}^2$, ${T_y}^2$, ${T_z}^2$ of $\left\langle {\vec{R}_g}^2 \right\rangle$ of some individual chains are taken along the axes of some arbitrary orthogonal coordinate system, then on average, one expects to find $\left\langle {T_x}^2 \right\rangle = \left\langle {T_y}^2 \right\rangle = \left\langle {T_z}^2 \right\rangle = \left\langle {\vec{R}_g}^2 \right\rangle /3$, as there is no preference in direction or orientation in space. After averaging over a large number of conformations, a polymer chain therefore may be considered to be a spherical object.

In 1934, it was pointed out by *Kuhn* that this is not true for the *instantaneous* shape of individual chains when observed without orientational averaging [116]. Much later, the foundations of the investigation of the shape of polymers were laid by *Sŏlc* and *Stockmayer* [182, 183]. They introduced the concept of analyzing the principal moments of the **gyration tensor** $\mathcal{T}$, defined as the outer product of the above defined vector $\vec{s}_i$ for a fixed conformation of the chain

$$\mathcal{T} = \frac{1}{N+1} \sum_{i=0}^{N} (\vec{s}_i \otimes \vec{s}_i). \tag{2.21}$$

Since then, many investigations by theoretical [9, 18, 58, 67, 79, 105, 177, 185, 212, 213] and numerical approaches [102, 123, 135, 190, 229, 231] for a variety of different chain topologies and spatial dimensions have been performed. While the *size* of a polymer chain R_e for linear random walks [73], as well as for star branched random walks [184, 228] could be treated theoretically, exact analytical results are available only for very few characteristic quantities of polymer *shapes* [173, 182, 213].

In some arbitrary chosen coordinate system the averaged components $\langle T^{mn} \rangle$ of $\mathcal{T}$ can be written in the form of a matrix $\mathbf{T}$:

$$\langle T^{mn} \rangle = \left\langle \frac{1}{N+1} \sum_{i=0}^{N} {s_i}^m {s_i}^n \right\rangle \quad m, n = 1, 2, 3, \tag{2.22}$$

[2] The term "θ-condition" corresponds to the $\chi = 1/2$ condition in *Flory-Huggins-Theory*, c.f. Fig. 1.2 on Page 3.

Architecture	$\langle {L_2}^2 \rangle_0 / \langle {L_3}^2 \rangle_0$	$\langle {L_1}^2 \rangle_0 / \langle {L_3}^2 \rangle_0$
linear chain	0.23	0.08
star $(f = 3)$	0.33	0.12
macro cycle	0.36-0.37	0.15-0.16
star $(f = 4)$	0.39-0.41	0.15-0.16

Table 2.3: *Examples of dimensionless ratios of the principal moments at θ-conditions. Values for the stars and macro cycles are taken from [136] and [184]. The number of beads per star arm is the same. Data for the linear chain from [182].*

with the brackets indicating an average over all equilibrium conformations of a chain of length $(N + 1)$.

The *individual components* of this matrix are dependent upon the particular choice of the reference system. The radius of gyration however is just a number and therefore the first invariant [3] that can be gained by the trace of $\mathbf{T}$:

$$\langle {R_g}^2 \rangle = \mathbf{Tr}(\mathbf{T}) = \langle T^{xx} \rangle + \langle T^{yy} \rangle + \langle T^{zz} \rangle . \tag{2.23}$$

The eigenvalues ${L_i}^2$ of $\mathbf{T}$ are the *principal moments* of the equivalent ellipsoid. In this work, the subscripts of the components ${L_i}^2$ are assigned such that ${L_1}^2 \leq {L_2}^2 \leq {L_3}^2$. The shape of a chain can be characterized by various manipulations of the principal moments.

2.4.1 Shape analysis

The *asymmetry* of chain conformations is characterized by the dimensionless ratios $1 \geq {L_2}^2/{L_3}^2 \geq {L_1}^2/{L_3}^2 \geq 0$ [182, 183]. Spherical symmetry requires ${L_2}^2/{L_3}^2 = {L_1}^2/{L_3}^2 = 1$. Averaging of the respective principal moments over many conformations obtained at equilibrium allows for a discussion of the asymmetry of conformations in terms of $\langle {L_2}^2 \rangle / \langle {L_3}^2 \rangle$ and $\langle {L_1}^2 \rangle / \langle {L_3}^2 \rangle$. Table 2.3 presents some examples of these dimensionless ratios for differently branched structures under θ-conditions.

Several additional measurements are useful to investigate other types of symmetries. These can be derived from the traceless form of the tensor $\mathcal{T}$:

$$\mathbf{T_{diag,trace=0}} = \mathbf{T_{diag}} - \frac{1}{3}\mathbf{Tr}(\mathbf{T})\mathbf{E}, \tag{2.24}$$

[3] The j^{th} invariant of a tensor $\mathcal{T}$ of rank 2 with eigenvalues λ_1, λ_2 and λ_3 is defined as the sum of all sub-determinants of order j, that is:

$$\begin{aligned} I_1 &= \lambda_1 + \lambda_2 + \lambda_3 = \mathbf{Tr}(\mathbf{T}) \\ I_2 &= \lambda_1\lambda_2 + \lambda_2\lambda_3 + \lambda_3\lambda_1 \\ I_3 &= \lambda_1\lambda_2\lambda_3 = \mathbf{det}(\mathbf{T}) \end{aligned}$$

where $\mathbf{E}$ is the unit tensor. Following *Mortensen's* treatment of the polarizability tensor [181], one can find another traceless tensor which is split into two terms, each consisting of a scalar and a constant numerical tensor:

$$\mathbf{T_{diag,trace=0}} = b\,\mathbf{T_{diag}}(2/3, -1/3, -1/3) + c\,\mathbf{T_{diag}}(0, 1/2, 1/2). \tag{2.25}$$

By comparison of Eq. (2.24) and (2.25), one yields definitions for the **asphericity** b and the **acylindricity** c as

$$b = \left\langle {L_1}^2 \right\rangle - \frac{1}{2}\left(\left\langle {L_2}^2 \right\rangle + \left\langle {L_3}^2 \right\rangle\right), \quad b \geq 0, \tag{2.26}$$

and

$$c = \left(\left\langle {L_2}^2 \right\rangle - \left\langle {L_3}^2 \right\rangle\right), \quad c \geq 0. \tag{2.27}$$

The value of b is zero if the considered chain has a tetrahedral or higher symmetry, otherwise $b > 0$. For very long linear SAW chains, $\langle b \rangle / \left\langle {R_g}^2 \right\rangle_0 = 0.66$ [196]. For shapes of cylindrical symmetry $c = 0$, otherwise $c > 0$. For long linear random walk chains, $\langle c \rangle / \left\langle {R_g}^2 \right\rangle_0 = 0.11$ [196].

Another definition of the asphericity which is most frequently used in literature was introduced by *Rudnick* and *Gaspari* [173] and *Aronowitz* and *Nelson* [9] and is defined as follows:

$$\delta^\star = 1 - 3\left\langle \frac{I_2}{{I_1}^2} \right\rangle = 1 - 3\left\langle \frac{{L_1}^2{L_2}^2 + {L_2}^2{L_3}^2 + {L_3}^2{L_1}^2}{({L_1}^2 + {L_2}^2 + {L_3}^2)^2} \right\rangle, \tag{2.28}$$

where the quantities I_i are the respective invariants of $\mathcal{T}$. For rod-like molecules, $\delta^\star$ takes a value of 1 and it vanishes for molecules with spherical symmetry. The analytical evaluation of $\delta^\star$ however is very difficult because the averaging of a *ratio* of fluctuating quantities is involved. Theoretical expressions are so far *only* available for linear chains. For linear random walks *Diel* and *Eisenriegler* [58] found $\delta^\star = 0.39427...$ in a $1/d$ expansion, where d is the dimension of space in which the polymer is embedded. *Jagodzinski et al* [105] calculated the ratio $\delta^\star$ with renormalization group methods and obtained $\delta^\star = 0.415$ and $\delta^\star = 0.394$ in a good and θ-solvent respectively.

Due to the above said, often a quantity δ is considered, instead of $\delta^\star$:

$$\delta = 1 - 3\frac{\langle I_2 \rangle}{\langle {I_1}^2 \rangle}. \tag{2.29}$$

In Eq. (2.29) the denominator and numerator are averaged *separately*. Therefore, theoretical expressions could be derived for this definition of asphericity, both, for linear [173] and star branched chains [212]. For infinitely large star branched random walk chains with f arms *Wei* and *Eichinger* found [212]:

$$\delta = \frac{150f^{-1} - 140f^{-2}}{135 - 120f^{-1} + 4f^{-2}}, \tag{2.30}$$

which is a generalization of the treatment by *Rudnik* and *Gaspari* [173] and reduces to $\delta \approx 0.5263$ with $f = 1$ for linear chains. By use of an ε-expansion [9] a slightly higher value of $\delta = 0.534$ has been found for self-avoiding random walks.

For a perfect sphere one gets $\left\langle {L_1}^2 \right\rangle / \left\langle {L_3}^2 \right\rangle = \left\langle {L_2}^2 \right\rangle / \left\langle {L_3}^2 \right\rangle = 1$ which immediately yields $\langle b \rangle = \langle c \rangle = \langle \delta \rangle = \langle \delta^\star \rangle = 0$.

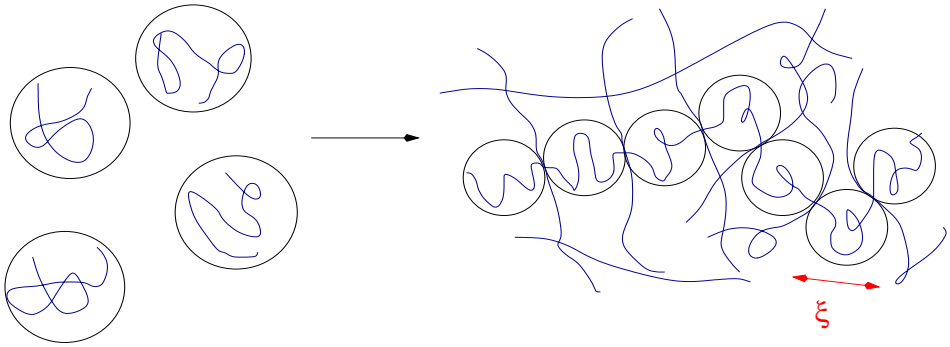

Figure 2.4: *Blob picture of polymer chains in dilute and semi-dilute solution. On distances r smaller than the screening length ξ the chain exhibits RW-behavior, whereas on length scales larger than ξ the concentration fluctuations have decreased so much that the excluded volume interactions do not play any role anymore and the chain behaves in an ideal (Gaussian) manner.*

2.5 Chain crossover and entanglement

2.5.1 The influence of concentration – blob picture

Polymer solutions are liquid mixtures of long polymer chains and small, light solvent molecules. Solvents interact with polymer molecules which generates additional varieties of sizes and shapes. In melts, macromolecules are "solvents" for their own kind. The conformation of a chain in solution is affected by temperature T just as much as by concentration c. The latter can be classified in three categories [192]: the dilute solution c', the semi-dilute solution $c^\star$ and the concentrated solution c''.

These three regimes are characterized by three important quantities: The number of elements N per chain, the segment density ρ and the correlation length ξ.

In a dilute solution, polymer chains behave like single blobs of radius $R = \xi \propto N^{3/5}$. The concentration c' is simply ρ/N, and the chains are separated from each other.

In the range between concentrated and dilute solutions there is a wide crossover concentration region at which the chain behavior can be appropriately described by the *blob picture* [56], see Fig. 2.4 and c.f. Fig. 1.2.

For a concentration just slightly above $c^\star$, the coils become entangled and a network of mesh size ξ is formed. An individual chain can then be divided into a sequence of blobs of radius ξ. At distances larger than $\xi \propto c^{-3/4}$, that is, outside the blobs, the chains behave in a Gaussian fashion, whereas inside the blobs the sub-chains obey SAW-statistics, as shown in Fig. 2.4.

2.5.2 The influence of solvent quality on chain conformations – excluded volume

A solvent is referred to as *good* when the prevailing form of the effective interaction between chain segments is the repulsive part of the potential energy at shorter distances. The chains tend to swell. In the opposite case of a *poor* solvent, polymers tend to shrink. The focus for the description of chains in different solvents is on an *expansion factor* that can be defined as

$$\alpha^2 = \frac{\left\langle \vec{R_g}^{\,2} \right\rangle}{\left\langle \vec{R_g}^{\,2} \right\rangle_0}, \tag{2.31}$$

where $\left\langle \vec{R_g}^{\,2} \right\rangle$ without the subscript $_0$ denotes the mean squared radius of gyration in the presence of excluded volume interactions. As N increases, α grows as $N^{1/5}$.

At the very point were the second virial coefficient A_2 intersects zero, the repulsive and attractive interactions just cancel each other which defines the θ*–point* and θ*–temperature*, respectively (c.f. Fig. 1.2 on Page 3). There are still three-body and higher interactions present in a θ–solvent, but their contribution to the free energy is negligibly small [56, 89].

To describe the distance of temperature T from the θ–temperature, a dimensionless parameter is used, the *reduced temperature* ζ which is defined as:

$$\zeta = \frac{T - T_\theta}{T_\theta} \quad \text{for} \quad T > T_\theta, \tag{2.32}$$

and

$$\zeta = \frac{T_\theta - T}{T_\theta} \quad \text{for} \quad T < T_\theta. \tag{2.33}$$

The argument of the crossover scaling function f is given by $\zeta\sqrt{N}$.

At θ–temperature,

$$f(\zeta\sqrt{N}) \simeq 1, \quad \zeta\sqrt{N} \ll 1, \quad R \propto R_0 \propto N^{1/2}. \tag{2.34}$$

At $T < T_\theta$,

$$f(\zeta\sqrt{N}) \simeq (\zeta\sqrt{N})^{1/3}, \quad \zeta\sqrt{N} \gg 1, \quad R \propto N^{1/3}\zeta^{1/3}. \tag{2.35}$$

At $T > T_\theta$,

$$f(\zeta\sqrt{N}) \simeq (\zeta\sqrt{N})^{3/5}, \quad \zeta\sqrt{N} > 1, \quad R \propto N^{3/5}. \tag{2.36}$$

2.6 Experimental methods

2.6.1 Scattering methods

Scattering methods are the most important methods for the direct determination of polymer shapes and dimensions. In particles, the incoming waves keep shifting electrons and nuclei relative to each other. This shifting creates induced dipoles which follow the oscillating electric field with the same frequency and produce scattered radiation. The more dipoles are generated per particle, i.e. per its mass or molar mass, the higher is the scattering intensity. The theory of scattering applies to any

wavelength. Most important for polymer science are visible light ($\lambda \approx 300\,\text{nm} - 700\,\text{nm}$), neutron beams ($\lambda \approx 0.1\,\text{nm} - 1\,\text{nm}$), X-rays ($\lambda \approx 0.02\,\text{nm} - 2\,\text{nm}$) and electron beams ($\lambda \approx 0.01\,\text{nm}$). *Static light scattering* depends on the difference in polarizabilities of polymers and solvents. **S***mall* **A***ngle* **X**-*ray* **S***cattering*, **SAXS**, registers differences in electron densities of solvents and polymers and **S***mall* **A***ngle* **N***eutron* **S***cattering* , **SANS**, differences in coherent neutron scattering lengths of, e.g. deuterated monomeric units and undeuterated solvent molecules. Static light scattering is the most affordable method, small angle neutron scattering the most expensive. An overview of these methods can be found in standard textbooks, e. g. [113, 188].

2.6.2 Viscometry

Dimensions of polymer molecules are not only obtainable by scattering experiments but also from the response of molecules to hydrodynamic forces, for example, during diffusion (see Sec. 4.2.4 for more details) and viscous flow. Viscometry of dilute solutions allows one to determine specific volumes of macromolecules that are directly related to the shape and dimensions of the dissolved molecules and indirectly to their molar masses. The viscosity η of dispersions of small spheres in solvents of viscosity η_s can be described by a power series with respect to the volume fraction $\phi = cN_L V_H/N$ occupied by the spheres with volume $V_H = \frac{4\pi}{3}{R_h}^3$:

$$\eta = \eta_s(1 + B_1\phi + B_2\phi^2 + \cdots). \tag{2.37}$$

The coefficient B_1 was calculated by Albert Einstein as $B_1 = 5/2$ for unsolvated, rigid spheres which is confirmed by experiment. The extension of the theory by *E. Guth* furnished $B_2 \approx 14.1$ [38]. Equation (2.37) can be applied to any polymer solutions, since macromolecules, being hydrodynamically impermeable, behave like hard spheres with volumes as given by the hydrodynamic radius R_h. The following definitions are useful in the context of polymer solutions:

relative viscosity	η_r	$=$	$\eta/\eta_s,$	(2.38)
specific viscosity	η_{sp}	$=$	$(\eta - \eta_s)/\eta_s,$	(2.39)
reduced viscosity	η_{red}	$=$	$\dfrac{1}{c}\,\eta_{sp}.$	(2.40)

The reduced viscosity of Eq. (2.40) is a quantity characteristic for a solute, which describes the soluted individual particles if they can move independently in the solvent. This usually is only the case for strongly diluted solvents which are easy to achieve with low-molecular substances. However, the dissolved coils of macromolecules on the other hand comprise almost all of the total available volume even at very high dilutions. The values obtained for η_{red} for such solutions are therefore not characteristic for the individual macromolecules, but they also contain contributions from interactions. In order to obtain information about size and shape of solvated macromolecules one has to perform an extrapolation to $c = 0$. This limiting value is called **intrinsic viscosity** and is defined as:

$$[\eta] = \lim_{c\to 0}\eta_{red} = \lim_{c\to 0}\frac{1}{c}\frac{\eta - \eta_{sp}}{\eta_{sp}} = \frac{5}{2}N_L V_H/N. \tag{2.41}$$

For the extrapolation of the reduced viscosity to zero concentration there exist several *empirical* equations, e.g. the *Huggins equation* for non-electrolytes:

object	α	d_f
swollen chain	0.8	5/3
ideal chain	0.5	2.0
hollow sphere	0.5	2.0
solid sphere	0.0	3.0
thin disk	0.5	2.0
thin rod	2.0	1.0

Table 2.4: *Examples of fractal dimensions d_f of several important particle shapes.*

$$\eta_{red} = [\eta] + k_H[\eta]^2 + \cdots \tag{2.42}$$

The *Huggins constant* k_H is a measure for the interaction of the solute particles with the solvent and usually has values between 0.33 and 0.8.

The dependence of intrinsic viscosities $[\eta]$ on molecular masses can often be described by the *empirical* **Kuhn-Mark-Houwink-Sakurada equation**:

$$[\eta] = K_\eta N^\alpha, \tag{2.43}$$

where K_η and α are system specific constants that depend on constitution, configuration and molar mass distribution of the polymer as well as on the solvent and temperature.

As by definition, the hydrodynamic volume scales as $V_H \propto {R_h}^3 \propto N^{3/d_f}$ one obtains

$$[\eta] \propto \frac{V_H}{N} \propto N^{3/(d_f-1)}, \tag{2.44}$$

which means that when using $\alpha = 3/(d_f - 1)$ and measuring $[\eta]$ as a function of N, one can determine the fractal dimension of a polymer which is an important information about shape and conformation. Table 2.4 summarizes fractal dimensions for a variety of particle shapes.

Chapter 3

Software design, algorithms and computer polymers

Table of Contents

This chapter first gives a short introduction of the two simulation techniques that were used in this work. It proceeds with a description of the implemented algorithmic optimizations that were used to speed up the integration scheme. This chapter ends with an illustration and discussion of the actual choice of the polymer model that was used and implemented on the computer. An annotated version of the simulation code that was written completely from scratch for this work can be found in the Appendix D.1.

3.1 Introduction

Computer simulations nowadays play a decisive and indispensable role as a helpful tool in many branches of science. In particular in polymer physics the use of computers proves very helpful due to the statistical nature of the investigated systems [26]. With many-particle systems which one usually has to deal with in polymer science, the use of computational methods allows one to test models by explicitly solving the appropriate equations of motion.

When performing simulations, usually a certain number N of particles are distributed in a cubic box [3]. The hyper surface of the potential among the particles generally is a function of the coordinates $\vec{r}$ of all particles and may be expressed by the following equation [108, 119, 130]:

$$V(r) = \sum_i v_1(\vec{r_i}) + \sum_i \sum_{j>i} v_2(\vec{r_i}, \vec{r_j}) + \sum_i \sum_{j>i} \sum_{k>j>i} v_3(\vec{r_i}, \vec{r_j}, \vec{r_k}) + \cdots . \tag{3.1}$$

The terms v_1, v_2, v_3, etc. are contributions due to external forces, pairwise and triple interactions. Mostly one assumes that the total potential can be written as a sum of simple pair-potentials. The term v_2 then can be considered to be an *effective* potential which, in the sum, contains many-particle contributions.

In essence, two different simulation methods have been developed: **Monte-Carlo (MC)** and **Molecular Dynamics (MD)**. Both are based on methods of statistical physics and probability theory and both were used in this work.

3.2 Monte-Carlo simulations

As the name implies, random processes, respectively random numbers, play a major role in this sort of simulation procedure. The MC-method allows one to change the location of a system in phase space in a stochastic way: With the aid of random numbers a specific coordinate in phase space is chosen and then changed according to certain side conditions. When using a good random number generator [1], see e.g. [157], the system thus will explore all available points in phase space after a long enough period of time.

In this work an implementation of *"RAN1"* of Ref. [157] was used for all computations that involved random numbers. In [78] there is an extensive test of *RAN1*, among several other pseudo-random number generators.

While there are many different variations of the MC-method, it can generally be divided into two groups which are described subsequently.

3.2.1 Simple sampling

The simulations of interacting many-particle systems are generally focused on the determination of ensemble averages, which represent the averages of physical thermodynamic quantities. For an observable A such averages can be written as many-dimensional integrals of the form

$$\int \int A(q,p,t)\rho(q,p,t)dpdq, \tag{3.2}$$

with ρ being the phase density of the corresponding statistical ensemble and p and q being the phase space coordinates. Characteristic of these ensemble averages is:

[1] Today, the most convenient and most reliable method of obtaining random numbers in practice is the use of a deterministic algorithm. Such a numerical method produces a sequence of *pseudorandom numbers* (PRNs) that mimic the statistical properties of true random numbers in the best possible manner.

- they are high-dimensional integrals, which in essence are dependent upon all coordinates and velocities of the considered N-particle system, e.g. $(N-6)$ – dimensional for a mono-atomic gas;
- they vary over many orders of magnitude, but only *very small* regions of phase space contribute to the averages.

Considering a canonical $(NVT–)$ ensemble, the corresponding average of some quantity A is given by

$$\langle A\rangle = \frac{\int\int A(q,p)e^{-\beta H(q,p)}\,dpdq}{\int\int e^{-\beta H(q,p)}\,dpdq}, \tag{3.3}$$

with $\beta = \frac{1}{kT}$ and the Hamiltonian

$$H(p,q) = \frac{1}{2m}\sum_{i=1}^{N}|\vec{p}_i|^2 + U(q). \tag{3.4}$$

$U(q)$ is the total potential energy and $\vec{p}_i$ is the momentum vector of the i-th particle. For an ideal gas $U(q) = 0$ and integration over p yields a factor of $(2\pi m k_B T)^{1/2}$ per degree of freedom. Consequently, the MC-method considers only configuration space, having eliminated the momentum part of phase space. The calculation of averaged quantities, such as $\langle A\rangle$, is thus reduced to the calculation of the configurational part which in turn is determined by the form of $U(q)$:

$$\langle A\rangle = \frac{\int\int A(q)e^{-\beta U(q)}\,dq}{\int\int e^{-\beta U(q)}\,dq}. \tag{3.5}$$

In general, Eq. (3.5) will be unsolvable for most considered systems, however, $\langle A\rangle$ can be approximated by replacing the phase space integrals by sums over a finite set of states S:

$$\langle A\rangle \approx \bar{A} = \frac{\sum_{i=1}^{S} A(S_i)e^{-\beta U(S_i)}}{\sum_{i=1}^{S} e^{-\beta U(S_i)}}. \tag{3.6}$$

Clearly, certain sets of states S will give a more accurate approximation of $\langle A\rangle$ than others. The **simple sampling** MC-method [26] uses equally distributed random numbers to select the S sampled states in phase space. Typical applications of this method in mathematics or physics are the calculation of volumes or surfaces by numerically calculating high-dimensional integrals [150], the numerical treatment of algebraic and differential equations or the simulation of lattice-systems, which is fundamental for many problems in solid state physics, e.g. the Ising-model or spin-systems. In combination with Percolation Theory [2] [187] the latter allows for the description of structural and transport properties as well as opening a door to the understanding of critical phenomena [31].

[2] This theory investigates the behavior of clusters on lattices and provides connections between cluster properties and lattice site distributions.

3.2.2 Importance sampling

The simple sampling MC-method has a severe drawback when the observable A is a strongly fluctuating function over the integration range. Any sharp peak in A will be missed by the simple sampling method. To overcome this problem, another Monte-Carlo method has been developed which is called **importance sampling**: One uses distributions of *weighted random numbers*, which allow for a shifting of sampled phase space points towards the areas where the function A changes the most. As a result, mostly those areas which contribute most to the phase space integral and hence are the most important ones, are sampled. This gives rise to the name *importance* sampling. The method of importance sampling was developed by *Metropolis, Rosenbluth et al.* [139] and yields the equation:

$$\langle A \rangle = \frac{\sum_{i=1}^{S} A(S_i) P^{-1}(S_i) e^{-\beta U(S_i)}}{\sum_{i=1}^{S} P^{-1}(S_i) e^{-\beta U(S_i)}}, \tag{3.7}$$

with $P(S_i)$ being the pre-defined probability with which states are chosen (importance sampling), such that the desired mean value is given by:

$$\langle A \rangle = \frac{1}{S} \sum_{i=1}^{S} A(S_i). \tag{3.8}$$

Clearly, for this to be true one requires $P(S_i) = P_{eq}(S_i) \propto e^{-\beta U(S_i)}$ and much of the art of MC-methods is to ensure that states are actually chosen with this probability [23], [24], [26].

Because $P_{eq}(S_i)$ at equilibrium is not explicitly known, one constructs a random flight of points S_i in phase space – a **Markov Chain** – in such a way that $P(S_i) \to P_{eq}(S_i)$ for $S \to \infty$. A sufficient condition for this to hold is that the transition probability $T(S_i \to S_{i'})$ for the transition from state S_i to state $S_{i'}$ fulfills the condition of **detailed balance**:

$$P_{eq}(S_i) T(S_i \to S_{i'}) = P_{eq}(S_{i'}) T(S_{i'} \to S_i). \tag{3.9}$$

This is the requirement of reversibility of states on a microscopic scale. From Eq. (3.9) one yields:

$$\frac{T(S_i \to S_{i'})}{T(S_{i'} \to S_i)} = e^{-\beta \delta U}, \tag{3.10}$$

with $\delta U = U(S_{i'}) - U(S_i)$. The ratio of transition probabilities is only dependent upon the *difference* of the potential energy of configurations S_i and $S_{i'}$. This does not specify $T(S_i \to S_{i'})$ in a unique way. According to Metropolis, one takes a convenient choice of T which is consistent with the principle of detailed balance:

$$T(S_i \to S_{i'}) = \begin{cases} e^{-\beta \delta U} & \delta U > 0, \\ 1 & \text{otherwise.} \end{cases} \tag{3.11}$$

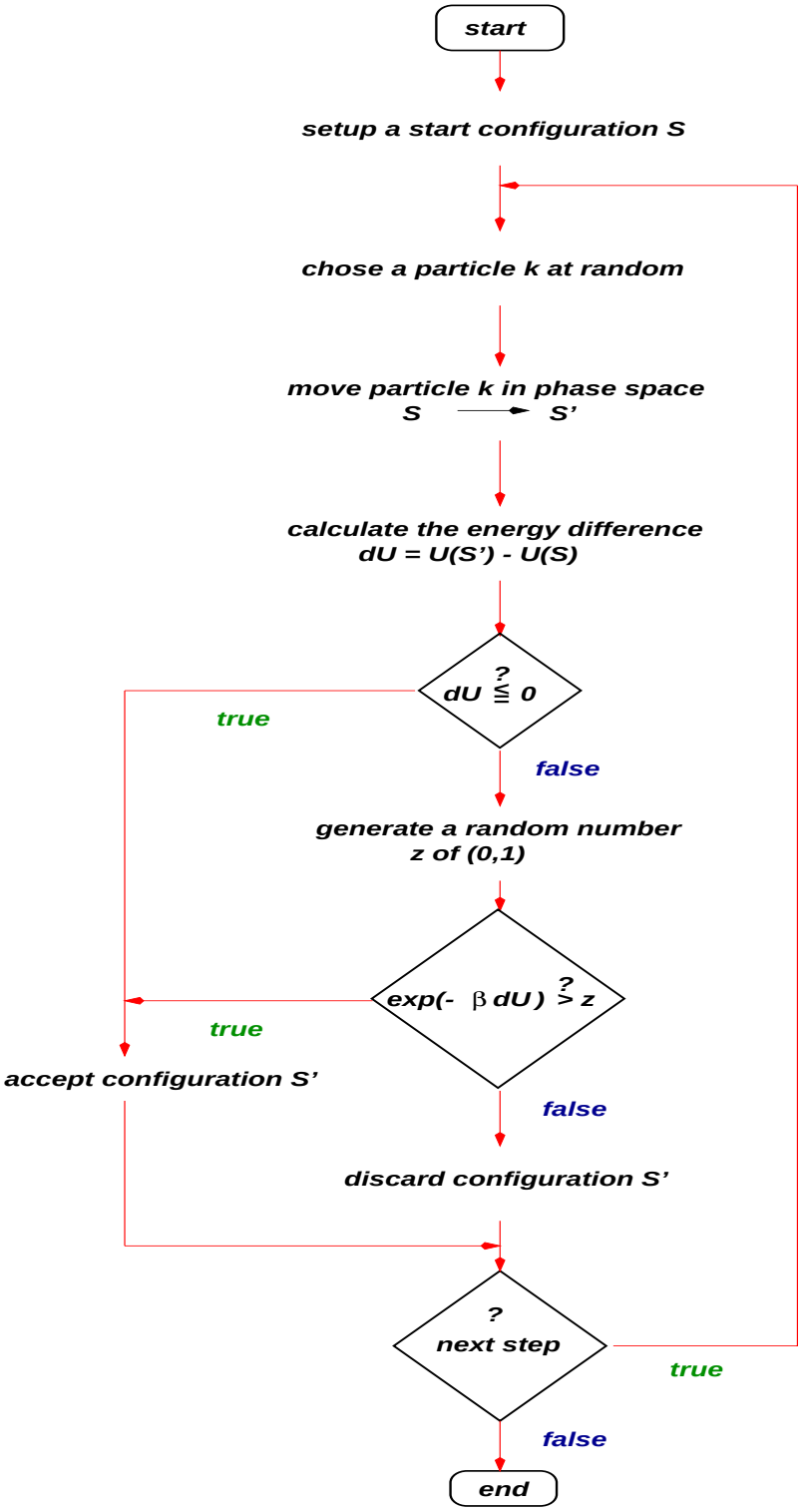

Figure 3.1: *The Metropolis algorithm as it was used in this work.*

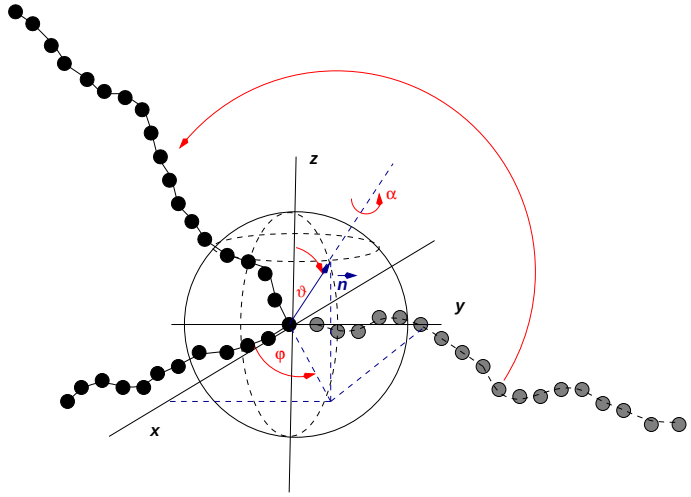

Figure 3.2: *Illustration of a pivot move. The grey-shaded part of the chain is rotated about a randomly chosen normal vector* $\vec{n}$.

The proof of convergence to the average of the desired canonical ensemble can be done with the aid of the *central limit theorem*, see e.g. [69]. *Metropolis et al.* give reasons for the correct convergence behavior on physical grounds [139]. In [204] it was shown that valid Monte-Carlo simulations can be obtained by sampling schemes that do not obey strict detailed balance as long as the set of Monte-Carlo moves leaves the Boltzmann distribution invariant and therefore leads to *regular* sampling. An overview of the Metropolis algorithm is given in the flow diagram of Fig. 3.1 on Page 25.

3.2.3 The pivot algorithm

Chain polymers were among the first objects simulated on electronic computers and they still present a challenge, because of the particular structure of this problem which involves the relaxation of the chain on different length scales. Straightforward algorithms such as *simple sampling* are often inefficient and a whole host of methods has been proposed, all with certain merits and disadvantages [23, 25, 26]. One very efficient method to obtain equilibrium samples on a simple-cubic lattice was proposed in [82, 83]. This method combines the Rosenbluth-Rosenbluth method with recursive enrichment and is called *PERM* (**P**runed-**E**nriched **R**osenbluth **M**ethod).

Today it seems that the **pivot algorithm**, which was proposed *by M. Lal* in 1969 [118] is the most popular one in order to gain equilibrium samples of single chains in the continuum or on a lattice.

Pivoting a chain in its configuration space proved to be most efficient for relatively open, dilute systems such as isolated linear chains [129, 227], but also for self-avoiding star-branched polymers [224, 225], where the segment density near the branching point is relatively large in comparison with the linear chain. The algorithm proved very efficient for both, lattice and continuum models [24]. However, it becomes inefficient in dense or constrained systems where most of the *global* moves (which make it fast in dilute systems) are rejected due to overlaps with other chains.

An illustration of a pivot move with a linear chain is given in Fig. 3.2: A configurational change of the chain is achieved by rotating one part of the chain around a randomly selected bond. This new configuration undergoes a Metropolis algorithm according to which the new configuration is either accepted or rejected. Thus, the pivot algorithm fits perfectly into the scheme of the Metropolis

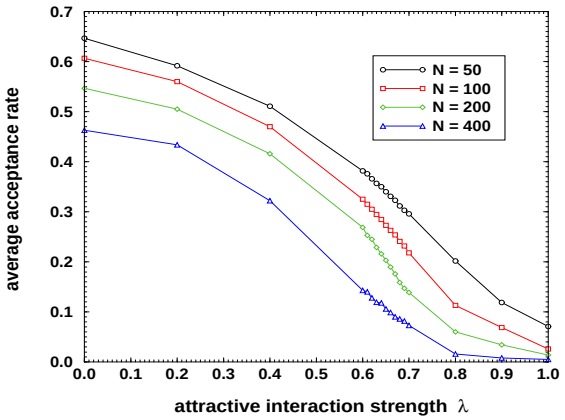

Figure 3.3: *Acceptance rate of pivot moves for linear chains as a function of the molecular weight N and the interaction strength λ during a hybrid-simulation in which pivot moves were used alternately with MD simulation steps. Only for very dense systems and very long chains the pivot algorithm does become inefficient.*

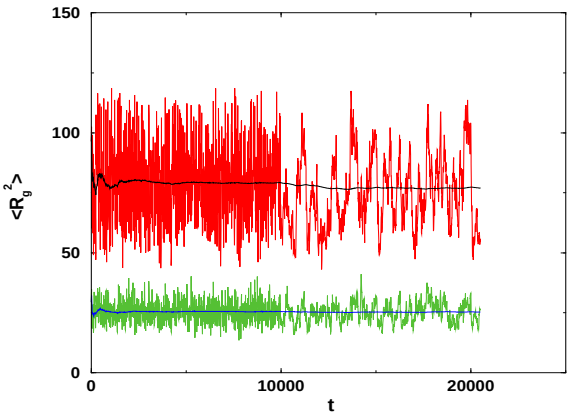

Figure 3.4: *Time evolution of $\langle {R_g}^2 \rangle (t)$ for an ensemble of 100 star polymers with $f = 4$ and $N_{arm} = 50$ monomers per arm. Time is displayed in Lennard-Jones units (see Section 3.4 on Page 40 for details). The upper curve displays $\langle {R_g}^2 \rangle (t)$ of the whole star. The lower curve corresponds to $\langle {R_g}^2 \rangle (t)$ averaged over the individual star-arms. After 10^6 integration steps the pivot moves were switched off and only Stochastic Dynamics simulation (see Section 3.3.1.2) steps were performed.*

algorithm with the only difference being that a whole part of the chain is moved in phase space as opposed to a single particle in the original scheme.

The pivot algorithm was applied in all simulations of single chains in this work: After having chosen at random a particle k with coordinate $\vec{r}_0$ of the chain as spin center, all the rest of the chain (to say, all particles with indices larger than k) is rotated about this particle k. To achieve this, a random rotation matrix $\mathcal{R}$ is calculated for each pivot move such that for the new positions $\vec{r}\,'$ of the rotated part the following equation holds:

$$\vec{r}\,' = \vec{r}_0 + \mathcal{R}_{\vec{n},\alpha}(\vec{r} - \vec{r}_0). \tag{3.12}$$

The random rotation matrix $\mathcal{R}$ is given by a normal vector $\vec{n} = \vec{n}(\vartheta, \varphi)$ in spherical coordinates and a rotation angle α. $\mathcal{R}$ applied to a vector $\vec{r}$ yields:

$$\mathcal{R}_{\vec{n},\alpha}\vec{r} = \vec{r}\cos\alpha + (\vec{n}\vec{r})(1 - \cos\alpha)\vec{n} + (\vec{n} \times \vec{r})\sin\alpha, \tag{3.13}$$

where α, φ and $\cos\vartheta$ are chosen equally distributed from the interval $[0, 2\pi]$ and $[-1, 1]$, respectively. A derivation of Eq. (3.12) can be found in Appendix C on Page 165.

The global moves of the pivot algorithm allow for a fast relaxation of a chain on large length scales. To speed up the relaxation on short length scales, too, MD simulation steps were also performed at certain time intervals. In Fig. 3.3 the efficiency of the pivot moves when applying this hybrid-algorithm is shown for different chain lengths and different values of the interaction parameter λ which will be defined in a subsequent chapter. The acceptance rate is well above 50% for

smaller systems and also under θ – conditions, in the vicinity of $\lambda \approx 0.65$, one still has a high enough acceptance of global moves to relax the chains very efficiently.

The fast relaxation by pivot moves is displayed in Fig. 3.4 which shows the time evolution of $\langle {R_g}^2 \rangle$ for a branched system at equilibrium. As long as pivot moves are performed the radius of gyration fluctuates very fast about an average value. As soon as no pivot moves are done anymore the autocorrelation function of the system is increased.

3.3 Molecular Dynamics simulations

In MD simulations, random numbers, if at all, are only used to set the initial conditions of a system or when one uses a heat bath to which the investigated system is to be coupled. Other than that the MD-approach evolves the considered system in phase space in a quasi-deterministic manner.

The MD-method was first proposed by *Alder* and *Wainwright* [5, 6]. They investigated a liquid of hard spheres. The first simulation of a more realistic continuous model of a liquid was published by *Raman* in 1964 [159]. He simulated liquid Argon using a set of Lennard-Jones particles. In 1971 it followed the investigation of a liquid – melted Carbon-Chloride – with coulomb interactions by *Woodcock* [221]. Shortly after this, *Rahman* and *Stillinger* reported on the simulation of water [160]. Influenced by these first successes the field of computer simulation developed rapidly and has been extended to many fields of interest, such as biology, bio-physics, chemistry and branches of engineering [106, 153].

A MD simulation program can generally be divided into three main parts, see Fig. 3.5.

1. The initialization of chains with coordinates and velocities.

2. Calculation of all forces acting upon each single particle.

3. Integration of the equations of motion using the positions, coordinates and forces of all particles.

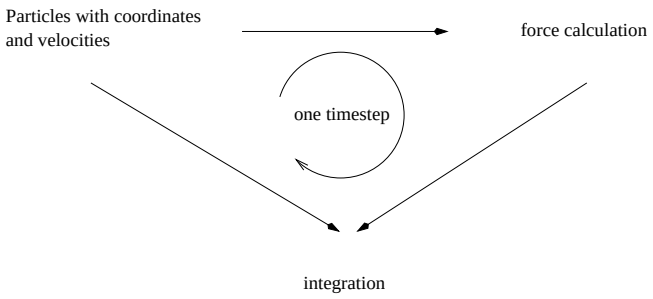

Figure 3.5: *General scheme of a Molecular Dynamics simulation.*

3.3.1 Integration scheme

Usually, in MD simulations, the classic equations of motion for the movement of a system of interacting point particles are solved numerically for many successive time steps Δt [3] with fixed boundary conditions. The individual particles of the considered system interact via phenomenological potentials which are to be as realistic as possible, but also numerically simple. In the simplest case one considers the Newtonian equations of motion for a system in a cubic simulation box.

The cubic box is used almost exclusively in MD simulations, due to its simple geometry in comparison to the other space-filling bodies, among which the Dodecahedron and the Octahedron are used particularly [3]. Spherical boundary conditions have also been investigated, with which the three-dimensional system is treated as surface of a hyper sphere [112].

3.3.1.1 Integration scheme for a NVE-ensemble

As for integration schemes, many different methods for different ensembles have been proposed [8, 80, 81, 90, 91, 97, 99, 161]. Quite common in simulations are different versions of the *Verlet algorithm* [205, 206].

In this work, a particular implementation of the Verlet algorithm, the *velocity-Verlet algorithm* [193], was used, which calculates the positions $\vec{r}$ and velocities $\vec{v}$ of i particles, exerted to external forces $\vec{F}_i$, as follows (see Fig. 3.6):

$$\vec{r}_i(t+\Delta t) = \vec{r}_i(t) + \Delta t \vec{v}_i(t) + \frac{\Delta t^2}{2m_i}\vec{F}_i(t), \tag{3.14}$$

$$\vec{v}_i(t+\Delta t) = \vec{v}_i(t) + \frac{\Delta t}{2m_i}\left(\vec{F}_i(t) + \vec{F}_i(t+\Delta t)\right). \tag{3.15}$$

This algorithm is very apt for the simulation of a *micro canonical* ensemble as it is time-reversible and keeps the total energy constant. Generally, when using a simulation box with hard walls, neither the total linear momentum $\vec{P}$, nor the total torque $\vec{L}$ are constants of motion. However, due to the use of *periodic boundary conditions* in the system (for details see Section 3.3.3.2), $\vec{P}$ becomes a conserved quantity. By rescaling the velocities of the particles at the beginning of the simulation such that $\vec{P} = \vec{L} = \vec{0}$, one avoids artificial movements of the system. If, in the following, no energy is added to or removed from the system, e.g. by velocity-dependent external forces, it follows $\frac{\partial H}{\partial t} = 0$ and hence energy conservation.

The system is simulated at the desired temperature T by rescaling the particle velocities at the beginning of the simulation in a way such that the classic partition theorem

$$\langle E_{kin} \rangle = \left\langle \frac{1}{2}\sum_{i=1}^{N} m_i {v_i}^2 \right\rangle = \frac{3}{2} N k_B T \tag{3.16}$$

[3] Unless otherwise stated, all time units are given in reduced *Lennard-Jones* units $\tau = \sigma\sqrt{m/\varepsilon}$. For further details refer to the comments on Page 40 in Section 3.4.

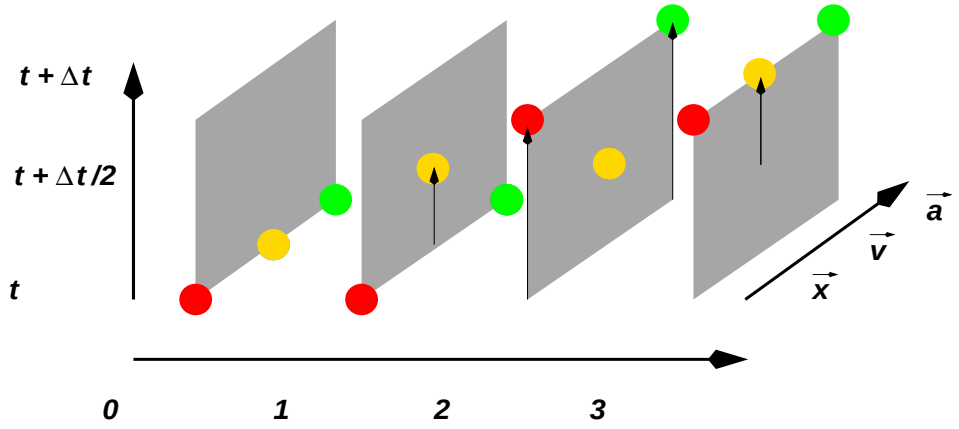

Figure 3.6: *Illustration of the velocity-Verlet integration scheme. The initial conditions are given by positions $\vec{x}(t)$, velocities $\vec{v}(t)$ and forces $\vec{a}(t)$ at time t. In Lennard–Jones units (see bottom of Page 40 for more details), the force is identical with acceleration $\vec{a}$. In the first step, the new velocities after a time $t + \Delta t/2$ are calculated. In the second step, the new positions $\vec{x}$ after a full timestep $t + \Delta t$ are determined along with the new forces acting upon the particles at their new positions. In the closing third step the new velocities $\vec{v}(t+\Delta t)$ of the particles are calculated.*

is fulfilled. This integration scheme is rather stable at a timestep Δt in the range of $\Delta t \approx 0.002 - 0.005\,\tau$.

The disadvantage of this integration scheme lies in the rather slow dynamics due to the small timestep, and, even more critical, the fact that the energy conservation impedes the system from attaining its equilibrium state.

3.3.1.2 Integration scheme for a NVT-ensemble

To simulate a *canonical ensemble* one has to couple the system to a heat bath. This can be done in several ways. A method was developed by *Nosé*, which couples the system to a heat bath by enlarging the degrees of freedom of phase space [151, 152] and a modified version was introduced in [220].

For the implementation in this work, a different coupling-method was chosen which controls the energy fluctuations on a *local* scale by splitting the force $\vec{F}(t)$ into a slowly changing friction force $\vec{F}_\gamma$ of Stoke's type and a fast fluctuating stochastic force $\vec{F}_S$. This leads to integrating a *Langevin Differential Equation*:

$$\ddot{\vec{r}}\,(t) = -\gamma\vec{v}(t) + \vec{f}(t) + \vec{\Gamma}(t), \tag{3.17}$$

with $-\gamma\vec{v}(t) = \vec{F}_\gamma/m,\ \vec{f}(t) = \vec{F}/m,\ \vec{\Gamma}(t) = \vec{F}_S/m$ and γ being the friction coefficient.

This kind of integration schemes is generally called **Stochastic Dynamics (SD)** or **Brownian Dynamics (BD) simulations** [4].

[4] In [90] a distinction between SD and BD simulations is made in terms of the latter referring only to stochastic forces which are void of space and time correlations. Sometimes the term BD simulations is used in literature referring to the over-damped case only. In this work no distinction will be made and both terms are used interchangeably.

One considers a *Gibbs Ensemble* of many identically prepared systems which consist of i particles each. For each one of these systems there is a Langevin-force $\vec{\Gamma}_i(t)$, the properties of which follow from the *fluctuation-dissipation theorem* [59, 162]:

$$\gamma = \frac{1}{6k_BT} \int_{-\infty}^{\infty} \left\langle \vec{\Gamma}_i(0)\vec{\Gamma}_j(t) \right\rangle dt. \tag{3.18}$$

Eq. (3.18) elucidates the connection between the energy dissipation of a system due to a frictional force with coefficient γ and the thermal fluctuations due to the influence of the surrounding.

- $\vec{\Gamma}_i(t)$ is as often positive as negative, such that the average vanishes:
  $\left\langle \vec{\Gamma}_i(t) \right\rangle = 0.$

- The time-correlation of $\vec{\Gamma}_i(t)$ is a δ–function:
  $\left\langle \vec{\Gamma}_i(t)\vec{\Gamma}_j(t') \right\rangle = \left\langle \vec{\Gamma}_i(0)\vec{\Gamma}_j(t-t') \right\rangle = 6\gamma k_BT\delta(t-t')\delta_{ij}.$

- There is no correlation of $\vec{\Gamma}_i(t)$ with velocities at an earlier time:
  $\left\langle \vec{v}_i(0)\vec{\Gamma}_j(t) \right\rangle = 0 \quad \text{for} \quad t \geq 0.$

- There also is no correlation of $\vec{\Gamma}_i(t)$ with other external forces $\vec{F}(t)$:
  $\left\langle \vec{F}_i(0)\vec{\Gamma}_j(t) \right\rangle = 0 \quad \text{for} \quad t \geq 0.$

The above properties of the forces can be fulfilled by Gaussian distributed random numbers. In [85] it was shown that also equally distributed numbers can be used which is numerically more advantageous. Integrating Eq. (3.17) after introducing the stochastic forces $\vec{\Gamma}_i(t)$ requires changing the integration algorithm according to the following equations:

$$\vec{r}_i(t+\Delta t) = \vec{r}_i(t) + \Delta t\vec{v}_i(t)\left[1 - \gamma\frac{\Delta t}{2m_i}\right] + \frac{\Delta t^2}{2m_i}\vec{T}_i(t), \tag{3.19}$$

$$\vec{v}_i(t+\Delta t) = \frac{\vec{v}_i(t)\left[1 - \gamma\frac{\Delta t}{2m_i}\right] + \frac{\Delta t}{2m_i}\left[\vec{T}_i(t) + \vec{T}_i(t+\Delta t)\right]}{1 + \gamma\frac{\Delta t}{2m_i}}, \tag{3.20}$$

with total force

$$\vec{T}_i = \vec{F}_i + \vec{\Gamma}_i. \tag{3.21}$$

The use of a stochastic term in the equations of motion explicitly destroys time-reversibility and avoids ergodicity problems of micro-canonical simulation schemes. It allows for a larger time step $\Delta t \geq 0.005\,\tau$ in the simulation as the coupling to a heat bath generally makes a simulation more stable. In this work, for all simulations a timestep of $\Delta t = 0.01\,\tau$ and a friction coefficient of $\gamma = 1.0$ were used. On the other hand, with stochastic simulations, it is not possible to investigate properties depending on long range correlations such as hydrodynamic interactions.

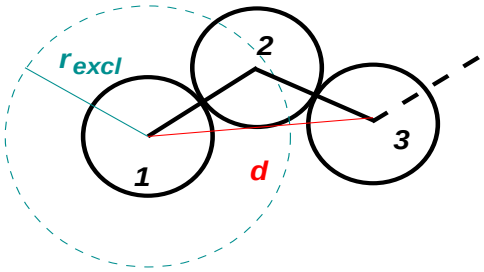

Figure 3.7: *Illustration of the backwards excluded volume of the initial chain generation.*

3.3.2 Setup of chains

The initial configuration of chains in the simulation box is generated one particle at a time by means of a random-process. The first monomer is chosen at random in the simulation volume. The second one is chosen in the same manner with a step length of $l_b = 0.97$, the equilibrium distance of Eq. (3.22). The location of the third and all subsequent particles, however, are only accepted if $d > r_{\text{excl}} = 1.02\sigma^2$, see Fig. 3.7. By way of this process, a random walk of monomers is created which corresponds to the static properties of polymers in a dense melt.

The manner in which the chains are initially generated, leads to possible singularities in the potential at the beginning of a simulation run, due to overlapping monomers. Therefore, one has to perform a *warmup procedure* which gradually switches on the full excluded volume interaction. This is done in the following manner: First of all, the absolute minimum distance d_{min} between *all* particles is calculated. Then the system is integrated for 1.000 time steps. However, instead of taking the actual, *calculated* distance r for the potential of Eq. (3.23), the distance $r' = r + \Delta d - n\Delta d/1000$ is used in each time step n with $\Delta d = r_{\text{cut}_{\text{max}}} - d_{\text{min}}$. By this shifting of distances during the warmup integration one gradually moves along the potential curve of Eq. (3.23) with more and more particles gradually being exposed to their actual potential, until, after 1.000 steps the full excluded volume is effective for all particles. This method has been tested extensively and works very well for all types of systems, e.g. linear or branched chains in a melt or in dilute solution.

In Figures 3.8 to 3.11 the instantaneous minimum squared distance ${d^2}_{\text{min}}$ of various systems during the warmup procedure and the first following-up 1000 MD-steps are displayed. At the beginning, ${d^2}_{\text{min}}$ in all cases expect for the linear chain in dilute solution is very small and the particles are only exerted to a very small effective potential.

After about 600 warmup integration steps the monomers start to "feel" the excluded volume forces which leads to a continuous increase of ${d^2}_{\text{min}}$ until at 1000 MD steps all particles are exerted to the *full* excluded volume forces. This is reflected in the saturation of ${d^2}_{\text{min}}$ after the warmup procedure. The value at which ${d^2}_{\text{min}}$ saturates, will, of course, be dependent upon the density of the monomers in the considered system. Due to this, ${d^2}_{\text{min}}$ after saturation is the lowest for the dense melt system in Fig. 3.11, and the largest for the linear chain in dilute solution.

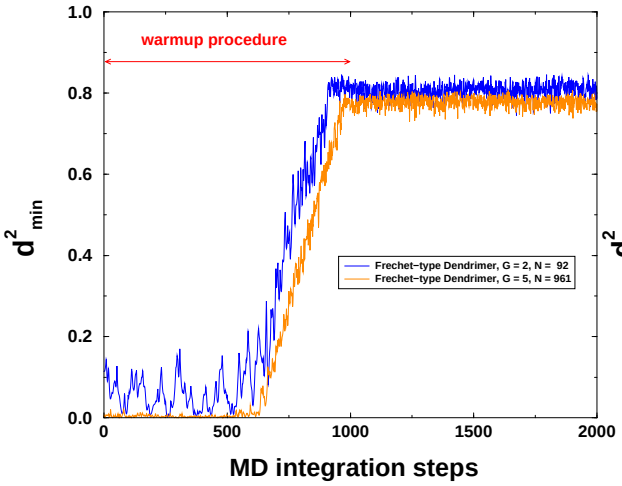

Figure 3.8: *Instantaneous squared minimum distance of all particles during the warmup procedure for Frechét dendrimers. After 1000 integration steps the* full *LJ-potential acts upon all particles.*

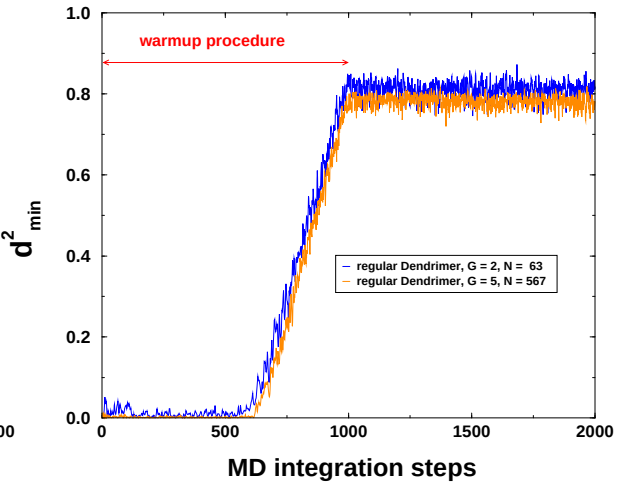

Figure 3.9: *Instantaneous squared minimum distance of all particles during the warmup procedure for regular dendrimers in dilute solution. After 1000 integration steps the* full *LJ-potential acts upon all particles.*

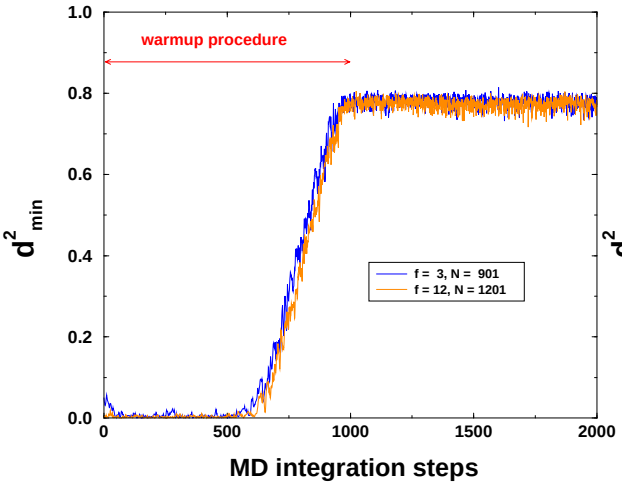

Figure 3.10: *Instantaneous squared minimum distance of all particles during the warmup procedure for star polymers in dilute solution. After 1000 integration steps the* full *LJ-potential acts upon all particles.*

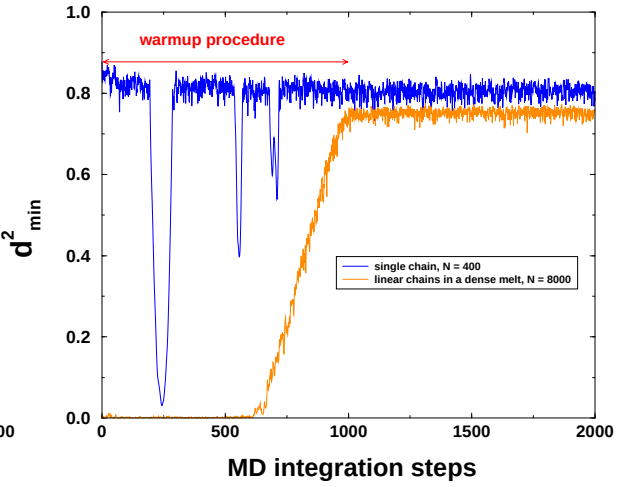

Figure 3.11: *Instantaneous squared minimum distance of all particles during the warmup procedure for linear chains in dilute solution and in a dense melt with* $\rho = 0.85$ *and 20 chains of length* $N = 400$*. After 1000 integration steps the* full *LJ-potential acts upon all particles.*

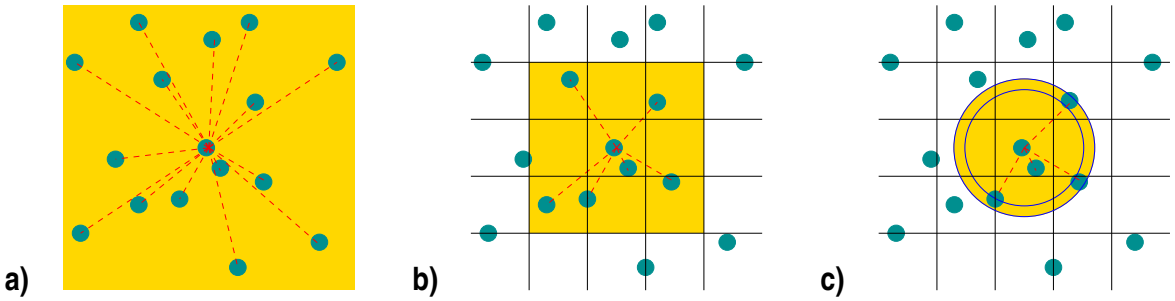

Figure 3.12: *Different approaches to the force calculation in a Molecular Dynamics simulation according to [161]. For clarity, the situation in two dimensions is shown. The color-coded regions display the size of the area that is scanned for interacting atom pairs*

3.3.3 Optimizations

3.3.3.1 The search-algorithm for the forces

In MD simulations, more than 97% of computation time is used up for the force calculations. Therefore all optimization efforts are usually devoted to the search-algorithm that determines the interacting particle-pairs. In [8] and [161], one finds a compilation of different strategies which are sketched in Fig. 3.12.

a) N^2*-loop approach.* This is the "brute-force" approach. The distances between *all* particle pairs in the central simulation box are calculated. It is the most costly method and only suitable for systems of up to a few hundred particles.

b) *Linked-cell-method.* The linked-cell algorithm owes its name to the way in which the particle data are arranged in computer memory, namely as linked-list. The central box is divided into sub-cells which have a length of at least one interaction cutoff r_{cut}. Thus, the number of distance calculations is restricted to those particle pairs of neighboring cells only.

For this method to function the size of the simulation box has to be at least $3r_{\text{cut}}$. For simulations of dense melts with many particles, this requirement is usually met. By this method, the search-loop effort is reduced to $\mathcal{O}(N)$, but with a pre-factor that still can be very large, depending on the density of particles ρ and the interaction range r_{cut}.

c) *Linked-cell-method with neighbor-lists.* In addition to the cell subdivision there is a neighbor list of potentially interacting atom pairs. Only the atom pairs within the inner circle of radius r_{cut} actually interact with each other. However, the area *between* the outer circle of radius $(r_{\text{cut}} + r_{\text{skin}})$ and the smaller one is also covered by the neighbor list for one of the atoms. Thus, this list contains not only actually interacting particles at some specific time, but it also contains all atoms that might enter the interaction range of the inner circle within the next few time steps. This greatly speeds up the simulation, because the list of potentially interacting particles will be valid for several time steps, in the order of 5–15, before it has to be rebuilt. The interval, at which list-reconstruction has to be done, depends upon r_{cut}, the particle density ρ and the skin radius r_{skin}. Once a particle has moved a distance larger than $d^2 = \left(\frac{r_{\text{skin}}}{2}\right)^2$, the update is due. The accumulated distance that each particle moved can be readily monitored during the distance calculation. Extensive tests of the implementation of this work with $r_{\text{cut}} = 1.5\sigma$ and $\rho = 0.85\sigma$, which were used throughout all simulations, showed that a radius of $r_{\text{skin}} \approx 0.35\sigma$ to 0.40σ is the optimal choice, see Fig. 3.13.

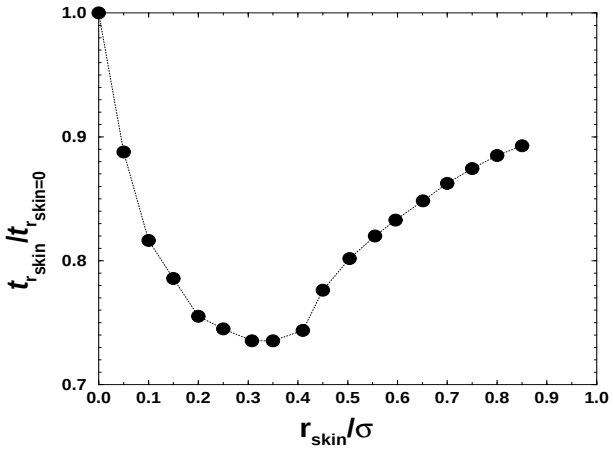

Figure 3.13: *Optimization of the simulation time t vs. the skin radius r_{skin}. The simulation time t is given in reference to a simulation with $r_{skin} = 0$.*

The length d_i of the sub-cells in each direction is given by $L_i/\text{modulo}(L_i/r_{\text{cut}_{\text{max}}})$ with L_i being the box size in each direction and $r_{\text{cut}_{\text{max}}}$ being the largest cutoff of all potentials that are used. The sub-cells are numbered, beginning with the one in the lower left corner of the simulation box where the origin of the coordinate system is located. Each time when an update of the verlet list is due, the particles are periodically back-folded into the simulation box and then sorted into the different sub-cells according to their coordinates. Subsequently, only the distances of particles of neighbor cells are calculated, with each sub-cell having 26 neighbors in three dimensions. Due to Newton's third law only half of them have to be considered. Fig. 3.14 displays the division of the simulation box into n_i sub-cells in each direction i and how these different sub-cells are scanned through. The search algorithm, as it was implemented in this work, first considers all particles of the cell itself and then scans through all remaining 13 neighbor cells.

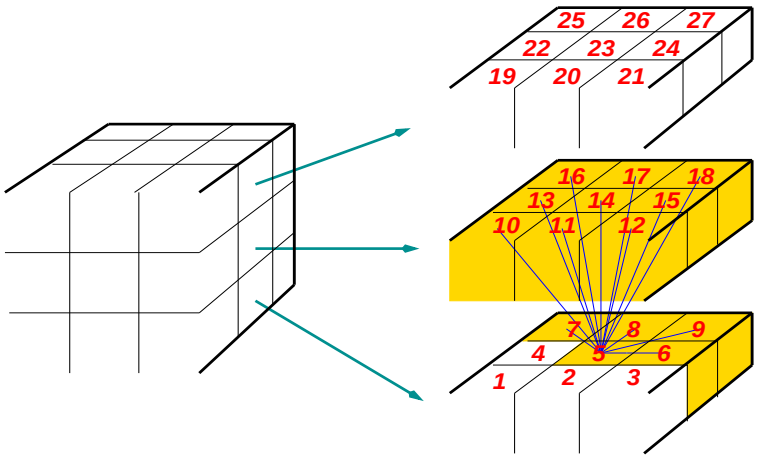

Figure 3.14: *Dividing the simulation box into sub-cells and scanning through them. All particles of the neighboring 14 sub-cells (including the cell itself) of cell number 5 are considered in this example. If one gets beyond the simulation box boundaries when scanning through cells with this algorithm, the particles of the corresponding periodic sub-boxes are considered instead.*

3.3.3.2 Ghost particles

In a MD simulation one can only investigate the properties of a relatively small number of particles compared to a real system. Therefore one introduces *periodic boundary conditions* for the volume in which the system is located. By way of performing this, the anisotropic forces that are ”felt” by particles close to the surface are suppressed. Thus, surface effects are removed and the overall density of the system is kept constant. One only measures properties of ”bulk” particles which are far away from the surface.

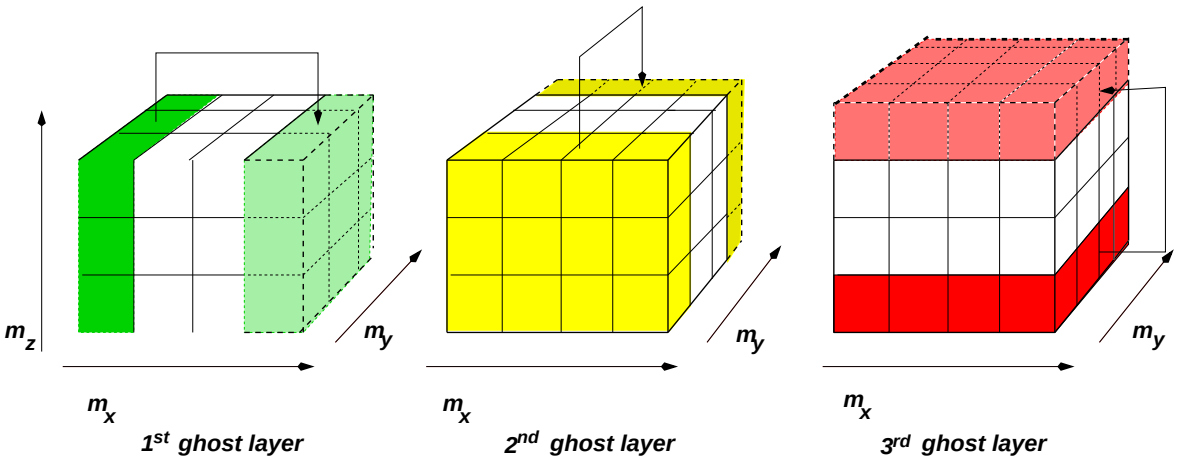

Figure 3.15: *Construction of the different ghost cell layers.*

The periodic boundary conditions are realized by performing distance calculations taking into account the *minimum image convention* according to which the real distance between any two particles is given by the shortest distance of any of their images. Once a particle has crossed the boundaries it is periodically back-folded into the simulation box. In the language C this can be conveniently done by the following lines of code:

$$dx -= L_x * \mathbf{anint}(dx/L_x);$$
$$dy -= L_y * \mathbf{anint}(dy/L_y);$$
$$dz -= L_z * \mathbf{anint}(dz/L_z);$$

where

$$\mathbf{anint}(x)(\,(double)(\,(int)(\,((x) + 0.5) - ((x) < -0.5)\,)\,)\,)$$

returns the next positive integer. This periodic wrap-around is done in the *innermost* loop of the force calculation and therefore is extremely expensive in terms of simulation time.

Consequently, another method of gaining speed in a MD simulation is to remove any mentioning of periodic boundaries in the force calculations. This can be done by using the concept of *ghost particles*, see e.g. [161].

With this concept, there are two sets of coordinates. The back-folded *periodic coordinates* which are used to sort the particles into the sub-cells and the *free coordinates* which are not back-folded at all and which are the ones used for later calculations of observables.

The idea with the ghost particles is the following: All particles that are in sub-cells which are on the surface of the simulation box are being duplicated right away into the extra ghost cells surrounding the whole box. These ghost particles are now used for distance calculations instead of the original

coordinates. As a result, the periodic back-folding only has to be done for a relatively small number of surface particles in the outermost sub-cells, but not anymore for the many particles in the force calculations.

As a result of Newton's third axiom, one actually needs only half of the ghost cells surrounding the original box. Figure 3.15 displays how the individual ghost layers in each direction are set up in the implementation of this work: An individual sub-cell can be identified by three integers (m_x, m_y, m_z). First of all, all particles of sub-cells with $(m_x = 1, m_y = 1, .., n_y, m_z = 1, .., n_z)$ are duplicated into the appropriate ghost cells. The second ghost layer contains particles pertaining to $(m_x = 1, .., n_x, m_y = 1, m_z = 1, .., n_z,)$ *including* the ghost particles of the first layer. Finally, the third ghost-layer contains particles with $(m_x = 1, .., n_x, m_y = 1, .., n_y, m_z = 1)$ *including* the ghost particles of layers 1 and 2.

The number of adjacent neighbor cells now depends upon the location of the considered cell. In a cube there are 18 different cases and according to Newton' s third law only half of them need to be considered. The sub-routine that contains the search algorithm which examines adjacent cells makes provision for all 9 different cases. The *number* of adjacent cells for these different cases is fixed, see Fig. 3.16, and can be written in a static array. The *location* of the respective adjacent cells can be found by using exactly the same search algorithm as before (see Fig. 3.14), only considering the following simple but crucial restriction:

All ghost cell pairs of the same ghost layer have to be left out.

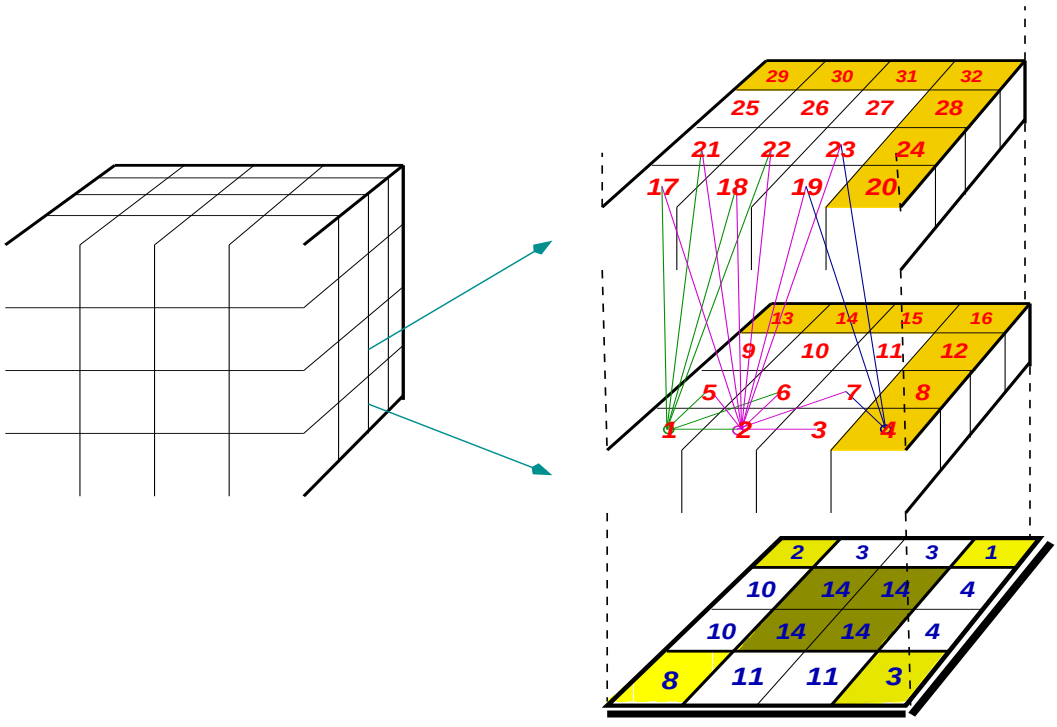

Figure 3.16: *Illustration of the search-algorithm for ghost particles with a fixed number of neighbor cells depending upon the location of the considered cell. The lowest square depicts the* 9 *possible cases of cell locations and displays the respective number of neighbor cells, always including the cell itself. For clarity, some of the cell locations are colored. Two layers of the simulation box are displayed along with the numbering of the sub-cells. The ghost cells are color-coded. As an example, the locations of the adjacent sub-cells that are scanned by the search-algorithm are displayed for three different sub-cells.*

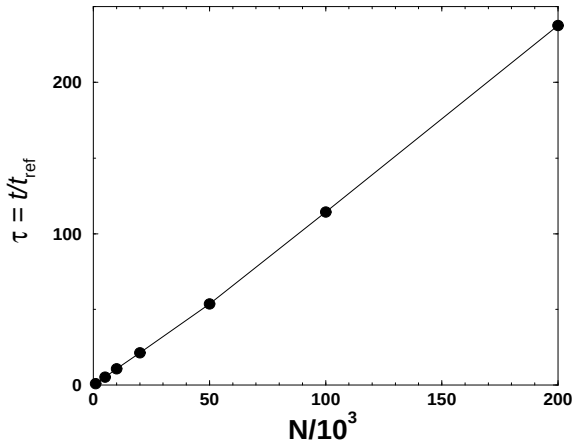

Figure 3.17: *Scaling of CPU-time with the size N of the system when using ghost particles.*

The implementation of ghost particles in this work lead to a considerable speed-up of a factor of 2. On the fastest available workstation, a *Compaq Professional WS XP 1000*, the code performs approx. 380,000 particle updates per second for a system of 100,000 particles, arranged in a linear topology of 200 chains of length $N = 500$ in a dense melt with $\rho = 0.85\sigma^{-3}$ and $\lambda = 0.0$. This performance is fast enough to simulate systems of a size that is relevant for comparison with experiment. For branched systems the performance decreases with the number of branch points, because of the additional checking of cross links, but still is above 300,000 updates per second for a system of the same size with each chain having 10 branch points. Figure 3.17 displays the scaling of simulation time τ with system size N when using ghost particles. As a reference time t_{ref} the time needed for the smallest system with $N = 1000$ was used. The scaling is almost perfectly linear ($\tau \propto N^{1.028}$) which indicates a very efficient implementation of the data structure. The additional advantage of using ghost cells lies in the fact, that the effort of setting up the cells and the effort of book-keeping *decreases* with system size, as the number of cells in the outermost layers of the simulation box *decrease*. E.g., for a system with $N = 1000$ particles, on average $\approx 73\%$ of all particles are ghosts, whereas this number has decreased to an average value of $\approx 13\%$ for a system with the same density, but $N = 200,000$.

The very efficient concept of ghost particles is realized only in few existing simulation codes. These codes are often highly optimized for very specific hardware architectures, by e.g. using 64-bit masks for variables which can be advantageous on hardware platforms such as a Cray T3E, or by optimizing the data structures and memory handling for certain chain topologies, c.f. [158]. However, a high optimization makes a code very sensitive to small changes in the underlying data structure, so that often adoptability to new demands, e.g. a variety of chain topologies, can pose a problem here. Additionally, in practice, one usually runs code on a variety of different hardware platforms. Therefore, a compromise between high performance on the one hand and high flexibility in the coding on the other hand is needed. These requirements are met by the design and implementation of the simulation code for this work which was performed from scratch. A more detailed description of the developed software can be found in Appendix D.1 on Page 168.

3.4 Characterization of the simulation model

When looking for a suitable model for the simulation of polymer chains one has to make up one's mind about how many microscopic details one wants to incorporate into it. To study the long-time dynamics of polymers in dilute solution, **coarse-grained models** are used because atomistic models of long polymer chains are intractable even numerically with present-day computer equipment. For many purposes it is sufficient to model just a few basic properties of polymer systems such as the **connectivity** of monomers, the **non-crossability** of different chains (topological constraints) and the **flexibility** of the monomer segments. The main advantage of this approach is that one has to deal with only few simulation parameters which in turn allows one to choose the model that is most convenient in terms of computational expenditure. Coarse-grained models are able to reproduce experimentally known parameters which appear in universal scaling laws. The fact that polymeric systems at various length and time scales show such common universal behavior makes this approach feasible.

A common class of such models are the so-called **bead-spring models** which are used in many variations see e.g. [27, 85, 88], where coarse-graining is achieved by replacing a sub-chain of a real polymer by a soft bead and a spring with a suitable force elongation law. Friction and mass of the sub-chains are lumped into the beads as depicted in Fig. 3.18. The excluded volume of the beads is modeled by a shifted Lennard-Jones potential (cf. Fig. 3.19 on Page 40) and Eq. (3.23)).

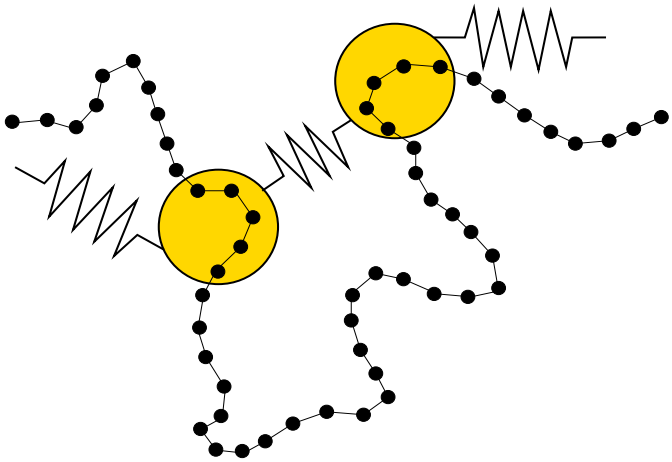

Figure 3.18: *Sketch of the coarse-grained procedure leading to the bead-spring model.*

For the intermolecular repulsion between beads there exists an empirical exponential decay law which is also suggested by quantum mechanical calculations. For numerical reasons one prefers a form of the potential of the following kind: $U(r) \propto \frac{1}{r^n}$ with $n \geq 10$. Very popular is the choice of $n = 12$, because this is just the squared Van–der–Waals attractive power law and therefore again has numerical advantages. Numerically simplest is the 6–12– or *Lennard–Jones potential*, which is also well known and widely used in Solid State Physics:

$$V_{LJ_{orig}}(r) = 4\epsilon \left\{ \left(\frac{\sigma}{r}\right)^{12} - \left(\frac{\sigma}{r}\right)^{6} \right\}. \tag{3.22}$$

The latter term in Eq. (3.22) describes the Van–der–Waals–attraction, and the former – the repulsive part – is often preferred to an exponential function due to its numerical advantages. The quantity $\epsilon = k_B T$ determines the energy scale and σ the length scale accordingly.

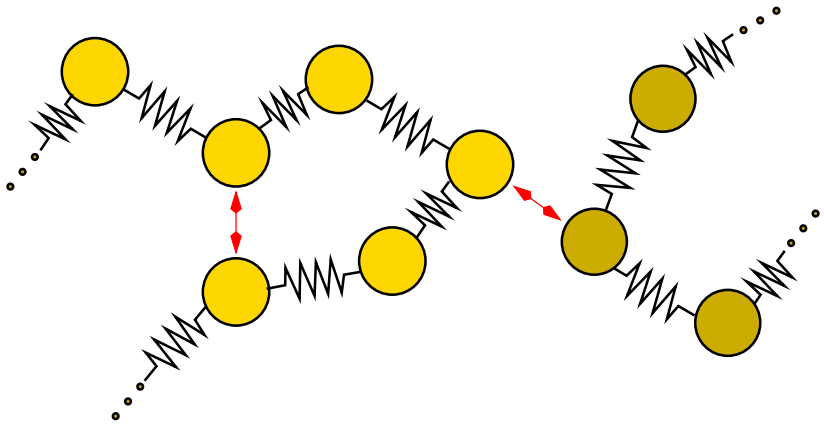

Figure 3.19: *Bead-spring model depicting the excluded volume interactions. Monomers along a single chain are connected with anharmonic springs and the excluded volume (red arrows) between monomer beads is modeled by a Lennard-Jones potential.*

For simulation purposes one introduces dimensionless *reduced* or *Lennard–Jones units* which have the advantage of being independent of any specific unit system and which also avoid numerical errors when processing very small numbers on computers. For further details, see e.g. Appendix B of Ref. [8] and the footnote on Page 9. In these units $\epsilon = k_B T = 1$, $\sigma = 1$ and time is measured in units of $\tau = \sqrt{\frac{m\sigma^2}{\epsilon}}$.

For reasons of efficiency, a potential that is to be used in simulations should be short-ranged in order to keep force calculations at a minimum. Therefore, instead of using the above original form of the Lennard–Jones potential it is common to use a slightly modified version: The potential is cut off at its minimum value $r = r_{min} = 2^{1/6}\,\sigma$ and shifted to positive values such that it becomes purely repulsive and smoothly approaches zero.

The expression for this WCA (***W**eeks-**C**handler-**A**ndersen*) potential [211] reads

$$V_{LJ}(r) = \begin{cases} 4\,\epsilon \left\{ \left(\frac{\sigma}{r}\right)^{12} - \left(\frac{\sigma}{r}\right)^{6} \right\} + \epsilon & r \le 2^{1/6}\sigma, \\ 0 & \text{otherwise.} \end{cases} \tag{3.23}$$

In order to be able to simulate systems at varying solvent qualities one has to add smoothly an attractive term to the potential in Eq. (3.23). This is done by a potential of the following form:

$$V_{cos}(r) = \left[\frac{1}{2} \cdot \cos(\alpha r^2 + \beta) \; + \gamma \right] \epsilon \qquad r_{min} < r < r_{cut}. \tag{3.24}$$

The parameters α, β and γ are obtained by demanding that the cosine part fits smoothly to the Lennard-Jones-Potential at the minimum value of $r_{min} = 2^{\frac{1}{6}}\,\sigma$ and that the combined potential is zero at the chosen cutoff $r_{cut} = 1.5\,\sigma$. Demanding this, one yields the following set of equations:

$$\alpha\, r_{min}^2 + \beta = \alpha\, \sqrt[3]{2} + \beta \;\; = \;\; \pi, \tag{3.25}$$

$$\alpha\, r_{cut}^2 + \beta = \alpha\;\; 2.25 + \beta \;\; = \;\; 2\pi, \tag{3.26}$$

$$\frac{1}{2}\cos(\alpha r_{min}^2 + \beta) + 1 \;\; = \;\; -\gamma, \tag{3.27}$$

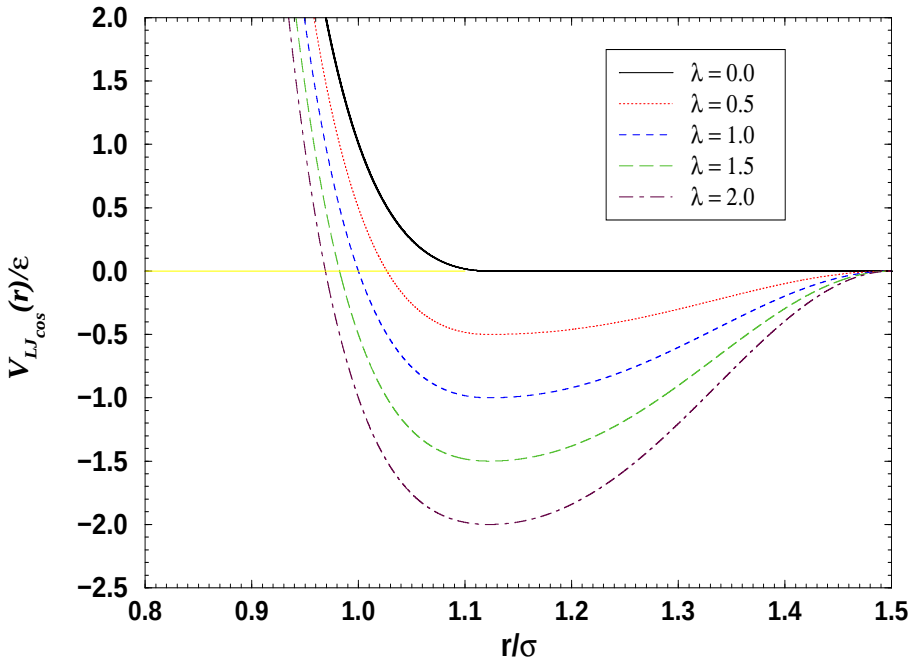

Figure 3.20: *Combined Lennard-Jones and cosine potential of non-bonded particles at different depths. This range of λ is the one for which the simulation code was tested for stability.*

which finally yields:

$$\alpha = 3.1730728678, \tag{3.28}$$
$$\beta = -0.856228645, \tag{3.29}$$
$$\gamma = -0.5. \tag{3.30}$$

The total form of the unbounded potential reads (see Fig. 3.20)

$$V_{LJcos}(r) = \begin{cases} V_{LJ}(r) - \lambda\epsilon & 0 < r < 2^{1/6}\,\sigma, \\ \lambda\, V_{cos}(r) & 2^{1/6}\,\sigma \le r < r_{cut}, \\ \infty & \text{otherwise}, \end{cases} \tag{3.31}$$

where λ is a newly introduced dimensionless parameter which determines the depth of the used potential. Instead of varying the solvent quality by changing temperature T directly, allowing for a phase transition of the system, the very same effect is achieved by varying the interaction parameter λ between particles. $\lambda = 0.0$ corresponds to the *athermal case* (ideal solvent), and values of $\lambda > 0$ correspond to decreasing solvent quality. Therefore, in all simulations, the temperature parameter T can be kept at a constant value $k_B T = 1.0\,\epsilon$ and only the parameter λ is varied.

Since chemical bonds have a fixed length, real polymers are rather inextensible. This can be modeled by a nonlinear spring law which keeps the stretching of the springs small even for large forces. Rather common in simulations is the phenomenological *FENE (**F**initely **E**xtendable **N**onlinear **E**lastic)* potential which is

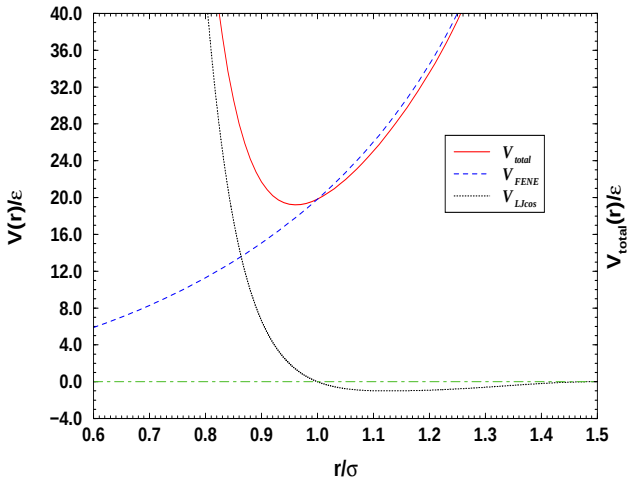

Figure 3.21: *Relative strength of different contributions to the total potential. λ was chosen as* 1.0.

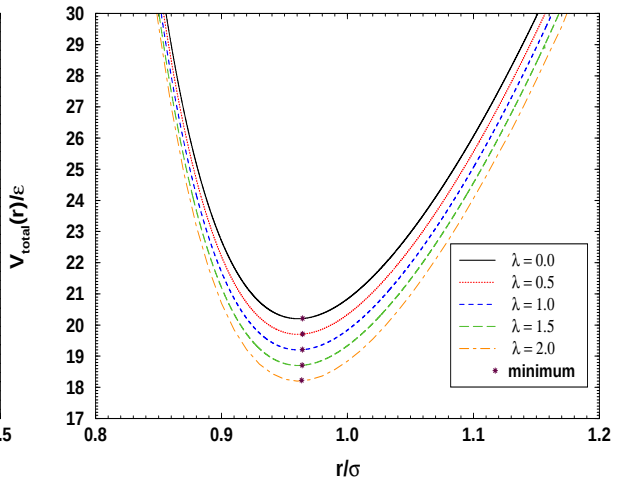

Figure 3.22: *Total potential for various values of λ. The minimum of the potential is not shifted for different choices of λ and is located at a distance $r \approx 0.97$.*

$$V_{FENE}(r) = \begin{cases} -\frac{1}{2}\kappa R_0^2 \ \ln(1 - \frac{r^2}{R_0^2}) & r < R_0, \\ \infty & \text{otherwise.} \end{cases} \tag{3.32}$$

The values for the parameters are chosen as $R_0 = 1.5\,\sigma$ and $\kappa = 30\,\epsilon/\sigma^2$ which have proven to be useful in practice [85].

The total potential finally is given by the following equation (see Fig. 3.22):

$$V_{total}(r) = V_{LJcos}(r) + V_{FENE}(r). \tag{3.33}$$

The density $\rho = N/V$ of the systems is chosen as $\rho = 0.85\,\sigma^{-3}$ throughout all simulations. This is the density of liquid polymer systems for which the potential parameters have been optimized. The code can be used for simulations of polymers in a melt, as well as for the simulation of single chain systems by switching off the inter-chain interaction. The latter allows for simulating large systems of isolated chains and, as a result, improves statistics considerably.

Chapter 4

Simulation results of linear chain systems

Table of Contents

Prior to the study of more complicated systems it is necessary to analyze the used model via the simulation data of single linear chain systems. This analysis gives a complete set of reference data for the chosen model with which the data of branched systems can be compared. It also includes a new result for the scaling property of the hydrodynamic radius R_h of linear model chains which was possible because of the high statistical quality of the obtained data. This is the first study that systematically investigates the properties of the previously described chain model. It will be shown that this model is suitable for the description of polymers on a coarse-grained level as it not only reproduces well-established theoretical results for certain limiting cases but also can be used to simulate model polymers under solvent conditions that are close to experimental systems.

4.1 Simulation results: θ – transition

In this section, the influence of temperature, respectively solvent quality on dilute solution properties of flexible linear chains will be studied over a wide temperature interval ranging from the athermal limit to far below the θ–temperature. In this analysis it was gone beyond most previous investigators who mostly concentrated on simulations of rather short chains in the vicinity of the θ–point. In this study, the whole temperature range from an ideally good solvent to a very bad solvent is covered with chain lengths of up to $N = 2000$. Simulations of chain lengths of $N = 5000$ were also done for the athermal case and at the θ–point.

The collapse transition of chains was subject of much theoretical work [61, 63–65, 72]. The type of transition in the limit of infinite chain length was discussed in [60, 126, 145, 175]. It was pointed

out by *de Gennes* [53] that the θ–point is a tri-critical point and that mean field theory can be applied, except for logarithmic corrections. Some early studies were done in [16] and [114]. An overview of early studies is given in [218]. Numerous simulations have been performed, mainly focusing on the use of various MC-methods both, on lattices [44, 138, 156, 186, 217, 230] and in the continuum [82, 83, 141, 174].

In experiments, it is difficult to obtain complete and conclusive results in the study of the collapse transition of chains, because one is restricted to solutions of extremely dilute polymer concentrations [48].

At the θ–temperature the chains behave as $\langle {R_g}^2 \rangle \propto \langle {R_e}^2 \rangle \propto (N-1)^{2\nu_\theta}$ with $\nu_\theta = 0.5$ besides logarithmic corrections in $d = 3$. Therefore, one expects that a plot of $\langle R^2 \rangle / (N-1)$ vs. T for different values of N shows a common intersection point at $T = T_\theta$ where the curvature changes: for $T > T_\theta$ the larger N, the larger the ratio $\langle R^2 \rangle / (N-1)$ has to be, while for $T < T_\theta$ the larger N, the *smaller* the ratio $\langle R^2 \rangle / (N-1)$ has to be. In our case, instead of varying temperature, different solvent qualities were obtained by tuning the interaction parameter λ.

The corresponding transition curves are displayed in Fig. 4.2 and 4.1 which show a clear intersection point at roughly $\lambda = \lambda_\theta \approx 0.65$. Moreover it can be seen that the transition becomes sharper with increasing chain length N in agreement with other investigators [141, 208]. The shape of the curves is in agreement to those obtained by numerical studies and experiments [191, 217].

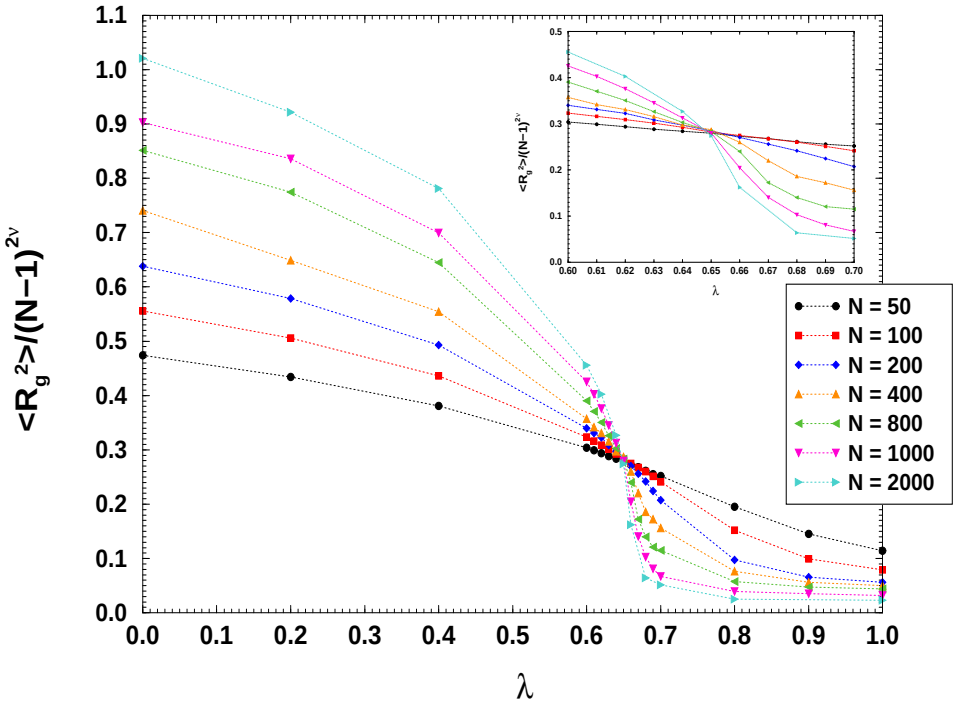

Figure 4.1: *Plot of $\langle {R_g}^2 \rangle / (N-1)^{2\nu}$ vs. interaction parameter λ for linear chains. The points represent the simulated data and the dotted lines are guides to the eye. $\nu = \nu_\theta = 0.5$. The inset shows an enlargement of the region around the θ-point which is located at $\lambda = 0.65$.*

The different curves do not intersect exactly at one single point, but there is an extended region in which the chains behave in a Gaussian manner. The size of this region is $\propto N^{-1/2}$ [56]. There is a very slight drift of the intersection point towards a smaller value of λ with increasing chain length. Therefore, to obtain a more precise estimate of the θ–temperature in the limit of ($N \to \infty$), one has

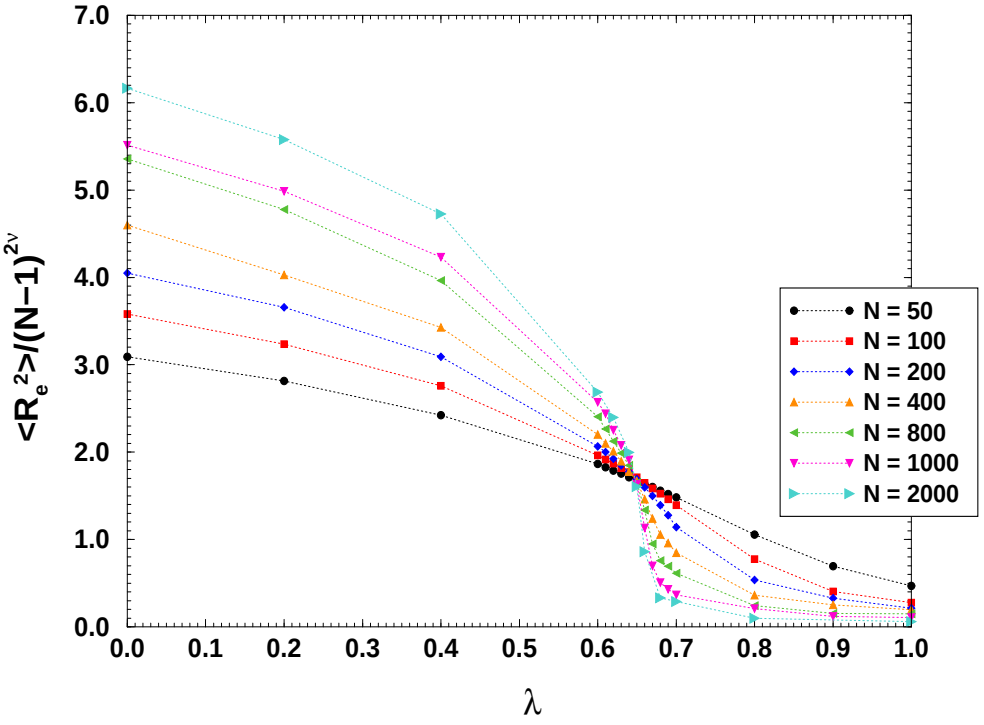

Figure 4.2: *Plot of* $\langle R_e{}^2 \rangle / (N-1)^{2\nu}$ *vs. interaction parameter* λ *for linear chains. The points represent the simulated data and the dotted lines are guides to the eye.* $\nu = \nu_\theta = 0.5$*. The inset shows an enlargement of the region around the* θ*-point which is located at* $\lambda = 0.65$*.*

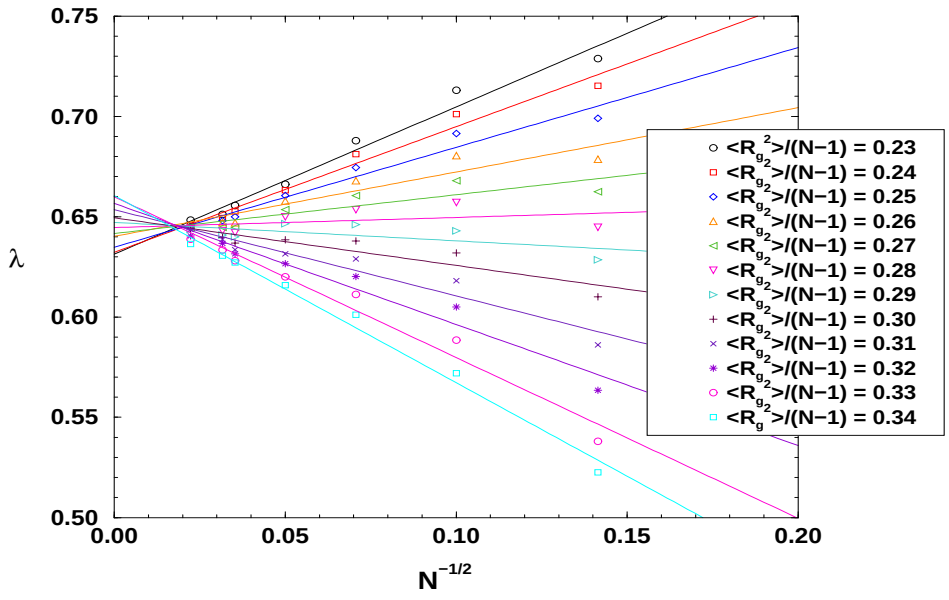

Figure 4.3: *Plot of* λ *vs.* $N^{-1/2}$ *for different values of the scaling function. Data are based on the radius of gyration of linear chains.*

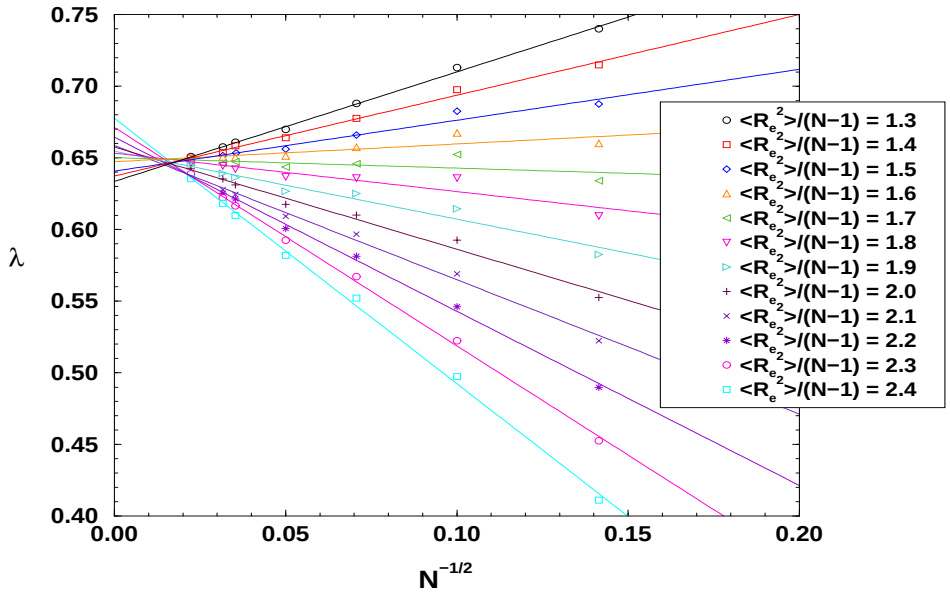

Figure 4.4: *Plot of λ vs. $N^{-1/2}$ for different values of the scaling function. Data are based on the end-to-end distance of linear chains.*

to chose a different graph that allows an appropriate extrapolation. If one draws straight horizontal lines in Fig. 4.1 and 4.2, the intersection points of these lines with the curves are points at which the scaling function $f(\sqrt{N}\zeta)$ of Eq. (2.36) is constant. Plotting different intersection points over $N^{-1/2}$ should therefore yield different straight lines that intersect each other exactly at $T = T_\theta$ and $\lambda = \lambda_\theta$ respectively. This extrapolation to $(N \to \infty)$ is displayed in Fig. 4.3 and 4.4. The different lines do not intersect at $N^{-1/2} = 0$ which is due to the finiteness of the chains. As a result of these plots one yields

$$\lambda_\theta = 0.65 \pm 0.02. \tag{4.1}$$

In principle, the hydrodynamic radius R_h should follow the same scaling laws as R_g and R_e. It turns out however, that R_h is not suited for a similar analysis of the θ–point, because of huge corrections to scaling. A detailed discussion and analysis of these finite size effects is included in Section 4.2.4.

4.2 Scaling analysis

This section provides an analysis of the scaling properties of the investigated systems.

4.2.1 Structure functions

An important property of individual chains is the *structure factor* $S(k)$ which is defined in its spherical average as [59]

$$S(k) = \left\langle \frac{1}{N^2} \left| \sum_{i=1}^{N} e^{-i\vec{k}\vec{r}_i} \right|^2 \right\rangle_{|\vec{k}|}, \tag{4.2}$$

with subscript $|\vec{k}|$ denoting the average over all $\vec{k}$-vectors of the same magnitude k. The importance of $S(k)$ lies in the fact that it is *directly* measurable in scattering experiments. For *ideal* linear chains the function $S(k)$ can be explicitly calculated and is given by the monotonously decreasing *Debye function* [223]

$$S(x) = \frac{2}{x^2}\left(x - 1 + e^{-x}\right), \tag{4.3}$$

where the quantity x is given by $x = k^2 \left\langle {R_g}^2 \right\rangle_0$. For small values of x, corresponding to large distances between scattering units, the Debye function $S(x)$ also gives a good description of a linear chain in a *good* solvent with the scaling variable x describing the expansion of the chain. For very small scattering vectors k one obtains the *Guinier approximation* by an expansion of $S(k)$, which is used in experiments to calculate the radius of gyration $\left\langle {R_g}^2 \right\rangle$. In the intermediate regime of scattering vectors, $S(k)$ obeys a scaling law which, in a double-logarithmic plot, should yield a slope of $-1/\nu$. For large k-values finally, $S(k)$ is expected to behave as $1/N$. The overall expected behavior of $S(k)$ can be summarized as follows

$$S(k) = \begin{cases} \left(1 - 1/3\, k^2 \left\langle {R_g}^2 \right\rangle\right) N & (2\pi)^2 / \left\langle {R_g}^2 \right\rangle \gg k^2, \\ k^{-1/\nu} & (2\pi)^2 / \left\langle {R_g}^2 \right\rangle \ll k^2 \ll (2\pi)^2 / {l_b}^2, \\ 1/N & (2\pi)^2 / {l_b}^2 \ll k^2. \end{cases} \tag{4.4}$$

Very good agreement with Eq. (4.4) is displayed in Fig. 4.5 for $S(k)\,N$ for all investigated chain lengths at infinite temperature (athermal case). For large and intermediate k-values, the curves are independent of N and fall onto one single curve.

For chains under θ–conditions, $S(k)$ provides a direct insight into the length scale on which the excluded volume interaction is screened. Figure 4.6 displays the static structure functions of all investigated linear chain lengths at the θ–point and elucidates that the chains do not display a perfect Gaussian behavior. The shape of the curves corresponds to the one expected by theory. The solid lines represent the Debye approximation for different chain lengths whereas the data points represent $S(k)$ obtained from simulations.

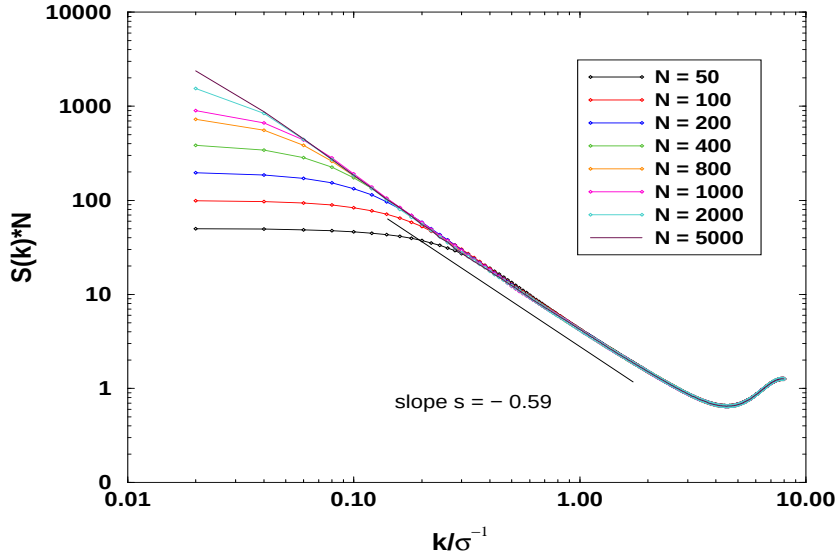

Figure 4.5: *Log-log plot of the structure function $S(k)N$ for athermal linear chains of different lengths N. The expected scaling behavior with a slope $s \approx -3/5$ is verified. For intermediate and large k-values, the different curves fall onto one single curve in accordance with Eq. (4.4).*

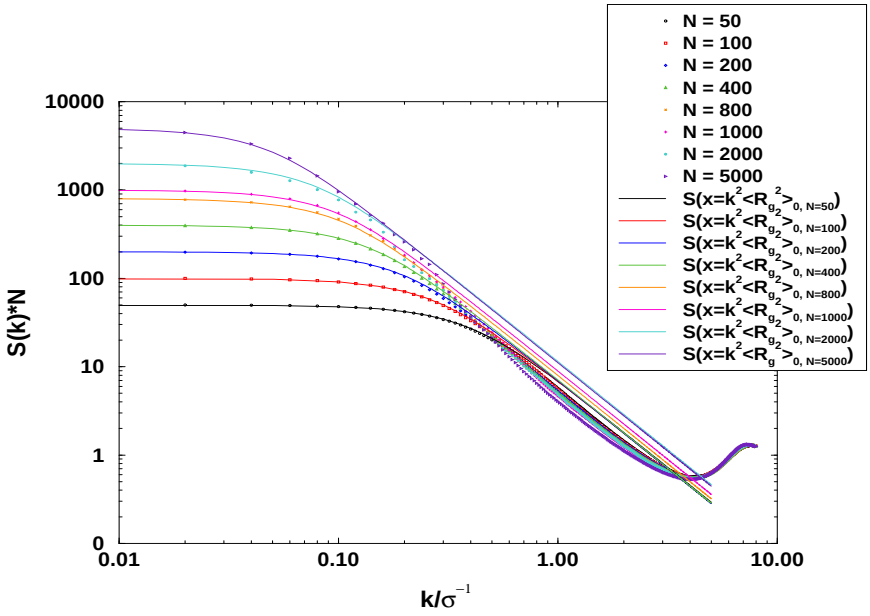

Figure 4.6: *Structure function $S(k)N$ at the θ–point for chains of different lengths N and $\lambda = 0.65$ in a double-logarithmic data representation. The data points represent the simulated data and the solid lines display the Debye function for different lengths, with $\langle {R_g}^2 \rangle_0$ taken from the simulations.*

For small k–values the lines correspond very well to the data points, up to a value of $k \approx 0.3$, except for the largest systems which already exhibit deviations at a value of $k \approx 0.1$. In general, the Debye function tends to systematically overestimate the radius of gyration.

For large k-values, $S(k)$ displays the local structure of the chain with a first peak at $2\pi/l_b \approx 7$ which corresponds to the average nearest neighbor distance $d_n \approx 0.97$ of particles in the chain. The deviations from the Debye-curves increase with increasing chain length. This might be due to a worse statistics of the largest simulated systems compared to the smaller systems with chain lengths of up to $N = 1000$. In the previous section it was shown that the θ–point is shifted slightly to a lower value of λ for increasing chain lengths. Therefore, the chosen data points with $\lambda = 0.65$ might correspond to a $\langle {R_g}^2 \rangle$ value that is already below the actual θ–point. For very large chains a small increase in λ leads to a considerably different $\langle {R_g}^2 \rangle$ value. This might account for the fact that the data points in the intermediate k-range of Fig. 4.6 do not perfectly lie on top of each other, decreasing with a slope $s = -1/\nu = -2$.

In the vicinity of the θ-region, the scaling exponent equals $\nu = \nu_\theta = 0.5$. Therefore $k^2 S(k)$, plotted against wave vector k should approach a constant value. Figures 4.7 to 4.13 display this behavior for the different investigated chain lengths with a high resolution in terms of λ. The respective dotted horizontal lines are a guide to the eye. For the longer chains there is a small shift of the θ–point towards a slightly smaller value of λ in accordance with the results of the previous chapter. This shift however is small and still within the error of Eq. (4.1). The larger the chains the smaller is the λ-range at which the chains display Gaussian behavior. As a result, these *Kratky plots* are in very good agreement with the obtained result for the θ–point in the previous Section.

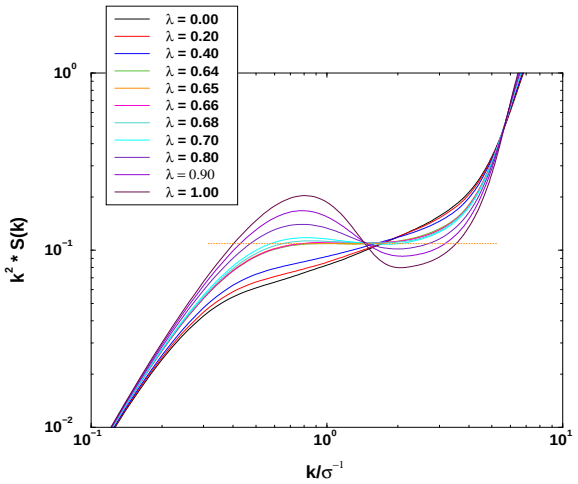

Figure 4.7: *Kratky plot of $S(k)$ of linear chains for different values of the interaction parameter λ. $N = 50$.*

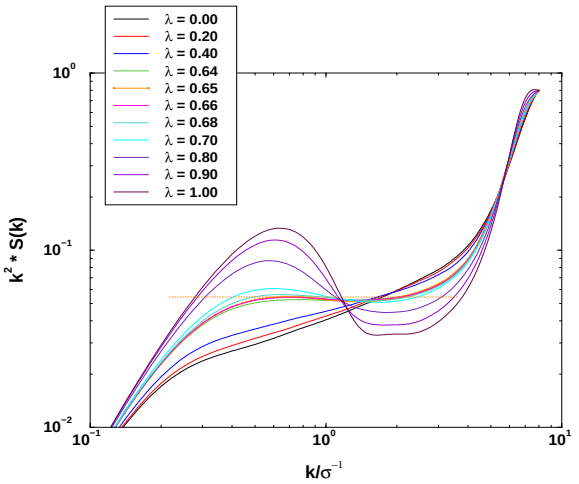

Figure 4.8: *Kratky plot of $S(k)$ of linear chains for different values of the interaction parameter λ. $N = 100$.*

For large values of λ the chains are collapsed and form compact globules the local structure of which is also reflected in the structure function by several distinct peaks for larger k-values. These peaks become the more pronounced the longer the chains are, reflecting the fact that the transition curves become ever sharper with increasing chain length. Hence, longer chains are already in the collapsed regime for values of λ at which the smaller chains still exhibit Gaussian behavior. The structure function of the largest system in Fig. 4.13 for $\lambda = 1.0$ already resembles very much the

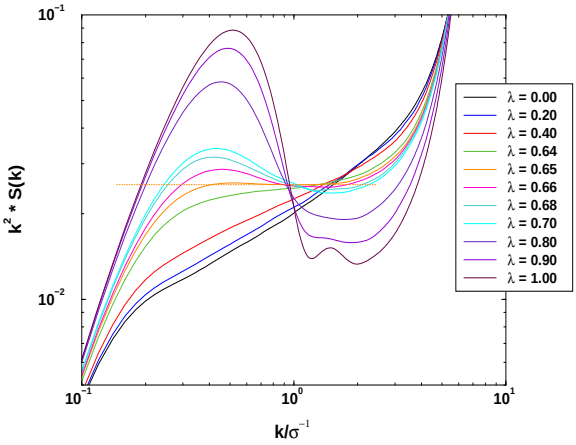

Figure 4.9: *Kratky plot of $S(k)$ of linear chains for different values of the interaction parameter λ. $N = 200$.*

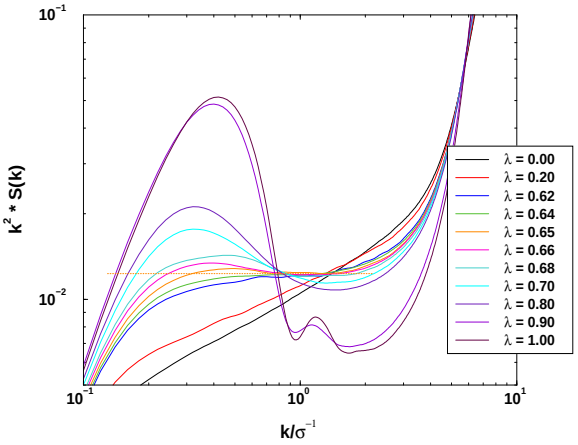

Figure 4.10: *Kratky plot of $S(k)$ of linear chains for different values of the interaction parameter λ. $N = 400$.*

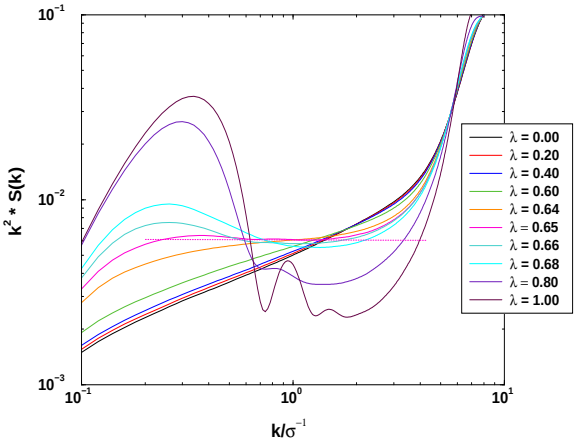

Figure 4.11: *Kratky plot of $S(k)$ of linear chains for different values of the interaction parameter λ. $N = 800$.*

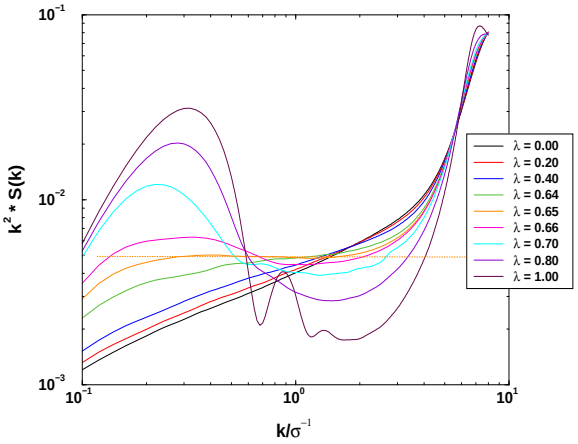

Figure 4.12: *Kratky plot of $S(k)$ of linear chains for different values of the interaction parameter λ. $N = 1000$.*

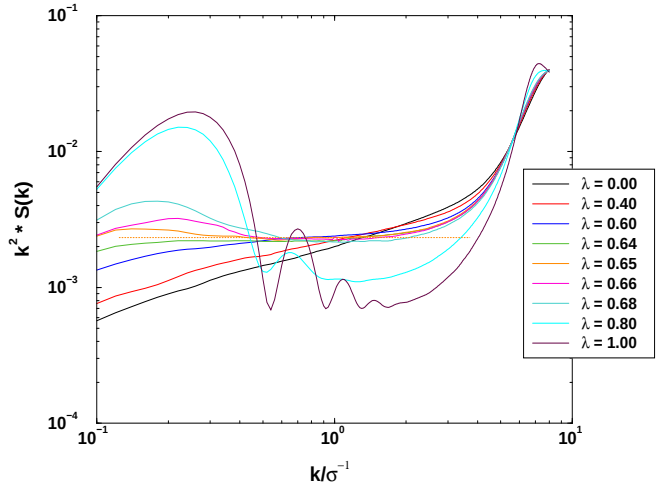

Figure 4.13: *Kratky plot of $S(k)$ of linear chains for different values of the interaction parameter λ. $N = 2000$.*

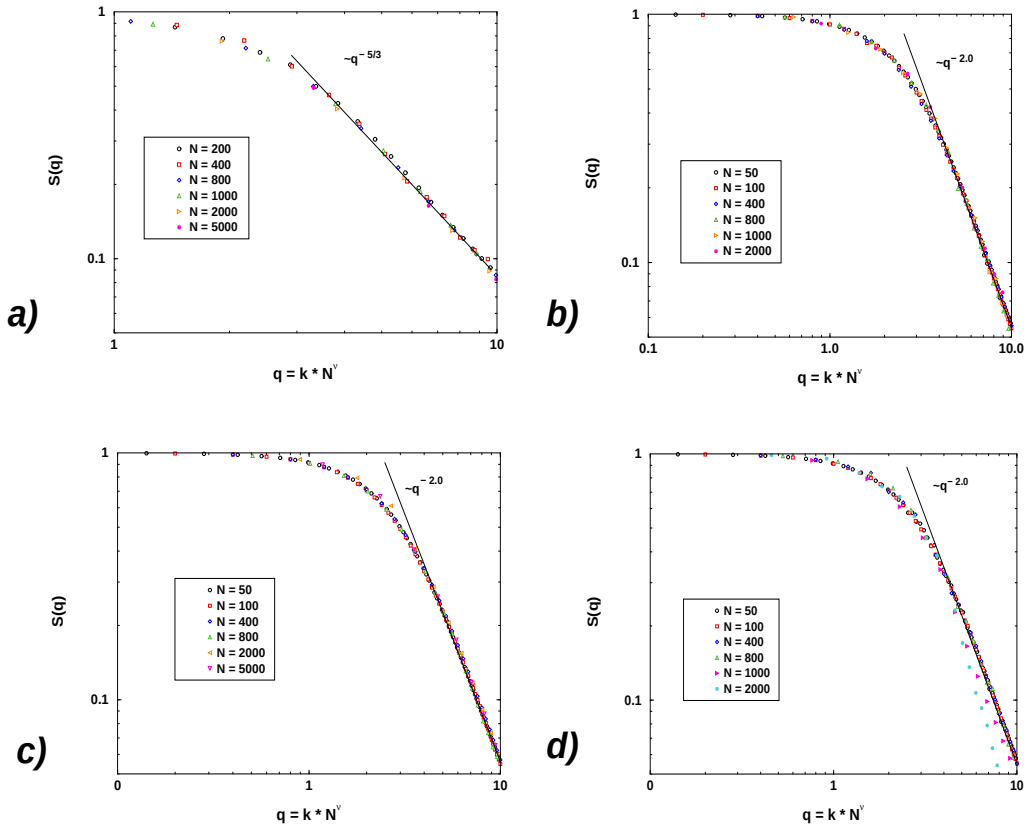

Figure 4.14: *Scaling plot of $S(q)$ with scaling variable $q = kN^{\nu}$. The scaling is verified for 6 different chain lengths N. a) $\lambda = 0.0$ and $\nu = 0.60$. b) $\lambda = 0.65$ and $\nu = \nu_\theta = 0.5$. c) $\lambda = 0.64$ and $\nu = \nu_\theta = 0.5$. d) $\lambda = 0.66$ and $\nu = \nu_\theta = 0.5$.*

scattering pattern of a sphere.

When varying the size of a chain at fixed temperature, in our case for a fixed value of λ, one expects $S(k)$ to be a function of the scaling variable $q = kN^{\nu}$ only, see e.g. [17]. Figure 4.14 displays plots of this type for the athermal case and in the vicinity of the θ–point. The expected scaling of $S(k)$ is verified for several chain lengths. In the latter three figures it can be seen that a value of $\lambda = 0.65$ is closer to the asymptotic θ–point for $N \to \infty$ than the other two values of λ for which deviations from the expected scaling are detected for the largest chains. These deviations are due to the fact that the crossover of long chains from an expanded coil to a collapsed globule is very sharp compared to the ones of short chains (cf. Fig. 4.1 and 4.2).

4.2.2 Tri-critical scaling

We next consider the tri-critical scaling of $\langle {R_e}^2 \rangle$ and $\langle {R_g}^2 \rangle$ as a function of the normalized temperature distance ζ from the θ point which in our case in terms of λ is defined as:

$$\xi = |(\lambda - \lambda_\theta)/\lambda_\theta)|. \tag{4.5}$$

According to the crossover scaling description of polymer chains by *de Gennes* [54, 55] and *Daoud* and *Jannink* [51], $\langle {R_e}^2 \rangle$ behaves as

$$\langle {R_e}^2 \rangle \propto N^{2\nu_t} f_{\pm}(N\xi^{1/\beta_t}), \tag{4.6}$$

where β_t is a crossover exponent with subscript t denoting the tri-criticality of the exponents.

The scaling function $f_{\pm}(x)$ exhibits the following asymptotic behavior:

$$f_{\pm}(x) = \begin{cases} x^{2(\nu-\nu_\theta)} & \text{for } T > T_\theta, \\ \text{constant} & \text{for } T = T_\theta, \\ x^{2(\nu_0-\nu_\theta)} & \text{for } T < T_\theta. \end{cases} \tag{4.7}$$

It should be noted that Eq. (4.6) and (4.7) also hold for the radius of gyration R_g.

Figure 4.15 displays the data of $\langle {R_e}^2 \rangle$ according to Eq. (4.7). The crossover exponent was chosen as $\beta_t = 0.5$ which is the well established value of de Genne's Blob scaling picture, c.f. Subsection 2.5.1 on Page 16. The expected scaling laws are drawn as straight lines and it can clearly be noted that the overall scaling is fairly good in the regime $\lambda > \lambda_\theta$. For the case $\lambda < \lambda_\theta$ there are deviations from the expected asymptotic scaling behavior. This result can be accounted for by the fact that the above equations hold only *exactly* in the limit ($\xi \to 0$) and ($N \to \infty$) with $x = N\xi^{1/\beta_t}$ finite. In the case of $\lambda \approx \lambda_\theta$ the relation $\lambda \approx 1/T$ is valid. However, in our simulations, the maximum value of ξ is one and the chain length N is a finite number. Therefore, the term ξ is not small anymore and this leads to the observed deviation from the expected scaling.

In MC simulations on a lattice with a different model [114] and [138] this problem is dealt with by replacing β_t by β_{eff}. In these studies however, *only* the good solvent case and *only* the scaling of R_g was investigated.

In general, the scaling is in good agreement with theory for the case $\lambda > \lambda_\theta$. As for the collapsed state, there is a larger slope of $\langle R^2 \rangle / (N-1)^{2\nu_\theta}$ than the expected asymptotic scaling law $x^{-1/3}$ at intermediate x-values which was also observed in [29] and [201].

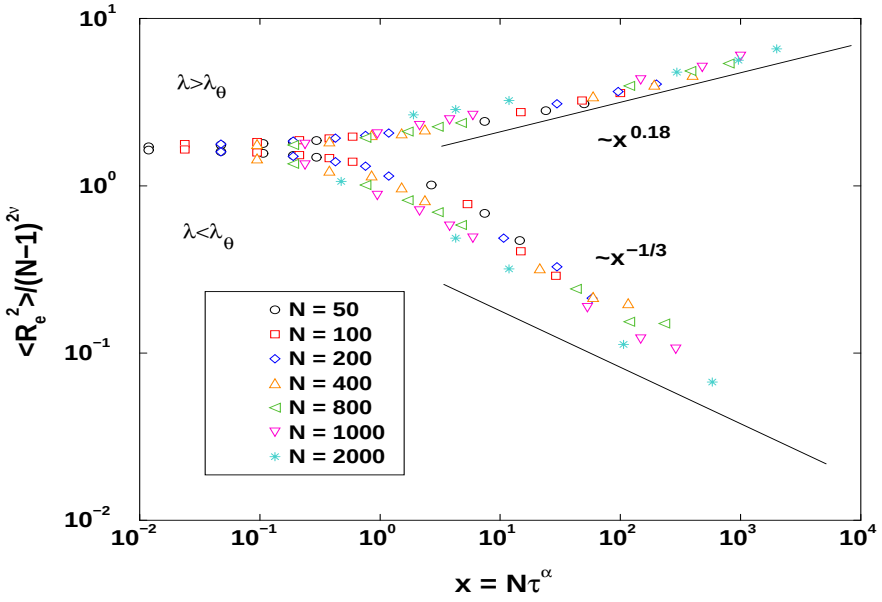

Figure 4.15: *Log-log plot of* $\langle {R_e}^2 \rangle / (N-1)^{2\nu_\theta}$ *vs. the scaling variable* $x = N\xi^\alpha$ *with* $\alpha = 1/\beta_t = 1/\nu_\theta = 2.0$. *The data points represent the simulated data and the straight lines display the expected asymptotic behavior of the scaling function.*

Summary

A detailed analysis of the simulation model has been performed. It has been shown that the chosen simulation model is capable of simulating a phase transition of polymer model-chains from the good solvent regime to the collapsed regime. The θ-point, as a characteristic quantity of this transition has been determined for the used model with very large chain lengths of up to $N = 5000$ which is well beyond the range of N of most previous investigations of θ-points for various chain models in literature. The collapse transition of chains approaches a step-function with increasing chain length N as is expected from theory. The capability of the exploited model to include a variety of solvent conditions is also important in light of the fact that most experiments are done in a variety of solvent qualities.

The measurements of the structure functions of this model for linear chains which lead to a value of λ_θ which is in excellent agreement with the value obtained from R_g and R_e measurements. In contrast to many other investigators, in this analysis, also the bad solvent case (collapsed state) of the model chains is included which is reflected in the changing scattering pattern of $S(k)$ for decreasing solvent quality.

A scaling analysis of the obtained simulation data has been performed. It was first shown that the structure function obeys the scaling laws expected from theory. By making use of an appropriate scaling variable one can make all curves of different N collapse onto one single master curve, exhibiting the correct scaling exponent as suggested by theory. The scaling gave the best result for the systems that correspond to a θ-solvent which is yet another confirmation of the correct determination of the θ-conditions of this polymer model.

It was then shown that also the results for R_g and R_e obey respective crossover scaling laws according to a theory by *Daoud* and *Jannink*. This was also done for the simulated chains in bad solvent conditions.

As a result one can conclude that the considered chain lengths in our study are obviously large enough for the systems to exhibit scaling law properties which are strictly only valid in the limit of ($N \to \infty$). Therefore these considered chain lengths are suitable for comparisons with experimental systems.

4.2.3 Chain expansion

We next study the chain length dependence of the coil size at several fixed temperatures, respectively solvent qualities in order to determine the different scaling exponents directly from the simulation data.

It has been observed that even in the best experimental good solvent systems the excluded volume effect is often surprisingly small [95]. An example for this apparent weakness of excluded volume effects even in the best of good experimental solvents is given in Fig. 4.16. The experimentally determined scaling exponent of R_g for Density Polyethylene (LDPE) in a good solvent (tri-chlorobenzene (TCB)) [194] is displayed along with the respective exponents obtained from the simulation data. Compared with the used simulation model this exponent corresponds to a value of λ that is closer to θ-conditions than to the athermal limit. This has to be taken into account when trying to compare experimentally determined static properties with the chosen simulation model.

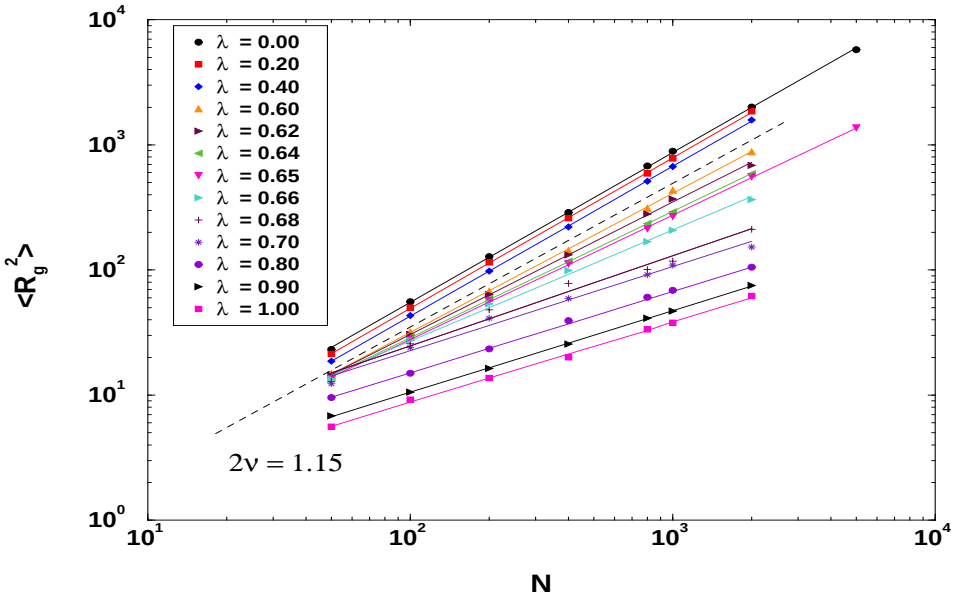

Figure 4.16: *Log-log plot of $\langle {R_g}^2 \rangle$ vs. N at different solvent qualities as displayed. Straight lines indicate effective exponents $2\nu_{\text{eff}}(\lambda)$. The exponent obtained for LDPE in tri-chlorobenzene [194] (dashed line) which is a good solvent is shown in comparison with the simulated systems. In the extremely collapsed regime with values of $\lambda \geq 0.7$ the chains exhibit a slightly larger slope than $2\nu = 2/3$, c.f. Figure 4.18.*

Figure 4.17 shows the scaling exponents of the model-chains based on simulation data of the end-to-end distance.

Figure 4.18 shows the obtained effective exponents $\nu_{\text{eff}}(\lambda)$ for R_g and R_e. One can see a smooth variation of the exponent with solvent quality, as one expects, since $\nu_{\text{eff}}(\lambda)$ has been determined from a fit of all chain lengths including the short ones. The sensitivity of our model with respect to solvent quality - expressed by the effective exponents ν_{eff} - is the largest in the vicinity of the θ-point. Here, a small change of λ leads to very different effective scaling exponents. On the other hand, there is an extended region of λ in the good and bad solvent regime where large changes of λ lead to almost the same effective exponents. A step-function-like variation of $\nu_{\text{eff}}(\lambda)$ is expected only in the true asymptotic limit of infinite chain lengths for which the θ–transition becomes a true phase transition. Hence, the data provided in Figure 4.18 allow for a direct comparison of any experimentally determined effective exponents ν_{eff} with the respective parameter λ that determines the solvent quality of

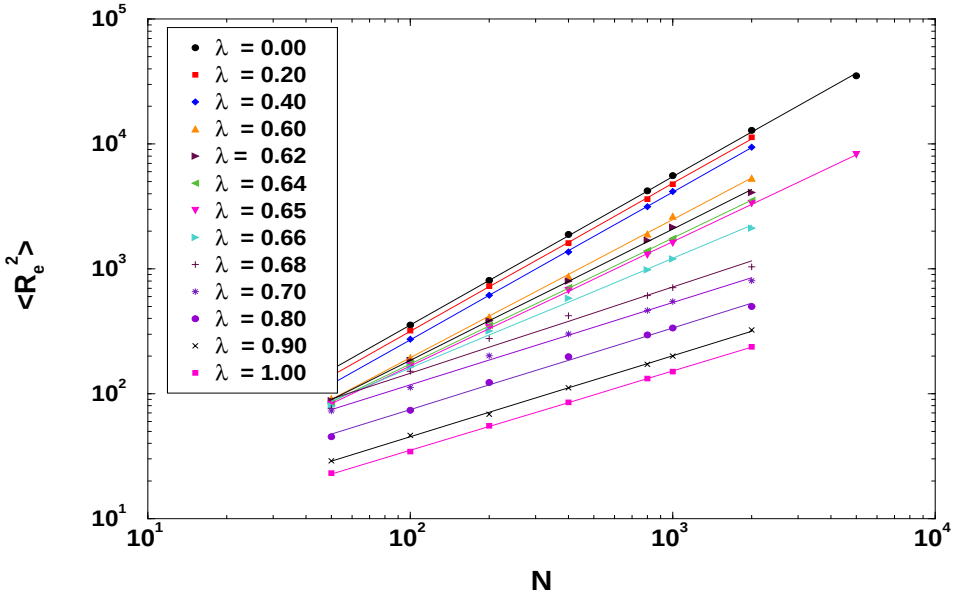

Figure 4.17: *Log-log plot of $\langle {R_e}^2 \rangle$ vs. N at different solvent qualities as displayed. Straight lines indicate effective exponents $2\nu_{\text{eff}}(\lambda)$.*

the generated chains in our simulation model. A comparison of our model with LDPE in TCB, which is a good solvent, is displayed in Figure 4.18 by straight lines. For this system one yields $\lambda \approx 0.505$.

In [125] it has been reported that $\nu_{\text{eff}}(\lambda = 0.0)$ is overestimated in simulations of smaller chains and decreases towards the expected value $\nu_{\text{eff}} = 0.5877$ (cf. Table 2.1 on page 11) as the chain length increases. To obtain the scaling exponent ν in the long chain limit with such high precision chain lengths larger than 24.000 have to be considered [24]. If one only takes the first four lengths $N = 50, .., 400$ of our simulation data into account one yields $\nu_{\text{eff}} = 0.601$ instead of $\nu_{\text{eff}} = 0.5938$. The deviation of the latter value from the expected $\nu_{\text{eff}} = 0.5877$ is less than 1%. Hence, our simulation results yield a reasonable approximation for the length-size relationship in the athermal case. For the θ–point the deviations of ν_{eff} from the expected value $1/2$ are less than 1%. The explicit numerical values of the obtained $\nu_{\text{eff}}(\lambda)$ are listed in Table A.18 in Appendix A on page 149.

Figure 4.19 shows the mean-square radius of gyration as a function of chain length N at $\lambda = \lambda_\theta = 0.65$. These values were obtained with particular high accuracy as they are used for the calculation of size expansion factors α^2 of the chains.

Figures 4.20 and 4.21 display the rescaled chain length dependence of $\langle {R_e}^2 \rangle$ and $\langle {R_g}^2 \rangle$ respectively, for various simulated solvent qualities. The deviations of the exponents obtained for R_g and R_e are obviously very small. However, the data for $\langle {R_g}^2 \rangle$ generally can be computed more accurately than the ones for $\langle {R_e}^2 \rangle$. In the vicinity of the θ–point the chains exhibit the expected scaling independent of chain size with an effective exponent $\nu_{\text{eff}} = 0.5$. This behavior provides yet another determination of the θ–condition which is in accordance with the results of the previous sections.

For very long chains the slopes of $\langle {R_{e/g}}^2 \rangle / (N-1)$ of different curves approach the same slope independent of λ which allows one to find a master curve representation of these static properties by rescaling all distances N. These master curve plots are shown in Figures 4.22 and 4.23 using the same shift factors $N^\star$ for rescaling the chain length N. The superposition was obtained as follows: The data points of the system with $\lambda = 0.60$ was used as a reference system and the data points of the other systems were shifted in a way such that they visually showed the best superposition with the

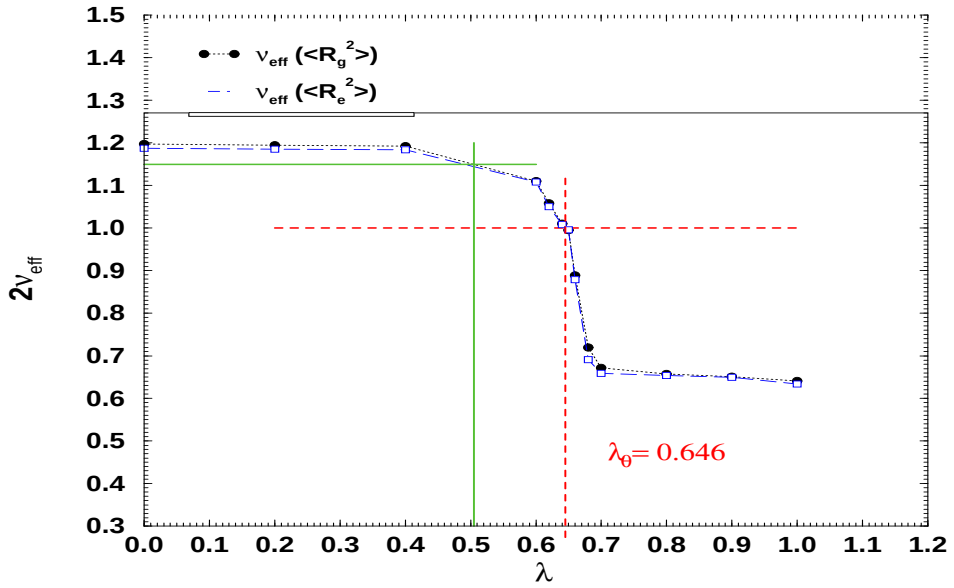

Figure 4.18: *Dependence of the effective exponent $2\nu_{eff}(\lambda)$ of linear chains on the simulation parameter λ. Dotted and dashed lines are a guide to the eye, connecting the data points and straight dashed lines indicate $2\nu_{eff}(\lambda = \lambda_\theta) = 1$ which yields another estimate of the θ–point in close correspondence of the previous sections. The straight lines indicate the exponent of an experimental system [194] and the corresponding λ-value of our simulation model.*

reference curve.

Fig. 4.26 displays the expansion factor α^2, according to Eq. (2.31), as a function of chain length. This quantity shows the same convergence behavior for long chain lengths N in the good solvent regime. The corresponding master curve for α^2, again using the same shift factors for N, is displayed in Fig. 4.28.

The scaling of ${R_g}^2$ and ${R_e}^2$ can be used to obtain the C_∞-value of the simulated model-chains in the following way: From Figures 4.30 and 4.31 one can read off $\langle {R_{g/e}}^2 \rangle / (N-1)$ at $\lambda = \lambda_\theta$ in units of average squared bond length ${l_b}^2$. Using Eq. (2.20) one obtains as a result

$$ {R_g}^2/(N-1) = C_\infty \, {l_b}^2 = 0.278 \, \sigma^2, \tag{4.8} $$

which is consistent with the value obtained from the extrapolation in Fig. 4.19. The average squared bond length ${l_b}^2$ of the simulated chains has been measured for different solvent qualities and the average over all chain lengths is displayed in Fig. 4.32. From this plot one obtains at the θ–point a value of ${l_b}^2 = 0.9425$.

Thus, according to Eq. (2.1) the value for ${R_e}^2/(N-1)$ in units of ${l_b}^2$ is

$$ 6 \cdot {R_g}^2/(N-1) = 1.668 \, \sigma^2, \tag{4.9} $$

which is in exact agreement with the one obtained from the scaling plot in Fig. 4.31 directly.

Thus, according to Eq. (2.20) the characteristic ratio of the model-chains in the long chain limit is

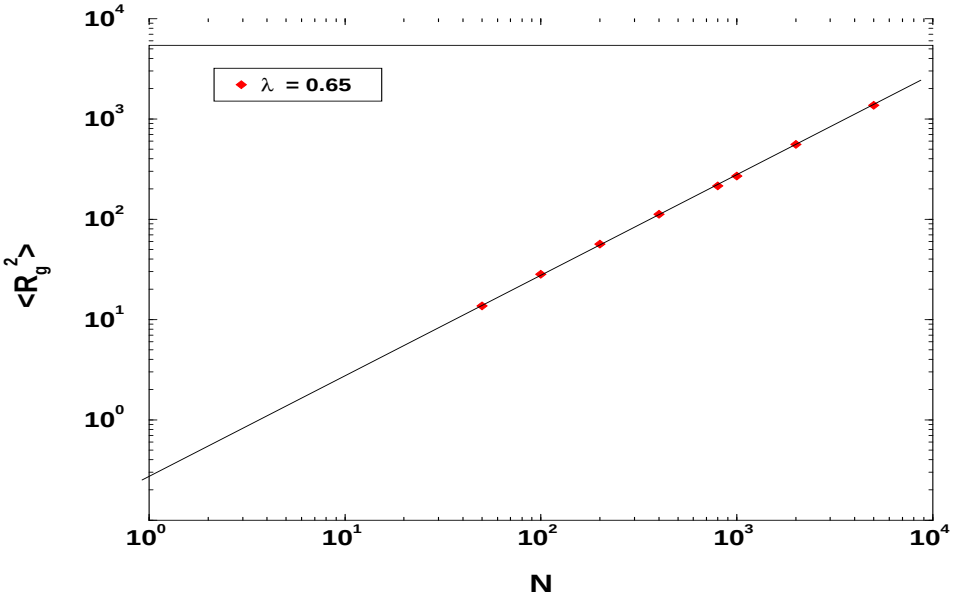

Figure 4.19: *Plot of $\langle {R_g}^2 \rangle$ vs. N under θ–conditions ($\lambda = 0.65$). The straight line is drawn with unit slope.*

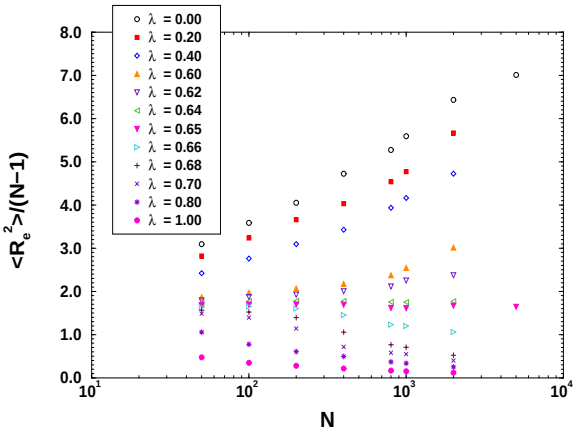

Figure 4.20: *Scaled end-to-end distance plotted vs. chain length N. At the θ–point one expects $\langle {R_e}^2 \rangle / (N-1)$ to be constant.*

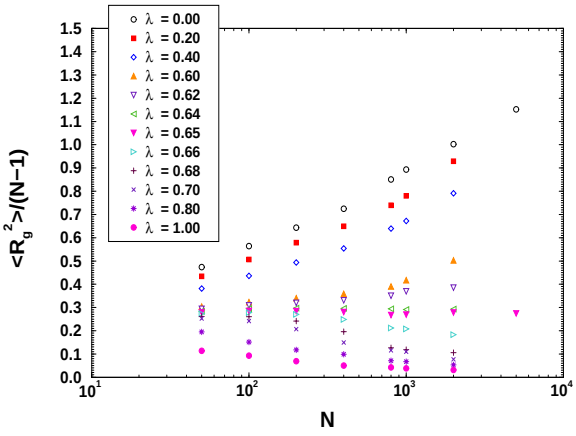

Figure 4.21: *Scaled radius of gyration plotted vs. chain length N. At the θ–point one expects $\langle {R_g}^2 \rangle / (N-1)$ to be constant.*

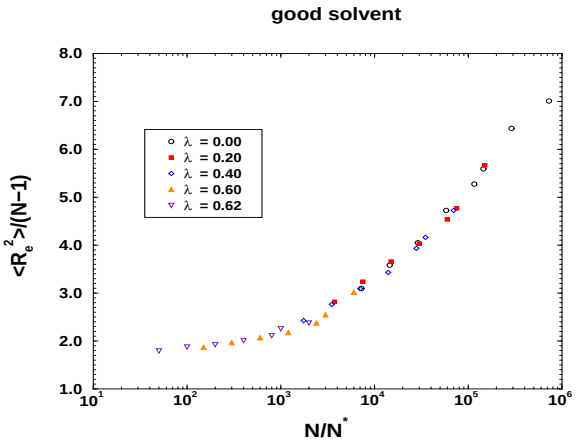

Figure 4.22: *Master curve for the end-to-end distance in the good solvent regime.*

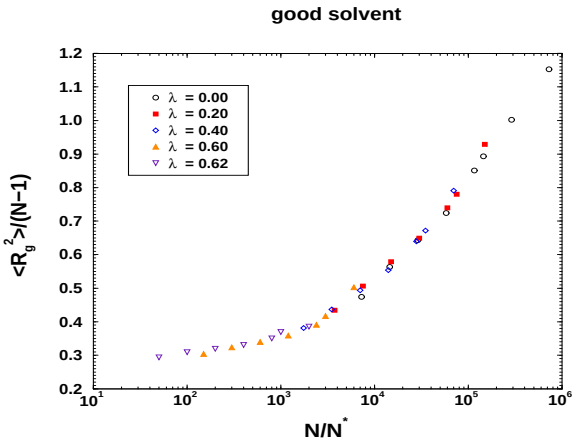

Figure 4.23: *Master curve for the radius of gyration in the good solvent regime.*

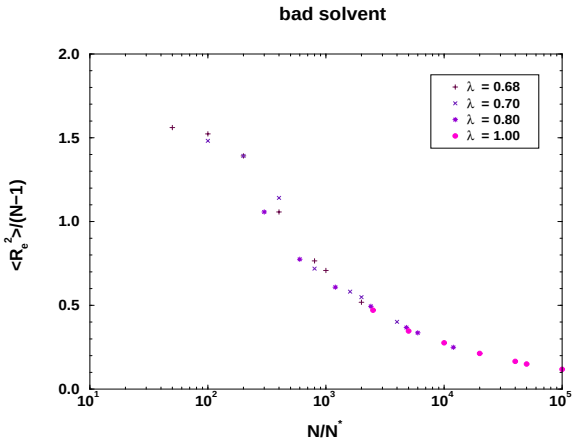

Figure 4.24: *Master curve for the end-to-end distance in the bad solvent regime.*

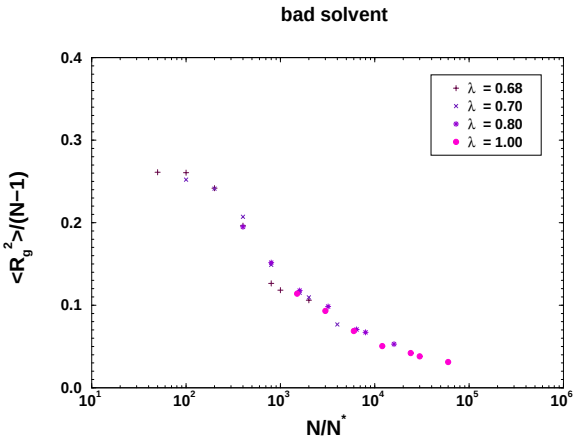

Figure 4.25: *Master curve for the radius of gyration in the bad solvent regime.*

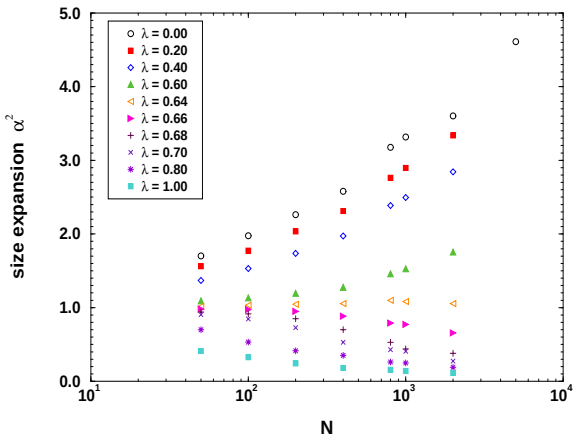

Figure 4.26: *Size expansion factor α^2 as a function of chain length for various values of λ.*

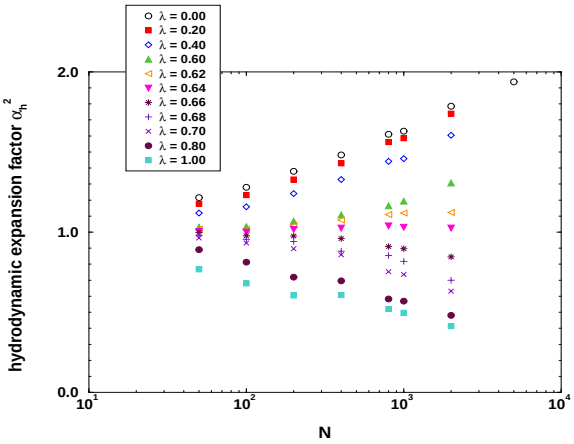

Figure 4.27: *Hydrodynamic size expansion factor $\alpha_h{}^2$ as a function of chain length for various values of λ.*

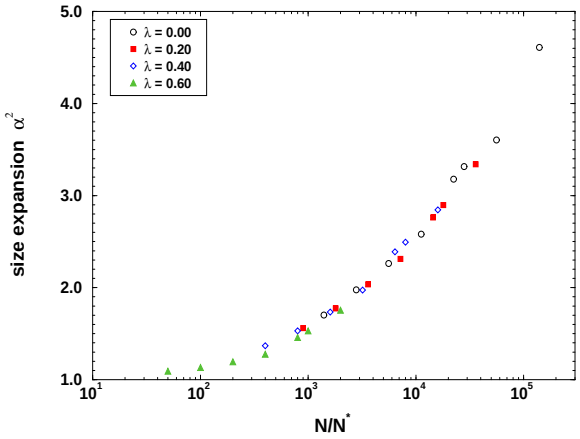

Figure 4.28: *Master curve for the size expansion factor α^2 in the good solvent regime.*

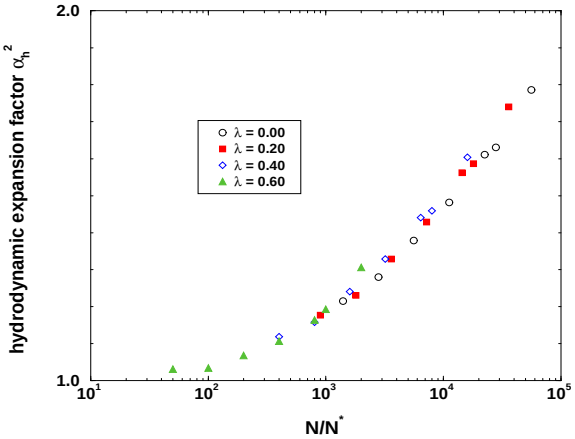

Figure 4.29: *Master curve for the hydrodynamic size expansion factor $\alpha_h{}^2$ in the good solvent regime.*

$$C_\infty = 6 \cdot 0.278\,\sigma^2/{l_b}^2 = 1.770, \tag{4.10}$$

and according to Eq. (2.17) one obtains for the corresponding Kuhn length

$$l_\mathrm{K} = C_\infty\, l_b = 1.718\,\sigma. \tag{4.11}$$

The corresponding Kuhn steps N_K per chain are hence given by

$$N_\mathrm{K} = N/C_\infty = 0.565\,N. \tag{4.12}$$

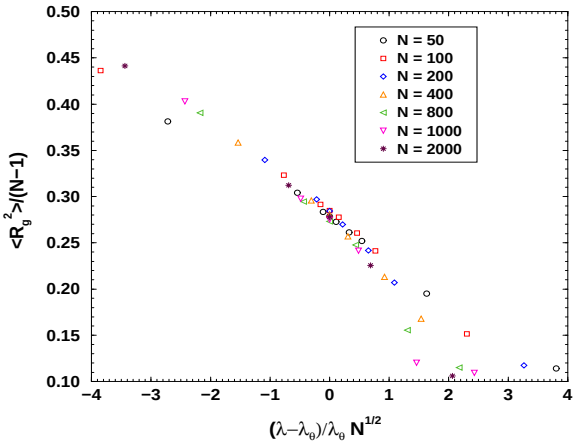

Figure 4.30: *Scaling plot of simulation data of R_g.*

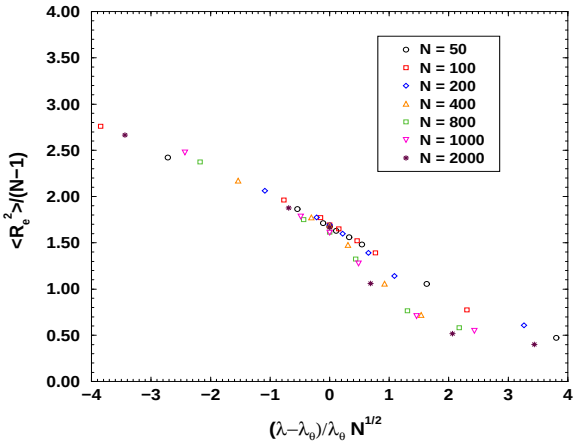

Figure 4.31: *Scaling plot of simulation data of R_e.*

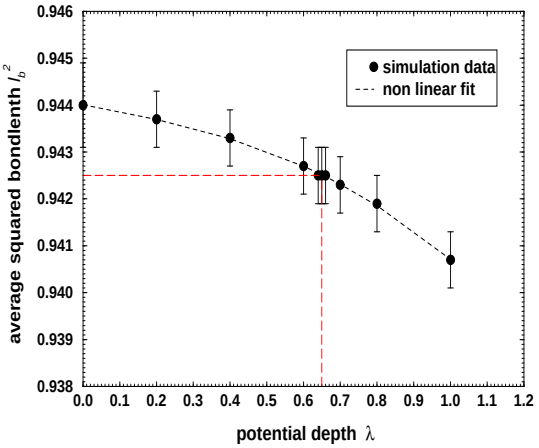

Figure 4.32: *Average bondlength ${l_b}^2$ of the simulated systems vs. interaction parameter λ averaged over all simulated chain lengths for each value of λ. The dashed curve is a non-linear fit of the simulated data and the straight long dashed lines are a guide to the eye. For λ_θ one obtains ${l_b}^2 = 0.9425$.*

Summary

By direct comparison with an experimental system it was shown that the experimentally obtained *good solvent* regimes are far from being close to the ideal athermal case in the exploited simulation model. The static scaling properties of the simulation data were then used to show that it is possible to combine all data points of the good solvent regime into a master curve by appropriately rescaling the lengths N. The superposition of data points is generally very good. The assignment of well-defined shift factors for the data in the vicinity of the θ-point is very difficult as they depart only slightly from a horizontal slope. For the data points in the *collapsed* regime, shift factors can be found as well which cause the data to collapse in a master curve representation. However, in experiments, these solutions are handled with great difficulty. The reduction of the extension of the chain requires that the quality of the solvent must be so poor that suppression of aggregation due to intermolecular attractions, and maintenance of stable solutions with measurable concentrations of the homopolymer, becomes a formidable challenge. Consequently, virtually no data of such systems can be found in literature. For the case of a good solvent many experimental data are scattered throughout literature, however, very often results are reported without providing the *explicit* numerical data so that an appropriate analysis is hardly possible. For R_g the experimental data can be plotted in the same manner as in the master curve representations of Figure 4.23. In [95] this representation was done in essence for numerous data collected from different sources for the expansion factor α^2 of R_g and showed that also for experimental systems in good solvents such a master curve representation of data is possible.

4.2.4 Corrections to scaling: The hydrodynamic radius R_h

In the interpretation of dynamic light scattering experiments the hydrodynamic radius R_h of a polymer is determined via the *Stokes-Einstein* Equation:

$$D_0 = \frac{k_B T}{6\pi\eta} \left\langle \frac{1}{R_h} \right\rangle \tag{4.13}$$

where η is the viscosity of the solvent and D_0 is the translational diffusion coefficient at zero concentration. It is this diffusion coefficient that is actually measured in a dynamic experiment, e.g. by observing the relaxation time of the dynamic scattering function $S(q,t)$ for small momentum transfers $qR_g \ll 1$. The quantity R_h may be interpreted as an equivalent radius, when the polymer is visualized as a rigid sphere with stick boundary conditions, obeying Stoke's law.

According to [56], R_h should follow the same scaling law as R_e or R_g, i. e.

$$R_h \propto R_e \propto R_g \propto N^{\nu} \tag{4.14}$$

with $\nu \approx 0.59$ in a good solvent and $\nu = 0.5$ in a θ-solvent.

However, it has long been observed that the experimentally determined effective exponent of R_h in good solvent is $\nu_{exp} \approx 0.55 \pm 0.02$ [1, 2, 203]. In order to account for the non-asymptotic exponent ν_{exp} in the experimental molecular range, a theory was introduced by *Weill* and *des Cloizeaux* [215] that is based on the blob model, in which the short segments (blobs) exhibit ideal scaling, and only segments larger than some critical size are swollen. Thus, the observed exponent for a finite length chain will be somewhere between ideal $(\nu = 0.5)$ and swollen $(\nu = 0.588)$.

The main point is that the exponent characterizing R_h does not reach its asymptotic value, as predicted by theory, within the range of experimental values of molecular weight $M \approx 10^4 - 10^7$ [21, 148]. The reason for this slow convergence of the exponent lies in the fact that the definition of R_h, see Eq. (2.10) gives a very large weight on short distances which, however, have large corrections to scaling. In [117] it was estimated that molecular weights of at least of the order of $M \approx 10^8$ would be necessary to reach the asymptotic regime for R_h.

In [13] it was shown in simulations of SAW on a fcc-lattice that the data fitted the relation

$$R_h N^{-\nu} = A + BN^{\Delta} \tag{4.15}$$

where $\nu = 0.59$ was used and the exponent $\Delta = -1/2$ was found empirically. However, in this analysis only very short chains $(N \approx 400)$ were simulated.

A simple argument was proposed in [66] which yields an exponent of $\Delta = (\nu - 1)$ for the leading correction to scaling instead of $-1/2$. This exponent could be verified by the simulation data of very long chains in this work and is shown in Fig. 4.33 using the asymptotic exponent $\nu = 0.588$. The correlation coefficient for a linear fit is $\chi = 0.99945$. For comparison, in Fig. 4.34 the very same data are plotted versus an exponent of $\Delta = -1/2$ as suggested in [13] and show a much worse scaling, in particular for the longest investigated chain lengths. A linear data fit in this case yields a correlation coefficient of $\chi = 0.9976$. Hence, the simulation results obtained in [13] with rather short chains give rise to an incorrect exponent Δ.

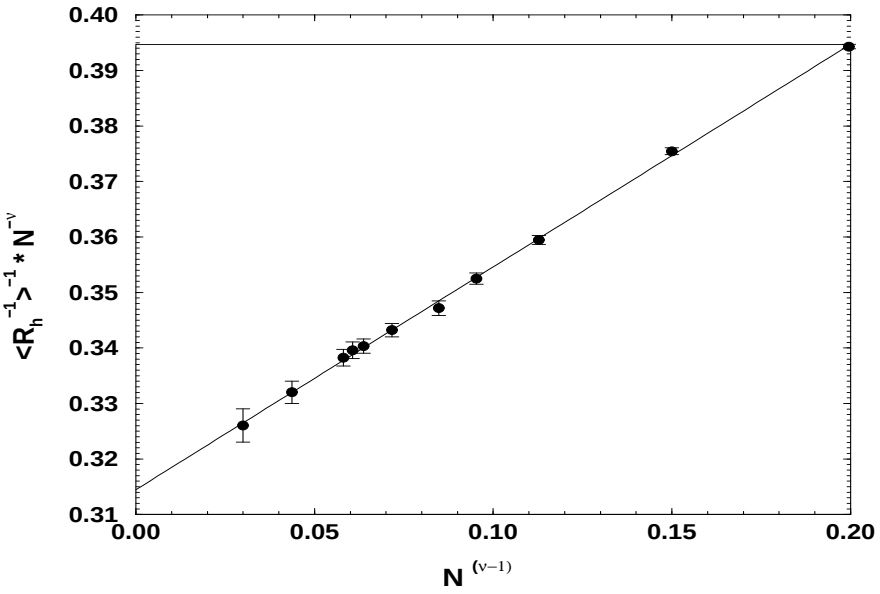

Figure 4.33: *Scaling plot of the corrections to scaling of the hydrodynamic radius R_h with an exponent $\Delta = (\nu - 1)$ and $\nu = 0.588$. The solid line is a linear fit of the simulation data according to the equation $f(x) = (0.406 \pm 0.005)x + 0.3138 \pm 0.0005$ and a correlation coefficient $\chi = 0.99945$.*

A derivation of the exponent $\Delta = (\nu - 1)$ can be found in Appendix E.

In Fig. 4.36 the dimensionless ratio

$$\varrho = \left\langle {R_g}^2 \right\rangle^{1/2} / \left\langle {R_h}^{-1} \right\rangle^{-1} \tag{4.16}$$

of the obtained simulation data is plotted for the full range of simulated solvent qualities, ranging from the athermal limit to the collapsed regime. The effective exponents ν_{eff} of R_g which were obtained in Section 4.2.3 (cf. Fig. 4.16 and Fig. 4.18) were used for these plots. The overall agreement with the expected corrections to scaling is very good.

The ratio ϱ can be used for comparisons with experiments, as it is a dimensionless quantity. For experimental systems of comparable solvent quality one should expect similar values of ϱ. However, as Figure 4.36 elucidates, ϱ strongly depends on both, the solvent quality, and the molecular weight N. In Fig. 4.37 ϱ is plotted only for the three limiting cases of an athermal solvent ($\lambda = 0.0$), a θ-solvent ($\lambda = 0.65$), and a poor solvent, using the limiting values of ν for the ($N \to \infty$) chain limit, $\nu = 0.588$, $\nu = 1/2$, and $\nu = 1/3$. From this Figure, one obtains limiting values of $\varrho = 1.634 \pm 0.005$ for the athermal case, $\varrho = 1.431 \pm 0.007$ for a θ-solvent and $\varrho = 0.971 \pm 0.001$, respectively.

In experiments, the ρ-values are usually not extrapolated but simply taken as the ratio R_g/R_h, where R_h is determined via Equation 4.13 from the extrapolated translational diffusion coefficient in the limit of zero scattering vector k and zero concentration c. Typical experimental values of ϱ range from $\varrho \approx 1.48$ to 1.51 for polyisoprenes in good solvent (cyclohexane) [202] and from $\varrho \approx 1.26$ to 1.29 for various polymers in θ–solvents [110].

The simulation data that are displayed in Figure 4.36 can be extrapolated to ($N \to \infty$). One then obtains the limiting values

$$\varrho_\infty = \lim_{N \to \infty} \varrho \tag{4.17}$$

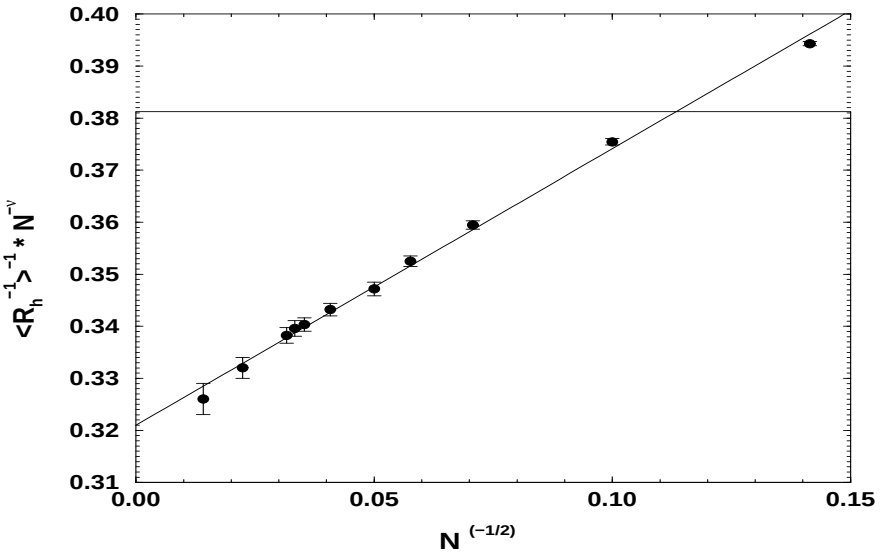

Figure 4.34: *Scaling plot of the corrections to scaling of the hydrodynamic radius R_h with an exponent $\Delta = 1/2$ and $\nu = 0.588$. The solid line is a linear fit of the simulation data according to the equation $f(x) = (0.538 \pm 0.014)x + 0.320 \pm 0.001$ and a correlation coefficient $\chi = 0.9976$.*

for the simulated chains for the whole range of solvent qualities. The scaling exponents in the scaling law of R_g and R_h are the same in the limit of infinite chain length. Therefore, only the pre-factors (a/c) remain in the quantity ϱ to give $\varrho_\infty = (a/c)$. This ratio is displayed in Figure 4.35. The theoretical limit in the bad solvent case is given by a hard sphere which yields $\varrho = 0.775$. The quantity ϱ_∞ undergoes a smooth transition from the good solvent to the bad solvent regime which is an effect of the finiteness of the chains. In the limit ($N \to \infty$) one would expect a step-function-like behavior of (a/c). In experimental systems, in addition to the finiteness of the chain lengths one has polydispersity effects, which also have an effect on the quantity ϱ. Therefore, in order to perform a unique mapping of experimental length scales onto the simulated model system of chains experimental systems, one has to consider polydispersity effects as well.

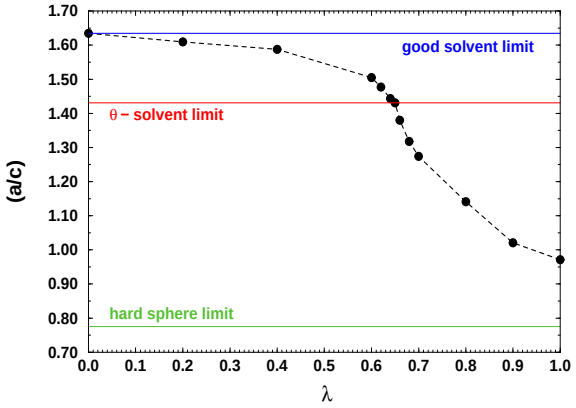

Figure 4.35: *Ratio $\rho_\infty = (a/c)$ of the pre-factors in the scaling law of Eq. (4.24) and (4.25). For the three limiting cases, the good solvent, θ-solvent and bad solvent, the theoretical exponents were used. The intermediate ϱ-values were obtained by using* effective *exponents, obtained from the simulation data of finite chains. In the limit of infinitely long chains, one expects a step-function-like behavior of ϱ_∞.*

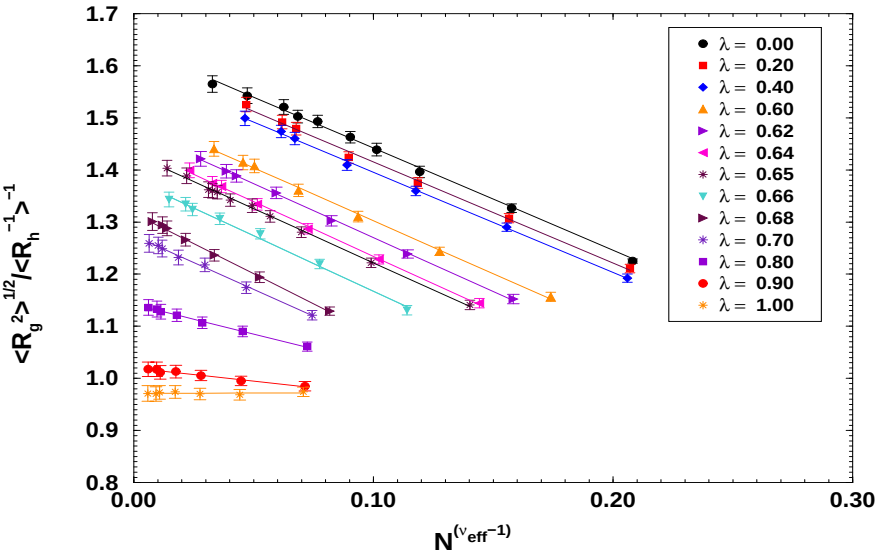

Figure 4.36: *Dimensionless ratio* $\varrho = \sqrt{\langle R_g{}^2 \rangle} / \left\langle R_h{}^{-1} \right\rangle^{-1}$ *of the simulated linear chains for different good solvent qualities using the effective exponents* ν_{eff} *obtained in Section 4.2.3 from Fig. 4.16.*

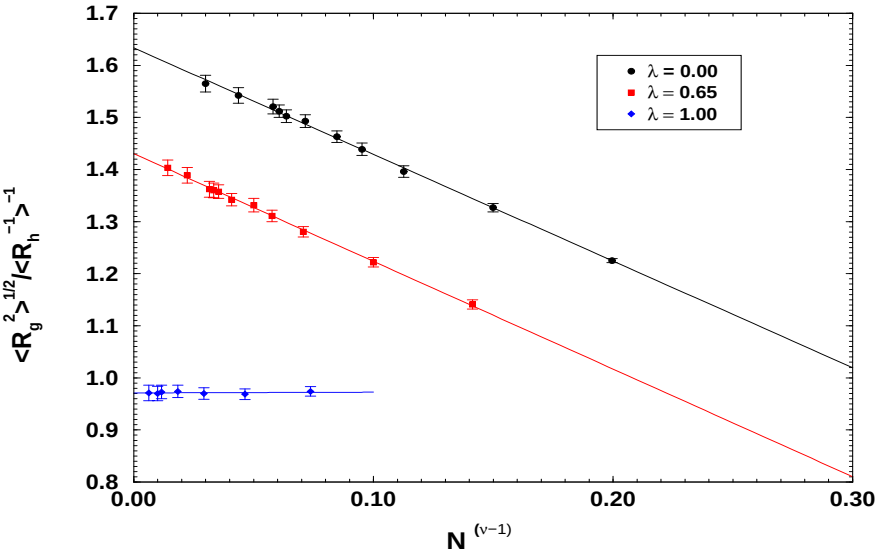

Figure 4.37: *Dimensionless ratio* $\varrho = \sqrt{\langle R_g{}^2 \rangle} / \left\langle R_h{}^{-1} \right\rangle^{-1}$ *of the simulated linear chains. The upper solid curve represents a linear fit of the data points according to the equation* $f(x) = -(1.96 \pm 0.04)x + 1.634 \pm 0.005$ *and a correlation coefficient* $\chi = 0.99990$*. The dotted line is a linear fit according to* $f(x) = -(2.09 \pm 0.04)x + 1.431 \pm 0.007$ *and has a correlation coefficient* $\chi = 0.99893$*. The dashed line for the bad solvent data is a linear fit according to* $f(x) = (0.009 \pm 0.003)x + 0.971 \pm 0.001$ *with* $\chi = 0.99981$*.*

4.3 Polydispersity

In our simulations, all individual runs are done with only one chain length at a time which corresponds to a polydispersity index $U = 0$ (see Eq. (4.22)) which means that one has exactly monodisperse chains. In experiments, however, this is usually not the case. Depending on the polymerization process and the synthesis method which is used to obtain the respective polymers under investigation one obtains a more or less broad molecular weight distribution (MWD). These distributions can be determined by **G**el **P**ermeation **C**hromatography (GPC) experiments. GPC measurements however are error prone as it is not an absolute method like static light scattering, but it needs calibration with a well known polymer sample. Therefore it is often difficult to obtain conclusive results with unknown polymer samples, because the equilibration will usually only work among polymers of the same homology class. Another experimental problem is the fact that from the MWD alone one does not get any information about the kind of branching that might be present in a polymer sample. Very often, however, this is of considerable interest in industrial applications because branching has an important influence on the properties of polymeric materials.

Relatively broad MWDs are usually obtained when performing *step polymerizations* where the polymer chain grows stepwise by reactions that can occur between any two molecular species A and B in the reaction mixture, e.g.:

$$AA + BB \rightarrow AABB, \tag{4.18}$$

$$AABB + AA \rightarrow AABBAA. \tag{4.19}$$

Typical products obtained by step growth polymerization are polyester, polycarbonate, polyamide and polyurethane. The relationship between the average molecular weight $\langle M_n \rangle$ or the average polymerization degree $\langle N_n \rangle$ and the conversion p is described by the *Carothers Equation*

$$\langle N_n \rangle = \frac{1}{1-p}, \tag{4.20}$$

where p is the fraction of functional groups that have reacted. Equation 4.20 is derived under the assumption of equal reactivity of the functional groups, i.e. the reactivity of the functional group is independent of the length of the chain and unaffected by the reaction of other functional groups in the monomer or polymer.

A reasonable representation of the obtained MWDs in experiments is given by the *Zimm-Schulz-Distribution*. The latter can be formulated in terms of the degree of polymerization N and is given by:

$$p(N) = \frac{1}{\Gamma(\beta)} \left(\frac{\beta}{\langle N_n \rangle} \right)^{\beta} N^{\beta-1} \exp\left(-\frac{\beta N}{\langle N_n \rangle} \right). \tag{4.21}$$

This function includes the two parameters β, which determines the shape, and $\langle N_n \rangle$, which denotes the *number average* of the degree of polymerization. Γ is the gamma-function. The parameter β is related to the polydispersity index U

$$U = \frac{\langle N_w \rangle}{\langle N_n \rangle} - 1 \tag{4.22}$$

by

$$U = \frac{1}{\beta}, \tag{4.23}$$

with $\langle N_w \rangle$ being the *weight average* of the degree of polymerization. For values $\beta \approx 2.0$, Eq. (4.21) often provides a reasonable data fit for experimental data [188]. In many experimental studies, $\langle N_w \rangle / \langle N_n \rangle$-values vary a great deal, usually between 1.1 and 2.4 (see e.g. [155]). Figure 4.38 displays different examples of $p(N)$, according to Eq. (4.21), each one with one particular value of $\langle N_w \rangle / \langle N_n \rangle$. Therefore, in order to systematically investigate the influence of polydispersity on the static properties of the simulated polymer systems, Eq. (4.21) was used as a distribution function. The results for R_g and R_h were then recalculated, assuming the distribution $p(N)$ for the different chain lengths N.

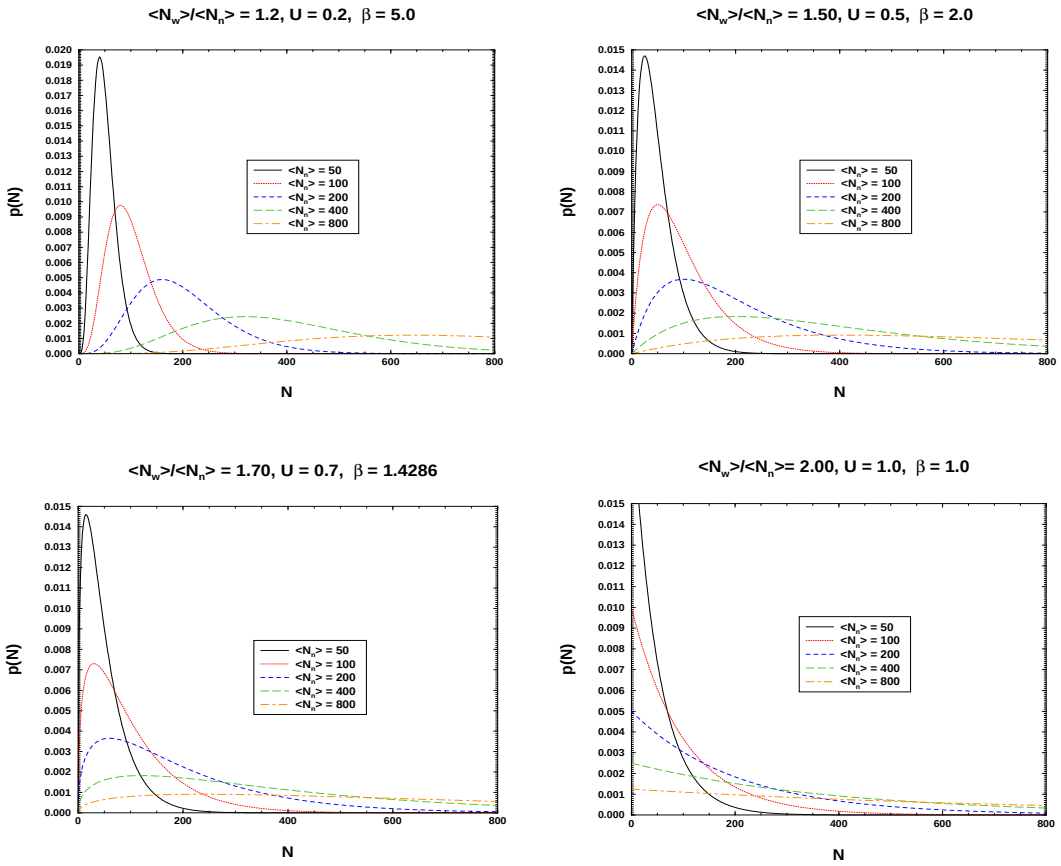

Figure 4.38: *Schulz-Zimm MWD for various polydispersities as displayed.*

With the Ansatz

$$\left\langle {R_g}^2 \right\rangle (N) = a^2 \, N^{2b} \tag{4.24}$$

and

$$R_H(N) \equiv \left\langle R_h^{-1} \right\rangle^{-1}(N) = c\, N^d, \tag{4.25}$$

one obtains for the radius of gyration:

$$\begin{aligned}\left\langle {R_g}^2 \right\rangle &= \int_0^\infty p(N) \left\langle {R_g}^2 \right\rangle (N)\, dN = 1/\Gamma(\beta) \left(\frac{\beta}{\langle N_n \rangle}\right)^\beta a^2 \frac{\underbrace{\int_0^\infty N^{(2b+\beta-1)} \exp\left(\frac{-\beta N}{\langle N_n \rangle}\right) dN}_{\Gamma(2b+\beta)}}{\left(\frac{\beta}{\langle N_n \rangle}\right)^{(2b+\beta)}} \\ &= a^2 \frac{\Gamma(2b+\beta)}{\Gamma(\beta)} \cdot \left(\frac{\beta}{\langle N_n \rangle}\right)^{-2b} = a^2 \langle N_n \rangle^{2b} \left(\frac{\Gamma(2b+\beta)}{\Gamma(\beta)} \cdot \beta^{-2b}\right).\end{aligned} \tag{4.26}$$

The analogous calculation for R_H yields:

$$R_H = c \frac{\Gamma(d+\beta)}{\Gamma(\beta)} \cdot \left(\frac{\beta}{\langle N_n \rangle}\right)^{-d} = c\, \langle N_n \rangle^{-d} \left(\frac{\Gamma(d+\beta)}{\Gamma(\beta)} \cdot \beta^{-d}\right) \tag{4.27}$$

The general expression for $\varrho = \dfrac{\left\langle {R_g}^2 \right\rangle^{1/2}}{R_H}$ reads:

$$\varrho = \varrho\left(\langle N_n \rangle, \beta, b, d\right) = a/c \left(\frac{\beta}{\langle N_n \rangle}\right)^{(d-b)} \left(\frac{\Gamma(\beta)\Gamma(2b+\beta)}{\left[\Gamma(d+\beta)\right]^2}\right)^{(1/2)}. \tag{4.28}$$

In Equation (4.28), there is no *explicit* N-dependence of ϱ anymore, however, an N-dependence comes in by the effective exponents d and b, which, in experiments and simulations, are a function of N. Asymptotically, $d = b$, so that the N-dependence of ϱ vanishes completely for ($N \to \infty$). In this case one yields:

$$\varrho = \varrho\left(\beta, b\right) = a/c \left(\frac{\Gamma(\beta)\Gamma(2b+\beta)}{\left[\Gamma(b+\beta)\right]^2}\right)^{(1/2)}. \tag{4.29}$$

In Eq. (4.29), ϱ is only a function of the polydispersity parameter β and the *asymptotic* scaling exponent b which is 0.588 in a good solvent and 0.5 in a θ-solvent, respectively. For all other solvent qualities in between these two limiting cases one can use effective exponents, obtained from a log-log plot of R_g vs. N. The ratio (a/c) can be obtained from simulation data by extrapolating the obtained ϱ-values to the limit ($N \to \infty$).

Using different asymptotic values for b in Eq. (4.29) one obtains a set of curves $\varrho = \varrho(\beta, b)$. Inserting the value $b = 0.5$ for a θ-solvent simplifies Eq. (4.29) further and one obtains:

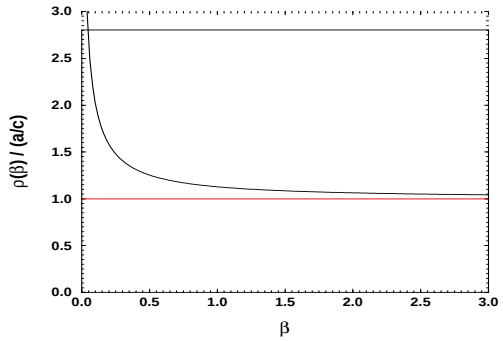

Figure 4.39: *Plot of $\varrho(\beta, b = 0.5)$ according to Eq. (4.30).*

$$\varrho = \varrho\,(\beta, b = 0.5) = a/c\;\beta^{1/2}\,\frac{\Gamma(\beta)}{\Gamma(\beta + 1/2)}. \tag{4.30}$$

This function is plotted in Figure 4.39 and exhibits the following limiting behavior:

$$\lim_{\substack{\beta\to\infty \\ U\to 0}} [\varrho/(a/c)] = 1, \tag{4.31}$$

$$\lim_{\substack{\beta\to 0 \\ U\to\infty}} [\varrho/(a/c)] \to \infty \tag{4.32}$$

The simulation data quantitatively exhibit the same limiting behavior. This is shown in Figures 4.40 and 4.41 where the function ϱ is plotted for four different polydispersities β. The function ϱ diverges with increasing polydispersity index U and it approaches the finite limiting value (a/c) as U approaches zero. The limiting values of monodisperse chains have been determined in a previous plot.

The calculation of the C_∞-value of our simulation model allows one to perform a minimal mapping of length scales onto experimental systems. C_∞ expresses the stiffness of a polymer chain in a dimensionless parameter. Thus, this is the smallest length scale at which a polymer chain exhibits flexibility. A mapping of C_∞ of our simulation model onto PS (see Table 2.2 on Page 13), which has long been regarded as the best model polymer of linear flexible chains, yields a ratio of $1 : 6$. However, for lengths larger than the persistence lengths, one has freedom in this rescaling of lengths, as was demonstrated in Section 4.2.3. This is valid as long as one does not leave the universality class of the chains, e.g. the good solvent or θ-solvent limit.

A potential uniqueness of a mapping of length scales is provided by the N-, respectively N_n-dependence of the dimensionless quantity ϱ. This dependence occurs because of the huge corrections to scaling that were subject of a previous chapter. We tested this mapping idea by taking into account polydispersity in our linear chains as described above. We used experimental data obtained by *Park et al* [155] for several polydispersities of PS in cyclohexane (θ-solvent) at $32.5\,^\circ$C. In performing this mapping we try to make use of the N-dependence of the corrections to scaling of the quantity ϱ. The results are displayed in Figure 4.42 and Table 4.1 and clearly reveal that this mapping procedure does not work. If it worked, then the obtained ratios in Table 4.1 for different polydispersities would

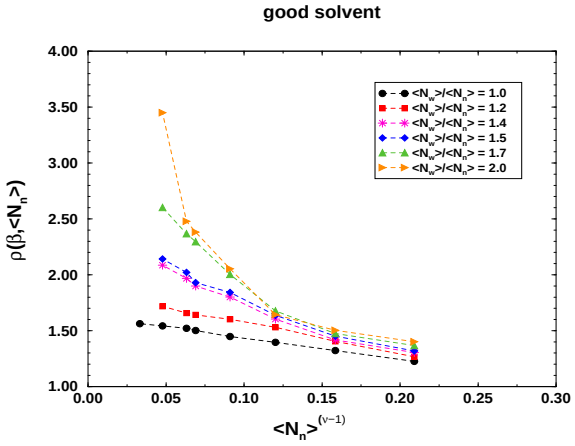

Figure 4.40: *Dimensionless ratio ϱ for various polydisperse linear chains in athermal solvent conditions.*

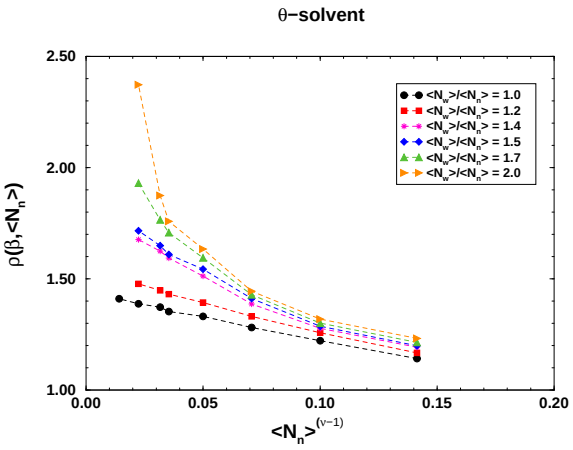

Figure 4.41: *Dimensionless ratio ϱ for various polydisperse linear chains in θ-solvent condition.*

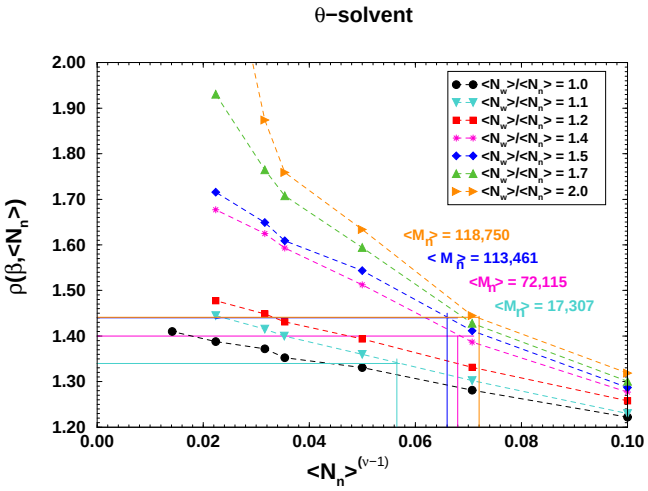

Figure 4.42: *The same plot as in Fig. 4.41 but with comparison to experiment. Experimental data by* Park et al *[155] on PS in θ-solvent have been used. The number average molecular weight is displayed in terms of PS-repeat units.*

Table 4.1: *Mapping of experimental PS in a θ-solvent onto the simulation model in this work. The errors of $\rho = R_g/R_h$ were calculated by using the errors of R_g ($\pm 3\%$) and R_h ($\pm 2\%$) as given in Ref. [155]. The errors of $\langle N_n \rangle_{sim}$ were obtained by taking into account the errors of ρ in Figure 4.42. If this mapping worked, the obtained ratios $\langle N_n \rangle_{exp}/\langle N_n \rangle_{sim}$ for various polydispersities should be the same. The obvious large scatter of ratios reveals that the experimental data scatter is too large in order to perform a unique mapping of length scales.*

$\langle N_w \rangle \,/\, \langle N_n \rangle$	1.1	1.4	1.5	2.0
sample[a]	2N	F-3	F-2	x
$\langle N_n \rangle_{\text{exp}}$ in experiment[a]	$17,307$	$72,115$	$113,461$	$118,750$
ρ in experiment[a]	1.34 ± 0.08	1.40 ± 0.08	1.44 ± 0.09	1.44 ± 0.09
$\langle N_n \rangle_{\text{sim}}$ in simulation[b]	313 ± 800	216 ± 126	229 ± 114	193 ± 75
$\langle N_n \rangle_{\text{exp}}/\langle N_n \rangle_{\text{sim}}$	55	334	363	615

[a] Data taken from Ref. [155]. PS in cyclohexane (θ-solvent). $\langle N_n \rangle$-values are displayed as multitudes of PS-repeat units.

[b] According to the data in Figure 4.42.

be more or less the same. However, they deviate strongly, which means, that no unique mapping of length scales can be performed.

The main reason why this approach to mapping length scales fails, lies in the fact that the quantity ϱ is only very slightly dependent upon $\langle N_n \rangle$. Therefore, the quantity ϱ changes only slightly while there is a huge change in $\langle N_n \rangle$, and as a result, making the mapping of $\langle N_n \rangle$-values arbitrary. In principle, when going from $\langle N_n \rangle = 50$ to $\langle N_n \rangle \to \infty$ the change in ϱ is roughly 30% for the monodisperse system, cf. Fig. 4.40, but the change in $\langle N_n \rangle$ is arbitrarily large. This effect decreases with increasing polydispersity, because then the curves in Figures 4.40 and 4.41 have a larger increase. This can be clearly seen in the corresponding errors of $\langle N_n \rangle$ in Table 4.1. The larger the polydispersity, the smaller is the error in the determination of $\langle N_n \rangle$. For the smallest considered polydispersity ($\langle N_w \rangle \,/\, \langle N_n \rangle = 1.1$) one obtains an uncertainty in the determination of $\langle N_n \rangle$ that is more than 2 times larger than the actually determined value which makes the result meaningless. Therefore, the main problem in this failure of the attempt to perform a mapping lies in the large data scatter of experimentally determined R_g- and R_h-values and the resulting uncertainty in the calculation of ρ.

As a test of the good solvent regime we used experimental data [202] of PIP in cyclohexane, which is a good solvent at $25°$C. In Ref. [202], practically monodisperse ($M_w/M_n \leq 1.1$) polymers were synthesized. As example we give the results for a mapping with two samples of Ref. [202], namely L-14 and L-12. For these two samples, ϱ was determined as $\varrho = 1.51$ and $\varrho = 1.48$, respectively. The N_n-values of their samples, expressed in multitudes of PIP monomer units, was 5433 and 9466, respectively. Both samples are monodisperse and our mapping yields a ratio of 1:22 for L-14 and 1:56 for L-12, which clearly demonstrates again, that the quantity ϱ is not suitable for a unique mapping of lengths due to experimental data scatter.

4.4 Shape analysis

This section provides a shape analysis of the simulated linear chains. In performing this analysis we go beyond any previous studies which usually concentrated on very short linear chains simulated on various lattices. To the best of our knowledge this is the first study of shape properties of the chain-model introduced in Section 3.4. No experimental data are available on shape properties and only few MC-studies of rather short linear chains have been performed.

The only results of shapes of linear chains obtained in MD simulations to the best of our knowledge, are a series of investigations published by *Bishop* and various co-workers. In each publication the results for δ were different and *always* larger than the value suggested by theory, see Table 4.2. These systematic deviations could be due to the nearest neighbor harmonic spring forces which are used in this series of publications having an equilibrium distance of 1.0 as opposed to 0.97 in our model. In [35] their model was applied to the simulation of star branched systems as well. However, there is a discrepancy between their obtained raw data for linear chains in Tables I and II of Ref. [35]. For the largest investigated linear chain length $N = 200$ they give values of $\left\langle {R_g}^2 \right\rangle = 136.96 \pm 0.90$ in Table I and $\left\langle {R_g}^2 \right\rangle = 151.14 \pm 1.87$ in Table II. This discrepancy of more than 10% for the same quantity is not resolved and therefore the results of this publication are at least questionable. In the first publication [32] in this series of papers, no extrapolation of the obtained values to $(N \to \infty)$ was done. However, our simulations clearly show that this has to be done, as there are rather large finite size effects, cf. Figure 4.43.

Batoulis and *Kremer* [13] performed MC simulations on a fcc lattice and performed an extrapolation of the obtained data to $(N \to \infty)$. They obtained a value for δ which is 4.5% larger than the one expected from theory. As their maximum chain length was $N = 400$ this discrepancy can be explained by finite size effects.

Zifferer et al [226, 231] performed MC simulations both, on- and off-lattice, with up to $N = 1000$ monomers and yielded values for δ and $\delta^\star$ which are slightly higher, respectively lower than the one that theory suggests, cf. Table 4.2.

Our simulations were performed with much longer chains than where used by either of these researchers. Furthermore, we obtained simulation data with a higher accuracy than in previous investigations of shape properties. The results of δ and $\delta^\star$ in an extrapolation to $(N \to \infty)$ are listed in Table 4.2 along with the results of other publications. Our result for δ is 3% larger than the theoretical value. Along with the results of other researchers this indicates that theory underestimates the influence of excluded volume on the shape of chains and that higher order terms should be taken into account in the ϵ-expansion of Ref. [9]. All other shape parameters listed in Table 4.2 are in fairly well agreement with theory. A complete overview of the obtained results of the asphericities is given in Fig. 4.43 according to the definitions in Section 2.4.1.

For the quantity b no theoretical values are available in literature. An extrapolation of the simulation data of b for the good solvent case and at the θ-point yields $b = 0.6599 \pm 0.0007$ and $b = 0.6255 \pm 0.0005$, respectively. In [196] a shape analysis of MC-simulated polypropylene chains using the rotational isomeric state model with excluded volume yielded $b = 0.66 \pm 0.33$ in excellent agreement with our result. From Figure 4.43 one can conclude that the quantity b is the most sensitive to both, solvent quality and chain length, and $\delta^\star$, the average of two fluctuating quantities, is the least sensitive one. As further illustration of this fact, the influence of finite size is displayed as well in Figure 4.43 by an extrapolation of $(N \to \infty)$ for two solvent qualities.

The quantity $\delta^\star$ has been determined in only very few MC simulation studies which considered only very short chains. In these simulations, finite size effects might contribute a systematic bias to

Table 4.2: *Table of extrapolated asphericities δ and $\delta^\star$ of linear chains obtained in this work in comparison with results obtained by other investigators.*

Reference	δ (good solvent)	$\delta^\star$ (good solvent)	δ (θ–point)	$\delta^\star$ (θ–point)
theory	0.534[a]	0.415[b]	0.5263[a]	0.394[b]
this work	0.5425 ± 0.0008	0.434 ± 0.004	0.5221 ± 0.0013	0.394 ± 0.003
Batoulis and Kremer[c]	0.55	$---$	$---$	$---$
Bishop and Michels[d]	0.558 ± 0.100	$---$	0.518 ± 0.095	$---$
Bishop and Clarke[e]	0.570 ± 0.035	$---$	0.521 ± 0.041	$---$
Bishop and Smith[f]	0.553 ± 0.025	$---$	$---$	$---$
Bishop et al[g]	0.543 ± 0.003	0.429 ± 0.002	0.529 ± 0.001	0.397 ± 0.001
Cannon et al[h]	0.543 ± 0.002	$---$	$---$	$---$
Jagodzinski et al.[i]	$---$	0.431	$---$	0.396
Zifferer[j]	$---$	$---$	0.5267	0.3945
Zifferer[k]	0.5467	0.4585	$---$	$---$

[a] According to [212] and [9].
[b] [105]. Renormalization group calculations.
[c] [13]. MC simulations of short chains on a fcc lattice. $(N \leq 400)$.
[d] [32]. BD simulations of very short chains in the continuum.($N \leq 48$).
[e] [34]. BD simulations of very short chains in the continuum. ($N \leq 97$).
[f] [35]. BD simulations of short chains in the continuum. ($N \leq 250$).
[g] [36]. Off-lattice MC simulations of very short chains. $(N \leq 200)$ with an error of $0.02 - 0.05\%$.
[h] [46]. Off-lattice MC simulations.
[i] [105]. MC Simulations on a simple cubic lattice. ($N \leq 220$).
[j] [231]. Off-lattice MC simulations. ($N \leq 963$).
[k] [226]. MC Simulations on a tetrahedral lattice. ($N \leq 1000$).

the obtained extrapolated values. In order to perform very precise measurements of shapes of chains one should best refer to $\delta^\star$ rather than b or δ. One the other hand, in literature, mostly the the latter quantity has been used.

Our study gives a complete account of δ, $\delta^\star$ and b for many different solvent qualities. In Figure 4.44 the results of an extrapolation of all obtained asphericity values to $(N \to \infty)$ are displayed. As one expects, all definitions yield the same values in the collapsed regime ($\lambda \geq 0.8$), gradually approaching a value of $\delta = \delta^\star = b = 0$. An extrapolation of the obtained curve indicates that zero would be obtained at $\lambda \approx 1.1$ but more likely the different curves will level off into a saturation just above zero due to the excluded volume effect.

In order to compare the results obtained for chains containing different number of beads, the normalized principal moments (**shape factors**)

$$sf_i = \left\langle {L_i}^2 \right\rangle / \left\langle {R_g}^2 \right\rangle \tag{4.33}$$

and

$$sf_i{}^\star = \left\langle {L_i}^2 / {R_g}^2 \right\rangle \tag{4.34}$$

were measured.

Figure 4.45 displays the determined values of sf_i versus the interaction parameter λ. For $sf_i^\star$ very similarly shaped curves are obtained. For highly symmetric (spherical) configurations $sf_i \approx 1/3$ whereas for rodlike molecules $sf_3 = sf_2 = 0$ and $sf_1 = 1$. Apart from these limiting values no exact analytical expressions are available for these quantities. In the three figures displaying sf_i one can clearly see that the curves exhibit a long plateau at high temperature which is only slightly dependent upon N. The changes in shape for larger values of λ are the more pronounced the longer the chains are and reach a value of $\approx 1/3$ for the longest investigated chain lengths. This behavior fits well to the observed sharp collapse transition of long chains in Section 4.1.

The extrapolation of all shape factors to $(N \to \infty)$ is displayed in Figure 4.46. In the collapsed regime all definitions, independent of the averaging process, approach the same value of $1/3$. There is only a slight difference between sf_i and $sf_i^\star$ in the good and θ-solvent regime, which diminishes for collapsed chains.

In Figure 4.47 the results of the extrapolated ratios of principal moments are displayed, indicating the gradual transition of the chains from a rod-like object to a more spherical object as the solvent quality decreases. In their original paper, *Sŏlc and Stockmayer* [183] performed MC simulations on a lattice and found a ratio of $\langle {L_3}^2 \rangle : \langle {L_2}^2 \rangle : \langle {L_1}^2 \rangle = 11.7 : 2.7 : 1$ for unrestricted random walks on a cubic lattice. Recent MC simulations with simple cubic lattice chains and polymer-polymer interactions were performed by *Tanaka and Mattice* [195] and resulted in a ratio of $15 : 3 : 1$ for athermal chains to $11.2 : 2.6 : 1$ for chains under θ-conditions to $1.9 : 1.4 : 1$ for collapsed chains in the low temperature regime. All of these data points are below our measurements. This might indicate effects of the used lattice models and also finite size effects, as the used chain lengths in these investigations were only $N = 200$ and $N = 1000$, respectively.

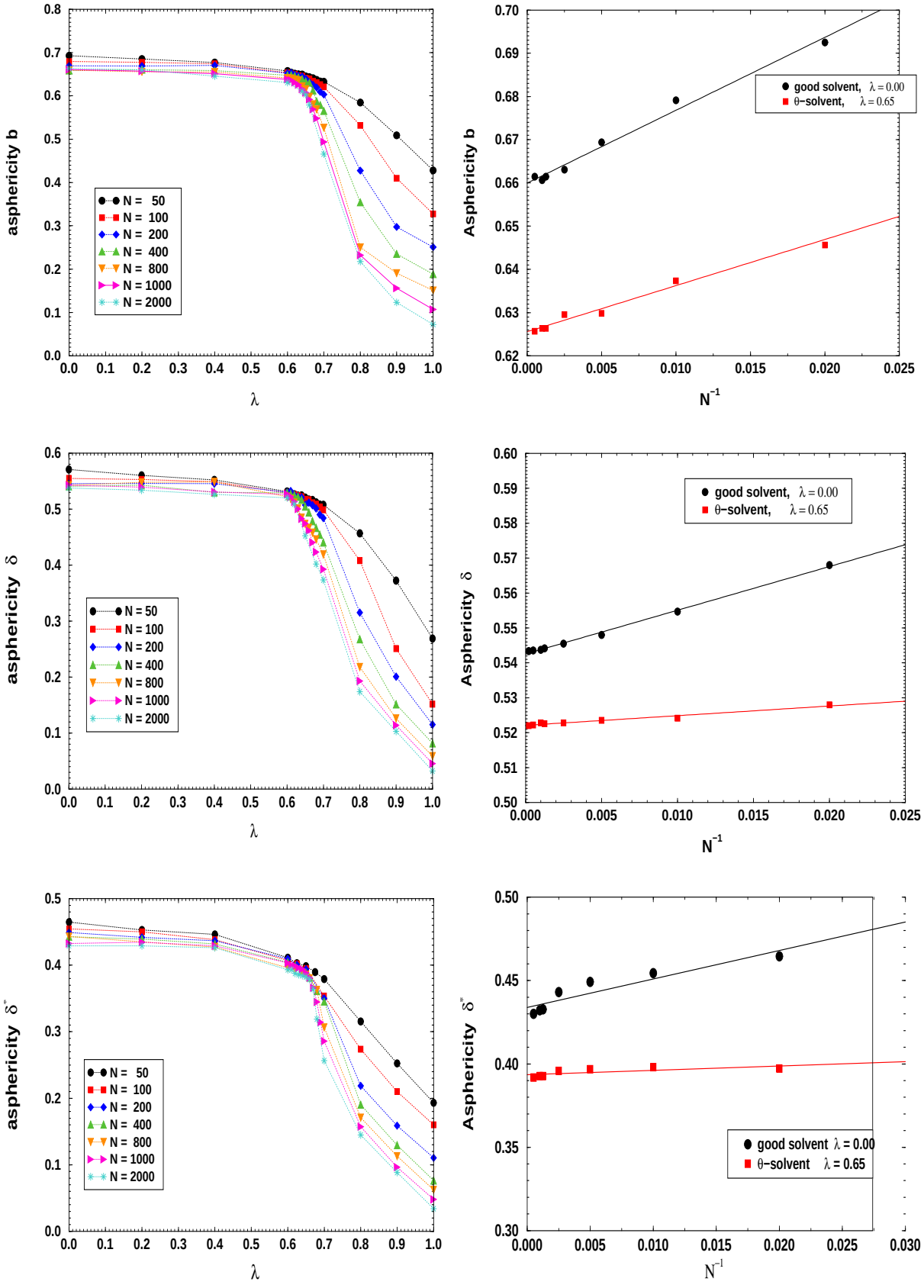

Figure 4.43: *Asphericites of linear chains of all investigated solvent qualities and chain lengths N and their extrapolation to $(N \to \infty)$ in a good solvent and a θ-solvent.*

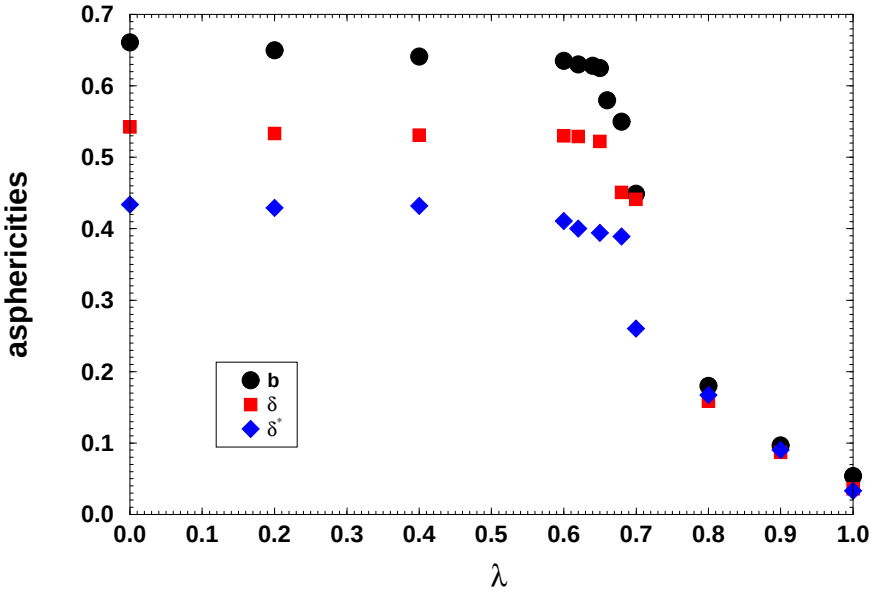

Figure 4.44: *Extrapolated ($N \to \infty$) asphericities of linear chains for different solvent qualities.*

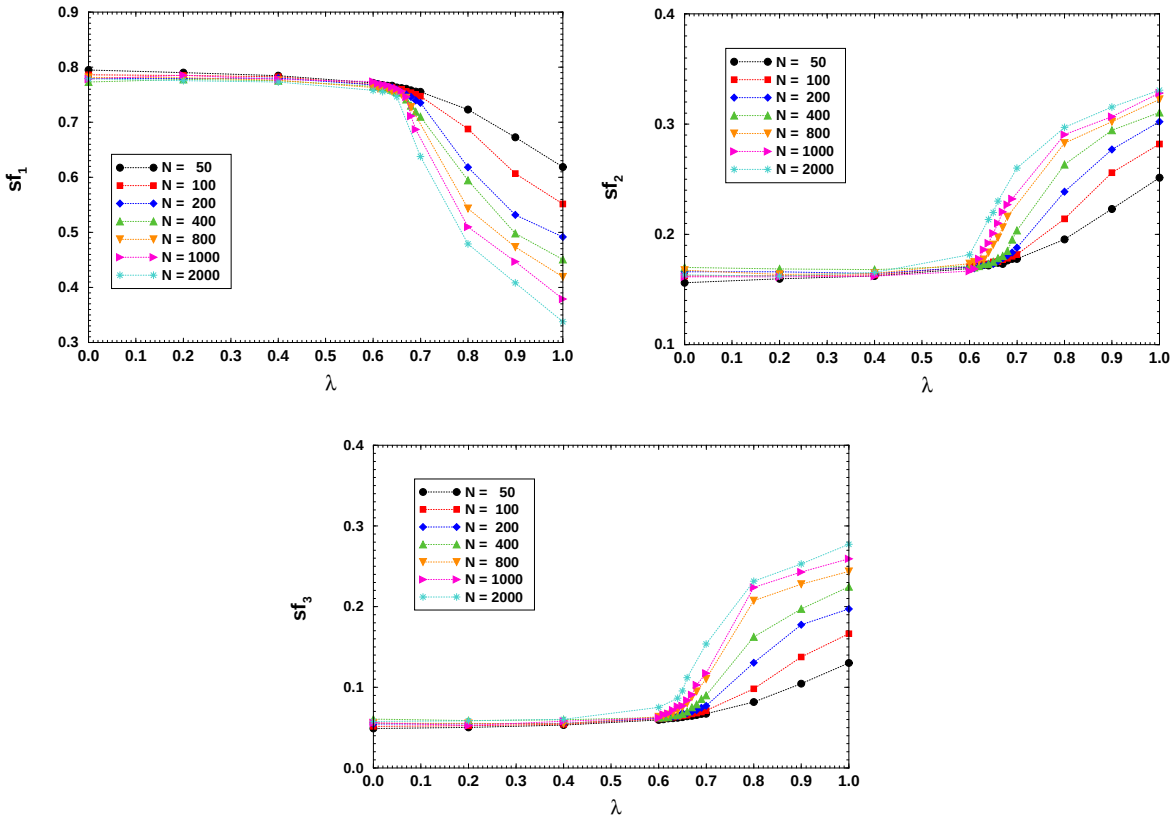

Figure 4.45: *Shape factors sf_i of linear chains of all investigated solvent qualities.*

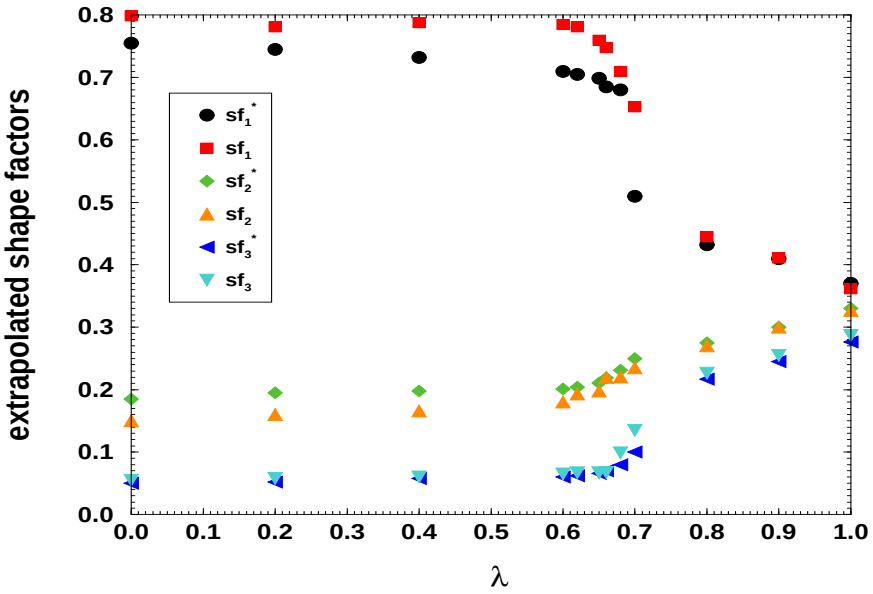

Figure 4.46: *Extrapolated ($N \to \infty$) shape factors sf_i and $sf_i^\star$ of linear chains of solvent qualities covered by simulations.*

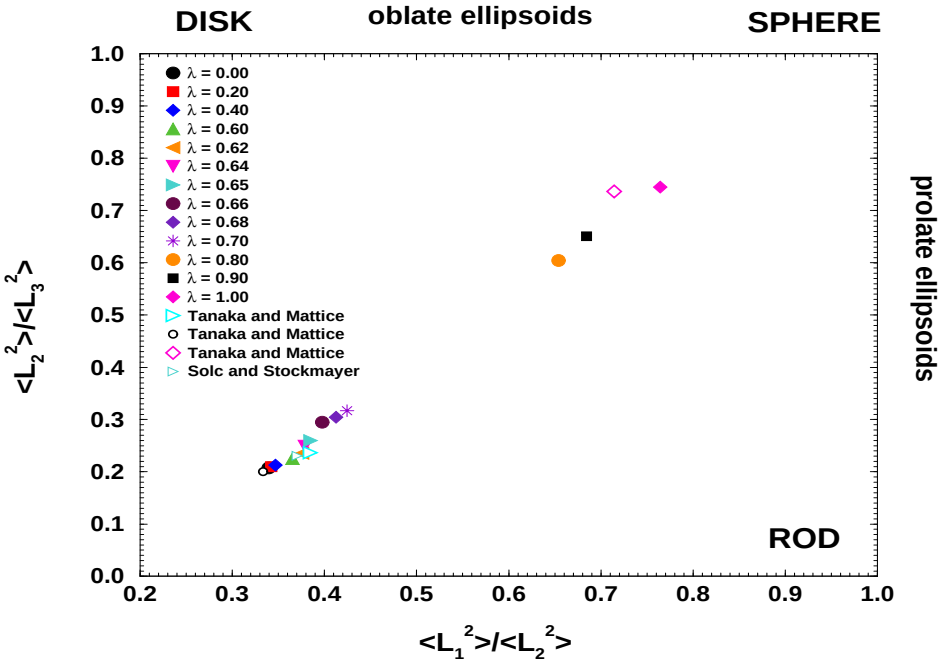

Figure 4.47: *Extrapolated ($N \to \infty$) ratios of principal moments for linear chains of different solvent qualities. Several data points from literature are displayed as well.*

4.5 Simulation details: θ – transition

Starting from the athermal case with $\lambda = 0.0$, the systems were allowed to equilibrate for a long time, typically ten times the relaxation time and statistical averages were then taken from runs extending typically over a time interval of about ten times the characteristic relaxation time. The last configuration was then used as starting point for the next run at a lower temperature. By this procedure the systems were gradually annealed to temperature below the θ–temperature. Snapshots of equilibrated linear chains at three different solvent qualities are displayed to scale in Fig. 4.48 to 4.50.

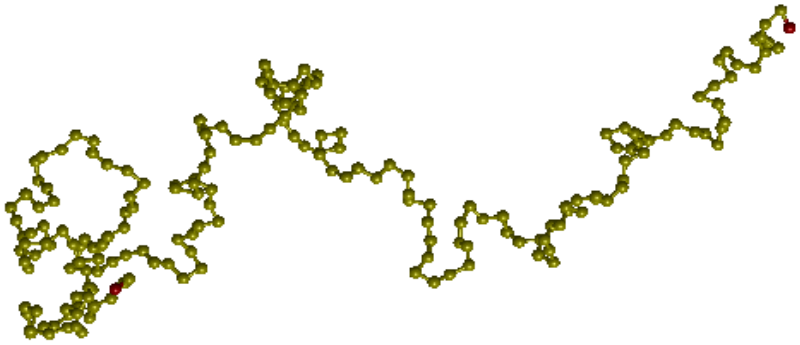

Figure 4.48: *Snapshot of a linear chain under athermal conditions. The first and last bead have a red color.* $\lambda = 0.0$, $N = 200$.

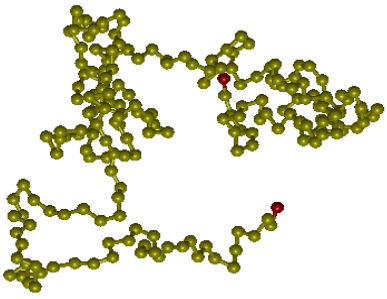

Figure 4.49: *Snapshot of a linear chain under θ-conditions.* $\lambda = 0.65$, $N = 200$.

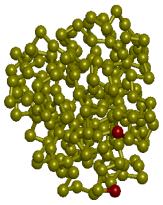

Figure 4.50: *Snapshot of a collapsed linear chain far below the transition point.* $\lambda = 1.0$, $N = 200$.

To obtain statistically independent samples, the systems were started using the MD procedure described in Section 3.3. This was done for about 50.000 integration steps to allow for a first relaxation of the chains on a small length scale. Then every 1.000 integration steps a series of pivot moves – usually about 100-500 attempted moves – was included, in order to also relax the chains on a large length scale. The pivot moves also decorrelate the consequtive configurations of the chains. In the

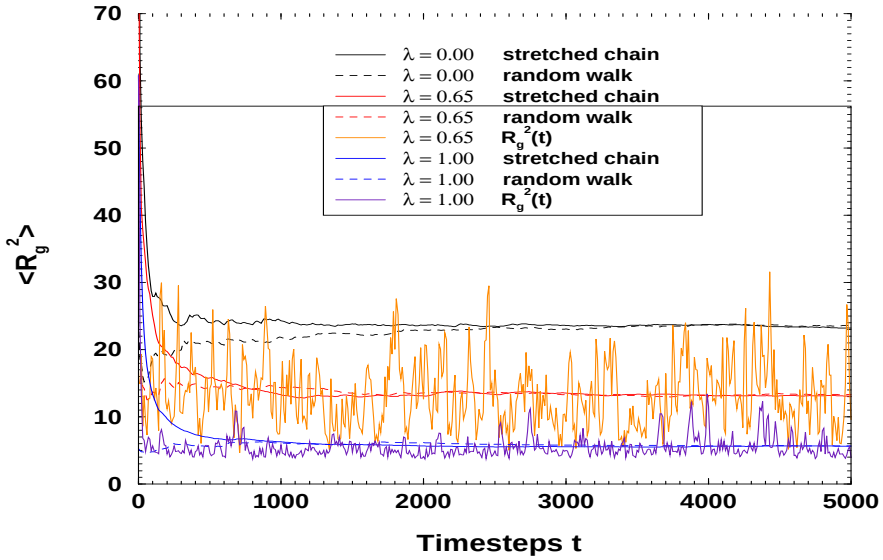

Figure 4.51: *Time evolution of $\langle {R_g}^2 \rangle$ for three different values of λ and two different initial configurations of the chain configuration. Time is displayed in Lennard–Jones units with integration time step $\Delta t = 0.01$. For the systems with $\lambda = 0.65$ and $\lambda = 1.0$ the fluctuations of ${R_g}^2$ are displayed as well.*

production runs, snapshots of the whole systems were then taken every 500-5.000 integration steps, depending upon the length of the chains. As a criterion for a system having reached its equilibrium state, ${R_g}^2(t)$, ${R_e}^2(t)$ and $R_h(t)$ were monitored. Tests of the implementation of this work, in terms of the chains reaching their equilibrium state, did not show any significant dependence on the ratio r of MD steps to pivot moves. Tests of different initial configurations of linear chains with, on the one hand, random walks generated by the procedure described in Section 3.3.2, and on the other hand, fully stretched chains with the monomers being set at their equilibrium distance of $d = 0.97$, are displayed in Fig. 4.51 and 4.52 for the end-to-end distance and the radius of gyration.

These figures elucidate that the choice of a random walk setup of chains is more favorable than starting with an elongated chain as in the former case the chains are much closer at their final equilibrium configuration. On the other hand, the different curves converge very quickly on a time scale of roughly 1.000-2.000 LJ-timesteps, so that this gain in speed is not as crucial for single chain systems as it is for chains in a melt, where slow reptation dynamics due to the presence of many other chains slows down the ralaxation behavior of each individual chain.

The figures also display the much larger fluctuations of the chain extensions at the θ–point compared to the collapsed globular state. The exact measured values of the fluctuations of $\langle {R_e}^2 \rangle$ and $\langle {R_g}^2 \rangle$ of all single chain systems are listed in the tables of Appendix A.

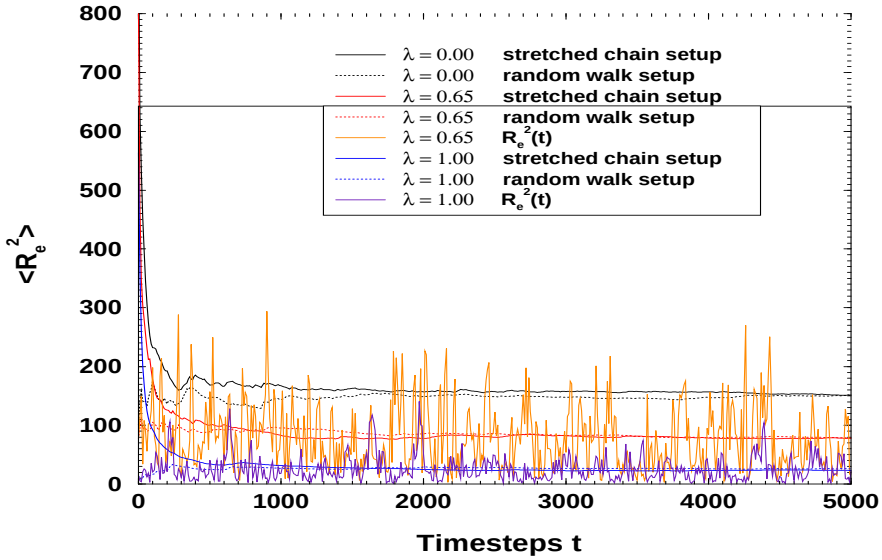

Figure 4.52: *Time evolution of $\langle {R_e}^2 \rangle$ for three different values of λ and two different initial configurations of the chain configuration. Time is displayed in Lennard–Jones units with integration time step $\Delta t = 0.01$. For the systems with $\lambda = 0.65$ and $\lambda = 1.0$ the fluctuations of ${R_e}^2$ are displayed as well.*

Summary

In Section 4.2.4 the obtained simulation data were used to demonstrate that the corrections to scaling of R_h are different from the ones for R_e and R_g. The reason for experiments to fail showing the limiting scaling behavior is due to the experimental systems exploiting too short chain lengths. With the simulation data in this work the correct scaling behavior of R_h could be demonstrated and is published for the first time.

Taking into account polydispersity with linear chain systems revealed that the quantity ϱ is not suitable for a unique mapping of length scales between experimental systems and simulation systems. It was shown that this is due to the small sensitivity of the quantity ϱ to the degree of polymerization when using experimental data. of this scatter of data a unique mapping cannot be performed.

In Section 4.4 an extensive shape analysis of the linear model-chains was performed, including an extrapolation of three different definitions of asphericity to the $N \rightarrow \infty$) limit. The relative sensitivity of these quantities to finite size effects was demonstrated in dependence of the solvent quality, covering the whole range from good solvents to bad solvent conditions. It was found that the asphericity of linear chains decreases with chain length.

Chapter 5

Simulation results of branched chain systems

Table of Contents

The properties of a polymer system can be significantly modified by a variation of the molecular architecture. As a result of topological constraints caused by branching or even loops, the local average polymer density increases relative to that of a linear chain. This effect is particularly important in the study of dilute solution properties of single chains as well as in polymer melt systems where branching has a major influence on the rheological properties.

This chapter gives a summary of the results obtained from simulations of single branched chain systems with a variety of different topologies.

5.1 Simulation of stars

5.1.1 Introduction

During the initial period of the development of theories concerning polymer chains and their solutions, star-branched polymers were used as the simplest idealized model of branched polymers [43]. For the theoretical description of this model, several techniques based on *de Gennes' blob theory* [56] were applied [28, 30]. *Daoud and Cotton* [52] introduced a model for the conformation of star polymers that is based on the blob concept. Their model assumes the blob size and consequently the monomer concentration to be a monotonically decreasing function of the distance from the center of the star. This scaling theory is strictly only valid in the limit of long enough chains focusing on scaling exponents and completely ignoring any pre-factors.

Other theoretical approaches were based on the renormalization group (RG) theory [143, 144]. For random flight chains some parameters which describe the influence of the presence of a branch point on the size and shape of macromolecules could be calculated [42].

Experimental progress in polymer chemistry allows for the preparation of regular many-arm stars, and stars with up to $f = 128$ arms have been synthesized [171, 219]. These many-arm star systems are used as ideal models for polymeric micelles. Light and neutron scattering have been useful in obtaining new insight into how the size of a star depends on the functionality, arm molecular weight, and solvent quality.

Many numerical simulations, both MC and MD, have been done [13, 34, 36, 86, 87, 178, 179] to test scaling predictions and to determine other properties such as structure factors. However, many studies included only a few arms or very short arm-lengths. In light of this, it is interesting to perform a systematic study of stars with our model-chains for different numbers of arms f and longer arm-lengths than were used in most of these studies.

By use of lattice-models, it is possible to investigate not only the properties of linear chains but also of star-branched chains in a highly efficient manner. Usually, the chains are generated by use of *biased sampling methods*, originally invented by *Rosenbluth et al.* [165] for linear chains, or by multimerization [13] of arms, which is a modification of the dimerization method by *Alexandrowicz* [7]. In our simulations of star systems, we applied the same MD/MC-method as was described for the linear chains in Section 4.5 on Page 79. The only difference is, that we apply the pivot algorithm to each individual arm of the stars.

Grest and Kremer [86] investigated many arm-systems with up to $f = 50$ and a constant arm length of $N_a = 50$ was simulated using MD. Also stars with $f = 10$ and $N_a = 200$ were included in this study which was focused on the investigation of scaling properties of the structure function in light of the scaling theory. No calculations of shape factors or characteristic ratios such as ϱ or g were done in this study.

Sikorski et al [178], performed MC simulations on a simple cubic lattice, where only ($f = 3$)-arm stars were considered and no shape factors were determined. Two years later, they performed another MC study [179], again only with ($f = 3$)-arm stars of the same length ${N_a}^{max} = 266$, including an analysis of δ and $\delta^\star$, including the effect of different solvent qualities. However, no extrapolation of the obtained values to ($N \to \infty$) was done.

Such an extrapolation was performed by *Zifferer and Olaj* [229] in a MC-study of shape factors and the asphericity of stars of constant arm-length $N_a = 160$ with $f = (3 - 96)$ arms. Later, *Zifferer* [231] performed another MC-study of stars of constant arm-length $N_a = 480$ with $f = (3 - 12)$ arms

and determined the same properties. In these simulation studies only RW-chains were considered and no g- or h-factors were calculated and no analysis of scaling properties was performed.

In [13], a systematic investigation of scaling properties of stars has been performed, including some results on the asphericity δ. However, in this study only very short arm lengths and only stars with $f \leq 6$ arms were considered. In the previous chapter, we demonstrated that in [13] a wrong exponent for the correction to scaling of R_h was confirmed ($\Delta = 1/2$ instead of $\Delta = (\nu - 1)$). In light of this new result it is interesting to perform a systematic simulation study of star systems, including effects of solvent quality and with arm-lengths that exhibit the correct scaling behavior. Up to date, to the best of our knowledge, no systematic study of shape factors of stars for many different arms, including different solvent qualities has been done. To our knowledge, this is the first systematic study of branched systems using the simulation model described in Section 3.4.

5.1.2 Simulation results: θ – transition of stars

The ideal solvent case and the θ–point are the two most important limiting cases of polymer solutions which can be treated in theoretical investigations. As most experiments are usually done in solvents of either quality, the simulations of branched systems will focus on polymers in the athermal limit and at the θ–point. The purpose of this section is to analyze star branched polymer chains in order to reveal a possible shift of the θ–point of the used model due to chain branching. The question whether there exists a possible shift of the θ–point was not only raised in the context of stars [52, 107], but also for cyclic chains the experimental data for different systems [168] have shown a depression in the θ–temperature of up to 8% with respect to those obtained for linear chains.

The θ-state is experimentally attained at the temperature at which the second virial coefficient A_2 vanishes, that is, when the molecules are non-interacting in pairs. Since the repulsive three-body interactions between two molecules must be compensated for by temperature-dependent two-body attractions, it turns out that in a star polymer the θ-temperature must be lower than in a linear chain even more so the larger is f or the smaller is N/f. In fact, because of its topology, the star has a larger multiplicity of three-body repulsions between two molecules than a linear chain. However, if the molar mass is very large (i.e. f fixed and ($N \to \infty$)), the region close to the branch point has a negligible effect and a universal asymptotic θ-temperature is reached.

Only very few simulation studies, mostly using lattice models, of the transition behavior of stars have been done, see e.g. [75, 107]. These studies focused on few physical quantities and did not include any shape analysis. In [14] one of the most detailed MC-study of arm lengths of up to $f = 8$ was performed. The simulation data obtained in this study suggest that the asymptotic θ–temperature of stars on a fcc-lattice is the same as for linear chains. However, in this study only a maximum arm length of $N_a = 100$ was considered.

In the following, the results of a θ–point analysis of star polymers with varying number of arms f and lengths N are displayed. In our investigation we simulated much larger chains than in previous studies. Figure 5.1 exhibits the appropriate scaling plots of stars with arm numbers $f = 3, 4, 5$. Figures 5.2 and 5.3 exhibit the same scaling plots for stars with $f = 10$ and $f = 12$ arms.

The determination of the respective θ–points was done as described in Section 4.1. The results are given in Table 5.1 on Page 88. Within the error-bars of the simulation data, there is no detectable shift of the θ–point for star branched systems when compared with the linear chains. The observed systematic decrease of λ_θ with $f \leq 10$ can be easily explained as a finite size effect, because the effective arm length N_a decreases in our simulations with increasing number of arms f. The star system with $f = 12$ arms however has been simulated with a larger arm length than the 10-arm

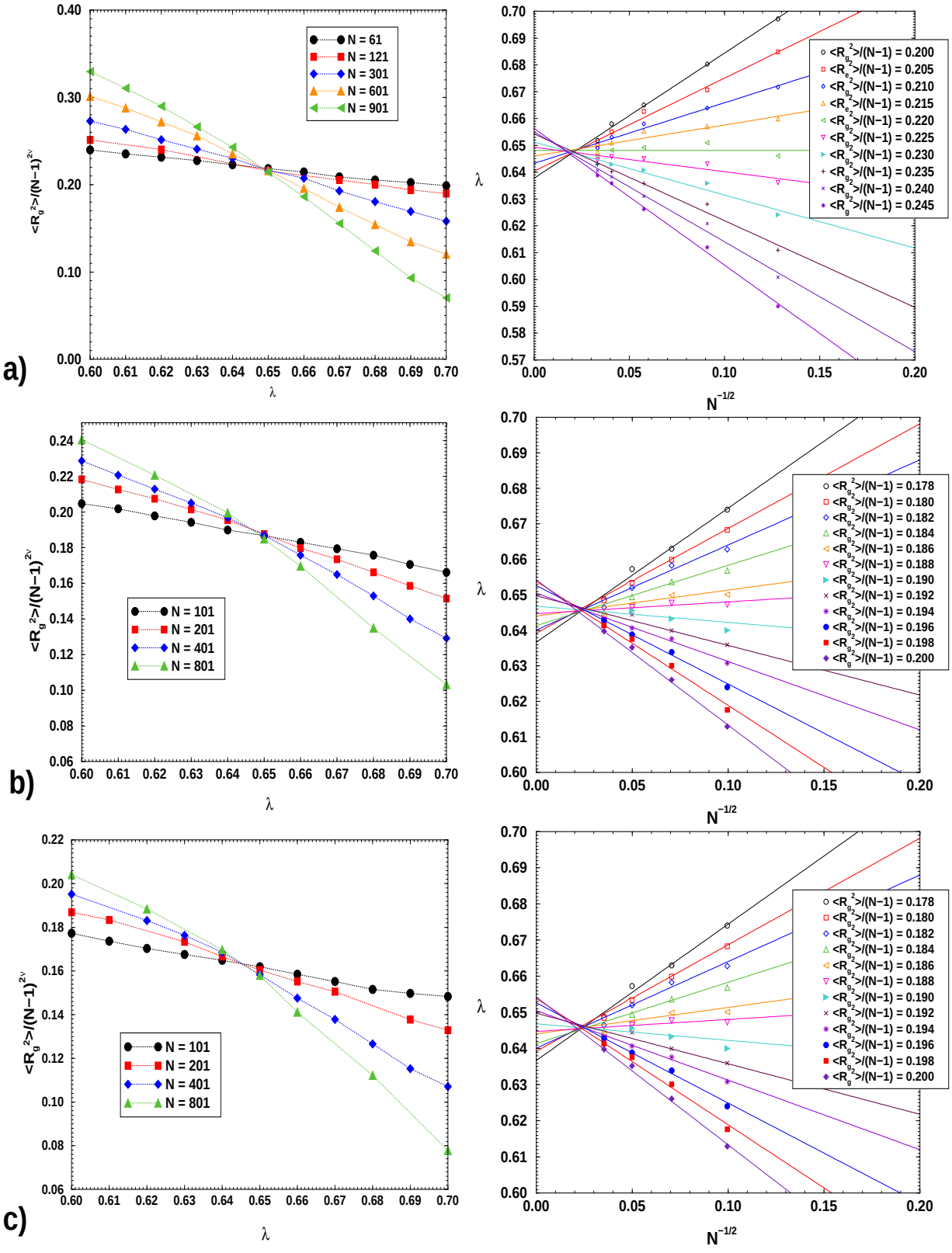

Figure 5.1: *Determination of the θ-point for different stars. Left: $\langle R_g{}^2 \rangle / (N-1)^{2\nu}$ vs. interaction parameter λ. Right: λ vs. $N^{-1/2}$ for different constant values of the scaling function. The extrapolations yield slightly smaller values of λ_θ, compared to the corresponding plot of linear chains in Figure 4.3 on Page 45.*
a) $f = 3$, **b)** $f = 4$, **c)** $f = 5$.

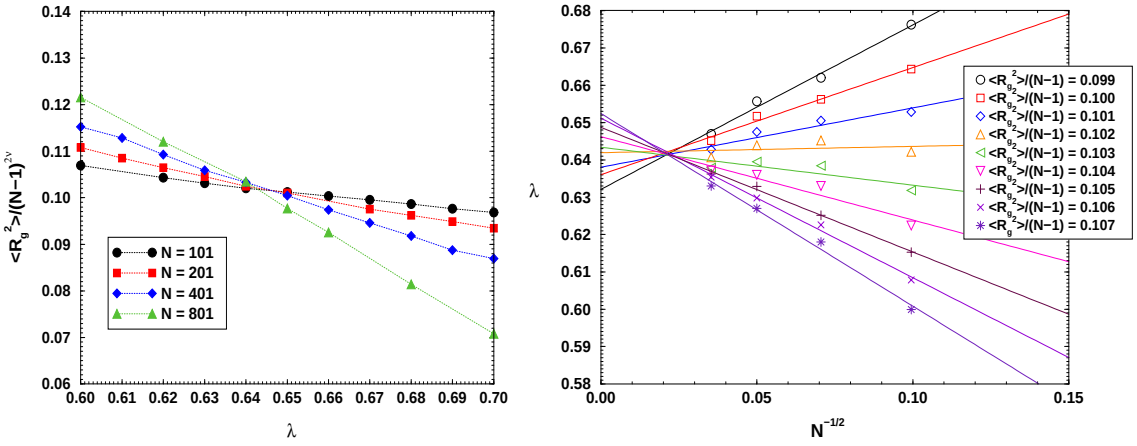

Figure 5.2: *Determination of the θ-point for stars with $f = 10$. Left: $\langle R_g{}^2 \rangle / (N-1)^{2\nu}$ vs. interaction parameter λ. Right: λ vs. $N^{-1/2}$ for different constant values of the scaling function. The extrapolation of these 10-arm stars yields the lowest θ-point of all investigated systems, as the individual arm length of these stars is the smallest one ($N_a = 80$).*

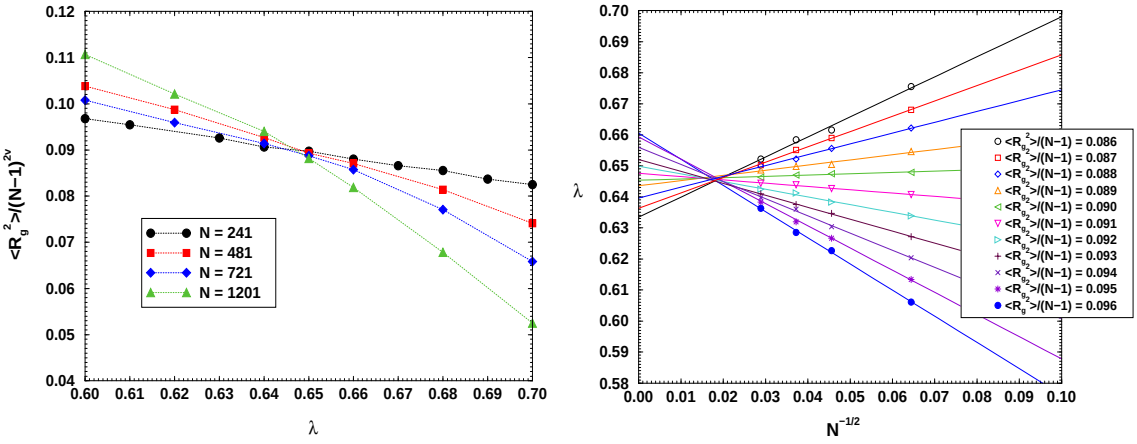

Figure 5.3: *Determination of the θ-point for stars with $f = 12$. Left: $\langle R_g{}^2 \rangle / (N-1)^{2\nu}$ vs. interaction parameter λ. Right: λ vs. $N^{-1/2}$ for different constant values of the scaling function. Due to larger arm lengths ($N_{max} = 120$), these stars exhibit a small increase of λ_θ, compared with the ($f = 10$)-arm systems.*

f	λ_θ	$N_a = N/f$
2	0.650 ± 0.020	2000
3	0.649 ± 0.010	300
4	0.648 ± 0.011	200
5	0.646 ± 0.007	160
10	0.643 ± 0.010	80
12	0.645 ± 0.012	120

Table 5.1: *Table of ($N \to \infty$) extrapolated θ–points of the simulation model described in Section 3.4 for different stars. The extrapolation shows that the θ-point for star branched systems approaches the one of linear chains with increasing effective arm length N_a. The apparent shift of the θ-point with stars thus is only a finite size effect which is due to small effective arm lengths. The deviations for the considered N_a-values in this work are within the statistical errors of the θ-point determination.*

Reference	f						
	3	4	5	6	10	12	18
this work	0.3424	0.2385	0.1803	0.1443	0.0708	0.0612	0.0300
Bishop et al [36]	0.345	0.243	0.185	−−	−−	−−	−−
Bishop and Smith [35]	0.353	0.244	0.177	−−	0.070	−−	−−
Batoulis et al [13]	0.344	0.245	0.187	0.150	−−	−−	−−
Cannon et al [46]	0.345	0.243	0.185	−−	−−	−−	−−
Zifferer [231]	0.3437	0.2438	−−	0.1483	0.0779	0.0616	−−

Table 5.2: *Table of extrapolated asphericities δ for the simulated star-branched chains of this work compared to other publications. Athermal chains with $\lambda = 0.0$. The results of our study are in excellent agreement with results of other researchers.*

system and shows a slight *increase* of λ_θ. The θ-point obtained by averaging over all systems of Table 5.1 is:

$$\lambda_\theta = 0.645 \pm 0.010. \tag{5.1}$$

From this systematic investigation one can draw the conclusion that the θ–point for star branched systems is *not* shifted within the statistical errors of the simulation and that the observed small shift is only due to the finite length of the star arms. This interpretation can also be applied to the experimentally observed apparent shift of θ-points for branched macromolecular systems. Additionally, as there is no shift of the θ–point with stars where all the arms emanate from one high-functional center with very high density, one can expect that this will also not be the case for other types of branched chains with a much lower monomer density in the vicinity of the branch point. Thus, the θ–point of linear chains that was determined in our study in Section 4.1 can also be used to simulate branched chains under θ–solvent conditions.

5.1.3 Shape analysis of stars

This section provides an analysis of the shape properties of the simulated star systems. No experimental data at all are available on shape properties of stars and only very few simulation studies have been done, e.g. [13, 179, 226, 230, 232]. To the best of our knowledge, in all studies of shapes of chains, pure MC-methods were employed.

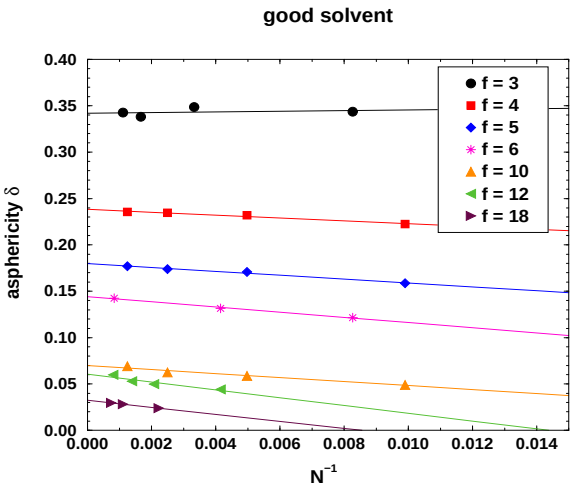

Figure 5.4: *Extrapolated ($N \to \infty$) asphericities δ for symmetric star polymers with $f = 3, 4, 5, 6, 10, 12$ and 18 arms under athermal conditions. Straight lines are linear fits to the data points. A comparison with results of other investigators is given in Table 5.2. $\lambda = 0.0$.*

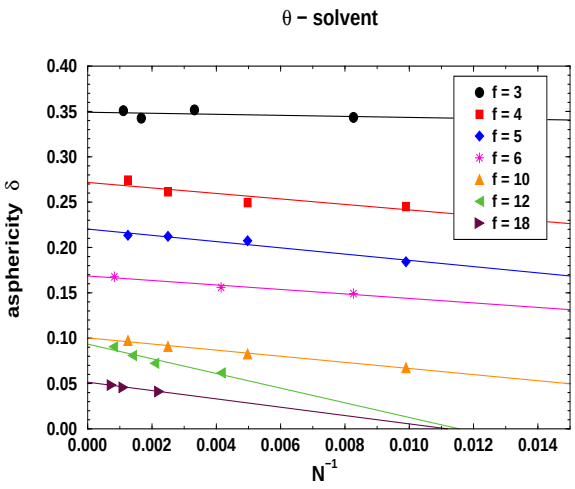

Figure 5.5: *Extrapolated ($N \to \infty$) asphericities δ for symmetric star polymers with $f = 3, 4, 5, 6, 10, 12$ and 18 arms under θ-conditions. As expected, the stars exhibit an increasing spherical structure with an increasing number of arms. A comparison with results of other investigators is given in Table 5.3. $\lambda = 0.65$.*

In one of the first more extensive studies on stars, *Batoulis and Kremer* [13] investigated the quantity δ with MC-simulations on a fcc-lattice and performed an ($N \to \infty$) extrapolation. However, they only considered stars with very few arms $f \leq 6$.

Zifferer [226] used MC-simulations on a tetrahedral lattice to investigate δ, $\delta^\star$ and the shape factors sf_i for stars with $f \leq 12$. However, they only focused on stars in a good solvent and did not perform an extrapolation of the obtained data to ($N \to \infty$).

Zifferer and Olaj [232] performed MC-simulations on various lattices and extrapolated the obtained data to ($N \to \infty$). In their study, only linear chains with $N \leq 1000$ were considered. Their determined results for δ and the shape factors sf_i turned out to be dependent upon the lattice type for finite chain lengths.

In [230], *Zifferer* considered shape factors and the asphericities $\delta^\star$ of stars with $f \leq 12$ in a MC study using a tetrahedral lattice. Athermal and θ-solvents were considered, but no extrapolation of the obtained data to ($N \to \infty$) was performed.

In a MC-study on a cubic lattice by *Sikorski and Romiszowski* [179], δ and sf_i of stars were considered for various solvent qualities. However, this study focused entirely on 3-arm stars and no extrapolation of the obtained quantities to ($N \to \infty$) was done.

In our study, we extrapolated all quantities δ, $\delta^\star$, b, the shape parameters sf_i and $sf_i^\star$ to ($N \to \infty$) in order to account for finite size effects of the simulated chains. We also used longer arm lengths of the stars and a larger number of arms ($f = 3, 4, 5, 6, 10, 12, 18$) than have been used in most of the previous studies. Additionally, our results on shape parameters are very accurate, exhibiting an uncertainty only in the fourth digit.

The results of an extrapolation to ($N \to \infty$) of the asphericity parameter δ are shown in Figures 5.4 and 5.5 for the two most important limiting cases, the athermal solvent limit and the θ-point. The

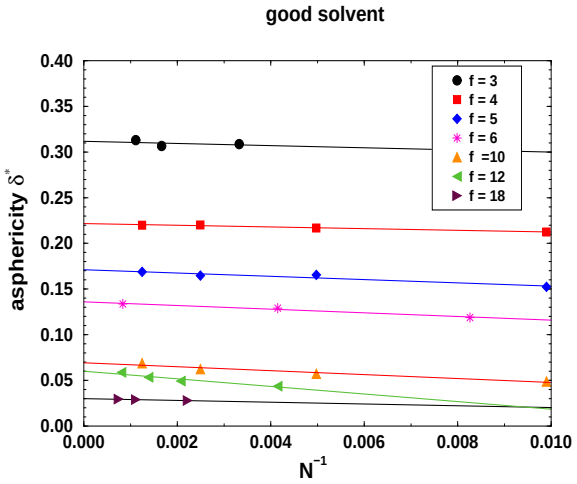

Figure 5.6: *Extrapolated ($N \to \infty$) asphericities δ for symmetric star polymers with $f = 3, 4, 5, 6, 10, 12$ and 18 arms under athermal conditions. Straight lines are linear fits to the data points. $\lambda = 0.0$.*

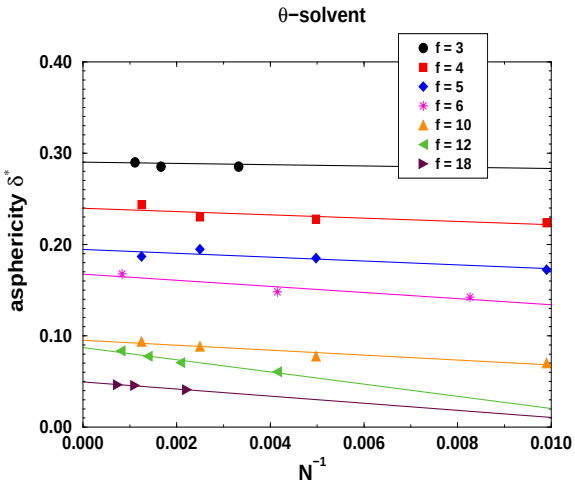

Figure 5.7: *Extrapolated ($N \to \infty$) asphericities δ for symmetric star polymers with $f = 3, 4, 5, 6, 10, 12$ and 18 arms under θ-conditions. $\lambda = 0.65$.*

Reference	f						
	3	4	5	6	10	12	18
this work	0.3492	0.2717	0.2204	0.1686	0.1002	0.0933	0.0512
Bishop et al [36]	0.360	0.274	0.218	−−	−−	−−	−−
Cannon et al [214]	0.3609	0.2732	0.2195	0.1834	−−	0.0922	−−
Zifferer [231]	0.3558	0.2692	−−	0.1778	0.1063	0.0868	−−

Table 5.3: *Table of extrapolated asphericities δ for the simulated star-branched θ-chains of this work. The results are in very good agreement with other publications. Our simulation study is the most extensive one, covering the whole range from few arm stars to highly symmetrical many-arm stars.*

obtained results are summarized in Tables 5.2 and 5.3. A comparison with the few data available in literature is displayed in these tables.

The extrapolations of $\delta^\star$ and b are shown in Figures 5.6 to 5.9. Figure 5.11 displays the extrapolations of the shape factors sf_i of the different stars. Such an extrapolation was also done for the shape factors $sf_i^\star$ which look very similar. Probably the most extensive series of investigations of shape factors sf_i in literature have been done so far by *Zifferer* in a series of papers [228, 229, 231]. Therefore, our obtained results are compared with these references in Table 5.4 on Page 94.

Generally, the results in this table are in excellent agreement with the values obtained in the studies by *Zifferer*. The agreement of the good solvent data is better than for the θ-chains. As for most data only finite chains were considered without extrapolation, there is less agreement with our results. Those values by *Zifferer* which were obtained by an extrapolation of chain lengths to ($N \to \infty$) are in better agreement with our data. This shows the importance of finite size effects for this quantity and the high quality of data of our simulation study.

Extrapolations of data for $sf_i^\star$ were performed as well and look similar to the ones displayed in Figure 5.11. The obtained results from these extrapolations for θ-chains and athermal chains are

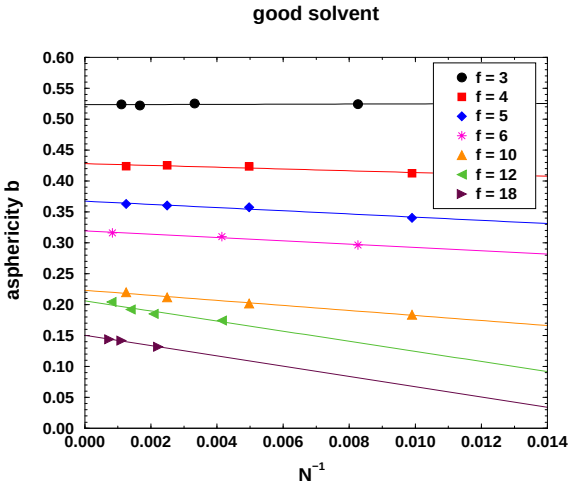

Figure 5.8: *Extrapolated ($N \to \infty$) asphericities b according to Eq. (2.26) for symmetric star polymers with $f = 3, 4, 5, 6, 10, 12$ and 18 in good solvent. $\lambda = 0.0$.*

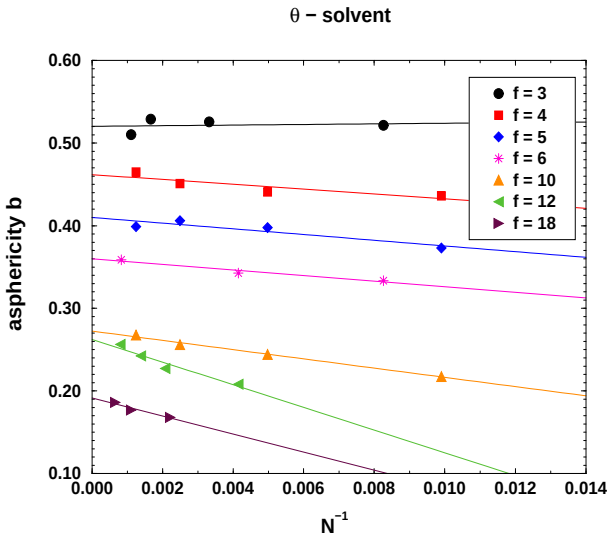

Figure 5.9: *Extrapolated asphericities b according to Eq. (2.26) for symmetric star polymers with $f = 3, 4, 5, 6, 10, 12$ and 18 in a θ-solvent. $\lambda = 0.65$.*

summarized in Table B.26 in the Appendix B. In this table, a comparison with simulation data by *Zifferer* [229] is done. There are some small deviations present in the third digit of most star data in this table. This can be explained however, by the fact that the obtained data in [229] were not extrapolated to infinite chain length.

In general, the results show that the size and the shape of molecules are closely related to each other. The global dimensions of symmetric configurations are small, whereas un-symmetric conformations are of extended size. The shape asymmetry of star-branched chains decreases clearly with increasing arm number. The chain-length dependence of the asphericities is very weak as the extrapolation reveals. However, finite size effects become more dominant with increasing arm number. The quantity b exhibits the largest sensitivity to this effect. Interestingly, we find that – except for the 3-arm star – the star polymer in a good solvent is *more* spherical than in a θ-solvent. This effect becomes stronger with increasing arm number. This is just the opposite behavior that was found for the asphericity of linear chains, cf. Fig. 4.43 on Page 76. Unlike the linear chain, the asphericity of a star *increases* with N.

The same change in the N-dependence from the linear chain to stars can be observed with the shape factors: While sf_1 of linear chains *decreases* with N and sf_2 and sf_3 *increase* (cf. Fig. 4.45), the opposite is true for stars. Also the dependence of the shape factors on chain length is much larger than for the different asphericities and this dependence increases with the number of arms.

Hence, it appears, as if the influence of the topological constraint of a star, which is given by the central core, is more important than any local effects which cause short linear chains to be stiffer. Because the influence of the star core diminishes in the limit ($N \to \infty$), the symmetry of star-branched chains decreases with chain length.

Another interesting quantity is the scaling behavior of $\delta(f)$. In [13] an exponent of $r = 1.19$ was determined for stars in a θ-solvent. However, only stars with up to $f = 6$ arms were considered. Our simulation data are displayed in Figure 5.10 and we obtain the equations

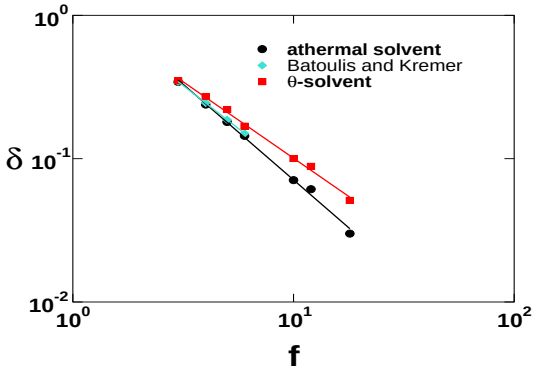

Figure 5.10: *Scaling of the asphericities of the stars with f. In the athermal solvent, the chains are more spherical than the ones in a θ-solvent. This is an opposite behavior to that of the linear chains, cf. Fig. 4.43. The obtained scaling of δ for athermal chains in [13] is displayed as well.*

$$\delta \propto f^{-1.33} \tag{5.2}$$

and

$$\delta \propto f^{-1.06} \tag{5.3}$$

for an athermal and θ-solvent, respectively.

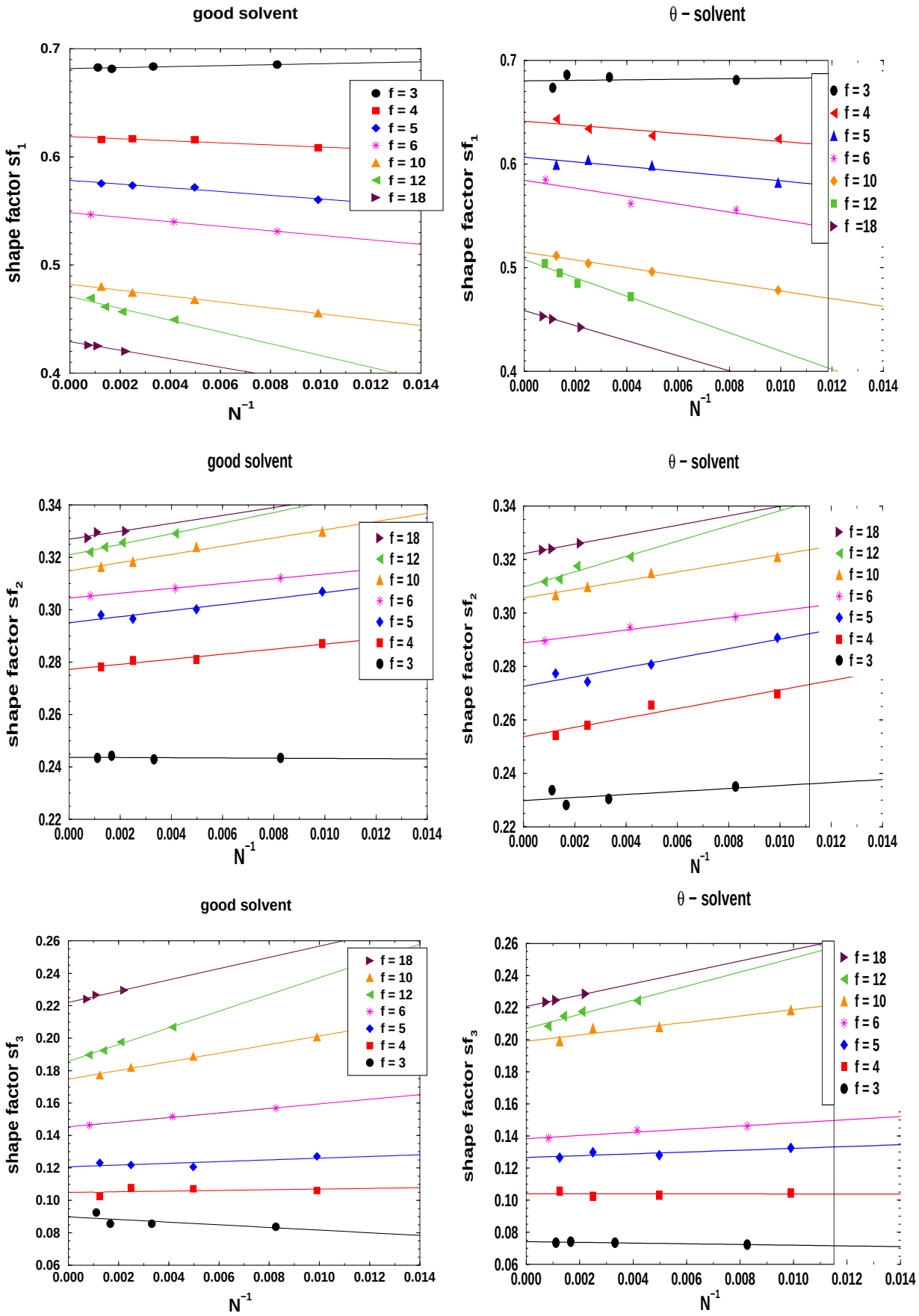

Figure 5.11: *Extrapolated shape factors of stars in the good and θ solvent limit.*

Table 5.4: *Table of extrapolated shape-factors sf_i obtained in this work, compared with other publications. Our study covers the largest range of arm numbers f and all results were obtained by an ($N \to \infty$) extrapolation.*

Reference	f							
	2	3	4	5	6	10	12	18
sf_1	**good solvent**							
this work	0.7792	0.6817	0.6288	0.5784	0.5485	0.4822	0.4702	0.4292
Zifferer[a]	0.7807	0.6837	0.6233	−−	0.5545	0.4902	0.4720	−−
Zifferer[b]	0.7804	0.6826	0.6237	0.6215	−−	0.4838	0.4710	−−
sf_2								
this work	0.1633	0.2437	0.2772	0.2950	0.3044	0.3148	0.3208	0.3269
Zifferer[a]	0.1639	0.2414	0.2746	0.3013	−−	0.3179	0.3214	−−
Zifferer[b]	0.1641	0.2427	0.2745	−−	0.3036	0.3199	0.3219	−−
sf_3								
this work	0.0575	0.0742	0.1040	0.1266	0.1384	0.1990	0.2070	0.2207
Zifferer[a]	0.0553	0.0749	0.1020	−−	0.1442	0.1919	0.2066	−−
Zifferer[b]	0.0555	0.0747	0.1019	−−	0.1461	0.1963	0.2071	−−
sf_1	**θ-solvent**							
this work	0.7381	0.6902	0.6412	0.6067	0.5842	0.5149	0.5079	0.4587
Zifferer[a]	0.7612	0.6872	0.6388	−−	0.5781	0.5196	0.5006	−−
Zifferer[c]	0.7646	0.6905	0.6416	−−	0.5826	−−	0.5063	−−
sf_2								
this work	0.2199	0.2299	0.2537	0.2726	0.2888	0.3056	0.3096	0.3221
Zifferer[a]	0.1740	0.2296	0.2578	−−	0.2865	0.3067	0.3122	−−
Zifferer[c]	0.1721	0.2281	0.2569	−−	0.2844	−−	0.3100	−−
sf_3								
this work	0.0665	0.0899	0.1049	0.1207	0.1454	0.1748	0.1858	0.2221
Zifferer[a]	0.0648	0.0833	0.1034	−−	0.1354	0.1737	0.1871	−−
Zifferer[c]	0.0633	0.0814	0.1015	−−	0.1330	−−	0.1837	−−

[a] [229]. MC simulation of stars of one single arm length $N_a = 480$ on a tetrahedral lattice.

[b] [228]. Off-lattice MC simulation of stars with $N_a^{\max} = 480$ on a tetrahedral lattice. The displayed results for the $f = 2, 4, 12$-arm stars were obtained by an ($N \to \infty$) extrapolation.

[c] [231]. MC simulation of stars with $N_a^{\max} = 160$. No extrapolation to ($N \to \infty$) was performed.

5.1.4 Scaling and branching factors of stars

In this section we investigate the scaling properties of the simulated stars and calculate important branching factors, that can be used for comparisons with theory and experiments.

In Figure 5.12 the scaling of $\langle {R_g}^2 \rangle$ as a function of N is displayed. From this double-logarithmic plot one obtains the scaling exponents of R_g for stars with different numbers of arms. The linear chain is displayed as well, for which the largest chain lengths were simulated. Within the errors of the simulation, the exponents do not depend on the number of arms, as expected. The exponents are summarized in Table 5.5 and exhibit a reasonable agreement with theory.

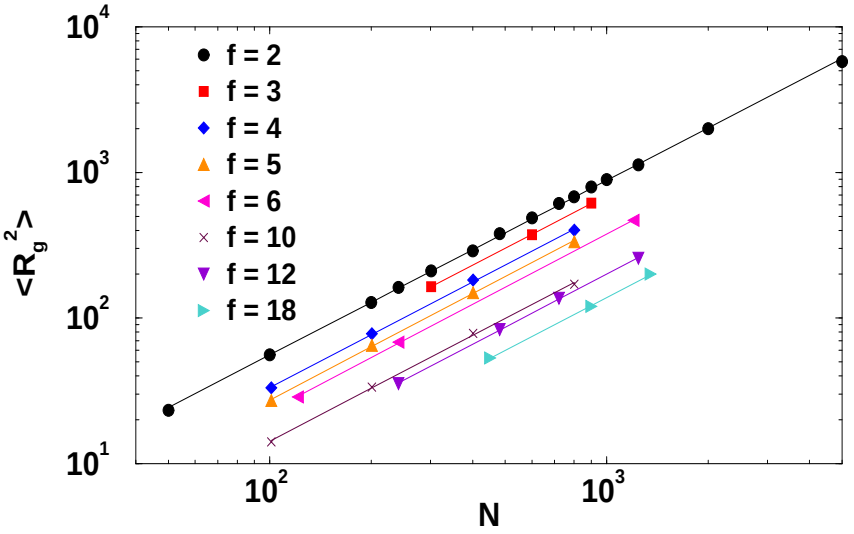

Figure 5.12: *Log-Log plot of $\langle {R_g}^2 \rangle$ vs. N of stars with different arm numbers f. For comparison, the linear chain data ($f = 2$) are displayed as well.*

f	2	3	4	5	6	10	12	18
ν	0.5989	0.601	0.603	0.614	0.617	0.603	0.599	0.601

Table 5.5: *Obtained scaling exponents ν for different numbers f of star arms.*

In Figure 5.13 we plotted the corrections to scaling of the radius of gyration for the systems with different arm numbers, including the linear chain ($f = 2$). In Figure 5.14 we demonstrate, that these corrections are $\propto N^{-1}$. A plot with exponents -2 and $-1/2$ led to worse correlation coefficients. The best linear fit of all data points was obtained with the exponent shown in Figure 5.14. In a lattice-MC simulation study [13] there were no corrections to scaling of R_g on a fcc-lattice.

Having determined the corrections to scaling of R_g, a linear regression analysis of the values of the branching factor g [1] for chains of different lengths vs. $1/N$ allows to give an extrapolated estimation of g for a given topology in the limit ($N \to \infty$). This has been done in Figures 5.15 and 5.16 for two limiting solvent qualities, the athermal solvent and the θ-solvent. Obviously, in both solvents, the data points exhibit only very small deviations which display the excellent quality of our obtained data.

[1] For the definition of the branching factor g, see Section 2.2.2 on Page 10.

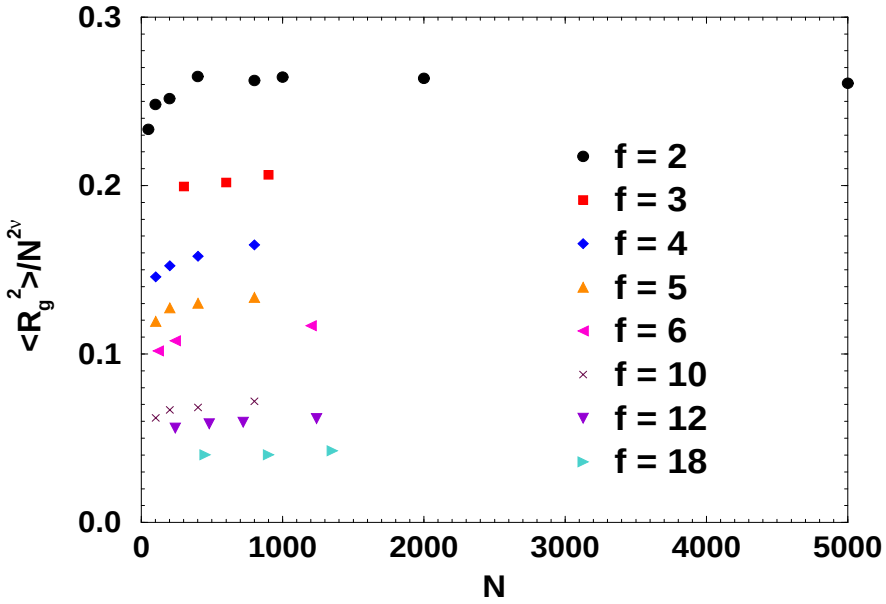

Figure 5.13: *Corrections to scaling of* $\langle {R_g}^2 \rangle (f)$ *with different arm numbers* f*. Good solvent limit.* $\lambda = 0.0$*.* $\nu = 0.588$*.*

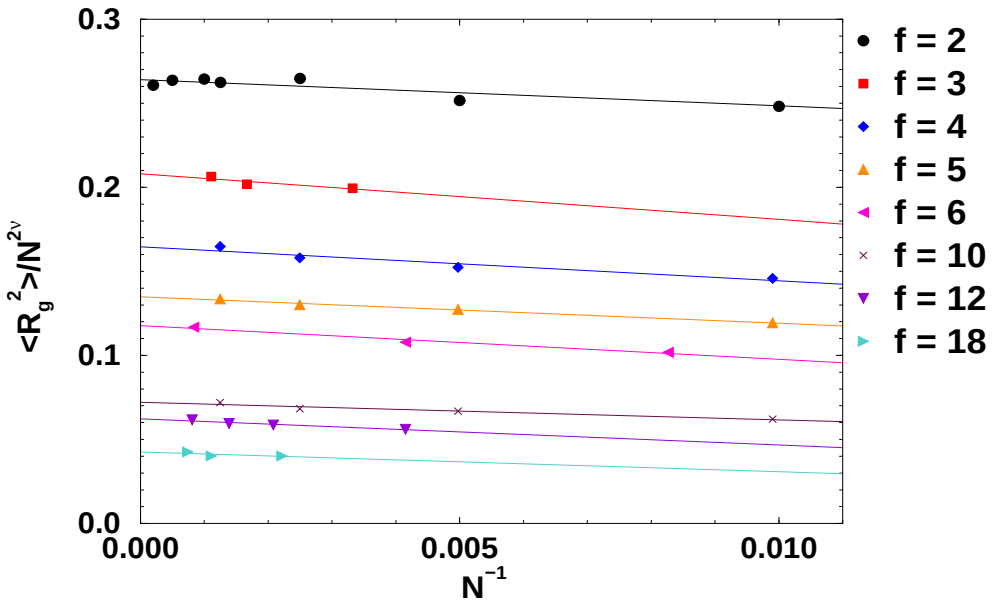

Figure 5.14: *Corrections to scaling of* $\langle {R_g}^2 \rangle (f)$ *plotted vs* $1/N$*. For clarity, the smallest data point of the linear chains (*$f = 2$*,* $N = 50$*) is not displayed.* $\lambda = 0.0$*.* $\nu = 0.558$*.*

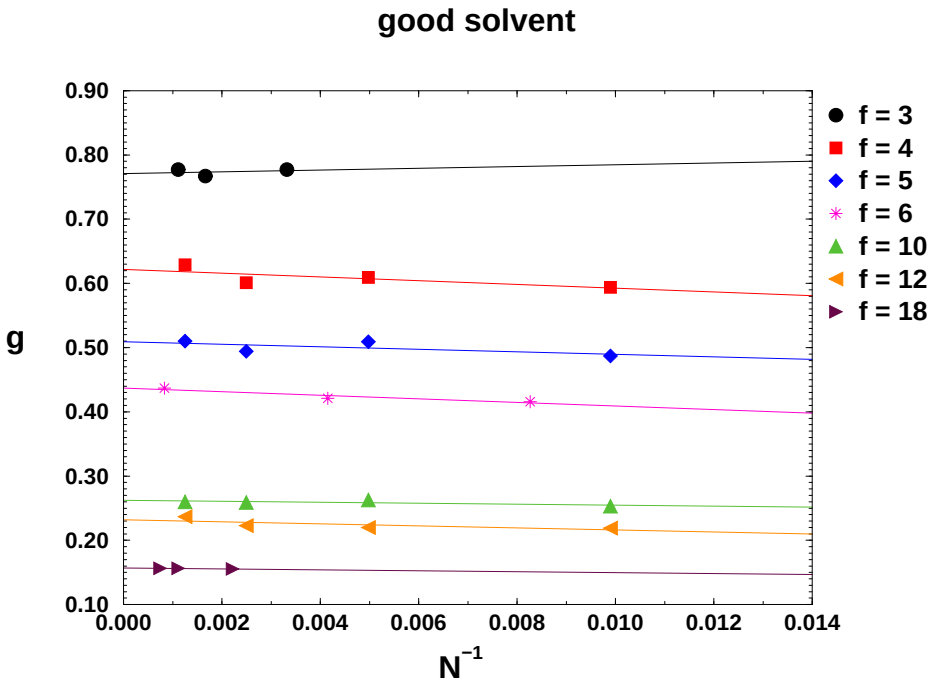

Figure 5.15: *Extrapolated g-factors of stars in the good solvent limit. $\lambda = 0.0$.*

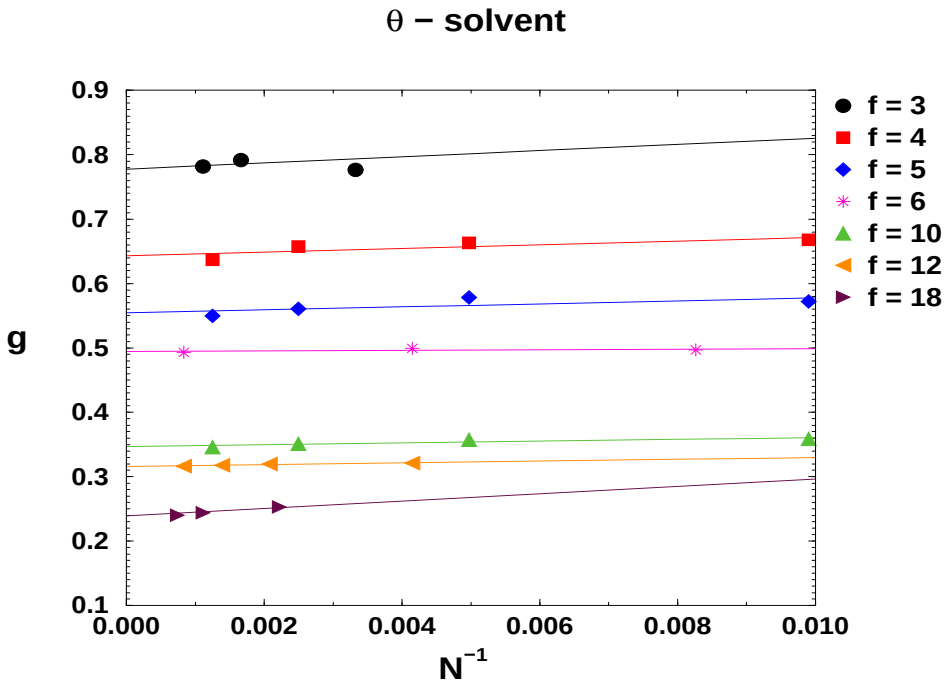

Figure 5.16: *Extrapolated g-factors of stars in a θ-solvent limit. $\lambda = 0.65$.*

The extrapolated values of g are displayed in Figures 5.17 and 5.18, again for a θ-solvent and the good solvent case, respectively. A comparison with data available in literature is displayed in these figures as well.

Our simulation data of θ-chains in Figure 5.17 reveal that the mean dimensions of θ-stars, expressed in the ratio g_θ of branched to linear chains, are greater than predicted by the RW theory. Additionally, the ratio g_θ is *always* larger than g, cf. Figure 5.18 and the corresponding tables. The observed deviations grow with increasing arm number f. This is also seen with experimental data of PIP and PS in θ-solvents. Note that the deviations from the *Zimm-Stockmayer* approach tend to occur for $f \geq 5$. For our largest considered star, the deviation from RW theory is about 50%. For $f = 64$ polybutadiene stars [171] the deviation has increased to 100% ($g_\theta = 0.092$ in the experiment compared to 0.046 of RW theory). Many previous simulations were done with only a few arm numbers and did not exhibit this effect as clear as our simulation data. For large arm numbers the experimental data of g_θ scatter considerably, indicating that these ratios may no longer be universal numbers for larger arm numbers.

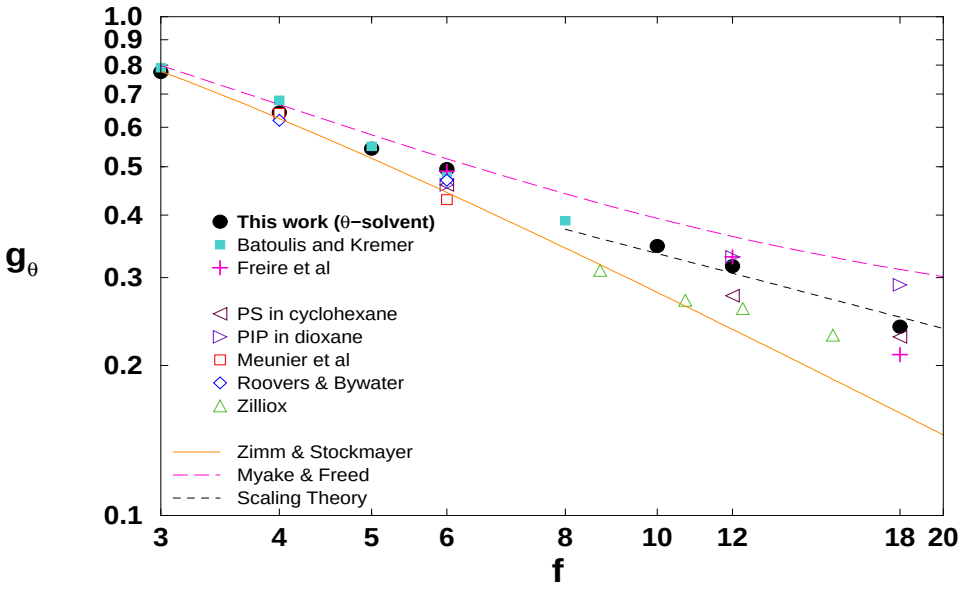

Figure 5.17: *Extrapolated g-factors of stars in a θ-solvent, obtained in this work, compared with theory, experiments and other simulations. $\lambda = 0.65$. Scaling theory, RW theory and RG calculations are presented. Two other simulation studies are displayed. In our study we used longer chains and more arms than most previous investigators. Experimental values of PIP and PS are displayed as well. The experimental data by* Zilliox *were obtained with multibranched star-like chains with arm numbers $f = 8.7, 10.7, 12.3$ and 15.3.*

At the θ-temperature, by definition, two-arm attractions are effectively canceled. Therefore, the experimental findings along with the results of simulations suggest that residual many-body interactions become relevant for many-arm stars because of the overcrowded core. In particular, three-body repulsions among three atoms on three different arms are inherently non-compensated by two-body attractions, since no intermolecular counterpart exists. If two or three atoms belong to the same arm, they can be included in a coarser grained description, and the interaction reduces to an effective two-body interaction. No such renormalization is possible if the three atoms belong to to three different arms. As a result, the star has a finite expansion and one always has $g_\theta > g$.

It has long been observed that the g-ratio for experimental good solvent systems closely coincide with the predictions of Gaussian chain statistics, see Figure 5.18. Further amplification of this ob-

Table 5.6: *Table of extrapolated g-factors of stars in a θ-solvent, obtained in this work, compared to other publications.*

Reference	f						
	3	4	5	6	10	12	18
this work	0.7776	0.6430	0.5544	0.4954	0.3470	0.3159	0.2392
Batoulis and Kremer[a]	0.79	0.68	0.55	−−	−−	−−	−−
Freire et al[b]	−−	−−	−−	0.49	−−	0.33	0.21
Zimm and Stockmayer[c]	0.778	0.625	0.520	0.444	0.280	0.236	0.160
Myake and Freed[d]	0.7985	0.6668	0.5799	0.5193	0.3942	0.3628	0.3114
Experiments	−−	−−	−−	0.46[e]	−−	0.276[f]	0.228[f]
Experiments[g]	−−	−−	−−	0.46	−−	0.33	0.29
Experiments[h]	−−	0.64	−−	0.43	−−	−−	−−
Experiments[i]	−−	0.62	−−	0.47	−−	−−	−−

[a] [13]. MC simulations on a fcc-lattice.
[b] [76]. MC off-lattice simulations with $N_a \leq 55$.
[c] Theory in the framework of Gaussian models for stars with f infinitely long arms.
[d] Renormalization group results according to Eq. (2.16).
[e] [167]. Atactic PS in cyclohexane at 34.5°C.
[f] [169]. Atactic PS in cyclohexane at 34.5°C.
[g] [15]. Polyisoprene in dioxan at 34°C.
[h] [140]. Atactic PS in cyclohexane at 34.5°C.
[i] [166]. Atactic PS in cyclohexane at 34.5°C.

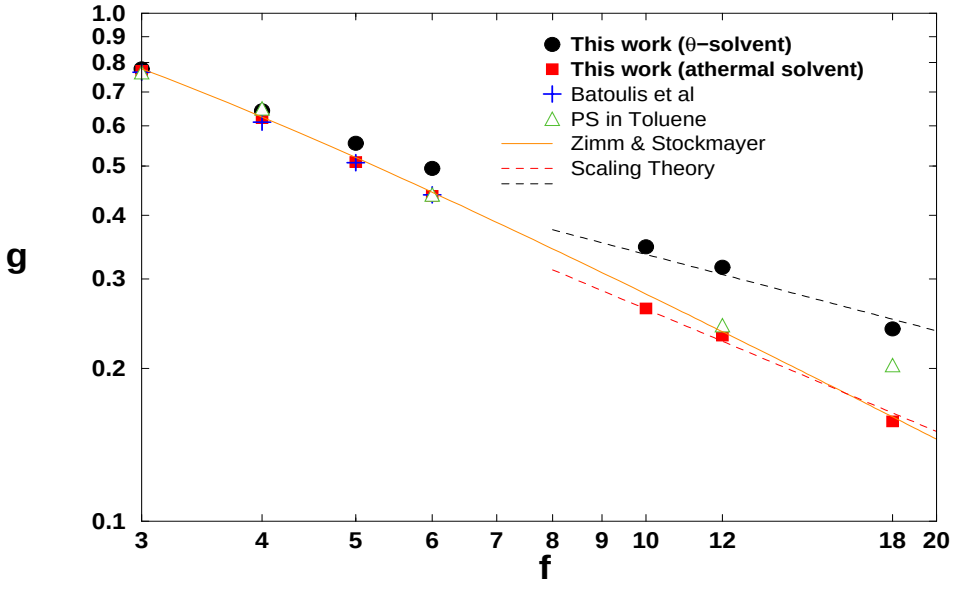

Figure 5.18: *Extrapolated g-factors of stars in a good solvent, obtained in this work, compared with theory, experiments and other simulations. $\lambda = 0.0$. For comparison, the obtained g-factors in a θ-solvent along with scaling theory are displayed as well. Our simulation study used larger arm lengths f than almost all previous studies. It is interesting that the simulation of the* athermal *solvent follows the curve of the RW theory almost perfectly, whereas the θ-chains are more expanded.*

Table 5.7: *Table of extrapolated g-factors of stars in an athermal solvent, obtained in this work, compared to other publications.*

Reference	f						
	3	4	5	6	10	12	18
this work	0.7708	0.6220	0.5092	0.4369	0.2623	0.2321	0.1571
Experiments	0.77[a]	0.65[b]	−−	0.44[c]	−−	0.243[d]	0.20[e]
Batoulis and Kremer[f]	0.766	0.611	0.508	0.439	−−	−−	18
Zifferer[g]	0.763	0.609	−−	0.431	0.274	0.234	−−
Rey et al[h]	−−	−−	−−	0.46	−−	0.28	0.217

[a] [15]. Bauer et al. PS in Toluene.
[b] [166]. Roovers and Bywater. PS in Toluene.
[c] [167]. Roovers and Bywater. PS in Toluene.
[d] [169]. Roovers et al. PS in Toluene.
[e] [168]. Roovers and Toporowski. PS in Toluene.
[f] [13]. MC simulation results on a fcc-lattice with $N_a \leq 100$.
[g] [226]. MC simulation on a tetrahedral lattice.
[h] [163]. MC simulation of very short arm lengths $N_a \leq 55$.

servation is provided by the RG group calculations by *Douglas and Freed* [61] and by simulations. RG calculations by *Myake and Freed* [144] showed, that chains are more expanded with increasing f due to the excluded volume in the inner region, rather than in the outer region where each chain end behaves almost like a linear chain end. Application of the RG theory should be restricted to few arm numbers, as the perturbation of the excluded volume interaction, relative to a linear chain becomes large for many-arm systems, so that RG theory no longer provides a useful description. The large f limit needs to be treated by separate methods such as mean-field theory [223] or scaling theory [52].

In the *Daoud-Cotton* blob-theory [52], one introduces a model with a central close-packed core. Then one invokes a surrounding inner region where the chains are unextended because of screening of the excluded volume due to the higher segmental density. In the outer region the chains are assumed to be swollen because of the geometrical conditions on the blob size with an increase in the distance from the star center. This model predicts that in the limit of large f and large N_a

$$g \propto f^{(1-3\nu)} \tag{5.4}$$

with $\nu = 1/2$ for a θ-solvent and $\nu \approx 0.6$ for self-avoiding chains in a good solvent.

The usefulness of scaling theory is limited by the uncertainty in the pre-factor. In our simulations, in the large f limit we obtain pre-factors of 1.65 and 1.06 in the good and θ-solvent, respectively. Both pre-factors are smaller than predicted by theory for the ($f \rightarrow \infty$) limit. In [62] a modified version of the classical two-parameter Flory theory [223] is given which derives the *Daoud-Cotton* scaling result for g along with the pre-factor as

$$g = 1.94\, f^{(-4/5)} \text{ for } (f \rightarrow \infty) \tag{5.5}$$

MC simulation estimates of *Wittington et al* [222] and of *Barrett and Tremain* [12] deduced a pre-factor of 1.86 and 1.83, respectively. Another mean-field calculation by *Di Marzio and Guttman*

Table 5.8: *Table of extrapolated h-factors of stars in a good solvent, obtained in this work, compared to other publications.*

Reference	f						
	3	4	5	6	10	12	18
this work	0.981	0.933	0.885	0.815	0.723	0.689	0.588
Batoulis and Kremer[a]	0.96	0.92	0.87	0.87	−−	−−	−−
Experiments	−−	0.93[b]	−−	0.86[c]	−−	0.70[d]	0.68[d]
Experiments	−−	0.92[e]	−−	−−	−−	0.73 − 0.83[f]	0.64[e]
Experiments	−−	−−	−−	−−	−−	0.77[e]	0.68[g]

[a] [13]. MC simulations on a fcc-lattice.
[b] [167]. Roovers and Bywater. PS in toluene at 35°C.
[c] [168]. Roovers and Toporowski. PS in toluene at 35°C.
[d] [169]. Roovers et al. PS in toluene at 35°C.
[e] [15]. Bauer et al. PI in toluene at 35°C.
[f] [100]. Huber et al. PS in toluene at 35°C.
[g] [170]. Roovers et al. PBd in dioxane at 26°C.

[134] which is based on geometrical arguments obtained a pre-factor of 1.74. In [77] a pre-factor of 1.15 was obtained for θ-chains by a fit to PIP experimental results.

The insensitivity of g to excluded volume (above the θ-point) can be understood in RG theory. In [61] it is shown by *Douglas and Freed* that an arbitrary radial polymer property Q, scaling as $Q \propto R^p$, has a universal scaling function as a function of excluded volume

$$Q = G_Q \left\langle {R_g}^2 \right\rangle_0^{p/2} E_p(z_2) P_Q(z_2) \tag{5.6}$$

where $\left\langle {R_g}^2 \right\rangle_0^{p/2}$ is the radius of gyration of a Gaussian chain and G_Q is a pre-factor obtained by calculating Q in the Gaussian chain limit, where the excluded volume parameter z_2 vanishes and where by definition $E_p(z_2 = 0) = 1$ and $P_Q(z_2 = 0) = 1$. The function $E_p(z_2)$ depends only on z_2 and the power p of the radial property and contains most of the excluded volume dependence. The function $P_Q(z_2)$ depends on the details of the particular measure of the mean dimensions on the branching architecture and varies only *weakly* with excluded volume. The crucial point is, that by forming a dimensionless ratio between measures of polymers for a branched and linear polymer at the same molecular weight, one obtains

$$g_Q = (Q_{\text{branched}}/Q_{\text{linear}}) = (P_Q(z_2)_{\text{branched}}/P_Q(z_2)_{\text{linear}})\, {g^\circ}_Q, \tag{5.7}$$

with ${g^\circ}_Q = g_Q(z_2 = 0)$. Thus, the predominant contribution to the variation of Q with excluded volume, i.e. the $E_p(z_2)$ factor, exactly cancel when forming the ratio g_Q. The remaining ratio of the P-function represents the variation of P_Q due to a variation of branching architecture, and this ratio is even more slowly varying than is either $P_Q(z_2)_{\text{branched}}$ or $P_Q(z_2)_{\text{linear}}$ alone. This insensitivity is predicted to apply to a wide class of dimensionless ratios of the type g_Q [61].

Another quantity that is often considered is the ratio $h = D_{\text{branched}}/D_{\text{linear}}$ of diffusion coefficients of star-branched and linear polymers (of the same molecular weight M). The theoretical value of h was calculated by *Stockmayer and Fixman* for a RW chain as [189]:

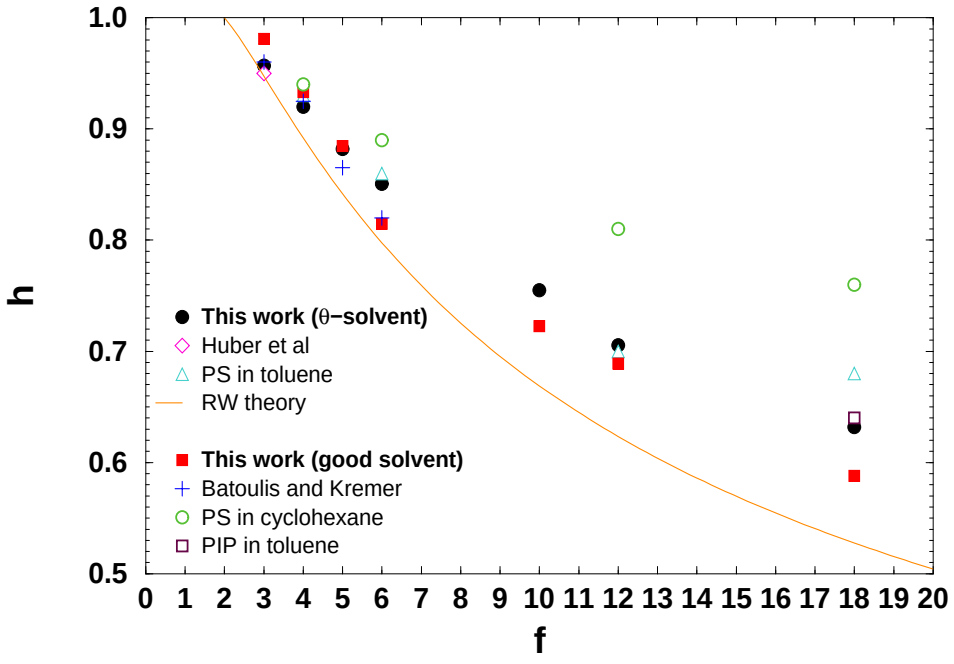

Figure 5.19: *($N \to \infty$) extrapolated h-factors of stars in good ($\lambda = 0.0$) and θ-solvent ($\lambda = 0.65$), obtained in this work, compared with theory, experiments and other simulations. Open symbols are experimental data.*

Table 5.9: *Table of extrapolated h-factors of stars in a θ-solvent, obtained in this work, compared to other publications.*

Reference	f						
	3	4	5	6	10	12	18
this work	0.957	0.920	0.882	0.851	0.755	0.705	0.612
Freire et al[a]	−−	−−	−−	0.93	−−	0.82	0.77
Rey et al[b]	−−	−−	−−	0.91	−−	0.81	0.73
Experiments	−−	0.94[c]	−−	0.89[d]	−−	0.81[e]	0.76[e]
Experiments	−−	−−	−−	−−	−−	0.81[f]	0.72[g]

[a] [76]. MC simulations with very short chains ($N_a \leq 55$).
[b] [163]. MC simulations.
[c] [167]. Roovers and Bywater. PS in cyclohexane at 35°C.
[d] [168]. Roovers and Toporowski. PS in cyclohexane at 35°C.
[e] [169]. Roovers et al. PS in cyclohexane at 35°C.
[f] [100]. Huber et al. PS in cyclohexane at 35°C.
[g] [170]. Roovers et al. PBd in dioxane at 26°C.

$$h^{\mathrm{RW}} = f^{1/2}\left[2 - f + 2^{1/2}(f-1)\right]^{-1}. \tag{5.8}$$

In simulations, the parameter h can be calculated in a different way as a ratio of appropriate hydrodynamic radii:

$$h = \frac{\langle R_h \rangle_{\text{branched}}}{\langle R_h \rangle_{\text{linear}}} \tag{5.9}$$

Experimental values of h and g are substantially higher than the corresponding RW calculations.

Theoretical predictions of the ratios h (and g) in the good solvent limit are very difficult because of two effects, excluded volume and hydrodynamic interactions between segments of the chain, should be considered. The former effect may be treated by the RG theory [143]. However, the ε-expansion method sometimes produces erroneous results because of its poor convergence.

Figure 5.19 displays our simulation results for h, obtained by an extrapolation of the data to $(N \to \infty)$. Both, the good and θ-solvent are displayed. Our data exhibit again, that the θ-chains are more swollen than the chains in a good solvent. h-values of both solvents are *always* larger than the ones of RW theory. This effect increases with larger arm number. Again, our simulation data exhibit this effect much clearer than most previous MC-simulations of only a few arms. The deviations from experimental PS data are increasing with larger arm number. However, the scatter between different experimental data of the same solvent/polymer systems is large.

We also calculated the dimensionless ratio

$$\varrho(f) = \frac{\left\langle {R_g}^2 \right\rangle^{-1/2}}{\left\langle {R_h}^{-1} \right\rangle^{-1}} \tag{5.10}$$

for all simulated stars. For random walks one obtains

$$\varrho(f) = \left(\frac{3f-2}{f\pi}\right)^{1/2} \frac{8\left[2 - f + 2^{1/2}(f-1)\right]}{3f} \tag{5.11}$$

In Figures 5.20 and 5.21 we demonstrate that the leading exponent in the corrections to scaling for R_h is $\Delta = (\nu - 1)$ not only for linear chains, but also for stars. Both figures display the same data, plotted vs. $\Delta = (\nu - 1)$ and $\Delta = -1/2$. For all star arms we determined a higher correlation coefficient of a linear regression when using the exponent $\Delta = (\nu - 1)$. This finding is summarized in Table 5.10.

We obtained our ϱ-values by an extrapolation of the data to $(N \to \infty)$, plotted vs. $N^{\nu-1}$, using the leading exponent in the corrections to scaling. These extrapolations are displayed in Figures 5.22 and 5.23 for all simulated arm numbers. The linear chain data are included again for comparison.

All obtained extrapolated values for ϱ are finally plotted in Figure 5.24 in comparison with other simulations, RW theory and experiment. The agreement with MC-simulations on a lattice by *Batoulis and Kremer* is reasonable, but their values are systematically too low. The agreement of RW theory

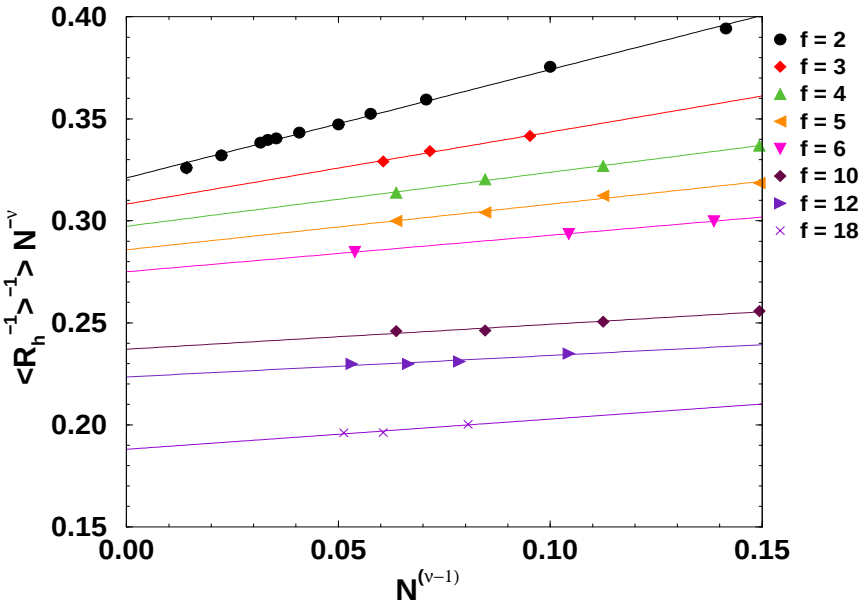

Figure 5.20: *Corrections to scaling of R_h for different topologies with an exponent $\Delta = (\nu - 1)$, $\nu = 0.588$. For comparison, the linear chain is displayed as well. $\lambda = 0.0$.*

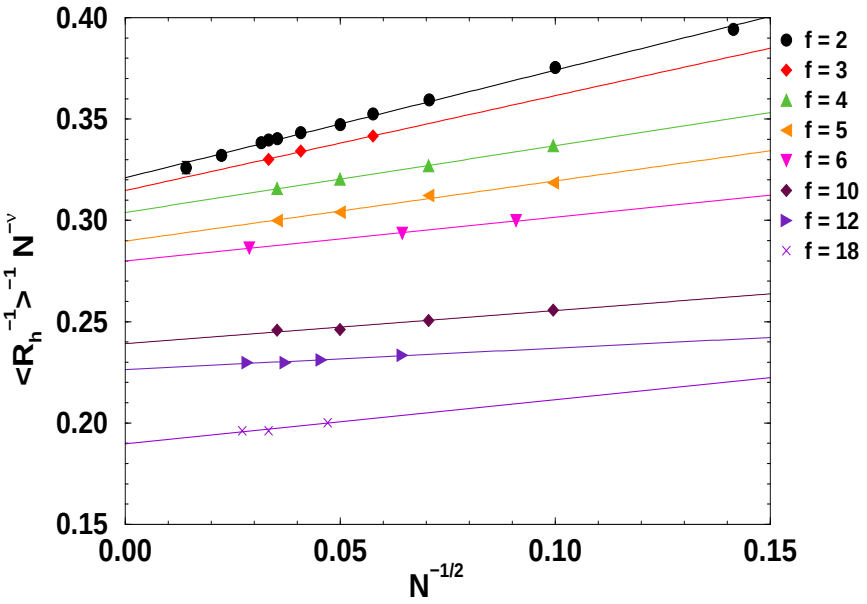

Figure 5.21: *Corrections to scaling of R_h for different topologies with an exponent $\Delta = -1/2$, $\nu = 0.588$. For comparison, the linear chain is displayed as well.*

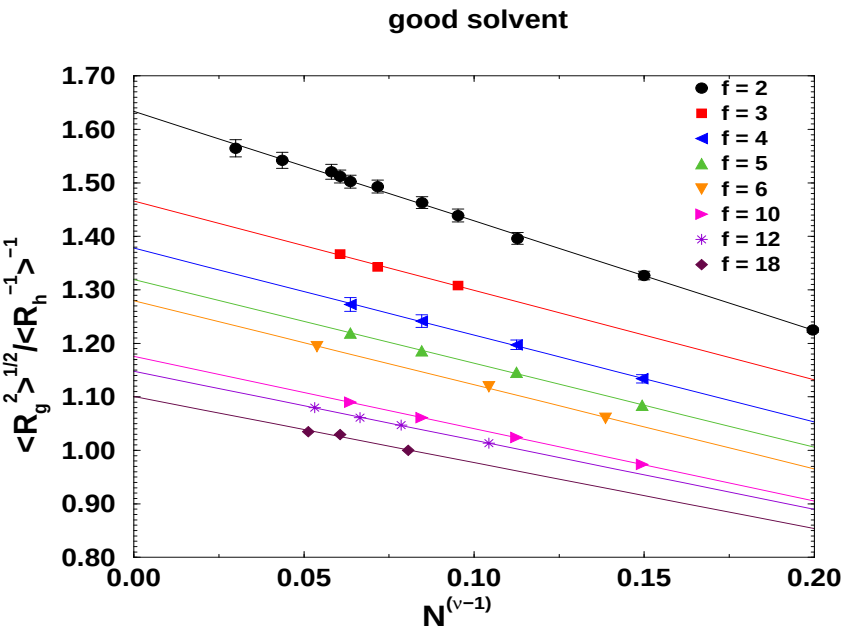

Figure 5.22: *Extrapolated ratios ϱ of stars in a good solvent with $\lambda = 0.0$. The stars become increasingly compact with the number of arms. For comparison, the linear chain $f = 2$ is displayed as well.*

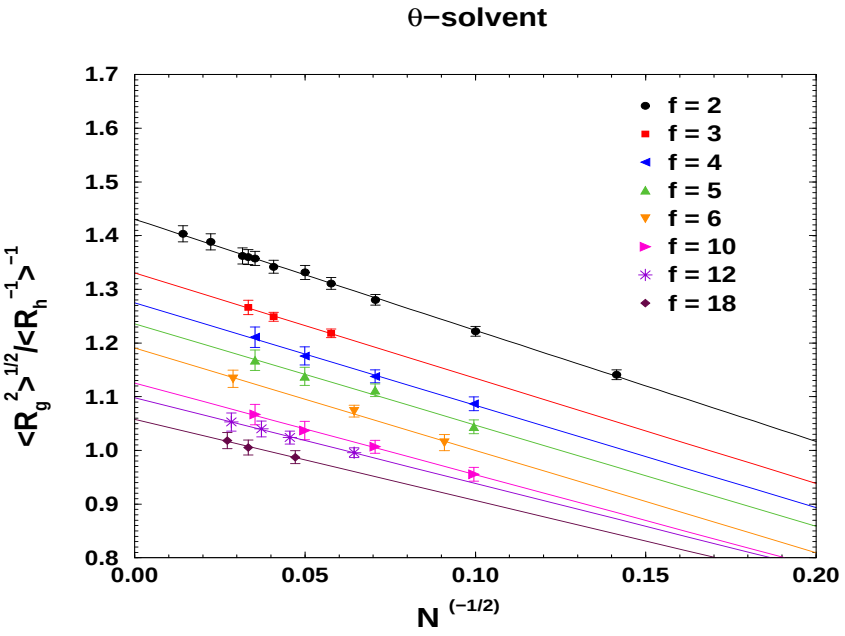

Figure 5.23: *Extrapolated ratios ϱ of stars in a θ-solvent. $\lambda = 0.65$. The stars become increasingly compact with the number of arms. For comparison, the linear chain $f = 2$ is displayed as well.*

f	A	B	χ	$A_\circ$	$B_\circ$	$\chi_\circ$
2	0.406 ± 0.005	0.3138 ± 0.0005	0.9995	0.538 ± 0.014	0.320 ± 0.001	0.9976
3	0.308 ± 0.002	0.331 ± 0.004	0.9994	0.314 ± 0.03	0.468 ± 0.002	0.9982
4	0.2973 ± 0.0008	0.264 ± 0.007	0.9991	0.3039 ± 0.0003	0.329 ± 0.004	0.9981
5	0.2857 ± 0.0008	0.2236 ± 0.0007	0.9934	0.289 ± 0.004	0.297 ± 0.003	0.9913
6	0.2750 ± 0.0001	0.178 ± 0.002	0.99995	0.280 ± 0.001	0.216 ± 0.002	0.9990
10	0.237 ± 0.004	0.122 ± 0.001	0.9885	0.239 ± 0.003	0.164 ± 0.003	0.9825
12	0.223 ± 0.002	0.105 ± 0.001	0.9785	0.2263 ± 0.002	0.106 ± 0.003	0.9743
18	0.188 ± 0.002	0.146 ± 0.002	0.9673	0.218 ± 0.002	0.189 ± 0.003	0.9605

Table 5.10: *Quality of a linear regression of the data displayed in Fig. 5.20 and 5.21 with an exponent of* $\Delta = (\nu - 1)$ *(*$f(x) = Ax + B$*) vs.* $\Delta = -1/2$ *(*$f(x) = A_\circ x + B_\circ$*). The correlation coefficient* χ *is in all cases larger for an exponent* $\Delta = (\nu - 1)$*.*

with the good solvent data is much better than with the θ-solvent data. For large arm numbers, the simulation data reach a ϱ-value which indicates a shape of the stars that corresponds to a compact structure. However, there is a striking deviation of our simulation data with experimental data on PS in a θ-solvent, which exhibits a much lower ϱ-value. Also, data obtained from very early MC-simulations in the 1980's by *Freire et al* and *Rey et al* exhibit huge deviations. Neither in these simulations, nor in the experiments however, were the results extrapolated to ($N \to \infty$) in the way as we suggest above. Due to the extremely slow convergence of R_h to the asymptotic scaling behavior, these deviations arise. Our simulations, to the best of our knowledge, are the first ones which obtained data for ϱ of many-arm stars in an extrapolation to infinite chain lengths, that takes into account the correct leading exponent ($\nu - 1$) in the corrections to scaling.

As conclusion, we have presented a detailed analysis of stars with a variety of different arms. In our study, we obtained data with higher precision and for more star arms than in most previous investigations.

Important results of our star-simulations are:

- The θ-point of stars for the exploited simulation model is not shifted within the accuracy of the simulation data.
- The finite size effects of asphericities and shape parameters become more dominant with the arm number. The behavior of shape factors and asphericities is just opposite to that of linear chains. The asphericity of a star increases with the degree of polymerization N.
- The compactness of stars, expressed in the asphericity parameters, increases with arm number f. The asphericity of stars in a θ-solvent is *larger* than in a good solvent.
- The leading exponent Δ in the corrections to scaling of R_h is in accordance with $\Delta \propto (\nu - 1)$ also for many-arm stars.
- Due to the slow convergence of R_h to the asymptotic scaling behavior, the branching ratio ϱ of experimental systems and all previous simulations of many-arm stars show huge deviations from our obtained simulation data. We argue that one should extrapolate obtained data in the way we suggested above to correct for finite size effects.
- There is a *decrease* of g and h upon chain expansion when going from θ to good solvent stars which is explained in RG theory. One can understand this basic trend as arising from the

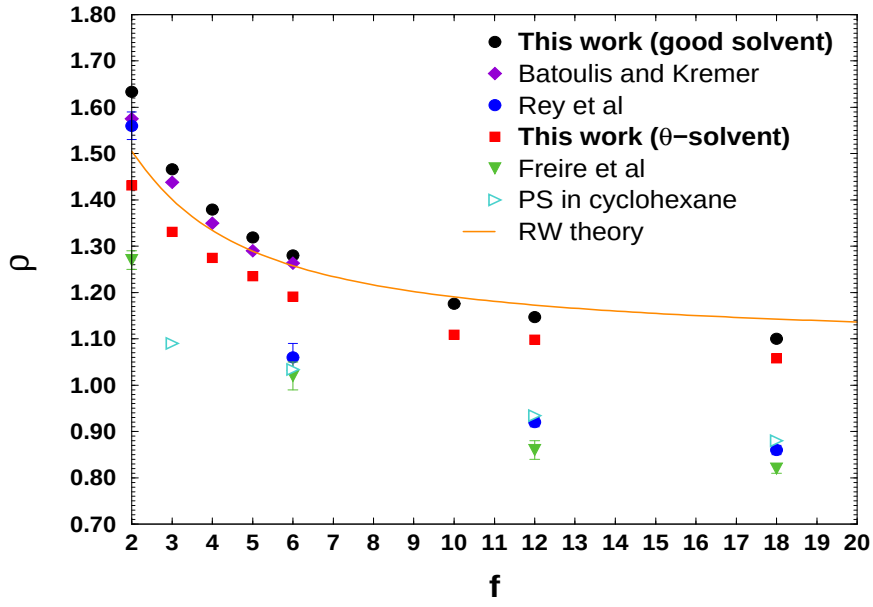

Figure 5.24: *Plot of the ratio* $\varrho(N) = \langle {R_g}^2 \rangle^{1/2} / \langle {R_h}^{-1} \rangle^{-1}$ *vs. arm number* f*. Filled symbols represent simulation data and the open symbol represents experimental PS data.*

decreasing influence of ternary interactions on the mean dimensions. This has been seen in previous simulation studies of few arm numbers f and also in experiments, but our data of many arm-stars exhibit this effect more distinct.

5.2 Simulation of other branched topologies

In this section the influence of branching on the static properties of a variety of chains with different topologies is investigated.

5.2.1 Introduction

When introducing branching, starting from a linear chain, the effect of a non-linear connectivity tree is governed by both, the *number* of additional side branches attached to the initial linear backbone chain and the specific *location* on the backbone where these side chains are attached. In industrial polymer production, *anionic polymerization* is an example of an important process which produces branches with a very narrow MWD which, for all practical purposes, is equal to $U = 1.0$. A post-polymerization involving the still active chain ends can then be performed to produce branched polymers with a predetermined number of arms [164]. These species of polymers are excellent model compounds for testing theories and simulations, as was demonstrated in the previous section on star polymers. However, in many polymerization processes, the occurrence of branched polymers in a *random* fashion is common. E.g., the high-pressure polymerization of LDPE leads to short- and long-chain branching in the resulting product. The polymerization process is a radical-chain-polymerization, usually initiated by an Oxide or Peroxide, and the occurrence of mainly uncontrollable chain transfer reactions leads to the typical Ethyl- and Butyl side chains of LDPE. In [194], two industrially produced samples of LDPE in a good solvent (Iupac Alpha and NBS 1476) where investigated by light scattering and a GPC analysis. In this investigation, several typical quantities describing the degree of branching where determined. Besides the branching parameter g as defined in Eq. 2.13 on Page 11, the analogous quantity

$$g' = \frac{[\eta]_{branched}}{[\eta]_{linear}}. \tag{5.12}$$

was measured. From the knowledge of these two quantities, the exponent b of the equation $g' = g^b$ was calculated. The figures displaying these quantities have been obtained from [194] and are displayed in Figure 5.25.

GPC experiments in principle give little to no insight into the kind of branching that is present in a polymer sample, because the equilibration of the GPC-columns is usually done with linear polymer standards. With light scattering methods on the other hand, one is restricted to systems where one still has enough contrast for receiving signals in order to resolve the branched structures. For these two industrial polymer samples, it was argued that there are probably only a few branches every few thousand repeat units along the backbone and therefore light scattering fails to give further insight into the exact structure. However, from the knowledge of dimensionless branching parameters, such as g and g', it is possible to perform simulations of sample topologies of chains and compare the experimentally determined branching parameters with the ones obtained in simulations. Hence, by performing simulations of various well-defined topologies of chains, one obtains information as to what kind of branching might be prevalent in the above polymer samples. This simulation study not only tests the assumption of the above LDPE samples having a structure which corresponds to a long backbone chain and several short or long side chains, but it also gives a set of reference data for a variety of different interesting topologies which are useful for further experimental studies in this direction.

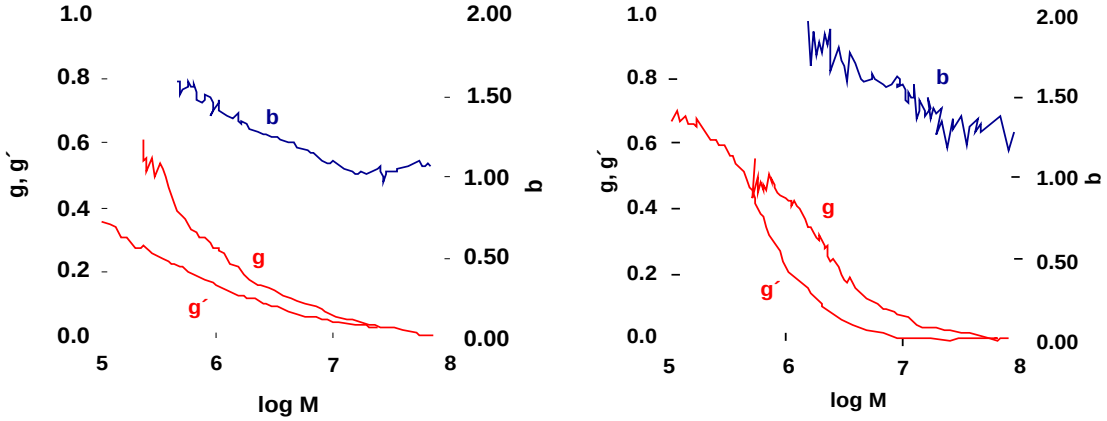

Figure 5.25: *Several branching indices of two samples of industrially produced LDPE. Displayed are the branching parameters g and g' and the exponent b of the relation $g' = g^b$. Left: Iupac Alpha sample. Right: NBS 1476 sample. Figure taken from from [194].*

5.2.2 Description of the branched topologies

Two particular classes of topologies were chosen for this study of branching effects that are, on the one hand, non-trivial, but on the other hand, allow for a systematic variation of parameters that govern the connectivity of monomers.

The first class of topologies, see Figure 5.26, focuses on the *number* of arms added to a backbone chain of constant length.

Starting from a star polymer with $f = 3$ arms, one arm is then splitted in two halves of equal length and attached to the same backbone in a symmetric manner. This procedure then continues, yielding polymer chains with two, four and ten side chains attached to a backbone chain of constant length. Three different chain lengths were simulated for this kind of topology in order to allow for an extrapolation of the measured properties to ($N \to \infty$). The above described branched topology can be characterized by two parameters l_s and m. The former is the number of monomers in a side chain and the latter is the monomer distance between consecutive side chains along the main backbone. For each branched structure all side chains have the same number of monomers l_s and the distance m is taken to be constant. The respective parameters are displayed in Table 5.11.

Topology	star ($f = 3$)	side2	H-molecule	side4	side10
Parameters	l_s / m / p_s	l_s / m / p_s	l_s / m / p_s	l_s / m / p_s	l_s / m / p_s
N = 301	100 / 0 / 33	50 / 67 / 33	50 / 99 / 33	25 / 40 / 33	10 / 17 / 33
N = 601	200 / 0 / 33	100 / 133 / 33	100 / 199 / 33	50 / 79 / 33	20 / 36 / 33
N = 901	300 / 0 / 33	200 / 199 / 33	200 / 299 / 33	100 / 119 / 44	40 / 54 / 44

Table 5.11: *Values of topological parameters for the first category of branched structures. The length of the sidearms l_s and the arm distance m along the main chain are displayed for the three different simulated chain lengths N. Additionally, the percentage of monomers of the whole molecule that are contained in side chains p_s is displayed. See Figure 5.26 for an explanation of the topology.*

The second investigated class of topologies keeps the number of branches *constant*, only *shifting* them along the backbone, see Figure 5.27.

We started out with a four-arm star polymer and then shifted the arms apart along the backbone chain. By performing this procedure, we investigate a transition from a star polymer to a linear chain. One detail has to be taken into account, when performing this procedure: As a backbone of a branched polymer chain one considers that part of the chain which has the largest number of consecutively linked monomers with each monomer having two bonds connecting it with two direct neighbors (except for the first and last monomer). By shifting the side chains apart, according to the procedure described above, one changes the monomer connectivity in such a way, that a different subchain of monomers becomes a new backbone chain. This is illustrated in Figure 5.27.

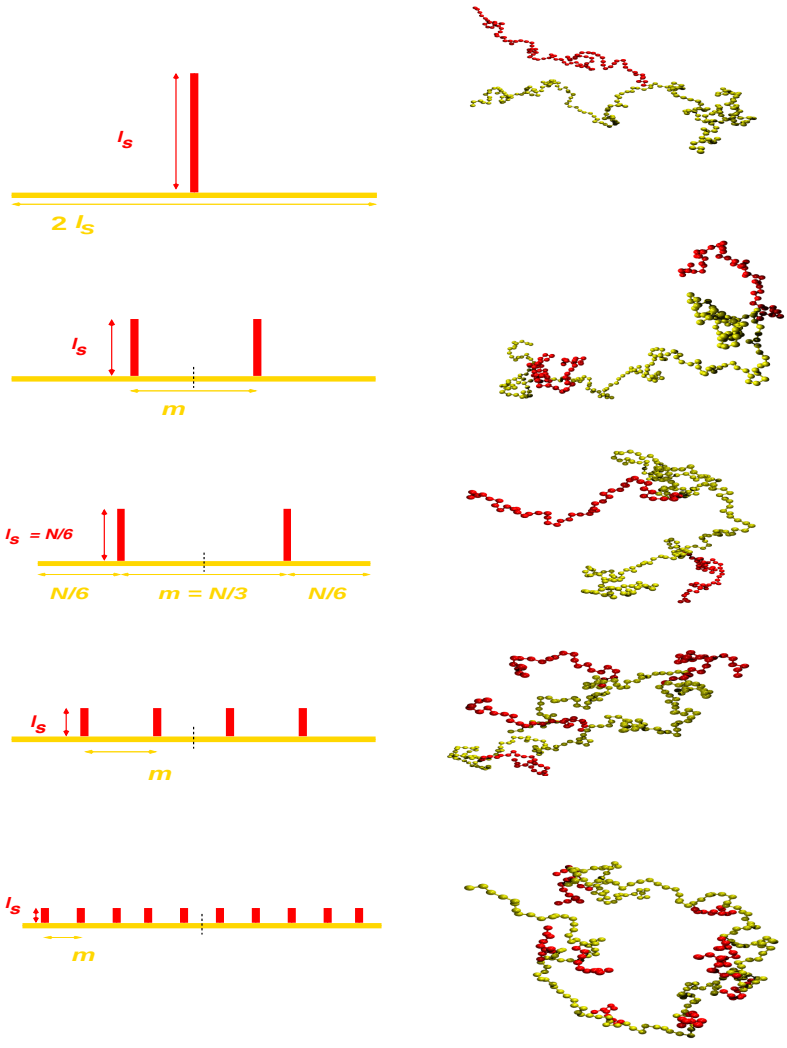

Figure 5.26: *Schematic pictures (left) and snapshots (right) of the simulated branched topologies according to Table 5.11. The snapshots are taken from systems with $N = 301$ and $\lambda = 0.0$. Starting from the top with a three-arm star, the red-colored side chain is splitted in two individual arms of equal length, leading to a backbone chain with two arms attached to it at equal distances from the center. Additionally, the topology of a so-called H-polymer has been modeled. Then the branching process continues, again dividing each side arm into two parts of equal length, resulting in a backbone chain with four and ten side chains, respectively.*

Table 5.12 gives an overview of the parameters characterizing the second class of branched systems. For this topology, four different chain lengths were simulated in order to detect possible finite

size effects and to allow for an extrapolation ($N \to \infty$).

Topology	10%	20%	40%	star ($f = 4$)
Parameters	l'_s / l_s / m / p_s	l'_s / l_s / m / p_s	l'_s / l_s / m / p_s	l'_s / l_s / m / p_s
N = 101	25 / 5 / 39 / 10	25 / 10 / 29 / 20	25 / 20 / 9 / 40	25 / 25 / 0 / 50
N = 201	50 / 10 / 79 / 10	50 / 20 / 59 / 20	50 / 40 / 19 / 40	50 50 / 0 / 50
N = 401	100 / 20 /159 / 10	100 / / 40 / 119 /20	100 / 80 / 39 / 40	100 / 100 / 0 /50
N = 801	200 / 40/ 319 / 10	200 / 80 / 239 / 20	200 / 160 / 79 / 40	200 / 200 / 0 / 50

Table 5.12: *Values of topological parameters for the second category of differently branched structures. The number of monomers l'_s in side chains is displayed along with the actual values l_s and m that correspond to the lowest pictures in Figure 5.27. The length of the sidearms l_s and the arm distance m along the main chain are displayed for the four different simulated chain lengths N. Additionally, the percentage of monomers contained in side chains p_s is displayed.*

Simulations have been performed for the described two topologies, both, in a good solvent regime and at the θ-point and the corresponding branching parameters have been determined. To our knowledge, this is the first simulation study that investigates the described different kind of topologies in a systematic manner including the effect of solvent quality.

The data of the performed simulations are summarized in the tables in Appendix B starting on Page 161.

5.2.3 Simulation results and discussion

5.2.3.1 Scaling properties

As an example, Figures 5.28 to 5.31 display the scaling exponents ν of the end-to-end distance and the radius of gyration for two different topologies: One system is referred to as "10%" in Table 5.12 and the second one is a system with 10 side chains attached to a backbone. Additionally to $\langle {R_g}^2 \rangle$ of the total molecule, the averaged values $\langle {R_{e/g}}^2 \rangle$ are displayed for the backbone and side chain monomers. The obtained exponents of all sub-units of the molecules are summarized in Table 5.13. Scaling plots of other types of topologies yield similar results of the exponents which are in reasonable agreement with the ones expected from theory. This is further exemplified in Figure 5.33 which displays $S(k)$ for a 10% system in a good solvent. When using the scaling variable $q = kN^{\nu}$, the curves of different N collapse into a single curve which exhibits the expected slope $\propto q^{-1/\nu}$ for intermediate q-values. In Figure 5.33 a more sensitive Kratky-plot is shown for $S(k)$ of different topologies but constant polymerization N. At small k values, the *Guinier Law* is valid and $S(k)$ changes according to:

$$S(k) = N \left[1 - 1/3\, k^2 \langle {R_g}^2 \rangle + \mathcal{O}(k^4 \langle {R_g}^2 \rangle) \right]. \tag{5.13}$$

Hence, at the same N, the different topologies of systems become apparent in a varying negative slope of $S(k)$ due to different radii of gyration. The curves then follow the scaling law $S(k) \propto k^{-1/\nu}$, which, close at the θ point should result in a set of horizontal curves with slope zero. Finally, the curves level off for large k-values where local structures become apparent. These differences in the structure function should be detectable in a light scattering experiment.

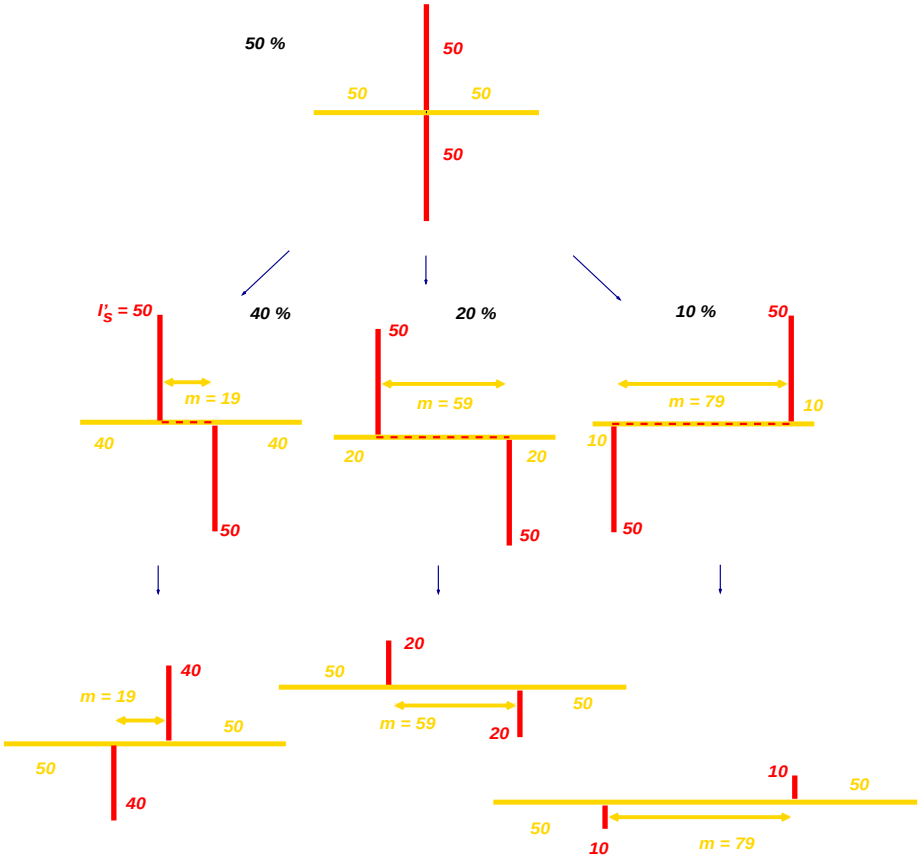

Figure 5.27: *Sketch of the simulated topologies with the same number of arms shifted along the initial backbone. As an example, a system with $N = 201$ is shown. All side chains (red color) are connected with the backbone via an additional crosslink monomer. Starting from the top, two of the star arms are shifted apart such that either one has an offset of 10, 20, and 40 percent of the backbone length. Consequently, these new topologies are called 40%, 20% and 10% respectively. As the total number N of monomers is kept at a constant value for all topologies, this branching procedure actually leads to a new backbone chain for each new connectivity of monomers, with the backbone having the largest number of consecutive monomers. The new backbone is yellow-colored and the side-chains are depicted in red in the three lowest figures which show the actual variation of the topology of the systems.*

	side 10		10% offset	
Quantity	good solvent	θ-solvent	good solvent	θ-solvent
$\langle {R_e}^2_{\text{backbone}} \rangle$	0.602 ± 0.003	0.492 ± 0.008	0.603 ± 0.003	0.500 ± 0.007
$\langle {R_e}^2_{\text{side chains}} \rangle$	0.605 ± 0.004	0.493 ± 0.008	0.614 ± 0.001	0.496 ± 0.008
$\langle {R_g}^2_{\text{total}} \rangle$	0.609 ± 0.008	0.492 ± 0.008	0.602 ± 0.002	0.498 ± 0.005
$\langle {R_g}^2_{\text{side chains}} \rangle$	0.611 ± 0.004	0.495 ± 0.006	0.605 ± 0.007	0.504 ± 0.006
$\langle {R_g}^2_{\text{backbone}} \rangle$	0.615 ± 0.009	0.500 ± 0.005	$- - -$	$- - -$

Table 5.13: *Scaling exponents of R_e and R_g for two branched topologies at different solvent qualities.*

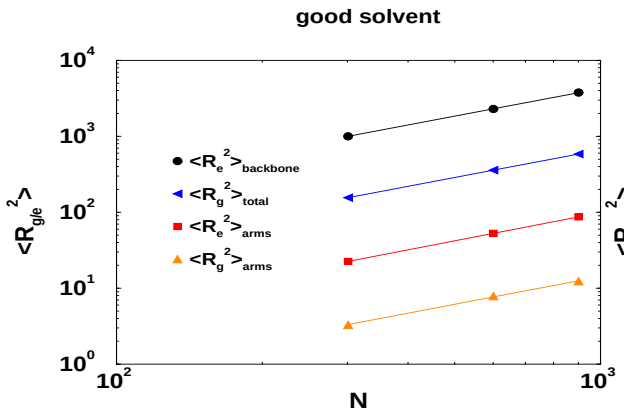

Figure 5.28: *Scaling of R_g and R_e of a branched system as a function of N. As sample system a backbone chain with 10 side chains was chosen. $\lambda = 0.0$.*

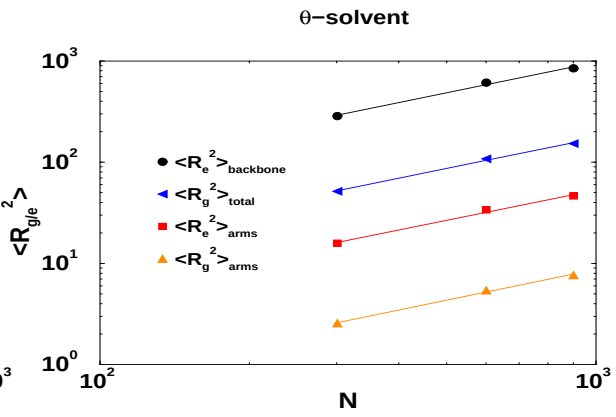

Figure 5.29: *Scaling of R_g and R_e of a branched system as a function of N. As sample system a backbone chain with 10 side chains was chosen. $\lambda = 0.65$.*

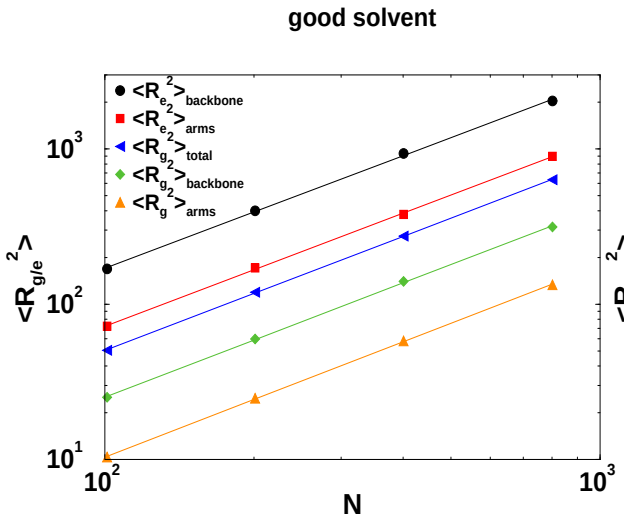

Figure 5.30: *Scaling of R_g and R_e of a branched system as a function of N. As sample system the topology 10% according to Table 5.12 was chosen. $\lambda = 0.65$.*

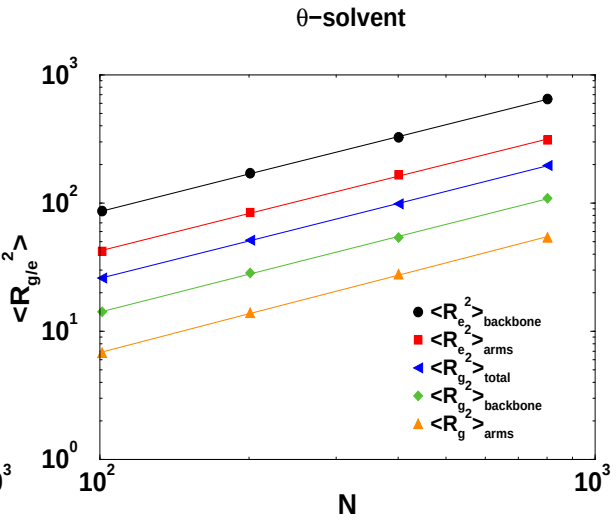

Figure 5.31: *Scaling of R_g and R_e of a branched system as a function of N. As sample system the topology 10% according to Table 5.12 was chosen. $\lambda = 0.65$.*

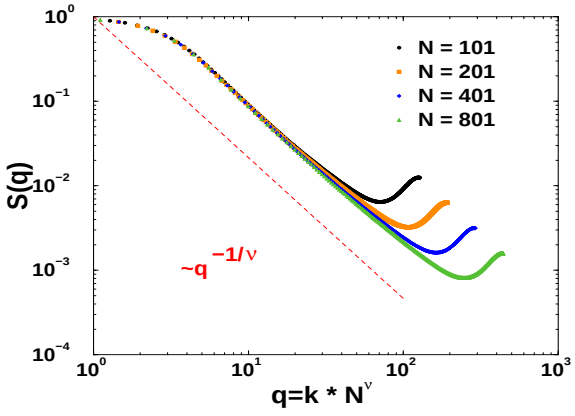

Figure 5.32: *Structure function $S(k)$ for a 10%-topology at different molecular weights N. The scaling of $S(k)$ with the variable $q = kN$ is displayed. $\lambda = 0.0$. The exponent ν was chosen as $\nu = 0.6$.*

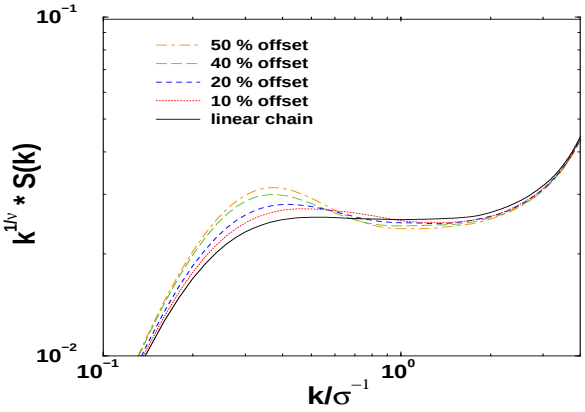

Figure 5.33: *Structure function of different branched topologies with the same molecular weight $N = 201$. $\nu = 0.5$.*

5.2.3.2 Determination of branching parameters

In Figure 5.34 the g-factors are displayed for all different topologies and for two limiting solvent qualities, the θ-point and the good solvent case.

Generally, the finite size effects are not very large, but seem to be bigger in the θ-solvent. The largest deviation between the asymptotic g-factor $g_\infty = \lim_{N\to\infty} g(N)$ and the one obtained from the smallest simulated system is about 6% for the side4-system in a θ-solvent.

We now discuss the branched topology in **a)** of Figure 5.34.
It is interesting that it is the g-factor of the H-molecule that has the closest vicinity to the linear chain – corresponding to $g = 1$ – and that the chain with four side chains has the lowest asymptotic g-value. This is the case in both, the good and the θ-solvent. In the side4- and side10-chains, 44% of all monomers are located in the branches but in the system with ten arms the side chains are much shorter and the system is less compact as can be seen from g. From this result we conclude that apparently not only the number and location of arms in a branched structure is crucial for the chain extension expressed by g, but also the individual arm lengths. Many short side chains cause a system to be more expanded than a system with the same molecular weight, but only a few long side chains.

The topologies in **b)** of Fig. 5.34 exhibit a clear, distinctive behavior. When switching the side chains towards the ends of the backbone, one observes a shift from low to high g-values. The most compact structure with the highest segment density at the branch-point is the four-arm star, which is the limiting case for two side chains being moved along a backbone. It is not possible to get lower g-values with only two side chains in a system when keeping the molecular weight N constant which is an important result on its own.

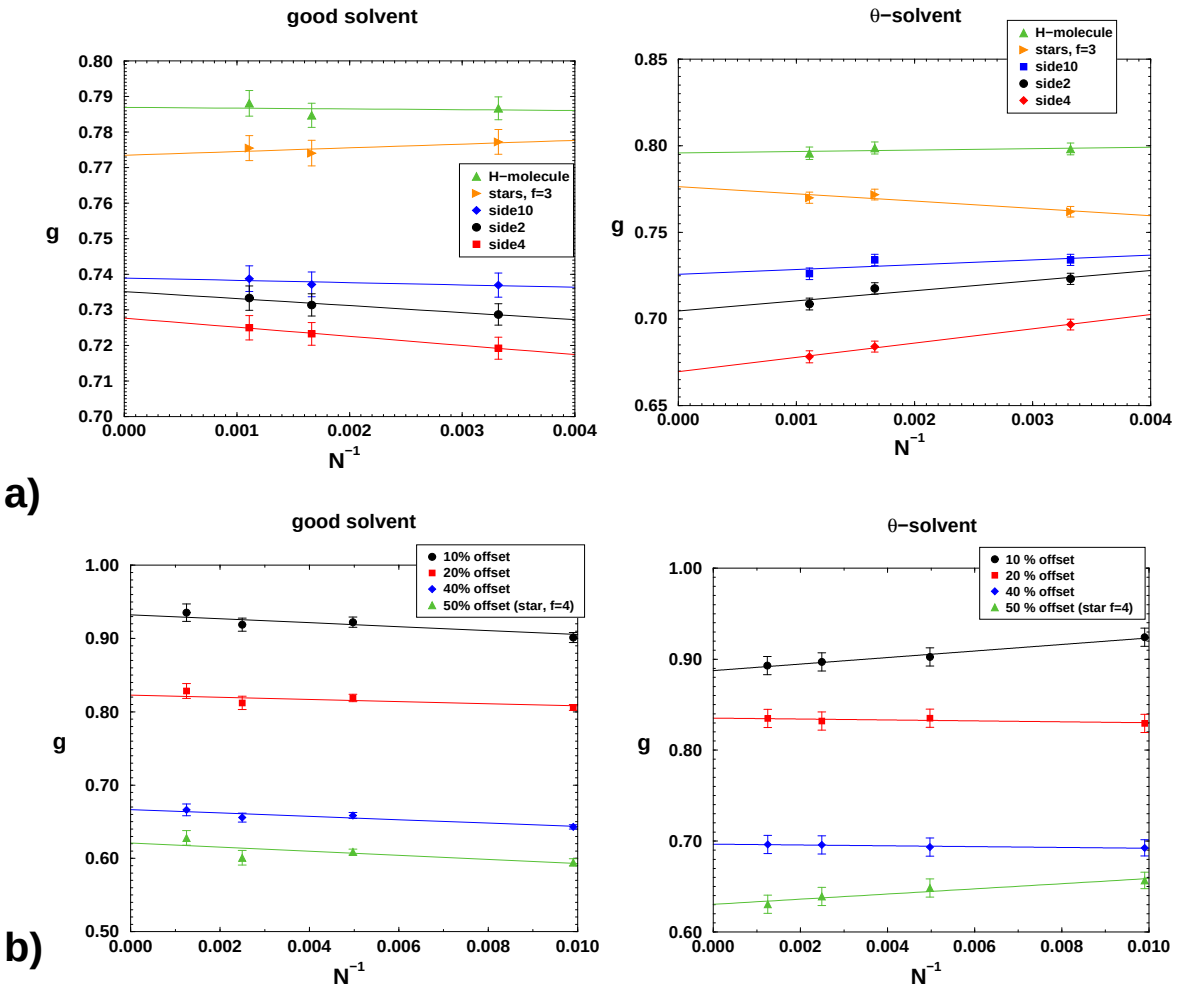

Figure 5.34: *Branching factors g for two solvent qualities in an extrapolation ($N \to \infty$).*
a) *Topologies with a backbone of constant length and a variable number of side chains.*
b) *Transition from a linear chain to a four-arm star.*

All g-values have been determined in the good and θ-solvent regime. It was shown, that the obtained scaling exponents correspond to the ones that one expects from theory for solvents of either quality. On the other hand, almost all experimental systems are synthesized in solvents of a quality that ranges anywhere between an athermal and a θ-solvent. Therefore, all experimentally investigated branched systems with a topology similar to the ones that were used in our study, have to have g-values that are in the range between ${g_\infty}^{\theta}$ and ${g_\infty}^{\text{good}}$, provided by our systematic investigation. The experimental g-values obtained in Ref. [194] are below our obtained values within the whole range from the athermal to θ-solvent regime.

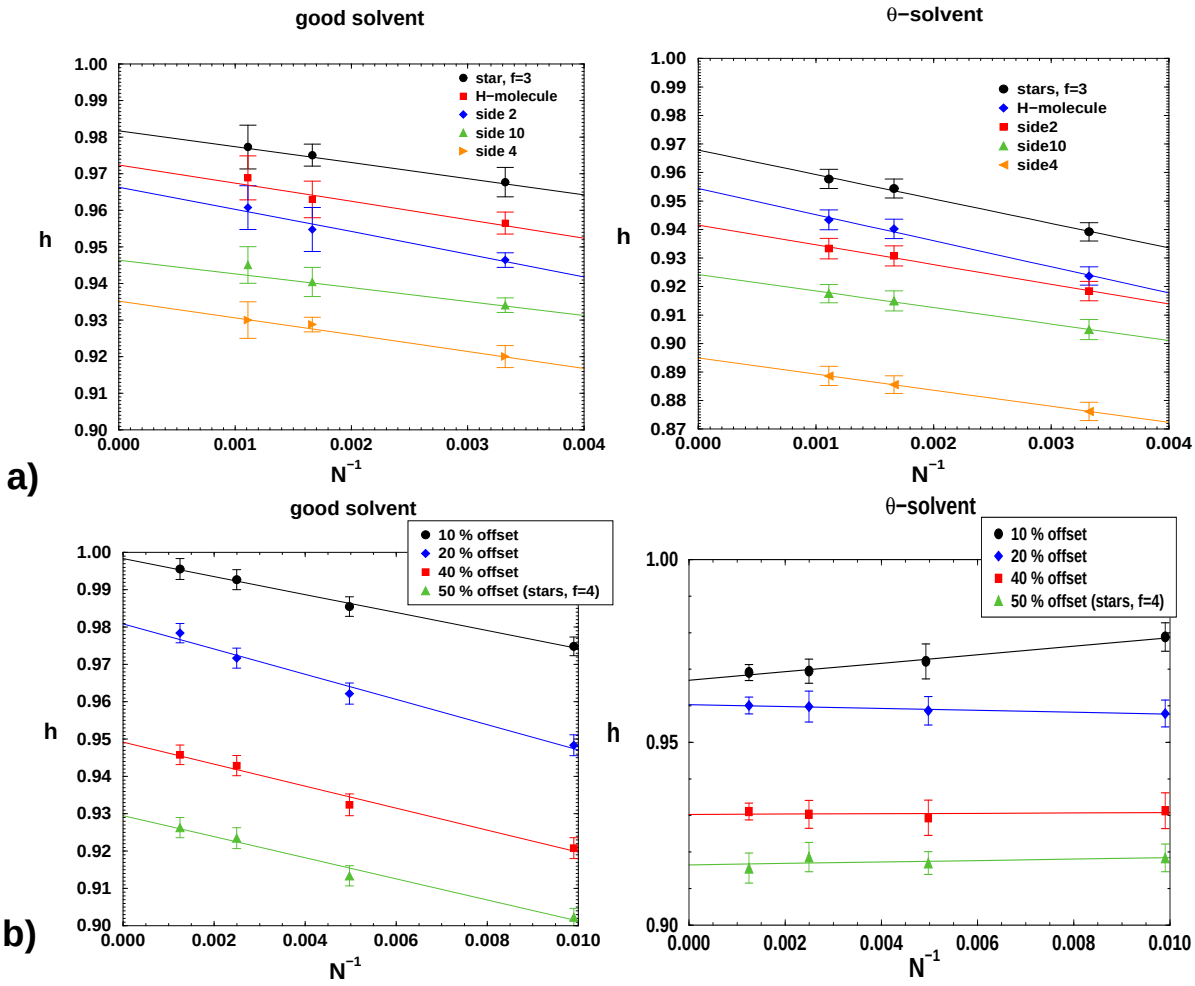

Figure 5.35: *Branching factors h for two solvent qualities in an extrapolation ($N \to \infty$).*
a) *Topologies with a backbone of constant length and a variable number of side chains.*
b) *Transition from a linear chain to a four-arm star.*

We now consider the numerical values of g.
All of our determined g-values are larger than the ones obtained in Ref. [194]. Furthermore, our simulation study shows, that finite size effects do not influence g much, whereas in [194], the g-value very strongly depends on the polymerization M. It remains unresolved in [194] whether this is due to an effect of polydispersity present in the samples or to a decreasing solvent quality with increasing M. In Ref. [194] it is argued that the branching parameters mainly are depending on chain architecture at the same temperature. This is in agreement with our simulations which show that the effect of solvent quality for the same polymer/solvent system has small influence on g. It is mainly the chain

architecture that leads to changes in g.

In order to further directly compare the experimental data with our simulation, we also calculated the ratios h, $g' = h^3$ of all topologies. All calculated g'-values are larger than the experimental values for LDPE. The smallest g'-value in the simulation is the one for a system with 10 sidechains in a θ-solvent ($g' = 0.88$). The largest value in Ref [194] however is about 0.7 in the low molecular weight regime. The discrepancy between simulation and experiment is obvious.

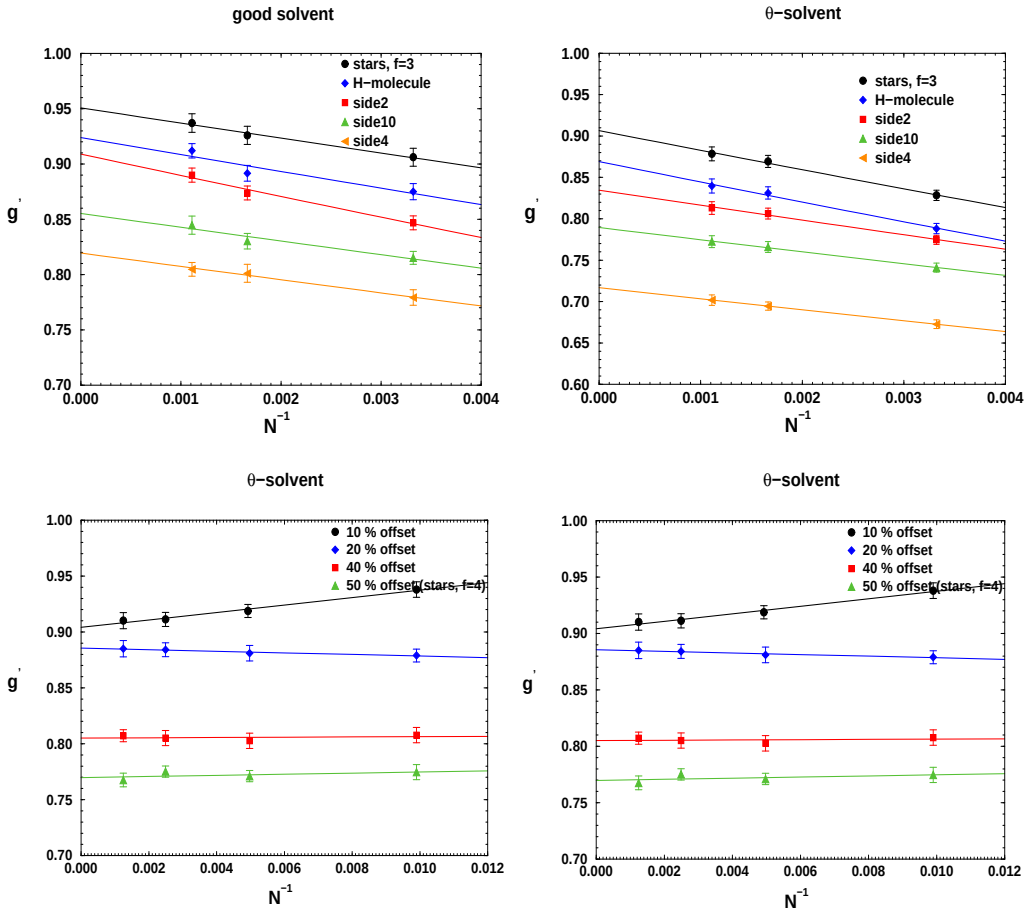

Figure 5.36: *Ratio g' for two solvent qualities extrapolated to ($N \to \infty$).*
a) *Topologies with a backbone of constant length and a variable number of side chains.*
b) *Transition from a linear chain to a four-arm star.*

Finally, we determined the dimensionless parameters ϱ for all of our sample topologies in both solvents, which can be used for comparisons with experiments. For monodisperse branched experimental systems, for which both, R_h and R_g were determined, one could use these data of ϱ for a mapping procedure of our simulation beads onto the monomer units in a real chemical compound. In Ref. [194], such data are not provided. It would be interesting to perform systematic experimental studies in this direction.

Summary

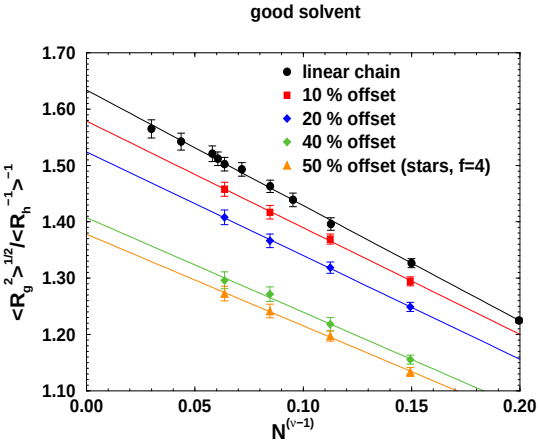

Figure 5.37: *Dimensionless ratio ϱ for a transition from a linear chain to a star with $f = 4$ arms. $\lambda = 0.0$.*

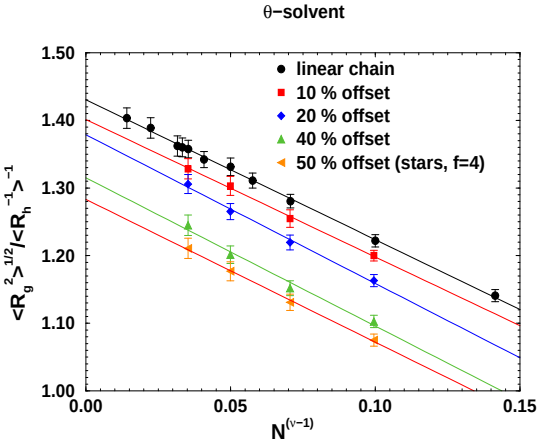

Figure 5.38: *Dimensionless ratio ϱ for a transition from a linear chain to a star with $f = 4$ arms. $\lambda = 0.65$.*

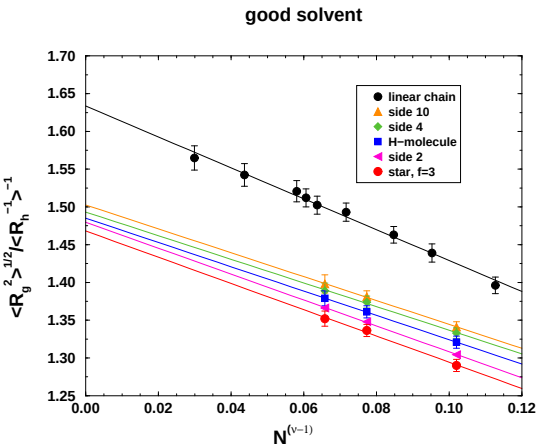

Figure 5.39: *Dimensionless ratio ϱ for different monomer topologies. $\lambda = 0.0$.*

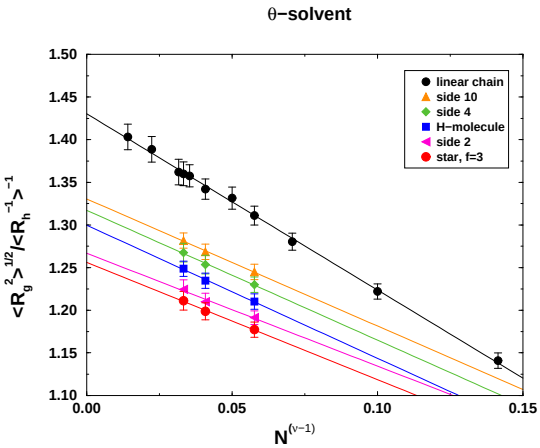

Figure 5.40: *Dimensionless ratio ϱ for different monomer topologies. $\lambda = 0.65$.*

In this section, our simulation model has been applied to a variety of differently branched structures. For these well-defined topologies, branching factors have been determined. A comparison of these branching factors with industrial LDPE revealed that non of these investigated structures is present in the experimental system. All branching parameters obtained in simulations are larger than the ones obtained for LDPE. With a four-arm star we obtain a value of $g \approx 0.62$ in the good solvent regime which, for LDPE is the upper limit for g. Our study shows that the lowest g-value which can be obtained by shifting two side chains along a backbone is the one of a four arm star. Using more than two arms, keeping the overall molecular weight constant, eventually leads to shorter side chains and hence larger g-values.

We conclude that in industrial LDPE hyper branched structures must be the prevalent form of branching. Only by hyper branching or by multi-arm stars with ($f \geq 5$) it is possible to get into the regime of experimental g-values that were obtained with LDPE. In light of the fact that our study provided important data on a variety of different topologies, it would be interesting to perform further experimental studies in this direction with well-defined architectures.

5.3 Simulation of dendritic polymer structures

5.3.1 Introduction

The chemical synthesis of dendritic polymers [2], which is a relatively new class of branched macromolecules, has been the subject of intense research. The number of publications in this research area has undergone an exponential increase in recent years.

Dendritic polymer structures are built from x-functional AB_{x-1} monomers where each B-group may be connected to an A-group of another monomer. The *perfect* representatives of this group of materials are the *(regular) dendrimers*, which are built layer-wise in generations G around a central core unit with all functional groups of each generation reacted before adding a new generation. As the molecule is built by adding one complete generation after another, a perfect dendrimer is monodisperse. All but the outermost repeat units continue in (x-1) branches of the same length giving rise to a tree-like structure that resembles a Cayley tree, see Fig. 5.41. The branching structure of dendrimers is characterized by the number of generations G which they contain, the functionality x of the end-groups, and the number of monomer (spacer length) m between the functional groups.

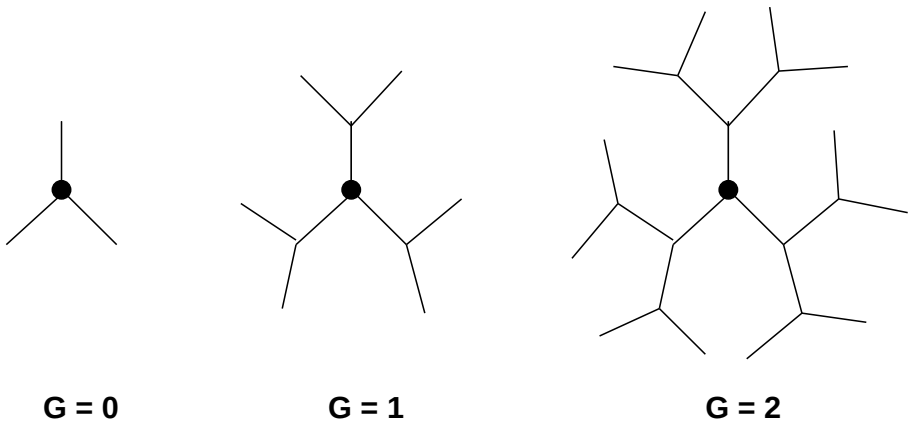

Figure 5.41: *Schematic diagram of different dendrimer generations G with a functionality $x = 3$. Consecutive generations are added layer-wise around a central core unit.*

Since their discovery in 1985 [197], the initial research in the field of dendrimers was primarily devoted to synthetic strategies to create these highly architectured macromolecules without defects. For the synthesis of dendrimers constructed by a *step-by-step process*, two different strategies, the *divergent approach* (from the inside out) [197, 198] and the *convergent approach* (from the outside in) [94] were employed. A large number of synthesized dendrimers has been presented in literature [94, 120, 142, 197, 199] with maybe one of the most frequently studied dendrimers being the polyaminoamide (**PAMAM**) molecule which is built from a trivalent nitrogen atom core [197], see Fig. 5.42.

[2] From Greek $\delta\epsilon\nu\delta\rho o\nu$=tree. Common notions of dendritic polymer structures in literature are arborols, cascade-, cauliflower-, or star-burst polymers.

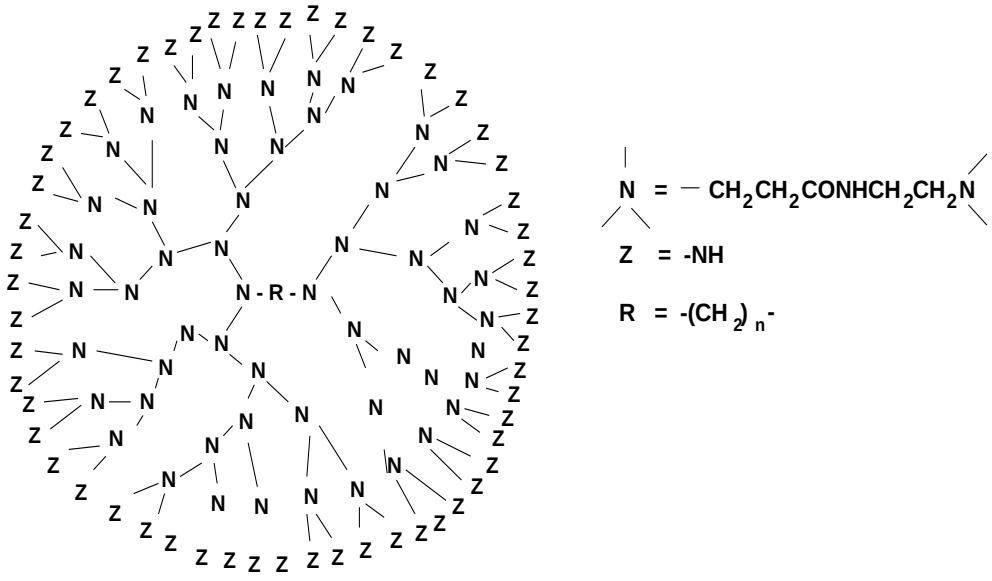

Figure 5.42: *The PAMAM dendrimer according to [103]. This is one of the most frequently studied dendrimer structures in literature.*

In contrast to dendrimers, *hyper-branched polymers* are usually synthesized in a *one-pot* reaction of x-functional AB_{x-1} monomers ($x \geq 3$) leading to a highly disperse mixture of variably sized, randomly branched macromolecules. Hence, the resulting structures of this synthesis are usually imperfect and the control over layers or generations vanishes. Experimental methods to prepare dendrimers efficiently or hyper-branched macromolecules with more regular structures have been explored by many researchers and some recent reviews on these different synthesis strategies can be found in [70, 149]. Fewer experimental studies are available on the spacial structure of dendrimers in solution, in bulk or at surfaces.

As the total mass M of a dendritic molecule increases *exponentially* with the number of generations G, it grows faster than the available volume $V \propto G^3$. The spacial structure therefore must saturate at a given number of generations. At low generation numbers one expects that the structures will be related to those of star polymers or lightly branched polymers with a large number of available conformations and will thus present strongly fluctuating structures in solution. When, on the other hand, the number of generations is increased, steric interactions between groups located at the periphery of the molecule must result, leading to a densely packed spherical structure with much less degrees of internal freedom. Therefore, dendrimers bridge the gap between strongly fluctuating polymer structures and dense colloidal particles. An understanding and a precise tuning of the conformational freedom of dendritic molecules is a prerequisite for all applications discussed so far in literature.

The physical properties and consequences of the particular architecture of dendrimers are now being explored because several dendrimers and hyper-branched polymers are now available, some dendrimers even commercially. Many useful applications have been proposed that exploit their topological characteristics. In particular, many dendritic supra-molecular complexes have been devised with possible uses as drug controlled-release systems, as sensors, as surface and rheology modifiers or as gene transfection agents [103].

An early theoretical attempt to analyze the structure of dendrimers was presented by *de Gennes and Hervet* [57]. They considered the problem in the limit of long flexible spacers between tri-

functional monomers, in an athermal solvent with each generation having fully reacted. Their self-consistent field analysis concluded that dendrimers have a *minimum* of the radial monomer density distribution $\rho(r)$ near the center of the molecule and increases monotonically to the outer edge. They found an effective fractal dimensionality of $d_f = 5$ and a limiting generation number of $G_{\max} \approx 2.88(\ln m + 1.5)$ up to which a perfect dendrimer can be grown. This model however suffers from the deficiencies that it assumes that all subsequent bonds point to the periphery of the molecule and that the monomers of each generation lie in concentric shells of their own which seems to be an erroneous assumption.

There are only very few simulation studies of flexible dendrimers in solution. One of the first simulation studies was performed by *Lescanec and Muthukumar* [124]. They performed a three-dimensional off-lattice simulation with a ball-and-stick model of starburst polymers using a kinetic growth algorithm for a SAW. They found a density profile that decreases monotonically outward from the center of the molecule. However, their simulation did not allow the structures to relax to more entropically favorable configurations. Thus their model is non-equilibrium in nature and it is not clear, whether their results hold for equilibrium dendrimers.

When comparing our simulation data with the ones obtained in very often cited MC-study of dendrimers by *Mansfield and Klushin* [132] we noticed considerable deviations that could not be explained by data scattering. In [207] it was recently shown that the simulation scheme, that was used in [132] was completely erroneous because it did not obey detailed balance and hence did not obtain correct equilibrium properties of polymers. In [207] a modification to this scheme was introduced which corrected for this problem.

A MD simulation study by *Murat et al* [146] gave evidence of a density distribution function which is maximal at the core and decays to the edge of the dendrimer.

Experimentally, small-angle scattering methods, such as SAXS and SANS are suitable to investigate the radial structure of dissolved dendrimers. Up to now, however, SANS- and SAXS-studies of dendrimers in solution did not come to a final conclusion regarding the average radial density distribution. A survey of literature may be found in [11].

In light of the fact that the analytical results by *de Gennes and Hervet*, and the findings of numerical studies conflict fundamentally, a self-consistent mean field model of dendrimers was developed by *Boris and Rubinstein* [39]. Their model allows to calculate the overall density profile of any generation G of interest in the system. However, this theory has all the inherent assumptions of any mean field theory, since they calculate the excluded volume interaction of a test branch with a mean density field found by pre-averaging over configurations of all the other monomers. In particular, they ignore all correlations along the branch. In addition, they assume the dendrimer molecules to be spherically symmetric with the center of mass at the core monomer and that the mass of each individual shell is uniformly distributed in the respective shell. With this model they obtained a density profile of dendrimers with features that supports the findings of the very few available simulation studies which found the density being the largest at the core and decaying to the edge.

The synthesis of high molecular weight dendrimers is expensive due to the many synthetic steps involved. The question therefore arises, whether irregular hyper-branched polymers that can be obtained in one single-pot reaction would show similar properties. Currently, there is little experimental evidence concerning the intrinsic viscosity $[\eta]$ of hyper-branched polymers. *Fréchet et al* [74] claim that $[\eta]$ always increases, but less rapidly than for equivalent linear chains whereas it was shown by *Hobson and Feast* [96] that certain hyper-branched polymers exhibit a dendrimer-like behavior in that $[\eta]$ passes through a characteristic maximum and then decreases with increasing molecular weight. Since experimental results are not consistent and there is no general theoretical explanation for the

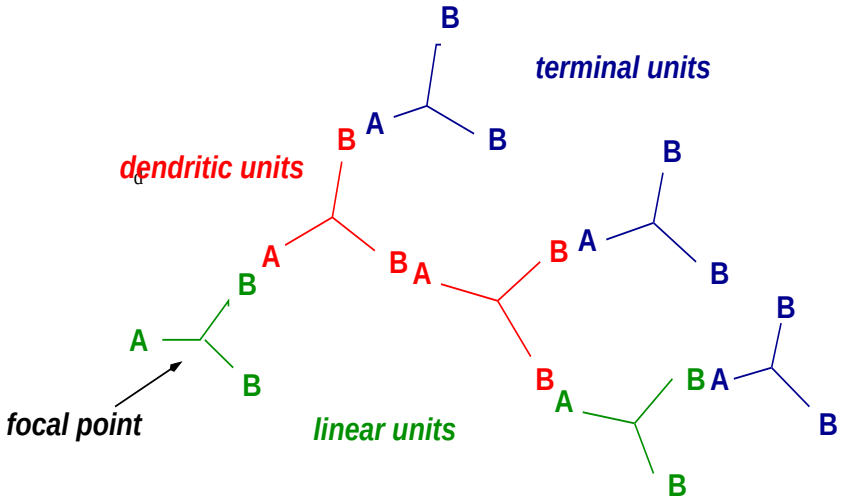

Figure 5.43: *Different types of repeat units present in a hyper-branched AB_2-polymer according to [172].*

behavior of dendritic systems, computer simulations appear to be an appropriate way to obtain insight into these kind of problems.

5.3.2 Description of the degree of branching with dendritic macromolecules

In a perfectly branched dendrimer, only one type of repeat-unit can be distinguished, apart from the terminal units carrying the chain ends. In an imperfect hyper-branched dendrimer one can distinguish three different repeat units as depicted in Figure 5.43. These repeat units are *terminal units* T, having the two B-groups unreacted, *linear units* L, having one B-group unreacted and the *dendritic units* D which are fully reacted AB_x monomers. The linear units are generally called *defects*.

The degree of branching DB is often used to characterize hyper-branched structures. It is traditionally defined by [171]

$$DB = \frac{\sum D + \sum T}{\sum D + \sum T + \sum L}. \tag{5.14}$$

This definition however, has the disadvantage that it overestimates the degree of branching of distributions of small molecules since unreacted monomers are counted as terminal units and contribute to the degree of branching. Another drawback is the fact that the degree of branching of linear chains is never zero but $1/N$ as linear chains always have a terminal group.

A better definition of DB is given by the ratio of the actual number of dendritic units, D, to the maximum number of dendritic units for a given molecular weight. Since two linear units L can always be rearranged to give one dendritic unit this leads to

$$DB = 2\sum D / \left(2\sum D + \sum L\right). \tag{5.15}$$

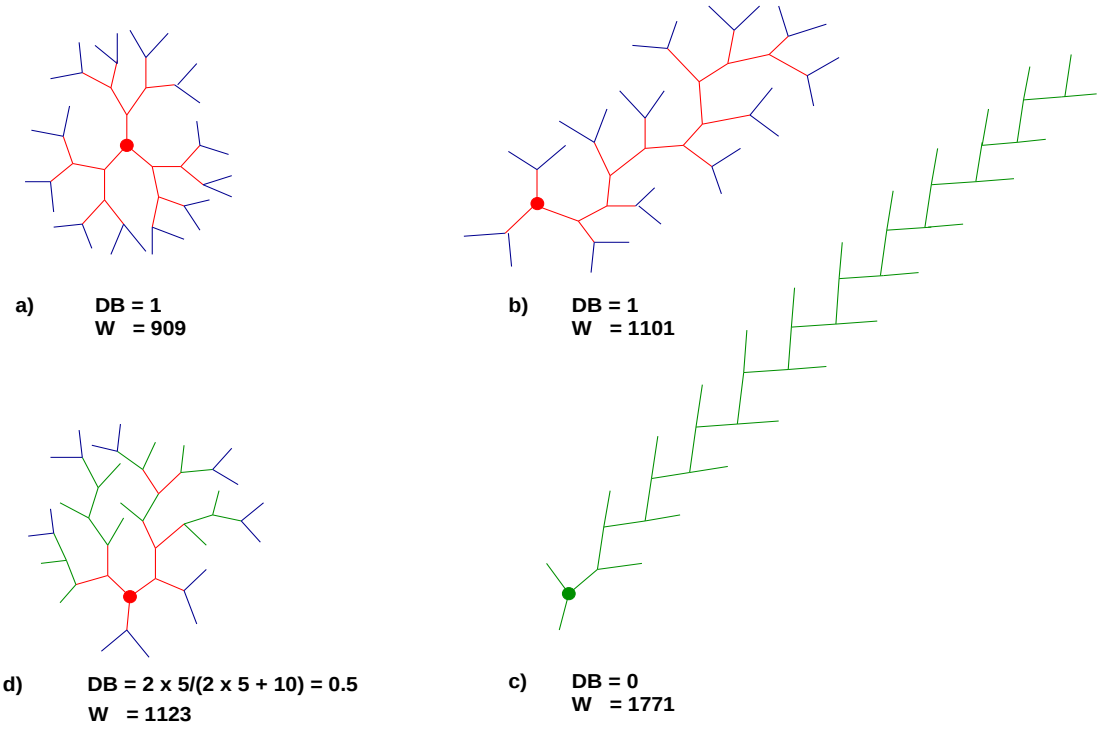

Figure 5.44: *Four different dendritic structures that contain the same number of AB_2-monomers ($N = 22$) as the regular dendrimer of generation $G = 3$ (a). (b) Random (hyper-branched) dendrimer with the same degree of branching as (a), containing no linear units. (c) Linear chain containing only linear units with $DB = 0$ (minimal) and $W = 1771$ (maximal). (d) Another random structure containing several linear and dendritic units. The core B_3-units of the different structures are emphasized by circles and the color coding to distinguish different units is done according to Figure 5.43. Examples are taken from Ref. [209].*

Terminal units do not contribute to DB in this definition, thereby avoiding the above mentioned disadvantages of Eq. (5.14). In the trivial case of unreacted monomer units ($D = L = 0$), Eq. (5.15) is *defined* as $DB = 0$. The AB_{x-1}-monomer of the focal point is counted as being linear if $(x - 2)$ of its B-groups have reacted. If all B-groups have reacted it is dendritic and in the case of zero B-groups having reacted it is counted as terminal unit.

Although Eq. (5.15) yields a better characterization of branching in terms of DB it still has the drawback that hyper-branched molecules with significantly different topologies may have the same DB value as displayed in Fig. 5.44.

A yet even more discriminating structural index is the *Wiener index* W which was introduced by *H. Wiener* [210]. He defined the connectivity index of a graph as the sum of distances between all pairs of vertices of the graph. As the molecules obtained from sequential polymerization are like trees and contain no rings or multiple connections between any two bonds one can adopt the same method to determine W as in the original paper [210]. Each bond, regardless of its branching status or molecular structure, is considered as a vertex of the graph. For each bond b of an N-vertex tree the product of the number of vertices on the "left" (V_l) and on the "right" (V_r) side of b is calculated and summed up, leading to the definition:

$$W = \sum_{b=1}^{N-1} V_l V_r . \tag{5.16}$$

N	$\langle {R_g}^2 \rangle_0$ simulation	$\langle {R_g}^2 \rangle_0$ according to Eq. (5.20)
50	13.64 ± 0.02	13.89
100	28.2 ± 0.4	27.80
200	56.6 ± 0.3	55.60
400	112 ± 1	111.2
800	224 ± 3	222.4
1000	236 ± 5	238
2000	559 ± 15	556
5000	1384 ± 39	1390

Table 5.14: *Comparison of $\langle {R_g}^2 \rangle_0$ measured in simulations with Eq. (5.20) using the Wiener index.*

This definition, applied to linear chains with N segments, where each chain segments represents a vertex of the graph, the Wiener index is simply:

$$W_{\text{linear}}(N) = N(N^2 - 1)/6, \tag{5.17}$$

and for dendrimers of generation G with tri-functional repeat units ($p = 3$) where each of the $N = 3(2^G - 1) + 1$ branch points represents a vertex, the Wiener index is [176]:

$$W_{\text{dendrimer, p=3}}(G) = 9 \cdot 4^G \cdot G - 15 \cdot 4^G + 18 \cdot 2^G - 3. \tag{5.18}$$

For symmetric star-branched chains with f ($f \geq 3$) arms and N_a monomers per arm the Wiener index is given by:

$$W(f, N_a) = f \left[\sum_{i=1}^{f-1} i(fN_a - i) \right] + f(f-1)N_a. \tag{5.19}$$

For graphs with the same number of vertices, W is always minimal for the most compact, dendritic structure and maximal for a linear structure with the same number of vertices N. E.g. for a 7^{th} generation regular dendrimer, the value obtained for W from Eq. (5.18) is about 12 times smaller than for a linear chain with the same number of vertices N. Structures that have the same degree of branching DB can usually be distinguished by their corresponding Wiener indices, see Fig. 5.44. Although some very small graphs may have the same W, even if their connectivity is different, the Wiener index is a good quantitative measure for characterizing the shape of larger connectivity trees of molecules. W reflects the actual surface-to-volume ratio of a structure and in [92] it was shown that it is related to physical and chemical properties depending on this ratio such as molar volume, viscosity or refractive index.

For linear ideal chains with N segments there is a simple connection between $\langle {R_g}^2 \rangle_0$ and W, because the pair summation over the number of segments in Eq. (5.16) is equal to the Wiener index. Therefore, R_g can be rewritten using the Wiener index in the following form:

$$\langle {R_g}^2 \rangle_0 = \frac{C_\infty {l_b}^2}{N^2} W \tag{5.20}$$

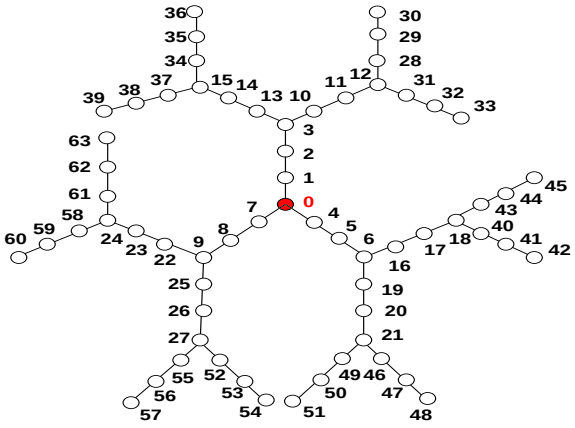

Figure 5.45: *Schematic picture of the simulated dendrimers showing the numbering of monomers in the simulation. The central B_3-unit (particle label 0) is highlighted. $G = 2$, $m = 3$.*

A comparison of $\langle {R_g}^2 \rangle_0$, that were measured directly in simulations and are listed in the tables in Appendix A on pages 143 to 148, and $\langle {R_g}^2 \rangle_0$ according to Eq. (5.20), using the measured ${l_b}^2$ and C_∞ for this model, is given in Table 5.14.

5.3.3 Simulations of dendrimers

In this work we concentrate on dendritic polymers built from **tri**-functional AB_2 monomers around a B_3 core with a spacer length of $m = 3$. The total number of monomers N^D_{total} of such a perfect dendrimer structure is determined by m and the generation number G:

$$N^D_{\text{total}} = 3 \cdot m \cdot (2^{G+1} - 1) + 1. \tag{5.21}$$

An example for $m = 3$ and $G = 2$ is given in Fig. 5.45 which also shows the numbering of the $N = N^D\text{total} = 64$ monomers, as it is done in the simulation. The dendrimer starts with the 0^{th} generation at the central core unit (label 0) with three spacers of length 3. Each of these spacers has a tri-functional end-monomer continuing into two daughter spacers which define the next generation. This process continues until the desired generation number, with each spacer of one generation having two daughter spacers of the same length. In this work we considered dendrimers in an athermal solvent and under θ-conditions. Sample snapshots from real simulations of regular dendrimers can be found in the Appendix F on Page 175.

5.3.4 Simulations of hyper-branched polymers

Hyper-branched monomers of **tri**-functional AB_2 monomers were simulated in this work for several spacer lengths m and different generations G. We focused on the simulation of a perfect hyper-branched structure which contains no linear repeat units and where all B-groups in each generation have fully reacted, expect for the terminal units. Such a perfect hyper-branched structure is known in literature as *Fréchet dendrimer*. A chemical realization of this type of hyper-branched structure is given in Fig. 5.46.

The total number of monomers N^F_{total} in a Fréchet-type dendron is given by

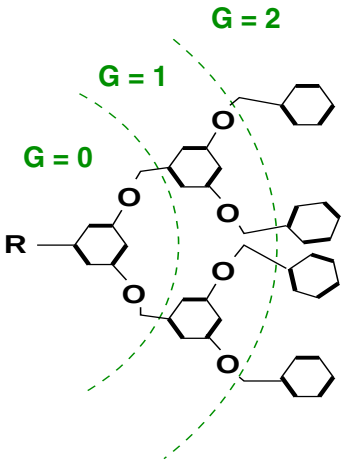

Figure 5.46: *Experimental realization of a Fréchet dendrimer as a second generation dendritic alcohol. Taken from [103].*

$$N_{\text{total}}^{F} = (2^{G+1} - 1)(1 + 3m). \tag{5.22}$$

For simulational purposes this structure can be viewed as a backbone chain with a total of

$$N_{\text{back}}^{F} = (4G + 2) \cdot m + (2G + 1) \tag{5.23}$$

monomers and a number of regularly attached side chains of various lengths which, depending on generation number G, have themselves attached side chains, see Fig. 5.47.

5.3.5 Simulation results

Figure 5.48 displays the variation of $\langle {R_g}^2 \rangle$ for regular dendrimers as a function of the generation number G for two considered solvent qualities, an athermal solvent ($\lambda = 0.0$) and a θ-solvent ($\lambda = 0.65$). The difference in size between dendrimers in both solvents becomes more apparent with an increase of the generation number G. Figure 5.48 suggests that a dendrimer can be grown to an infinite size. However, at some critical generation number, a dendrimer can be grown only in an imperfect manner anymore. Therefore one would expect R_g to saturate eventually which is not yet the case for the generations that were simulated. In Figure 5.49 the same quantities are shown on a double-logarithmic scale as a function of the number of monomers N in the system. The solid lines are linear fits of the data points according to $\langle {R_g}^2 \rangle \propto N^{2\nu}$ and using only generations 3 to 7. The scaling exponent ν is not a constant as it is for other connectivities of monomers such as linear chains or stars, but it decreases with generation number. This means that self-similarity of dendrimers of different generations is restricted to much smaller length scales than for objects with a simpler branching structure. The results for ν taking into account different numbers of generations are listed in Table 5.15.

As the fractal dimension of an object in Euclidian space is limited by the dimensionality of the space we consider the fractal dimensionality of our model dendrimers to be $d_f = 3.0$ within the accuracy of the simulation data in both considered solvents. The slightly larger values than $d_f = 3$ are probably due to the finite size of our chains. As mentioned above, scaling laws of the form

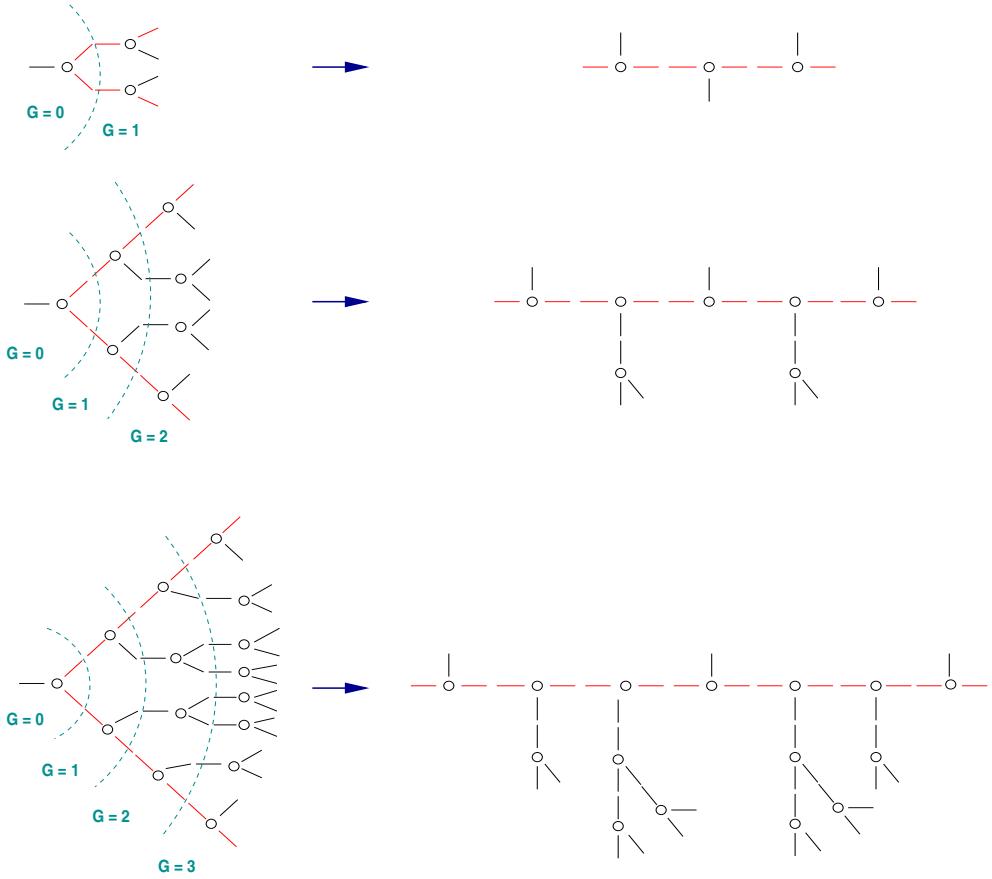

Figure 5.47: *Schematic picture of the simulated Fréchet dendrimers. For simulation purposes the branched structure can be visualized as a backbone chain with side chains attached to it in a symmetric manner. Depending on generation number, the side chains themselves have branches. The central B_3 core-monomers of the AB_2-units are depicted as circles. The spacers of length m are depicted as separate lines. In the simulation, only* two *parameters determine the whole connectivity tree completely: the number of monomers m per spacer and the generation G. Each B_3 core-monomer of the branched structure is taken account of by one extra monomer in the simulation.*

$\langle {R_g}^2 \rangle \propto N^{\nu}$ are strictly only valid in the $(N \to \infty)$-limit. Hence we obtain the observed deviations. Thus, according to our results, dendrimers are very dense, completely space-filling objects.

Mansfield determined the fractal dimension of dendrimers by using the *box method* [133]. In this study, a range of d_f was determined as $d_f = 2.45 - 2.76$. These results are not consistent with our study.

A determination of d_f by *Murat and Grest* gave $d_f = 3.1$ and $d_f = 3.0$ for the good and athermal case, respectively. The result of this publication is in accord with our d_f-value of 3.

Finally we present in Figure 5.50 the time evolution of R_g with simulation time. To ensure equilibration of the systems, R_g and R_h were monitored and production runs were started only when these quantities had saturated to a common mean value from different initial conditions.

5.3.5.1 Monomer density distribution $\rho(r)$

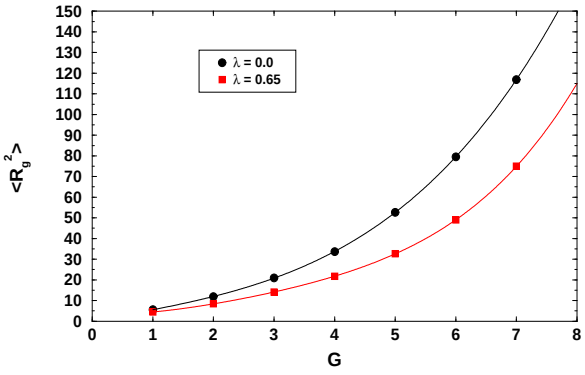

Figure 5.48: *Size of regular dendrimers.* $\langle {R_g}^2 \rangle$ *is plotted vs. generation number* G *for two different solvent qualities, the athermal case* ($\lambda = 0.0$) *and a* θ*-solvent* ($\lambda = 0.65$). *The solid lines are* 4^{th} *order polynomial fits to the data points. The errors are smaller than the symbol size.*

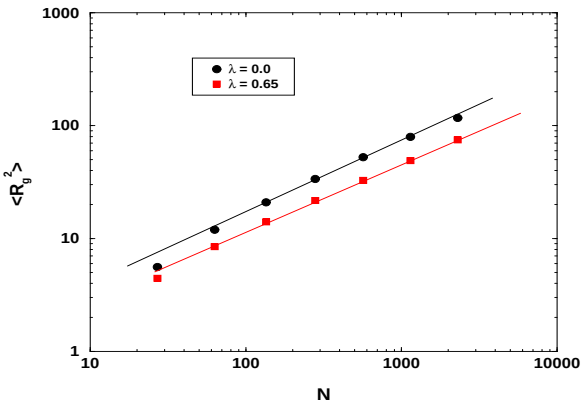

Figure 5.49: *Log-log plot of* $\langle {R_g}^2 \rangle$ *vs. the number of monomers* N. *Two solvent conditions are considered. The straight lines are best linear fits to the data points taking into account only generations* 3 *to* 7.

G considered	ν $(\lambda = 0.0)$	d_f $(\lambda = 0.0)$	ν $(\lambda = 0.65)$	d_f $(\lambda = 0.65)$
$1-7$	0.336 ± 0.012	2.97	0.313 ± 0.005	3.20
$2-7$	0.314 ± 0.010	3.18	0.303 ± 0.003	3.30
$3-7$	0.304 ± 0.006	3.29	0.295 ± 0.005	3.40

Table 5.15: *Scaling exponents* ν *obtained for regular dendrimers in a good and* θ*-solvent. The correspondent fractal dimensions* d_f *are displayed as well.*

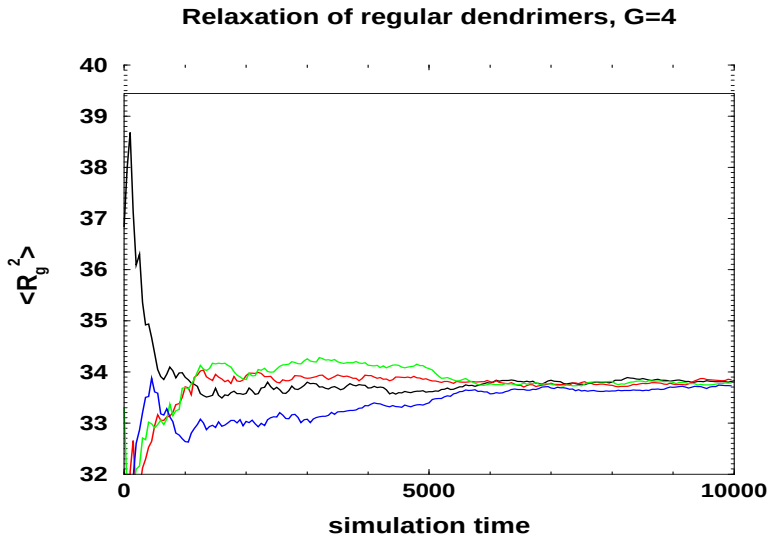

Figure 5.50: *Time evolution of $\langle {R_g}^2 \rangle$ of various dendrimer systems starting from different initial configurations. $G = 4$, $\lambda = 0.0$. Time is displayed in LJ-units.*

In this section we focus on the average radial monomer density, $\rho(r)$, which is calculated by counting the number Z of monomers whose centers of mass are located within a spherical shell of radius r and thickness Δr. We used a typical value of $\Delta r = 0.1\sigma$. Integration over r yields the total number of monomers as:

$$Z(r) = 4\pi \int_0^\infty r'^2 \rho(r')\, dr' \tag{5.24}$$

The rheological and thermodynamic properties of dendrimers in solution depend on the location of the end-groups and the density distribution in the molecule. A very recent experimental study of 7^{th} generation dendrimers [200] concluded that the internal structure of the molecule is rather uniform, with the end groups being preferably located at the periphery of the molecule. This result is in contradiction with a number of simulation studies on the structure of dendrimers [124, 127, 146, 216]. A self-consistent mean-field theory developed by *Boris and Rubinstein* [39] predicts a monotonic decrease of ρ from the center of the molecule.

On the other hand, in [37], a study of dendrimers with deuterated end-groups shows a rather uniform overall density distribution, suggesting that the end groups can significantly penetrate the interior of the molecule.

As the experiments concerning radial density distributions are rather contradictory it must be concluded, that the question of the overall structure of dissolved dendrimers has not yet found a generally accepted answer.

In our simulation study we consider the density $\rho_G(r)$ of generation $G = 1 - 7$ dendrimers. We analyze the overall density of all monomers and the individual contributions of the monomers of each generation. The results of this study are displayed in Figures 5.51 to 5.57.

The influence of solvent quality is displayed as well. The shape of the curves for both solvent conditions look very similar for small generation ($G_{max} \leq 3$) dendrimers. For higher generation

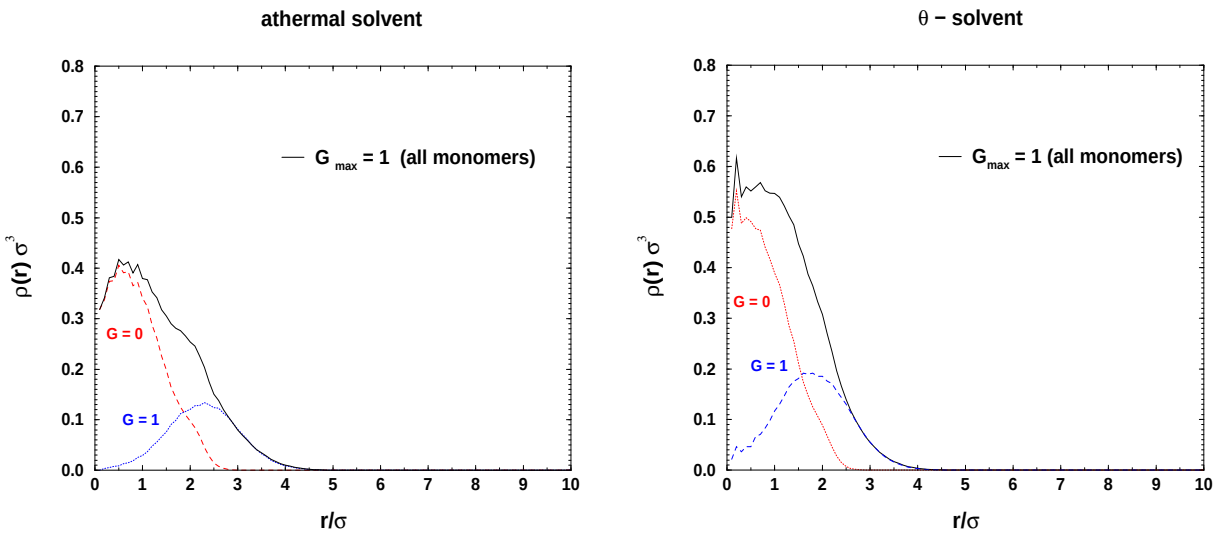

Figure 5.51: *Radial monomer densities of a regular dendrimer. The contributions of the monomers pertaining to consecutive generations are shown.* $G_{max} = 1$.

dendrimers, the athermal chains become more extended in space, with the density ρ of all monomers exhibiting an extended plateau. Interestingly, in the athermal solvent in Fig. 5.58, which displays the contributions of all monomers for the different generations, one can see, that a local minimum in ρ is developing when going from generation $G = 1 - 6$. With generation 7 this local minimum has disappeared. For both solvent qualities, one can see that the end-groups of the different sub-generations of a given dendrimer are almost completely flexible and interpenetrate the whole molecule. In particular, the end-groups of higher sub-generations come very close to the core of the molecule. This effect increases with the total number of generations G_{max} and is stronger in the θ-solvent. Here, for $G = 5$, the end-groups of sub-generation 5 come *closer* to the central core than the end-groups of the first sub-generation. In the athermal solvent, this effect is clearly seen in Figure 5.56 in which the core is excluded by the monomers of the first sub-generation but not by the monomers of the outermost region.

With increasing sub-generation, the density becomes more and more uniform within the whole dendrimer, down to the core region, where even monomers of the innermost sub-generation are excluded.

Finally, in Fig. 5.59, we have displayed the measured bondlengths ${l_b}^2$ of regular dendrimers for various sub-generations G_s. This Figure elucidates, that the segments of inner monomers are more stretched on average than the segments at the periphery of the dendrimers. This effect increases with increasing dendrimer size, respectively with increasing maximum generation G_{max}. The larger a dendrimer, the more stretching of the inner segments. This effect is stronger at the athermal case and decreases with solvent quality. The effect of stretching of inner bonds of a dendrimer might be a possible explanation for the strong back-folding of outer end-groups into the core region of dendrimers.

5.3.5.2 Branching factors

In Figures 5.60 and 5.61 we display the g-factors for regular dendrimers as a function of G and of molecular weight N, respectively. The branching factor g for dendrimers is defined according to

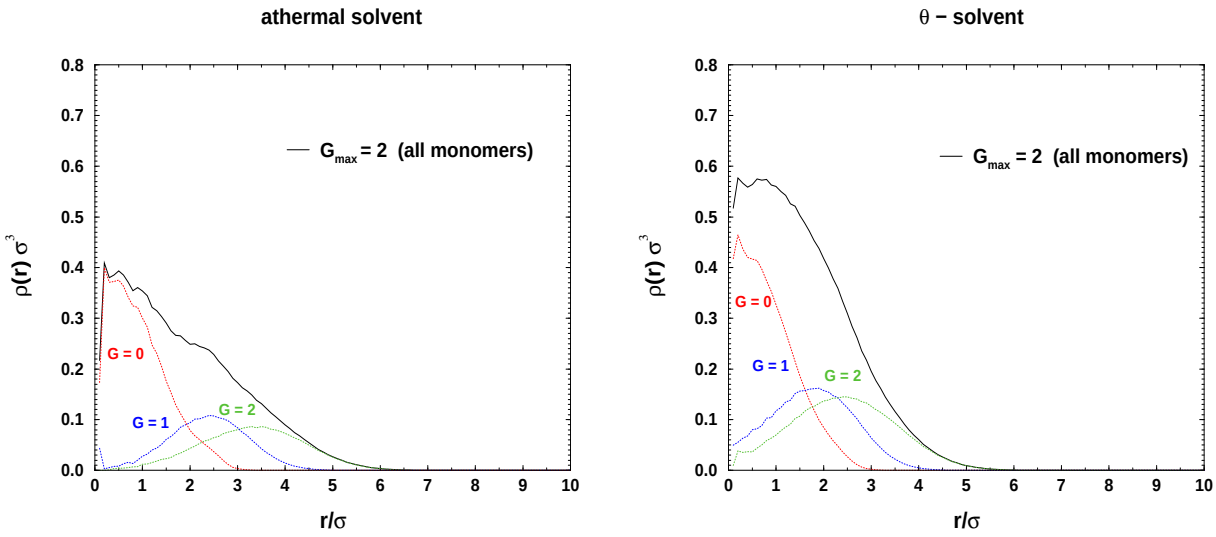

Figure 5.52: *Radial monomer densities of a regular dendrimer. The contributions of the monomers pertaining to consecutive generations are shown.* $G_{max} = 2$.

Eq. 2.13 on Page 11. The most interesting point in the functionality of $g = g(N)$ is the fact, that g is a strongly monotonously decreasing function of N, just like the g-factors of industrial LDPE that were investigated in Section 5.2. In that section, a comparison of the monotonously decreasing LDPE g-values with various branched structures resulted in the conclusion that hyper-branched structures must be prevalent in the experimental systems of Ref. [194]. Figures 5.60 and 5.61 strongly support our conclusions of Section 5.2.

The θ-solvent g-value is larger than the one for the athermal solvent, in accordance with the behavior of g with star-branched polymers. The g-value in the athermal case however, is much smaller than the smallest one obtained with stars in study. The overall structure therefore is very compact. The numerical value of g for the θ-case is of the order of the one obtained for an 18-arm star. This suggests a similar overall structure of many-arm stars and a regular dendrimer under θ-conditions.

Finally, the dimensionless values ϱ were calculated from the simulation data and are displayed in Figures 5.62 and 5.63. No simple scaling form of ϱ can be found anymore. Interestingly, ϱ approaches a maximum with increasing polymer size before leveling off to a long plateau with ϱ-values that indicate a globular structure.

5.3.5.3 Shape analysis of the dendrimers

The asphericities of dendrimers in Figures 5.64 and 5.65 reveal a strongly globular structure of dendrimers, approaching a saturation value very close to zero. The dendrimers are by far the most compact objects of all topologies that were investigated in this study, reaching the lowest values for asphericities.

The corresponding asphericities of a hyper-branched polymer, displayed in Figure 5.66, are not quite as low which leads to the conclusion that regular dendrimer structures are on average slightly less aspherical than hyper-branched ones.

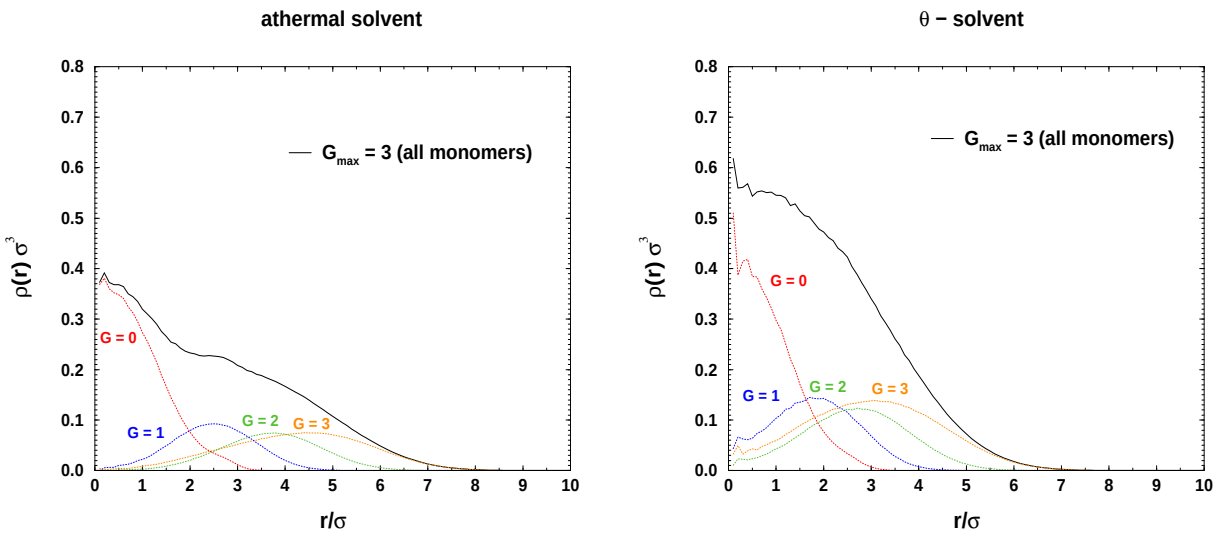

Figure 5.53: *Radial monomer densities of a regular dendrimer. The contributions of the monomers pertaining to consecutive generations are shown.* $G_{max} = 3$.

5.3.5.4 Structure functions

As further illustration of the dendrimer structure, the structure function $S(k)$ is displayed in Figures 5.67 to 5.72. $S(k)$ vs. scattering vector k is shown, as well as the more sensitive Kratky-Plot for both simulated solvent qualities. Finally, in Figures 5.71 and 5.72 we have plotted the rescaled Kratky representations of the data in order to compare systems of different sizes. In Figure 5.72 the scattering factor of a solid sphere is displayed as well. It can readily be seen that the dendrimers approach a sphere-like structure with increasing generation.

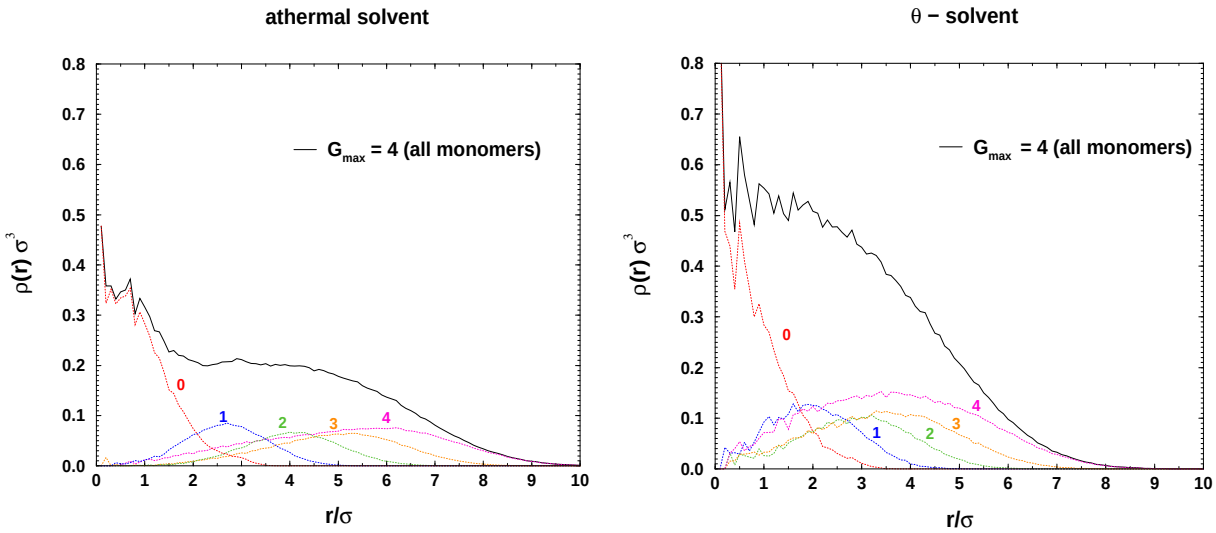

Figure 5.54: *Radial monomer densities of a regular dendrimer. The contributions of the monomers pertaining to consecutive generations are shown.* $G_{max} = 4$.

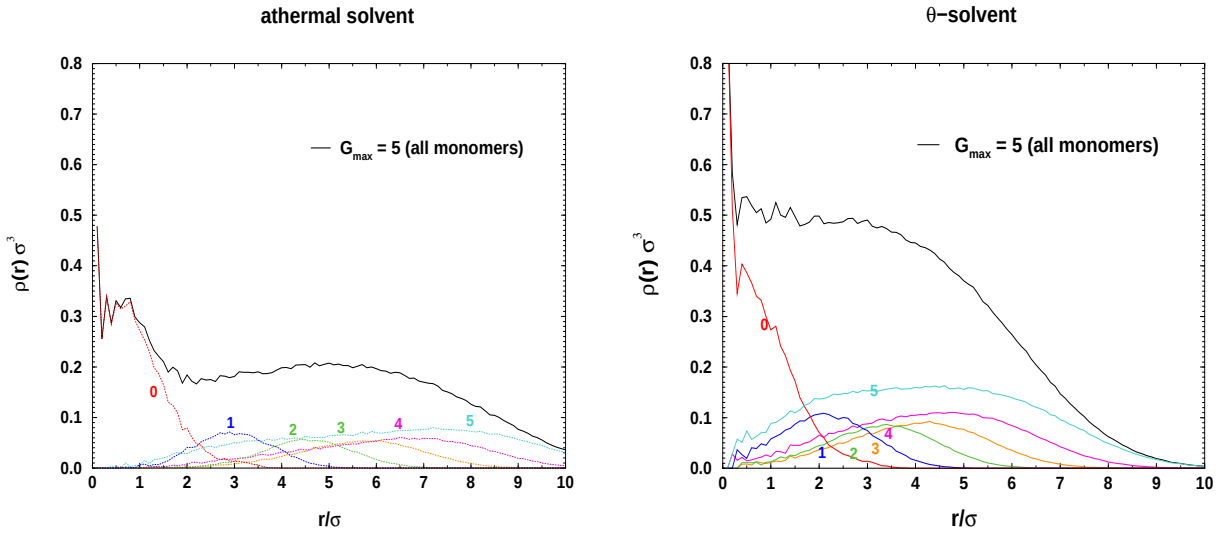

Figure 5.55: *Radial monomer densities of a regular dendrimer. The contributions of the monomers pertaining to consecutive generations are shown.* $G_{max} = 5$.

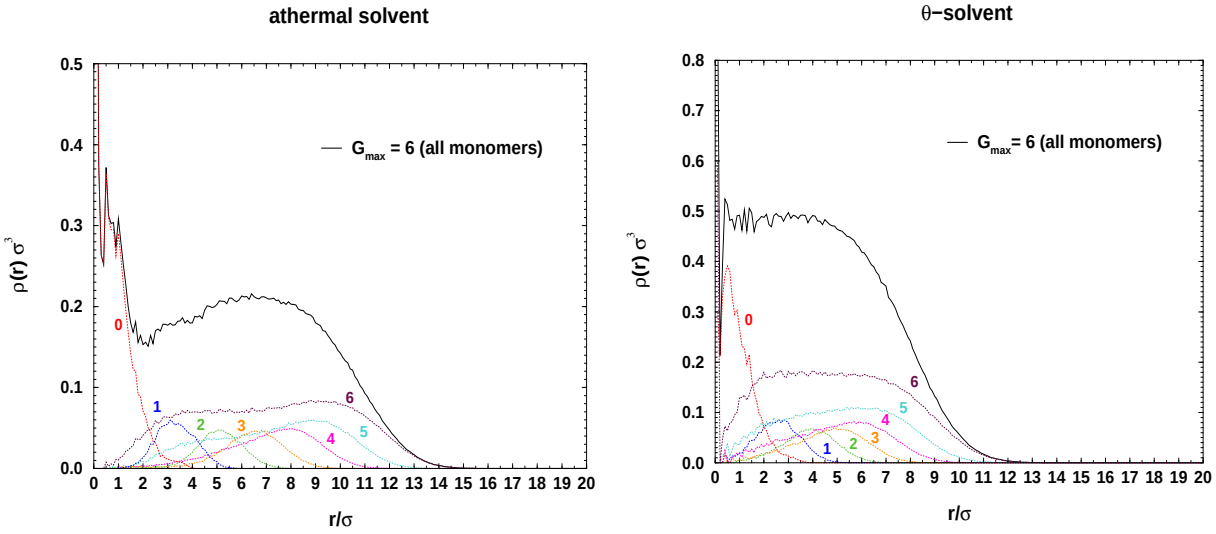

Figure 5.56: *Radial monomer densities of a regular dendrimer. The contributions of the monomers pertaining to consecutive generations are shown.* $G_{max} = 6$.

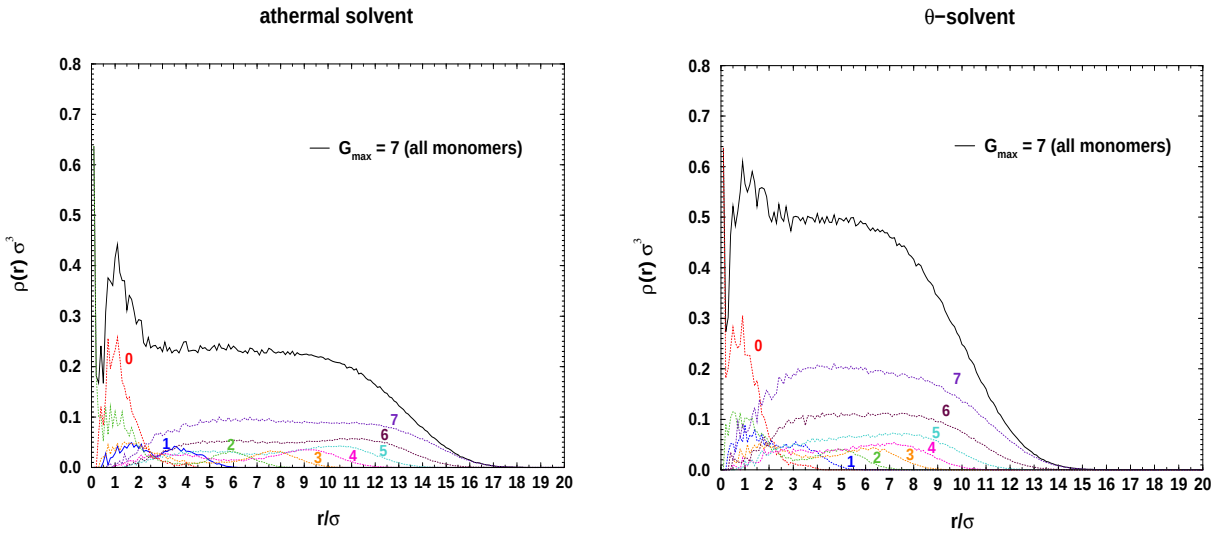

Figure 5.57: *Radial monomer densities of a regular dendrimer. The contributions of the monomers pertaining to consecutive generations are shown.* $G_{max} = 7$.

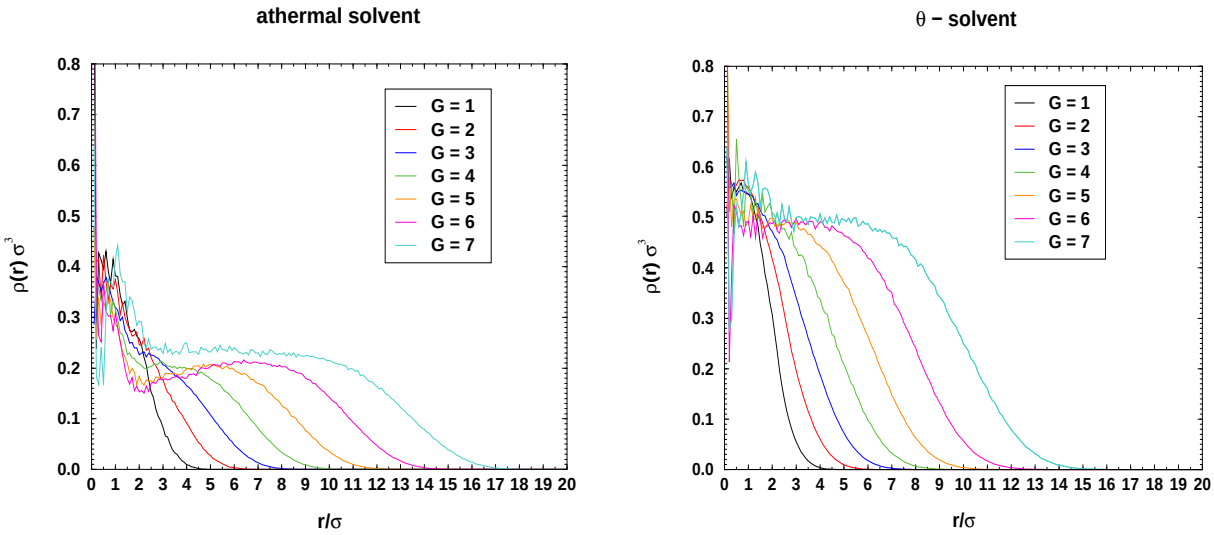

Figure 5.58: *Total radial monomer densities of a regular dendrimer vs. generation number G.*

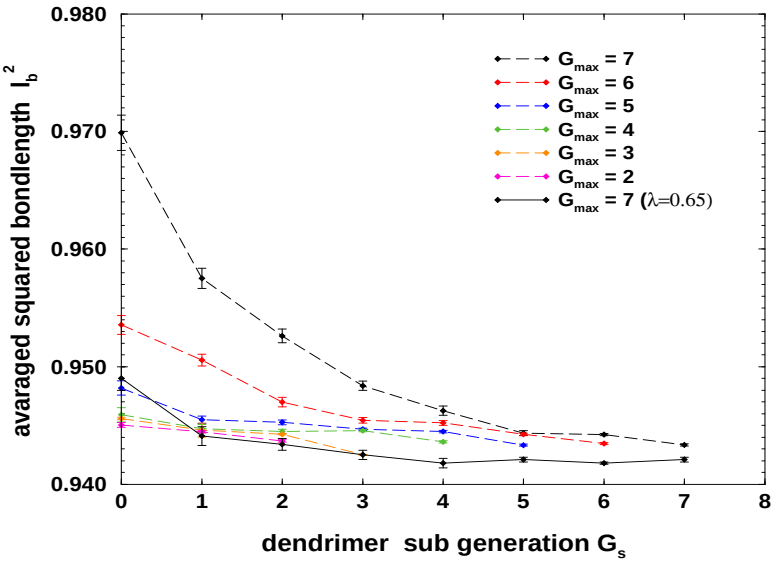

Figure 5.59: *Averaged squared bondlength l_b^2 of regular dendrimers for generations 2 to 7 with ($\lambda = 0.0$). The bondlengths between the monomers pertaining to the different sub generations are displayed as well (dashed lines). For comparison, l_b^2 of a dendrimer in a θ-solvent ($\lambda = 0.65$) is displayed (solid line).*

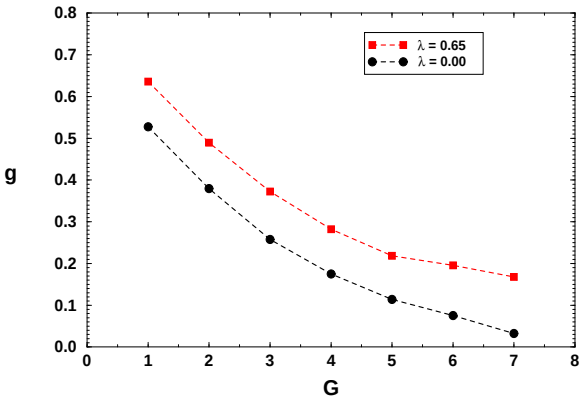

Figure 5.60: *g-factor of a regular dendrimer in good and θ-solvent conditions as a function of generation G.*

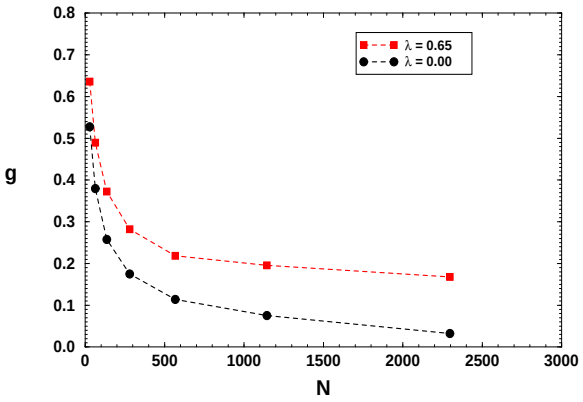

Figure 5.61: *g-factor of a regular dendrimer in good and θ-solvent conditions as a function of polydispersity N.*

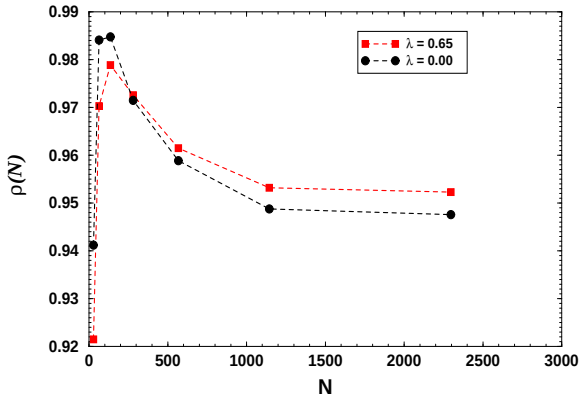

Figure 5.62: *Dimensionless ratio ϱ for regular dendrimers at θ- and good solvent conditions as a function of N.*

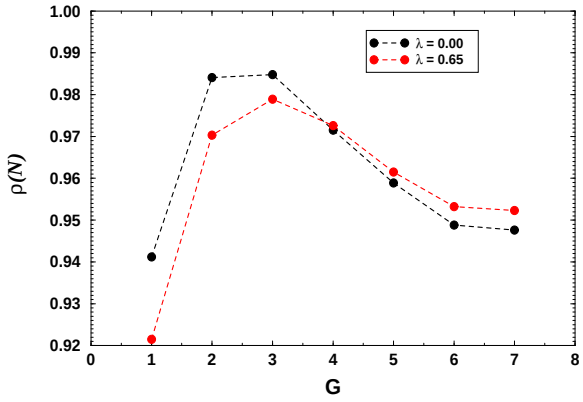

Figure 5.63: *Dimensionless ratio ϱ for regular dendrimers at θ- and good solvent conditions as a function of G .*

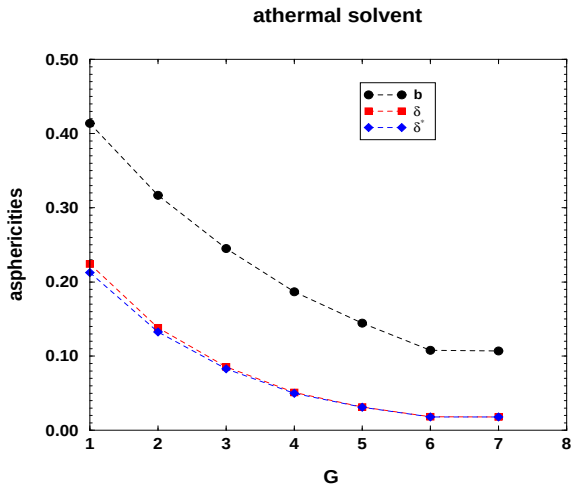

Figure 5.64: *Different asphericities of regular dendrimers with $m = 3$ and $x = 3$ for a number of generations G. λ = 0.0 (athermal solvent conditions).*

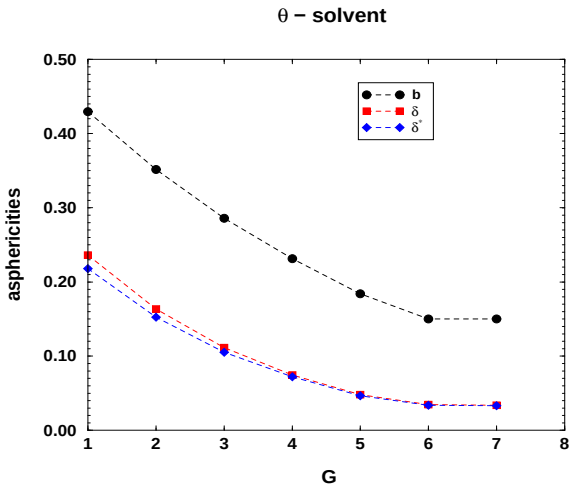

Figure 5.65: *Different asphericities of regular dendrimers with $m = 3$ and $x = 3$ for a number of generations G. $\lambda = 0.65$ (θ-conditions).*

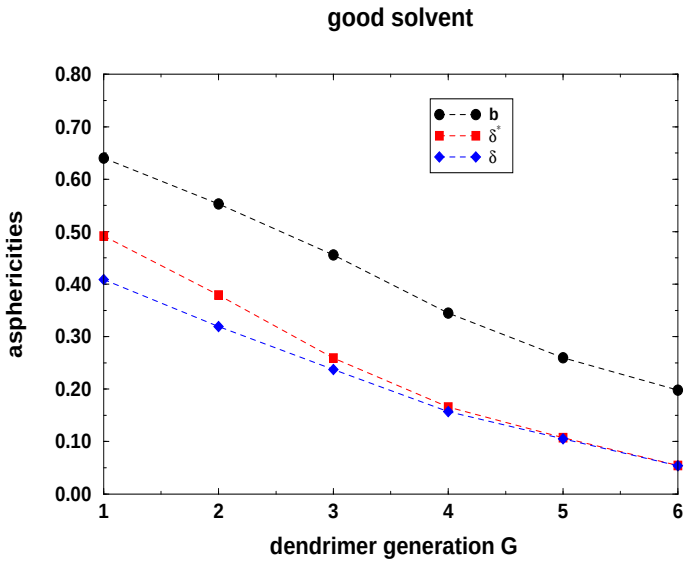

Figure 5.66: *Shape asphericities for Fréchet dendrimers vs. generation number G under athermal conditions. The spacer length was chosen as $m = 10$*

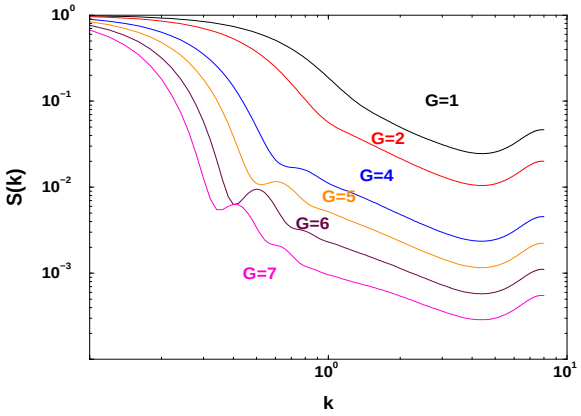

Figure 5.67: *Structure function S(k) for regular dendrimers of different generations G. $\lambda = 0.0$.*

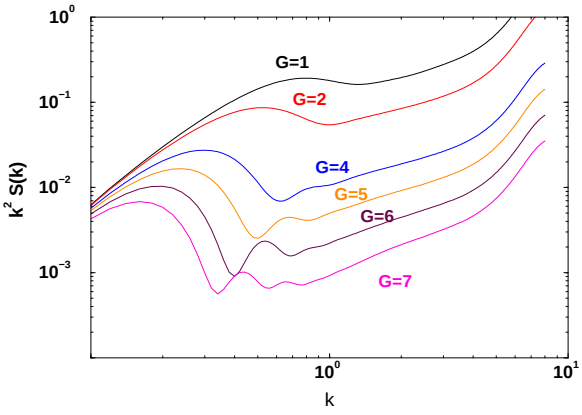

Figure 5.68: *Kratky-plot of regular dendrimers of different generations G. $\lambda = 0.0$.*

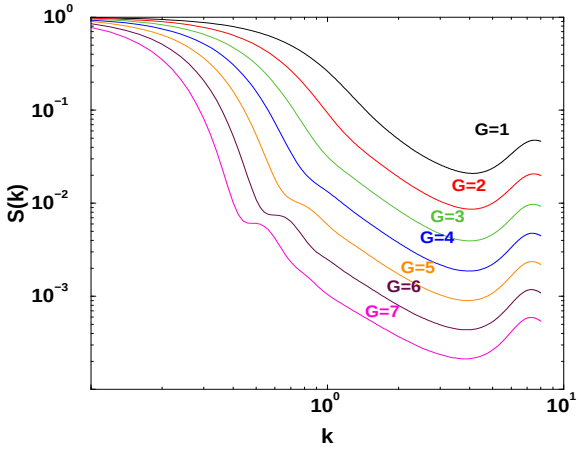

Figure 5.69: *Structure function S(k) for regular dendrimers of different generations G. $\lambda = 0.65$.*

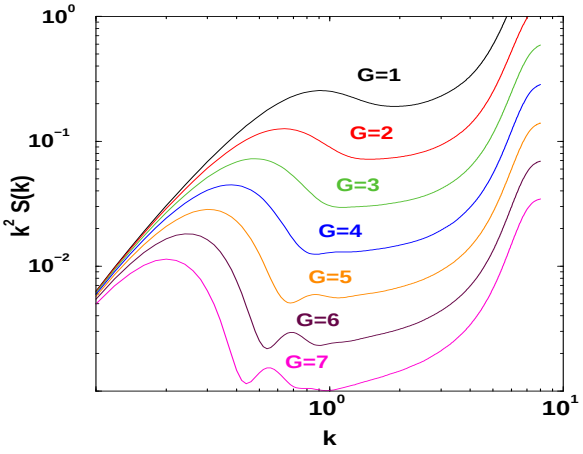

Figure 5.70: *Kratky-plot of regular dendrimers of different generations G. $\lambda = 0.65$.*

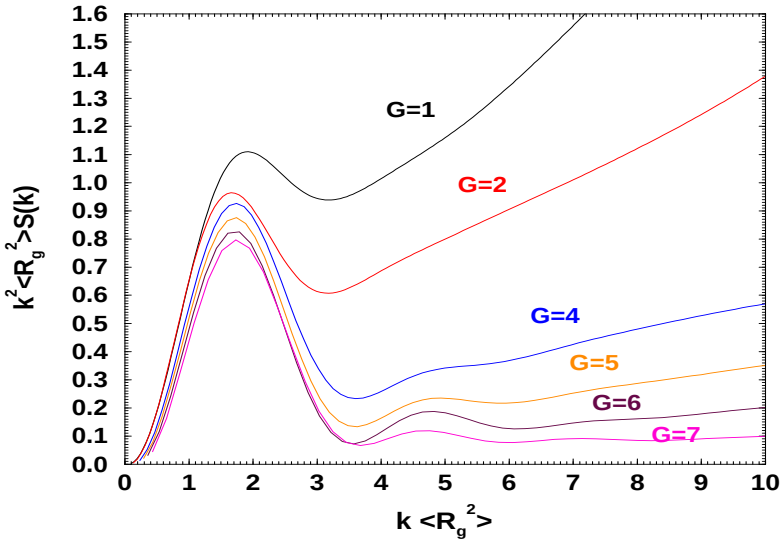

Figure 5.71: *Kratky representation of various regular dendrimers of the indicated G value. $\lambda = 0.0$.*

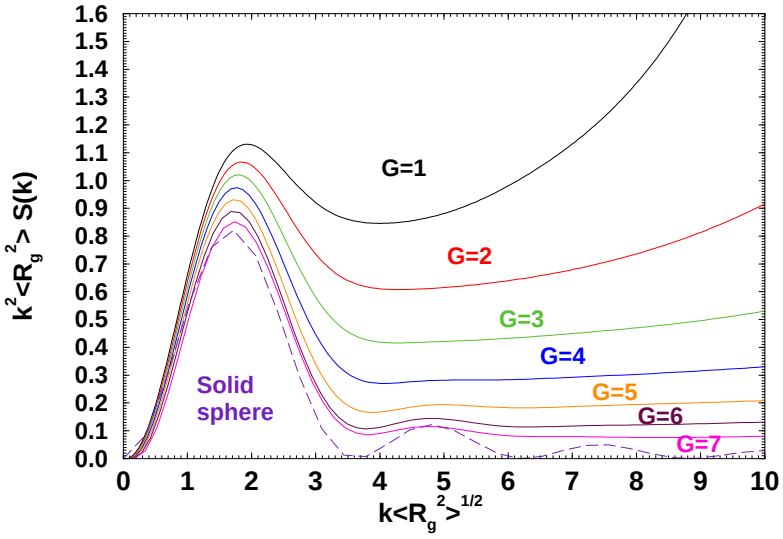

Figure 5.72: *Single particle scattering factors in Kratky representation for various regular dendrimers of the indicated G value. The dashed curve gives the scattering factor of a solid sphere. $\lambda = 0.65$.*

Summary

In conclusion, we can state the following points:

- Dendrimers are the most spherical objects of all topologies that were investigated in this study.
- The branching factor g for θ-chains is larger than the one in good solvent conditions. This behavior was also observed with the stars.
- Not all the end-groups of dendrimers lie near the exterior of the molecule. In contrast to this, they are almost completely dispersed throughout the molecule and can even be found in close proximity to the core.
- There is a range of generation numbers for which some hollowness in the molecule is present. This is indicated by a relative minimum of the density distribution.
- The segments of monomers pertaining to the inner generations are more expanded than the ones at the periphery of the molecule. This effect increases with solvent quality and with the total number of generations in the molecule. This stretching of monomer bonds can be understood as a consequence of molecular crowding in the core region.
- The structure functions of dendrimers exhibit a structure that approaches the one of a solid sphere with increasing generation number.

Appendix A

Data of linear single chains

The following tables list the measured static properties of the linear single chains. These data were used for the determination of the θ-point of the linear chains as well as for comparisons with branched chain systems. The data were achieved by simulating at least 20 chains in parallel, with the inter-chain interaction being switched off. For the smaller systems, at least 200.000 statistically independent snapshots were averaged, for systems larger than $N = 1000$ at least 5.000 independent samples were averaged. The errors of the smaller systems are well below 1%.

λ	$\langle {R_e}^2 \rangle$	$\langle {R_g}^2 \rangle$	$\langle {R_h}^{-1} \rangle$	$\frac{\langle {R_e}^2 \rangle}{\langle {R_g}^2 \rangle}$	$\frac{\langle {R_e}^4 \rangle}{\langle {R_e}^2 \rangle^2}$	$\frac{\langle {R_g}^4 \rangle}{\langle {R_g}^2 \rangle^2}$	$\frac{\langle {R_g}^2 \rangle^{1/2}}{\langle {R_h}^{-1} \rangle^{-1}}$
0.00	151.5 ± 0.7	23.23 ± 0.16	0.254 ± 0.007	6.52	1.41	1.13	1.225
0.20	138.0 ± 0.4	21.29 ± 0.03	0.262 ± 0.006	6.48	1.42	1.14	1.211
0.40	118.7 ± 0.3	18.68 ± 0.03	0.276 ± 0.005	6.35	1.45	1.15	1.193
0.60	91.4 ± 0.2	14.90 ± 0.03	0.300 ± 0.005	6.13	1.52	1.17	1.156
0.61	89.4 ± 0.2	14.65 ± 0.02	0.302 ± 0.004	6.10	1.55	1.17	1.152
0.62	87.7 ± 0.3	14.39 ± 0.03	0.304 ± 0.001	6.09	1.56	1.17	1.151
0.64	83.9 ± 0.3	13.89 ± 0.02	0.307 ± 0.002	6.04	1.60	1.18	1.145
0.65	82.2 ± 0.2	13.64 ± 0.02	0.309 ± 0.002	6.03	1.62	1.18	1.141
0.66	79.9 ± 0.3	13.30 ± 0.02	0.309 ± 0.001	6.01	1.55	1.18	1.139
0.68	76.0 ± 0.2	12.80 ± 0.02	0.316 ± 0.003	5.98	1.57	1.18	1.129
0.70	71.5 ± 0.3	12.24 ± 0.02	0.321 ± 0.004	5.88	1.62	1.18	1.121
0.80	53.1 ± 0.3	9.45 ± 0.01	0.345 ± 0.003	5.61	1.70	1.17	1.061
0.90	29.4 ± 0.4	7.07 ± 0.01	0.377 ± 0.002	4.16	1.76	1.14	1.001
1.00	23.0 ± 0.4	5.57 ± 0.01	0.402 ± 0.003	4.13	1.78	1.09	0.949

Table A.1: *Data of static properties of simulated linear chains.* $N = 50$ *with different values of the potential depth* λ*. Ensembles of at least* 100 *chains were simulated in parallel and averages were taken from at least* 300.000 *statistically independent configurations.*

λ	$\langle {R_e}^2 \rangle$	$\langle {R_g}^2 \rangle$	$\langle {R_h}^{-1} \rangle$	$\frac{\langle {R_e}^2 \rangle}{\langle {R_g}^2 \rangle}$	$\frac{\langle {R_e}^4 \rangle}{\langle {R_e}^2 \rangle^2}$	$\frac{\langle {R_g}^4 \rangle}{\langle {R_g}^2 \rangle^2}$	$\frac{\langle {R_g}^2 \rangle^{1/2}}{\langle {R_h}^{-1} \rangle^{-1}}$
0.00	354.7 ± 0.7	55.8 ± 0.6	0.178 ± 0.007	6.44	1.46	1.15	1.326
0.20	320.3 ± 0.6	50.1 ± 0.6	0.184 ± 0.005	6.39	1.45	1.16	1.307
0.40	273.3 ± 0.5	43.2 ± 0.5	0.196 ± 0.005	6.32	1.49	1.17	1.290
0.60	194.5 ± 0.5	32.0 ± 0.4	0.220 ± 0.005	6.08	1.58	1.19	1.244
0.61	189.7 ± 0.5	31.2 ± 0.4	0.222 ± 0.005	6.05	1.58	1.19	1.241
0.62	185.3 ± 0.5	30.6 ± 0.4	0.224 ± 0.005	6.02	1.60	1.19	1.237
0.64	175.4 ± 0.4	29.2 ± 0.4	0.227 ± 0.005	6.01	1.58	1.20	1.228
0.65	167.7 ± 0.5	28.2 ± 0.4	0.227 ± 0.005	5.95	1.58	1.22	1.221
0.66	163.4 ± 0.5	27.5 ± 0.3	0.233 ± 0.005	5.94	1.60	1.23	1.219
0.68	139.8 ± 0.5	25.2 ± 0.3	0.238 ± 0.005	5.75	1.68	1.22	1.194
0.70	137.8 ± 1.3	23.9 ± 0.3	0.243 ± 0.006	5.77	1.77	1.22	1.177
0.80	76.7 ± 0.2	15.47 ± 0.2	0.281 ± 0.008	4.95	1.75	1.19	1.097
0.90	46.2 ± 0.2	9.8 ± 0.2	0.316 ± 0.005	4.71	1.76	1.11	0.990
1.00	28.1 ± 0.3	8.1 ± 0.2	0.335 ± 0.005	3.46	1.70	1.06	0.954

Table A.2: *Data of static properties of simulated linear chains.* $N = 100$ *with different values of the potential depth* λ*. Ensembles of at least* 100 *chains were simulated in parallel and averages were taken from at least* 300.000 *statistically independent configurations.*

λ	$\langle {R_e}^2 \rangle$	$\langle {R_g}^2 \rangle$	$\langle {R_h}^{-1} \rangle$	$\frac{\langle {R_e}^2 \rangle}{\langle {R_g}^2 \rangle}$	$\frac{\langle {R_e}^4 \rangle}{\langle {R_e}^2 \rangle^2}$	$\frac{\langle {R_g}^4 \rangle}{\langle {R_g}^2 \rangle^2}$	$\frac{\langle {R_g}^2 \rangle^{1/2}}{\langle {R_h}^{-1} \rangle^{-1}}$
0.00	806 ± 9	127.9 ± 0.6	0.123 ± 0.005	6.35	1.46	1.16	1.396
0.20	728 ± 12	115.2 ± 0.4	0.128 ± 0.006	6.32	1.45	1.16	1.375
0.40	615 ± 6	98.2 ± 0.3	0.137 ± 0.004	6.26	1.49	1.17	1.360
0.60	411 ± 6	67.6 ± 0.2	0.159 ± 0.005	6.08	1.58	1.21	1.311
0.61	398 ± 4	65.9 ± 0.2	0.161 ± 0.005	6.04	1.58	1.21	1.307
0.62	383 ± 5	63.6 ± 0.2	0.163 ± 0.004	6.02	1.60	1.21	1.300
0.64	353 ± 2	59.1 ± 0.3	0.167 ± 0.005	5.97	1.58	1.22	1.287
0.65	337 ± 2	56.6 ± 0.3	0.170 ± 0.005	5.95	1.58	1.22	1.280
0.66	318 ± 2	53.7 ± 0.2	0.174 ± 0.004	5.92	1.60	1.24	1.277
0.67	298 ± 1	50.9 ± 0.1	0.177 ± 0.005	5.85	1.63	1.25	1.263
0.68	277 ± 1	46.8 ± 0.1	0.181 ± 0.004	5.76	1.58	1.24	1.236
0.69	254 ± 1	44.7 ± 0.1	0.185 ± 0.005	5.68	1.58	1.21	1.236
0.70	227 ± 1	41.2 ± 0.1	0.190 ± 0.004	5.51	1.67	1.20	1.218
0.80	89.1 ± 1.1	22.3 ± 0.8	0.236 ± 0.005	4.31	1.85	1.14	1.116
0.90	68.5 ± 1.0	16.4 ± 0.1	0.266 ± 0.006	4.18	1.86	1.02	1.045
1.00	37.1 ± 0.9	11.62 ± 0.05	0.279 ± 0.005	3.19	1.75	1.01	0.950

Table A.3: *Data of static properties of simulated linear chains.* $N = 200$ *with different values for the potential depth* λ*. Ensembles of at least* 100 *chains were simulated in parallel and 300.00 independent snapshots were taken.*

$N = 241$	$\langle {R_e}^2 \rangle$	$\langle {R_g}^2 \rangle$	$\langle {R_h}^{-1} \rangle$	$\frac{\langle {R_e}^2 \rangle}{\langle {R_g}^2 \rangle}$	ϱ
$\lambda = 0.0$	1030 ± 11	162 ± 2	0.110 ± 0.002	6.33	1.405
$\lambda = 0.65$	393 ± 7	64.5 ± 0.6	0.160 ± 0.001	6.03	1.283

Table A.4: *Data of linear chains with the same molecular weights as the simulated stars. C.f. Table B.19.*

$N = 301$	$\langle {R_e}^2 \rangle$	$\langle {R_g}^2 \rangle$	$\langle {R_h}^{-1} \rangle$	$\frac{\langle {R_e}^2 \rangle}{\langle {R_g}^2 \rangle}$	ϱ
$\lambda = 0.0$	1331 ± 15	211 ± 1	0.099 ± 0.001	6.30	1.439
$\lambda = 0.65$	520 ± 19	86.1 ± 0.7	0.141 ± 0.003	6.04	1.311

Table A.5: *Data of linear chains with the same molecular weights as the simulated stars. C.f. Table B.1.*

λ	$\langle {R_e}^2 \rangle$	$\langle {R_g}^2 \rangle$	$\langle {R_h}^{-1} \rangle$	$\frac{\langle {R_e}^2 \rangle}{\langle {R_g}^2 \rangle}$	$\frac{\langle {R_e}^4 \rangle}{\langle {R_e}^2 \rangle^2}$	$\frac{\langle {R_g}^4 \rangle}{\langle {R_g}^2 \rangle^2}$	$\frac{\langle {R_g}^2 \rangle^{1/2}}{\langle {R_h}^{-1} \rangle^{-1}}$
0.00	1885 ± 30	303 ± 3	0.085 ± 0.003	6.22	1.64	1.16	1.479
0.20	1607 ± 22	259 ± 4	0.088 ± 0.002	6.20	1.50	1.17	1.419
0.40	1368 ± 26	221 ± 3	0.095 ± 0.002	6.19	1.49	1.17	1.410
0.60	866 ± 14	143 ± 1	0.114 ± 0.002	6.06	1.79	1.21	1.359
0.61	833 ± 16	137 ± 1	0.116 ± 0.002	6.08	1.79	1.22	1.345
0.62	800 ± 18	132 ± 1	0.117 ± 0.002	6.06	1.78	1.26	1.347
0.64	710 ± 16	118 ± 1	0.123 ± 0.002	6.02	1.75	1.24	1.334
0.65	674 ± 18	112 ± 1	0.126 ± 0.001	6.02	1.71	1.22	1.329
0.66	580 ± 14	99 ± 1	0.131 ± 0.002	5.83	1.70	1.24	1.306
0.68	422 ± 10	78.3 ± 0.6	0.143 ± 0.002	5.66	1.68	1.23	1.266
0.70	287 ± 4	59.4 ± 0.4	0.147 ± 0.002	5.43	1.43	1.17	1.232
0.80	197 ± 4	39.3 ± 0.2	0.181 ± 0.002	5.01	1.32	1.16	1.134
0.90	101 ± 2	22.3 ± 0.2	0.199 ± 0.002	4.53	0.94	1.01	0.941
1.00	82 ± 1	18.3 ± 0.2	0.208 ± 0.002	4.48	0.94	1.00	0.974

Table A.6: *Data of static properties of simulated linear chains. $N = 400$ with different values for the potential depth λ. Ensembles of at least 100 chains were simulated in parallel and at least 200.000 independent snapshots were taken.*

$N = 481$	$\langle {R_e}^2 \rangle$	$\langle {R_g}^2 \rangle$	$\langle {R_h}^{-1} \rangle$	$\frac{\langle {R_e}^2 \rangle}{\langle {R_g}^2 \rangle}$	ϱ
$\lambda = 0.0$	2415 ± 44	379 ± 5	0.076 ± 0.001	6.23	1.483
$\lambda = 0.65$	805 ± 16	132 ± 1	0.117 ± 0.001	6.02	1.330

Table A.7: *Data of linear chains with the same molecular weights as the simulated stars. C.f. Table B.20.*

$N = 601$	$\langle {R_e}^2 \rangle$	$\langle {R_g}^2 \rangle$	$\langle {R_h}^{-1} \rangle$	$\frac{\langle {R_e}^2 \rangle}{\langle {R_g}^2 \rangle}$	ϱ
$\lambda = 0.0$	3034 ± 46	487 ± 6	0.0677 ± 0.0008	6.21	1.493
$\lambda = 0.65$	921 ± 17	154 ± 1	0.107 ± 0.001	5.98	1.332

Table A.8: *Data of linear chains with the same molecular weights as the simulated stars. C.f. Table B.2.*

$N = 721$	$\langle {R_e}^2 \rangle$	$\langle {R_g}^2 \rangle$	$\langle {R_h}^{-1} \rangle$	$\frac{\langle {R_e}^2 \rangle}{\langle {R_g}^2 \rangle}$	ϱ
$\lambda = 0.0$	3794 ± 74	611 ± 9	0.061 ± 0.002	6.21	1.498
$\lambda = 0.65$	1024 ± 17	176 ± 1	0.101 ± 0.001	5.94	1.344

Table A.9: *Data of linear chains with the same molecular weights as the simulated stars. C.f. Table B.21.*

λ	$\langle {R_e}^2 \rangle$	$\langle {R_g}^2 \rangle$	$\langle {R_h}^{-1} \rangle$	$\frac{\langle {R_e}^2 \rangle}{\langle {R_g}^2 \rangle}$	$\frac{\langle {R_e}^4 \rangle}{\langle {R_e}^2 \rangle^2}$	$\frac{\langle {R_g}^4 \rangle}{\langle {R_g}^2 \rangle^2}$	$\frac{\langle {R_g}^2 \rangle^{1/2}}{\langle {R_h}^{-1} \rangle^{-1}}$
0.00	4212 ± 64	680 ± 12	0.058 ± 0.009	6.19	1.48	1.16	1.502
0.20	3816 ± 53	621 ± 11	0.059 ± 0.009	6.14	1.49	1.17	1.479
0.40	3169 ± 55	515 ± 8	0.065 ± 0.008	6.15	1.51	1.18	1.460
0.60	1897 ± 49	312 ± 6	0.080 ± 0.007	6.10	1.62	1.21	1.407
0.61	1797 ± 44	296 ± 5	0.082 ± 0.006	6.07	1.60	1.23	1.403
0.62	1687 ± 33	280 ± 5	0.084 ± 0.005	6.03	1.60	1.23	1.401
0.64	1420 ± 19	233 ± 3	0.089 ± 0.006	6.09	1.67	1.26	1.368
0.65	1353 ± 17	224 ± 3	0.093 ± 0.002	5.99	1.62	1.25	1.358
0.66	1052 ± 16	175 ± 2	0.102 ± 0.003	6.01	1.55	1.25	1.326
0.68	615 ± 13	134 ± 2	0.111 ± 0.001	5.40	1.48	1.24	1.288
0.70	434 ± 10	92 ± 1	0.130 ± 0.001	3.27	1.40	1.10	1.248
0.80	161 ± 6	47 ± 1	0.164 ± 0.001	4.21	1.30	1.16	1.121
0.90	120 ± 2	32 ± 0.4	0.171 ± 0.001	3.75	1.86	1.00	0.964
1.00	68.0 ± 2	26.3 ± 0.1	0.184 ± 0.001	2.59	1.75	1.01	0.947

Table A.10: *Data of static properties of simulated linear chains. $N = 800$ with different values for the potential depth λ. Ensembles of at least 200 chains were simulated in parallel and at least 40.000 independent snapshots were taken.*

$N = 901$	$\langle {R_e}^2 \rangle$	$\langle {R_g}^2 \rangle$	$\langle {R_h}^{-1} \rangle$	$\frac{\langle {R_e}^2 \rangle}{\langle {R_g}^2 \rangle}$	ϱ
$\lambda = 0.0$	4924 ± 112	793 ± 9	0.0539 ± 0.0008	6.11	1.518
$\lambda = 0.65$	1386 ± 23	230 ± 5	0.090 ± 0.001	6.02	1.360

Table A.11: *Data of linear chains with the same molecular weights as the simulated stars. C.f. Table B.3.*

λ	$\langle {R_e}^2 \rangle$	$\langle {R_g}^2 \rangle$	$\langle {R_h}^{-1} \rangle$	$\frac{\langle {R_e}^2 \rangle}{\langle {R_g}^2 \rangle}$	$\frac{\langle {R_e}^4 \rangle}{\langle {R_e}^2 \rangle^2}$	$\frac{\langle {R_g}^4 \rangle}{\langle {R_g}^2 \rangle^2}$	$\frac{\langle {R_g}^2 \rangle^{1/2}}{\langle {R_h}^{-1} \rangle^{-1}}$
0.00	5512 ± 67	892 ± 19	0.051 ± 0.009	6.18	1.46	1.19	1.523
0.20	4765 ± 75	797 ± 21	0.053 ± 0.009	6.11	1.45	1.19	1.492
0.40	4228 ± 68	699 ± 14	0.057 ± 0.008	6.05	1.49	1.20	1.474
0.60	2636 ± 65	433 ± 13	0.068 ± 0.008	6.09	1.58	1.21	1.415
0.61	2402 ± 45	395 ± 12	0.073 ± 0.008	6.08	1.58	1.24	1.468
0.62	2250 ± 40	358 ± 8	0.074 ± 0.007	6.02	1.60	1.25	1.396
0.64	1720 ± 36	286 ± 7	0.081 ± 0.005	6.01	1.58	1.22	1.374
0.65	1415 ± 29	236 ± 5	0.083 ± 0.005	5.99	1.58	1.22	1.362
0.66	857 ± 28	166 ± 4	0.093 ± 0.004	5.16	1.60	1.24	1.334
0.68	756 ± 14	153 ± 2	0.105 ± 0.004	4.94	1.58	1.24	1.294
0.70	365 ± 11	93 ± 2	0.130 ± 0.002	3.92	1.37	1.22	1.255
0.80	182 ± 4	50.3 ± 0.2	0.160 ± 0.002	3.32	1.35	1.10	1.133
0.90	115 ± 5	35 ± 1	0.130 ± 0.002	3.28	1.31	1.24	1.017
1.00	105 ± 2	33 ± 1	0.168 ± 0.001	3.18	1.15	1.00	0.97

Table A.12: *Data of static properties of simulated linear chains.* $N = 1000$ *with different values for the potential depth* λ*. Ensembles of at least* 200 *chains were simulated in parallel and at least 20.000 independent snapshots were taken.*

$N = 1241$	$\langle {R_e}^2 \rangle$	$\langle {R_g}^2 \rangle$	$\langle {R_h}^{-1} \rangle$	$\frac{\langle {R_e}^2 \rangle}{\langle {R_g}^2 \rangle}$	ϱ
$\lambda = 0.0$	6897 ± 156	1129 ± 25	0.046 ± 0.008	6.10	1.528
$\lambda = 0.65$	2275 ± 113	378 ± 10	0.071 ± 0.009	6.02	1.371

Table A.13: *Data of linear chains with the same molecular weights as the simulated stars. C.f. Table B.22.*

λ	$\langle {R_e}^2 \rangle$	$\langle {R_g}^2 \rangle$	$\langle {R_h}^{-1} \rangle$	$\frac{\langle {R_e}^2 \rangle}{\langle {R_g}^2 \rangle}$	$\frac{\langle {R_e}^4 \rangle}{\langle {R_e}^2 \rangle^2}$	$\frac{\langle {R_g}^4 \rangle}{\langle {R_g}^2 \rangle^2}$	$\frac{\langle {R_g}^2 \rangle^{1/2}}{\langle {R_h}^{-1} \rangle^{-1}}$
0.0	12321 ± 545	2010 ± 115	0.034 ± 0.006	6.13	1.50	1.17	1.542
0.20	11150 ± 411	1857 ± 93	0.035 ± 0.005	6.09	1.51	1.18	1.520
0.40	9437 ± 344	1581 ± 42	0.038 ± 0.005	6.05	1.50	1.18	1.499
0.60	5326 ± 210	882 ± 15	0.049 ± 0.005	6.04	1.76	1.22	1.440
0.62	4081 ± 167	676 ± 15	0.055 ± 0.007	6.04	1.56	1.23	1.421
0.64	3536 ± 226	587 ± 35	0.058 ± 0.005	6.03	1.76	1.24	1.399
0.65	3331 ± 116	557 ± 15	0.062 ± 0.005	5.99	1.76	1.26	1.389
0.66	1386 ± 97	366 ± 17	0.070 ± 0.005	3.79	1.76	1.24	1.343
0.68	972 ± 41	302 ± 7	0.075 ± 0.004	3.23	1.76	1.16	1.301
0.70	578 ± 32	186 ± 9	0.092 ± 0.003	3.10	1.76	1.08	1.259
0.80	165 ± 7	75.5 ± 4	0.131 ± 0.007	2.19	1.42	1.02	1.144
0.90	130 ± 5	58.3 ± 4	0.133 ± 0.006	2.23	1.40	1.02	1.017
1.0	105 ± 4	50.7 ± 0.7	0.136 ± 0.003	2.07	1.37	1.01	0.971

Table A.14: *Data of static properties of simulated linear chains.* $N = 2000$ *with different values for the potential depth* λ*. Ensembles of at least* 200 *chains were simulated in parallel and at least 5.000 independent snapshots were taken.*

λ	$\langle {R_e}^2 \rangle$	$\langle {R_g}^2 \rangle$	$\langle {R_h}^{-1} \rangle$	$\frac{\langle {R_e}^2 \rangle}{\langle {R_g}^2 \rangle}$	$\frac{\langle {R_e}^4 \rangle}{\langle {R_e}^2 \rangle^2}$	$\frac{\langle {R_g}^4 \rangle}{\langle {R_g}^2 \rangle^2}$	$\frac{\langle {R_g}^2 \rangle^{1/2}}{\langle {R_h}^{-1} \rangle^{-1}}$
0.0	35335 ± 890	5798 ± 115	0.021 ± 0.002	6.09	1.58	1.19	1.561
0.65	8195 ± 127	1364 ± 30	0.038 ± 0.003	6.01	1.34	1.10	1.410

Table A.15: *Data of static properties of simulated linear chains.* $N = 5000$ *with different values for the potential depth* λ.

N	$\langle {R_e}^2 \rangle$	$\langle {R_g}^2 \rangle$	$\langle {R_h}^{-1} \rangle$	$\frac{\langle {R_e}^2 \rangle}{\langle {R_g}^2 \rangle}$	ϱ	W_{linear}
28	69.9 ± 0.9	10.6 ± 0.2	0.342 ± 0.002	6.61	1.11	3276
64	206 ± 7	31.5 ± 0.2	0.225 ± 0.003	6.54	1.263	41664
136	521 ± 17	81 ± 1	0.151 ± 0.002	6.43	1.357	410040
280	1168 ± 46	194 ± 4	0.102 ± 0.003	6.27	1.419	3619560
568	2914 ± 70	461 ± 4	0.068 ± 0.001	6.32	1.466	30380616
1144	6561 ± 280	1056 ± 4	0.047 ± 0.001	6.18	1.527	248878344
2296	15234 ± 489	2458 ± 41	0.031 ± 0.001	6.17	1.547	2014636680

Table A.16: *Simulation data of linear single chains with the same number of monomers as the simulated regular dendrimers. C.f. Table B.27.* $\lambda = 0.0$.

N	$\langle {R_e}^2 \rangle$	$\langle {R_g}^2 \rangle$	$\langle {R_h}^{-1} \rangle$	$\frac{\langle {R_e}^2 \rangle}{\langle {R_g}^2 \rangle}$	ϱ	W_{linear}
28	42.3 ± 0.7	7.00 ± 0.02	0.395 ± 0.003	6.04	1.046	3276
64	104 ± 4	17.3 ± 0.1	0.281 ± 0.004	6.01	1.168	41664
136	228 ± 9	37.8 ± 0.4	0.203 ± 0.004	6.03	1.247	410040
280	465 ± 19	77 ± 1	0.148 ± 0.005	6.04	1.297	3619560
568	885 ± 32	147 ± 3	0.108 ± 0.004	6.02	1.308	30380616
1144	1493 ± 52	250 ± 4	0.087 ± 0.003	5.97	1.370	248878344
2296	2532 ± 100	446 ± 14	0.067 ± 0.003	5.99	1.392	2014636680

Table A.17: *Simulation data of linear single chains with the same number of monomers as the simulated regular dendrimers. C.f. Table B.28.* $\lambda = 0.65$.

λ	$2\nu_{\text{eff}}(\langle {R_g}^2 \rangle)$	$2\nu_{\text{eff}}(\langle {R_e}^2 \rangle)$
0.00	1.1977	1.1876
0.20	1.1948	1.1852
0.40	1.1923	1.1837
0.60	1.1107	1.1081
0.62	1.0580	1.0507
0.64	1.0100	1.0080
0.65	0.9956	0.9963
0.66	0.8899	0.8788
0.68	0.7196	0.6909
0.70	0.6709	0.6592
0.80	0.6578	0.6541
0.90	0.6509	0.6499
1.00	0.6409	0.6340

Table A.18: *Effective exponents $2\nu_{\text{eff}}$ of $\langle {R_{e/g}}^2 \rangle$ determined from Figures 4.16 and 4.17.*

Appendix B

Data of branched chain systems

$N = 301$	$\langle {R_e}^2 \rangle$	$\langle {R_g}^2 \rangle_{\text{arms}}$	$\langle {R_g}^2 \rangle$	$\langle {R_h}^{-1} \rangle$	ϱ
$\lambda = 0.00$	409 ± 3	58.8 ± 0.5	164 ± 1	0.102 ± 0.001	1.308
$\lambda = 0.60$	201 ± 2	33.2 ± 0.2	83.6 ± 0.3	0.136 ± 0.001	1.248
$\lambda = 0.61$	195 ± 1	31.6 ± 0.2	79.0 ± 1	0.138 ± 0.002	1.242
$\lambda = 0.62$	191 ± 1	31.0 ± 0.1	75.7 ± 1	0.142 ± 0.002	1.235
$\lambda = 0.63$	181 ± 1	29.7 ± 0.2	72.9 ± 1	0.14 ± 0.002	1.229
$\lambda = 0.64$	177 ± 1	29.3 ± 0.2	69.5 ± 1	0.1472 ± 0.002	1.227
$\lambda = 0.65$	168 ± 1	28.3 ± 0.1	65.6 ± 0.1	0.151 ± 0.001	1.218
$\lambda = 0.66$	156 ± 1	26.9 ± 0.1	61.2 ± 1	0.154 ± 0.001	1.207
$\lambda = 0.67$	152 ± 1	26.2 ± 0.1	59.5 ± 1	0.156 ± 0.001	1.205
$\lambda = 0.68$	140 ± 1	25.0 ± 0.1	53.5 ± 1	0.162 ± 0.002	1.188
$\lambda = 0.69$	128.7 ± 0.7	23.7 ± 0.1	49.7 ± 1	0.167 ± 0.002	1.174
$\lambda = 0.70$	105.2 ± 0.3	23.05 ± 0.09	47.2 ± 1	0.169 ± 0.002	1.164

Table B.1: *Data of star polymers under various solvent conditions.* $f = 3$, $N = 301$.

$N = 601$	$\langle {R_e}^2 \rangle$	$\langle {R_g}^2 \rangle_{\text{arms}}$	$\langle {R_g}^2 \rangle$	$\langle {R_h}^{-1} \rangle$	ϱ
$\lambda = 0.00$	938 ± 4	136.4 ± 0.6	374 ± 2	0.070 ± 0.001	1.343
$\lambda = 0.60$	431 ± 2	68.4 ± 0.6	175 ± 1	0.100 ± 0.002	1.283
$\lambda = 0.61$	423 ± 2	66.6 ± 0.6	167 ± 1	0.099 ± 0.002	1.287
$\lambda = 0.62$	380 ± 2	63.6 ± 0.6	150 ± 1	0.104 ± 0.002	1.273
$\lambda = 0.63$	374 ± 2	61.2 ± 0.4	145.9 ± 0.8	0.105 ± 0.002	1.266
$\lambda = 0.64$	355 ± 1	59.8 ± 0.5	141.0 ± 0.9	0.106 ± 0.002	1.263
$\lambda = 0.65$	324 ± 2	55.4 ± 0.5	126.5 ± 0.8	0.111 ± 0.002	1.249
$\lambda = 0.66$	276 ± 2	47.6 ± 0.4	98.7 ± 0.7	0.122 ± 0.001	1.207
$\lambda = 0.67$	268 ± 2	45.1 ± 0.5	91.1 ± 0.7	0.126 ± 0.001	1.198
$\lambda = 0.68$	257 ± 2	44.5 ± 0.4	94.7 ± 0.7	0.124 ± 0.001	1.194
$\lambda = 0.69$	245 ± 2	43.7 ± 0.5	83.3 ± 0.7	0.130 ± 0.003	1.185
$\lambda = 0.70$	225 ± 1	38.8 ± 0.5	56.0 ± 0.5	0.132 ± 0.001	1.093

Table B.2: *Data of star polymers under various solvent conditions.* $f = 3$, $N = 601$.

$N = 901$	$\langle {R_e}^2 \rangle$	$\langle {R_g}^2 \rangle_{\text{arms}}$	$\langle {R_g}^2 \rangle$	$\langle {R_h}^{-1} \rangle$	ϱ
$\lambda = 0.00$	1530 ± 12	224 ± 2	616 ± 8	0.055 ± 0.002	1.367
$\lambda = 0.60$	693 ± 5	115 ± 1	264 ± 4	0.081 ± 0.002	1.307
$\lambda = 0.61$	645 ± 5	103 ± 1	262 ± 1	0.080 ± 0.002	1.292
$\lambda = 0.62$	521 ± 4	94.1 ± 1	205 ± 1	0.089 ± 0.003	1.279
$\lambda = 0.63$	478 ± 1	81.7 ± 1	187 ± 1	0.093 ± 0.004	1.268
$\lambda = 0.64$	457 ± 1	72.5 ± 1	174 ± 1	0.096 ± 0.002	1.265
$\lambda = 0.65$	436 ± 1	68.7 ± 1	166 ± 1	0.098 ± 0.002	1.260
$\lambda = 0.66$	425 ± 1	64.2 ± 0.8	161 ± 1	0.098 ± 0.002	1.239
$\lambda = 0.67$	399 ± 1	62.1 ± 1	154 ± 1	0.097 ± 0.002	1.206
$\lambda = 0.68$	269 ± 1	60.3 ± 0.8	126 ± 1	0.107 ± 0.002	1.203
$\lambda = 0.69$	260 ± 1	55.0 ± 0.6	93 ± 0.7	0.123 ± 0.002	1.190
$\lambda = 0.70$	256 ± 1	49.1 ± 0.4	89.6 ± 1	0.124 ± 0.001	1.160

Table B.3: *Data of star polymers under various solvent conditions.* $f = 3$, $N = 901$.

$N = 101$	$\langle {R_e}^2 \rangle$	$\langle {R_g}^2 \rangle_{\text{arms}}$	$\langle {R_g}^2 \rangle$	$\langle {R_h}^{-1} \rangle$	ϱ
$\lambda = 0.00$	76.8 ± 0.5	10.65 ± 0.02	33.18 ± 0.08	0.197 ± 0.006	1.134
$\lambda = 0.60$	47.31 ± 0.03	7.33 ± 0.02	20.68 ± 0.03	0.241 ± 0.009	1.097
$\lambda = 0.61$	46.72 ± 0.03	7.26 ± 0.01	20.39 ± 0.03	0.243 ± 0.009	1.096
$\lambda = 0.62$	45.78 ± 0.03	7.15 ± 0.02	19.94 ± 0.03	0.245 ± 0.001	1.093
$\lambda = 0.63$	44.79 ± 0.03	7.05 ± 0.01	19.60 ± 0.03	0.247 ± 0.001	1.091
$\lambda = 0.64$	43.99 ± 0.02	6.97 ± 0.01	19.21 ± 0.03	0.249 ± 0.001	1.089
$\lambda = 0.65$	43.10 ± 0.02	6.88 ± 0.01	18.84 ± 0.02	0.251 ± 0.001	1.087
$\lambda = 0.66$	42.30 ± 0.02	6.79 ± 0.01	18.42 ± 0.02	0.253 ± 0.001	1.085
$\lambda = 0.67$	41.51 ± 0.02	6.70 ± 0.01	18.14 ± 0.02	0.254 ± 0.001	1.083
$\lambda = 0.68$	40.44 ± 0.02	6.59 ± 0.01	17.64 ± 0.02	0.257 ± 0.001	1.080
$\lambda = 0.69$	39.50 ± 0.02	6.50 ± 0.01	17.23 ± 0.02	0.260 ± 0.001	1.077
$\lambda = 0.70$	38.58 ± 0.02	6.40 ± 0.01	16.77 ± 0.02	0.262 ± 0.001	1.073
$\lambda = 1.00$	16.32 ± 0.01	4.34 ± 0.01	7.91 ± 0.01	0.336 ± 0.007	0.946

Table B.4: *Data of star polymers under various solvent conditions.* $f = 4$, $N = 101$.

$N = 201$	$\langle {R_e}^2 \rangle$	$\langle {R_g}^2 \rangle_{\text{arms}}$	$\langle {R_g}^2 \rangle$	$\langle {R_h}^{-1} \rangle$	ϱ
$\lambda = 0.00$	181 ± 0.4	25.3 ± 0.1	77.9 ± 0.2	0.135 ± 0.001	1.194
$\lambda = 0.62$	96.4 ± 0.1	15.1 ± 0.1	41.7 ± 0.2	0.178 ± 0.003	1.153
$\lambda = 0.63$	92.4 ± 0.1	14.8 ± 0.1	39.9 ± 0.2	0.181 ± 0.003	1.146
$\lambda = 0.64$	90.8 ± 0.1	14.7 ± 0.1	38.9 ± 0.2	0.183 ± 0.003	1.143
$\lambda = 0.65$	87.0 ± 0.1	14.3 ± 0.1	37.4 ± 0.2	0.186 ± 0.003	1.138
$\lambda = 0.67$	80.7 ± 0.1	13.5 ± 0.1	34.6 ± 0.2	0.192 ± 0.003	1.128
$\lambda = 0.68$	78.1 ± 0.1	13.2 ± 0.1	33.6 ± 0.2	0.195 ± 0.003	1.127
$\lambda = 0.69$	75.9 ± 0.1	13.1 ± 0.1	32.6 ± 0.2	0.197 ± 0.003	1.123
$\lambda = 0.70$	71.2 ± 0.1	12.4 ± 0.1	30.7 ± 0.2	0.201 ± 0.004	1.115
$\lambda = 1.00$	23.72 ± 0.02	7.19 ± 0.04	11.24 ± 0.02	0.280 ± 0.001	0.938

Table B.5: *Data of star polymers under various solvent conditions.* $f = 4$, $N = 201$.

$N = 401$	$\langle {R_e}^2 \rangle$	$\langle {R_g}^2 \rangle_{\text{arms}}$	$\langle {R_g}^2 \rangle$	$\langle {R_h}^{-1} \rangle$	ϱ
$\lambda = 0.00$	424 ± 0.5	59.9 ± 0.4	182 ± 1	0.092 ± 0.001	1.241
$\lambda = 0.60$	209.5 ± 0.3	32.8 ± 0.3	90.7 ± 0.4	0.126 ± 0.002	1.196
$\lambda = 0.61$	205.8 ± 0.2	32.5 ± 0.2	87.7 ± 0.4	0.128 ± 0.002	1.193
$\lambda = 0.62$	200.1 ± 0.2	32.2 ± 0.3	86.0 ± 0.5	0.129 ± 0.003	1.196
$\lambda = 0.63$	191.0 ± 0.2	30.4 ± 0.2	82.0 ± 0.4	0.132 ± 0.002	1.190
$\lambda = 0.64$	177.9 ± 0.2	29.1 ± 0.2	76.5 ± 0.4	0.135 ± 0.002	1.182
$\lambda = 0.65$	170.9 ± 0.2	28.6 ± 0.2	74.0 ± 0.4	0.137 ± 0.002	1.176
$\lambda = 0.66$	167.9 ± 0.2	27.9 ± 0.2	71.7 ± 0.4	0.139 ± 0.002	1.173
$\lambda = 0.67$	150.9 ± 0.2	26.5 ± 0.3	65.4 ± 0.4	0.144 ± 0.003	1.164
$\lambda = 0.68$	148.4 ± 0.2	25.2 ± 0.2	61.0 ± 0.4	0.148 ± 0.003	1.156
$\lambda = 0.69$	136.1 ± 0.2	24.2 ± 0.2	57.7 ± 0.3	0.151 ± 0.003	1.148
$\lambda = 0.70$	119.2 ± 0.2	24.0 ± 0.2	51.9 ± 0.4	0.158 ± 0.003	1.135

Table B.6: *Data of star polymers under various solvent conditions.* $f = 4$, $N = 401$.

$N = 801$	$\langle {R_e}^2 \rangle$	$\langle {R_g}^2 \rangle_{\text{arms}}$	$\langle {R_g}^2 \rangle$	$\langle {R_h}^{-1} \rangle$	ϱ
$\lambda = 0.00$	1004 ± 3	142.6 ± 2.7	400 ± 5	0.064 ± 0.002	1.277
$\lambda = 0.60$	433 ± 1	68.6 ± 1.5	189 ± 3	0.090 ± 0.005	1.234
$\lambda = 0.62$	397 ± 1	64.7 ± 0.6	171 ± 1	0.094 ± 0.002	1.221
$\lambda = 0.64$	338 ± 1	58.2 ± 0.4	141.6 ± 0.6	0.100 ± 0.001	1.202
$\lambda = 0.65$	334 ± 1	57.1 ± 0.4	142.7 ± 0.6	0.101 ± 0.002	1.211
$\lambda = 0.66$	275.9 ± 1	50.7 ± 0.4	110.6 ± 0.6	0.112 ± 0.003	1.176
$\lambda = 0.68$	236 ± 1	43.2 ± 0.6	103.5 ± 0.9	0.115 ± 0.002	1.170
$\lambda = 0.70$	162 ± 1	35.8 ± 0.3	65.0 ± 0.3	0.134 ± 0.002	1.081
$\lambda = 1.00$	52.4 ± 0.5	19.7 ± 0.1	25.52 ± 0.01	0.185 ± 0.003	0.936

Table B.7: *Data of star polymers under various solvent conditions.* $f = 4$, $N = 801$.

$N = 101$	$\langle {R_e}^2 \rangle$	$\langle {R_g}^2 \rangle_{\text{arms}}$	$\langle {R_g}^2 \rangle$	$\langle {R_h}^{-1} \rangle$	ϱ
$\lambda = 0.00$	60.1 ± 0.1	8.20 ± 0.07	27.15 ± 0.08	0.208 ± 0.003	1.084
$\lambda = 0.60$	38.71 ± 0.07	5.83 ± 0.06	17.72 ± 0.08	0.253 ± 0.005	1.067
$\lambda = 0.61$	37.52 ± 0.07	5.75 ± 0.06	17.35 ± 0.08	0.254 ± 0.005	1.056
$\lambda = 0.62$	37.08 ± 0.07	5.67 ± 0.06	17.03 ± 0.11	0.256 ± 0.005	1.055
$\lambda = 0.63$	37.04 ± 0.07	5.66 ± 0.08	16.86 ± 0.10	0.256 ± 0.007	1.053
$\lambda = 0.64$	35.59 ± 0.07	5.53 ± 0.06	16.27 ± 0.09	0.260 ± 0.005	1.048
$\lambda = 0.65$	35.05 ± 0.07	5.51 ± 0.08	16.16 ± 0.16	0.260 ± 0.005	1.044
$\lambda = 0.66$	34.07 ± 0.07	5.42 ± 0.08	16.00 ± 0.13	0.261 ± 0.007	1.050
$\lambda = 0.67$	33.87 ± 0.06	5.38 ± 0.05	15.68 ± 0.09	0.264 ± 0.005	1.046
$\lambda = 0.68$	32.64 ± 0.06	5.25 ± 0.05	15.18 ± 0.09	0.268 ± 0.005	1.042
$\lambda = 0.69$	32.91 ± 0.06	5.28 ± 0.05	15.00 ± 0.09	0.268 ± 0.005	1.044
$\lambda = 0.70$	31.93 ± 0.06	5.14 ± 0.05	14.83 ± 0.08	0.270 ± 0.005	1.040
$\lambda = 1.00$	16.28 ± 0.03	3.68 ± 0.03	7.81 ± 0.03	0.337 ± 0.003	0.942

Table B.8: *Data of star polymers under various solvent conditions.* $f = 5$, $N = 101$.

$N = 201$	$\langle {R_e}^2 \rangle$	$\langle {R_g}^2 \rangle_{\text{arms}}$	$\langle {R_g}^2 \rangle$	$\langle {R_h}^{-1} \rangle$	ϱ
$\lambda = 0.00$	147 ± 1	19.8 ± 0.3	65.1 ± 0.5	0.273 ± 0.004	1.146
$\lambda = 0.61$	79.8 ± 0.3	12.1 ± 0.2	$36,2 \pm 0.3$	0.185 ± 0.006	1.109
$\lambda = 0.63$	78.7 ± 0.1	11.9 ± 0.3	35.4 ± 0.3	0.189 ± 0.006	1.110
$\lambda = 0.64$	70.3 ± 0.1	11.7 ± 0.2	34.7 ± 0.3	0.187 ± 0.006	1.100
$\lambda = 0.65$	75.7 ± 0.2	11.6 ± 0.3	34.0 ± 0.3	0.185 ± 0.006	1.112
$\lambda = 0.66$	71.0 ± 0.1	11.3 ± 0.2	31.9 ± 0.3	0.179 ± 0.006	1.102
$\lambda = 0.67$	66.7 ± 0.1	10.8 ± 0.2	30.1 ± 0.3	0.177 ± 0.006	1.089
$\lambda = 0.69$	64.1 ± 0.1	10.7 ± 0.2	28.8 ± 0.3	0.170 ± 0.006	1.090
$\lambda = 0.70$	59.4 ± 0.1	10.2 ± 0.2	26.6 ± 0.3	0.162 ± 0.006	1.079

Table B.9: *Data of star polymers under various solvent conditions.* $f = 5$, $N = 201$.

$N = 401$	$\langle {R_e}^2 \rangle$	$\langle {R_g}^2 \rangle_{\text{arms}}$	$\langle {R_g}^2 \rangle$	$\langle {R_h}^{-1} \rangle$	ϱ
$\lambda = 0.00$	336 ± 2	46.0 ± 0.4	149.8 ± 0.8	0.097 ± 0.001	1.186
$\lambda = 0.60$	171.6 ± 0.8	26.6 ± 0.4	76.6 ± 0.4	0.132 ± 0.003	1.154
$\lambda = 0.62$	163.6 ± 0.7	25.9 ± 0.3	73.2 ± 0.5	0.134 ± 0.003	1.149
$\lambda = 0.63$	154.3 ± 0.7	24.5 ± 0.3	70.4 ± 0.5	0.137 ± 0.003	1.146
$\lambda = 0.64$	147.4 ± 0.7	23.6 ± 0.3	66.7 ± 0.3	0.140 ± 0.003	1.139
$\lambda = 0.65$	139.5 ± 0.7	22.9 ± 0.2	62.8 ± 0.3	0.144 ± 0.003	1.138
$\lambda = 0.66$	130.8 ± 0.6	22.1 ± 0.2	59.5 ± 0.3	0.147 ± 0.003	1.130
$\lambda = 0.67$	125.5 ± 0.6	21.3 ± 0.3	57.5 ± 0.4	0.149 ± 0.004	1.127
$\lambda = 0.68$	110.6 ± 0.5	20.8 ± 0.2	38.7 ± 0.3	0.155 ± 0.003	1.075
$\lambda = 0.69$	104.0 ± 0.4	20.2 ± 0.2	42.9 ± 0.3	0.166 ± 0.004	1.085
$\lambda = 0.70$	100.7 ± 0.5	19.1 ± 0.2	42.1 ± 0.3	0.169 ± 0.003	1.096

Table B.10: *Data of star polymers under various solvent conditions.* $f = 5$, $N = 401$.

$N = 801$	$\langle {R_e}^2 \rangle$	$\langle {R_g}^2 \rangle_{\text{arms}}$	$\langle {R_g}^2 \rangle$	$\langle {R_h}^{-1} \rangle$	ϱ
$\lambda = 0.00$	777 ± 5	107.4 ± 0.9	335 ± 2	0.066 ± 0.001	1.219
$\lambda = 0.60$	362 ± 1	56.3 ± 0.5	162.9 ± 0.7	0.093 ± 0.001	1.182
$\lambda = 0.62$	341 ± 1	48.1 ± 0.4	129.9 ± 0.6	0.104 ± 0.002	1.180
$\lambda = 0.64$	299 ± 1	49.0 ± 0.3	130.2 ± 0.7	0.102 ± 0.002	1.168
$\lambda = 0.65$	286 ± 1	47.4 ± 0.5	123.2 ± 0.8	0.105 ± 0.002	1.168
$\lambda = 0.66$	225 ± 1	39.6 ± 0.5	95.3 ± 0.7	0.118 ± 0.003	1.152
$\lambda = 0.68$	205 ± 1	39.0 ± 0.3	87.6 ± 0.4	0.120 ± 0.002	1.123
$\lambda = 0.70$	129.9 ± 0.2	29.3 ± 0.3	56.2 ± 0.3	0.141 ± 0.002	1.054
$\lambda = 1.00$	44.87 ± 0.05	18.5 ± 0.1	25.42 ± 0.02	0.185 ± 0.001	0.935

Table B.11: *Data of star polymers under various solvent conditions.* $f = 5$, $N = 801$.

$N = 121$	$\langle {R_e}^2 \rangle$	$\langle {R_g}^2 \rangle_{\text{arms}}$	$\langle {R_g}^2 \rangle$	$\langle {R_h}^{-1} \rangle$	ϱ
$\lambda = 0.00$	62.0 ± 0.1	8.28 ± 0.03	28.67 ± 0.05	0.199 ± 0.001	1.064
$\lambda = 0.65$	36.34 ± 0.08	5.58 ± 0.03	17.24 ± 0.04	0.270 ± 0.005	1.121

Table B.12: *Data of star polymers under various solvent conditions.* $f = 6$, $N = 121$.

$N = 241$	$\langle {R_e}^2 \rangle$	$\langle {R_g}^2 \rangle_{\text{arms}}$	$\langle {R_g}^2 \rangle$	$\langle {R_h}^{-1} \rangle$	ϱ
$\lambda = 0.00$	148.9 ± 0.4	19.8 ± 0.1	68.2 ± 0.3	0.135 ± 0.001	1.118
$\lambda = 0.65$	70.7 ± 0.2	11.3 ± 0.1	33.3 ± 0.2	0.187 ± 0.004	1.077

Table B.13: *Data of star polymers under various solvent conditions.* $f = 6$, $N = 241$.

$N = 1201$	$\langle {R_e}^2 \rangle$	$\langle {R_g}^2 \rangle_{\text{arms}}$	$\langle {R_g}^2 \rangle$	$\langle {R_h}^{-1} \rangle$	ϱ
$\lambda = 0.00$	712 ± 10	143 ± 1	469 ± 4	0.0551 ± 0.001	1.194
$\lambda = 0.65$	296 ± 3	55.9 ± 0.9	121 ± 1	0.1031 ± 0.002	1.134

Table B.14: *Data of star polymers under various solvent conditions.* $f = 6$, $N = 1201$.

$N = 101$	$\langle {R_e}^2 \rangle$	$\langle {R_g}^2 \rangle_{\text{arms}}$	$\langle {R_g}^2 \rangle$	$\langle {R_h}^{-1} \rangle$	ϱ
$\lambda = 0.00$	28.81 ± 0.05	3.74 ± 0.01	14.12 ± 0.01	0.259 ± 0.001	0.9740
$\lambda = 0.60$	20.48 ± 0.04	2.92 ± 0.01	10.55 ± 0.01	0.296 ± 0.001	0.9618
$\lambda = 0.62$	20.14 ± 0.03	2.90 ± 0.05	10.43 ± 0.04	0.298 ± 0.002	0.9633
$\lambda = 0.63$	19.89 ± 0.03	2.87 ± 0.01	10.29 ± 0.01	0.299 ± 0.001	0.9604
$\lambda = 0.64$	19.72 ± 0.03	2.85 ± 0.01	10.22 ± 0.01	0.300 ± 0.002	0.9599
$\lambda = 0.65$	19.48 ± 0.03	2.83 ± 0.01	10.12 ± 0.02	0.302 ± 0.002	0.9595
$\lambda = 0.66$	19.35 ± 0.03	2.81 ± 0.01	10.03 ± 0.02	0.303 ± 0.002	0.9585
$\lambda = 0.67$	19.05 ± 0.03	2.79 ± 0.01	9.95 ± 0.02	0.304 ± 0.002	0.9582
$\lambda = 0.68$	18.85 ± 0.03	2.77 ± 0.01	9.86 ± 0.01	0.305 ± 0.002	0.9577
$\lambda = 0.69$	18.26 ± 0.01	2.76 ± 0.01	9.76 ± 0.02	0.306 ± 0.002	0.9567
$\lambda = 0.70$	18.44 ± 0.01	2.73 ± 0.01	9.68 ± 0.01	0.307 ± 0.001	0.9563

Table B.15: *Data of star polymers under various solvent conditions.* $f = 10$, $N = 101$.

$N = 201$	$\langle {R_e}^2 \rangle$	$\langle {R_g}^2 \rangle_{\text{arms}}$	$\langle {R_g}^2 \rangle$	$\langle {R_h}^{-1} \rangle$	ϱ
$\lambda = 0.00$	69.7 ± 0.1	8.8 ± 0.1	33.6 ± 0.1	0.177 ± 0.002	1.024
$\lambda = 0.60$	43.85 ± 0.08	6.16 ± 0.05	22.20 ± 0.06	0.215 ± 0.002	1.011
$\lambda = 0.61$	42.06 ± 0.08	6.03 ± 0.08	21.5 ± 0.1	0.217 ± 0.004	1.007
$\lambda = 0.62$	42.71 ± 0.08	6.05 ± 0.08	21.4 ± 0.1	0.217 ± 0.004	1.009
$\lambda = 0.63$	41.17 ± 0.07	5.94 ± 0.08	21.0 ± 0.1	0.220 ± 0.004	1.007
$\lambda = 0.64$	41.54 ± 0.08	5.91 ± 0.08	21.1 ± 0.1	0.220 ± 0.004	1.009
$\lambda = 0.65$	40.37 ± 0.07	5.84 ± 0.08	20.6 ± 0.1	0.222 ± 0.004	1.007
$\lambda = 0.67$	38.78 ± 0.07	5.71 ± 0.08	19.8 ± 0.1	0.225 ± 0.004	1.003
$\lambda = 0.68$	37.47 ± 0.07	5.59 ± 0.08	19.4 ± 0.1	0.227 ± 0.004	1.001
$\lambda = 0.69$	37.287 ± 0.07	5.52 ± 0.05	19.2 ± 01	0.229 ± 0.003	1.000
$\lambda = 0.70$	36.36 ± 0.07	5.46 ± 0.08	18.8 ± 0.1	0.231 ± 0.004	0.995
$\lambda = 1.00$	19.55 ± 0.04	3.97 ± 0.05	11.45 ± 0.04	0.279 ± 0.003	0.944

Table B.16: *Data of star polymers under various solvent conditions.* $f = 10$, $N = 201$.

$N = 401$	$\langle {R_e}^2 \rangle$	$\langle {R_g}^2 \rangle_{\text{arms}}$	$\langle {R_g}^2 \rangle$	$\langle {R_h}^{-1} \rangle$	ϱ
$\lambda = 0.00$	163.9 ± 0.7	20.6 ± 0.4	78.6 ± 0.5	0.120 ± 0.003	1.061
$\lambda = 0.60$	92.5 ± 0.4	13.1 ± 0.1	46.4 ± 0.2	0.154 ± 0.002	1.048
$\lambda = 0.61$	91.1 ± 0.4	12.9 ± 0.2	45.5 ± 0.2	0.155 ± 0.003	1.046
$\lambda = 0.62$	86.1 ± 0.9	12.4 ± 0.2	43.4 ± 0.2	0.159 ± 0.003	1.043
$\lambda = 0.63$	85.6 ± 0.9	12.2 ± 0.2	42.7 ± 0.2	0.160 ± 0.003	1.040
$\lambda = 0.64$	80.4 ± 0.4	11.9 ± 0.2	41.0 ± 0.2	0.162 ± 0.002	1.039
$\lambda = 0.65$	79.6 ± 0.4	11.7 ± 0.1	40.5 ± 0.2	0.163 ± 0.003	1.037
$\lambda = 0.66$	78.7 ± 0.4	11.5 ± 0.1	39.9 ± 0.2	0.165 ± 0.003	1.034
$\lambda = 0.67$	73.4 ± 0.4	11.3 ± 0.1	37.2 ± 0.2	0.169 ± 0.003	1.032
$\lambda = 0.68$	72.0 ± 0.4	11.2 ± 0.3	37.1 ± 0.2	0.169 ± 0.003	1.031
$\lambda = 0.69$	69.9 ± 0.4	11.0 ± 0.2	35.5 ± 0.2	0.172 ± 0.003	1.028
$\lambda = 0.70$	49.2 ± 0.4	10.5 ± 0.2	35.0 ± 0.2	0.174 ± 0.002	1.032
$\lambda = 1.00$	28.6 ± 0.1	6.97 ± 0.09	16.88 ± 0.04	0.229 ± 0.002	0.9391

Table B.17: *Data of star polymers under various solvent conditions.* $f = 10$, $N = 401$.

$N = 801$	$\langle {R_e}^2 \rangle$	$\langle {R_g}^2 \rangle_{\text{arms}}$	$\langle {R_g}^2 \rangle$	$\langle {R_h}^{-1} \rangle$	ϱ
$\lambda = 0.00$	384 ± 2	49.0 ± 0.6	170 ± 0.8	0.083 ± 0.001	1.0902
$\lambda = 0.60$	194 ± 1	27.9 ± 0.4	97.4 ± 0.5	0.109 ± 0.001	1.077
$\lambda = 0.62$	169 ± 1	26.3 ± 0.4	83.0 ± 0.4	0.117 ± 0.002	1.069
$\lambda = 0.64$	162 ± 1	24.5 ± 0.3	80.4 ± 0.4	0.119 ± 0.002	1.068
$\lambda = 0.65$	147 ± 1	24.1 ± 0.2	71.9 ± 0.2	0.126 ± 0.002	1.067
$\lambda = 0.66$	135 ± 1	23.2 ± 0.3	65.0 ± 0.3	0.131 ± 0.003	1.060
$\lambda = 0.68$	124 ± 1	21.6 ± 0.3	63.2 ± 0.3	0.132 ± 0.002	1.048
$\lambda = 0.70$	99.9 ± 0.6	21.5 ± 0.3	50.1 ± 0.3	0.145 ± 0.002	1.026
$\lambda = 1.00$	40.83 ± 0.05	13.4 ± 0.1	25.23 ± 0.02	0.186 ± 0.0006	0.935

Table B.18: *Data of star polymers under various solvent conditions.* $f = 10$, $N = 801$.

$N = 241$	$\langle {R_e}^2 \rangle$	$\langle {R_g}^2 \rangle_{\text{arms}}$	$\langle {R_g}^2 \rangle$	$\langle {R_h}^{-1} \rangle$	ϱ
$\lambda = 0.00$	72.5 ± 0.15	8.96 ± 0.05	35.43 ± 0.06	0.170 ± 0.001	1.0133
$\lambda = 0.60$	45.45 ± 0.10	6.24 ± 0.04	23.32 ± 0.05	0.207 ± 0.002	0.9994
$\lambda = 0.62$	44.70 ± 0.10	6.18 ± 0.04	23.00 ± 0.04	0.210 ± 0.002	1.0054
$\lambda = 0.63$	43.16 ± 0.10	6.04 ± 0.04	22.32 ± 0.05	0.211 ± 0.002	0.9977
$\lambda = 0.64$	42.15 ± 0.09	5.94 ± 0.04	21.84 ± 0.05	0.213 ± 0.002	0.9960
$\lambda = 0.65$	41.59 ± 0.09	5.90 ± 0.04	21.63 ± 0.05	0.214 ± 0.002	0.9959
$\lambda = 0.66$	40.56 ± 0.09	5.83 ± 0.04	21.15 ± 0.04	0.216 ± 0.002	0.9940
$\lambda = 0.67$	39.98 ± 0.09	5.74 ± 0.04	20.87 ± 0.05	0.217 ± 0.002	0.9932
$\lambda = 0.68$	39.59 ± 0.08	5.72 ± 0.04	20.62 ± 0.05	0.219 ± 0.002	0.9931
$\lambda = 0.69$	38.39 ± 0.08	5.60 ± 0.04	20.17 ± 0.04	0.221 ± 0.002	0.9907
$\lambda = 0.70$	37.85 ± 0.08	5.53 ± 0.04	19.89 ± 0.04	0.222 ± 0.002	0.9899
$\lambda = 1.00$	20.62 ± 0.04	4.07 ± 0.03	12.40 ± 0.02	0.267 ± 0.001	0.9396

Table B.19: *Data of star polymers under various solvent conditions.* $f = 12$, $N = 241$.

$N = 201$	$\langle {R_e}^2 \rangle$	$\langle {R_g}^2 \rangle_{\text{arms}}$	$\langle {R_g}^2 \rangle$	$\langle {R_h}^{-1} \rangle$	ϱ
$\lambda = 0.00$	170.8 ± 0.4	21.1 ± 0.1	83.5 ± 0.2	0.115 ± 0.002	1.047
$\lambda = 0.60$	95.0 ± 0.2	13.2 ± 0.1	48.1 ± 0.1	0.149 ± 0.002	1.032
$\lambda = 0.62$	89.9 ± 0.2	12.6 ± 0.1	45.9 ± 0.2	0.152 ± 0.004	1.029
$\lambda = 0.64$	83.7 ± 0.2	12.2 ± 0.1	43.1 ± 0.1	0.156 ± 0.004	1.026
$\lambda = 0.65$	82.4 ± 0.2	12.0 ± 0.1	42.7 ± 0.1	0.157 ± 0.004	1.024
$\lambda = 0.66$	79.9 ± 0.2	11.7 ± 0.1	41.1 ± 0.1	0.160 ± 0.004	1.023
$\lambda = 0.68$	73.7 ± 0.2	11.3 ± 0.1	38.3 ± 0.1	0.165 ± 0.004	1.019
$\lambda = 0.70$	67.8 ± 0.2	10.8 ± 0.1	35.7 ± 0.1	0.170 ± 0.004	1.014
$\lambda = 1.00$	29.29 ± 0.06	7.23 ± 0.05	18.65 ± 0.06	0.217 ± 0.004	0.938

Table B.20: *Data of star polymers under various solvent conditions.* $f = 12$, $N = 481$.

$N = 721$	$\langle {R_e}^2 \rangle$	$\langle {R_g}^2 \rangle_{\text{arms}}$	$\langle {R_g}^2 \rangle$	$\langle {R_h}^{-1} \rangle$	ϱ
$\lambda = 0.00$	280 ± 2	34.5 ± 0.6	136.5 ± 0.7	0.091 ± 0.002	1.061
$\lambda = 0.60$	140.6 ± 0.2	20.6 ± 0.2	7.7 ± 0.2	0.123 ± 0.001	1.050
$\lambda = 0.62$	132.7 ± 0.2	19.2 ± 0.2	67.9 ± 0.3	0.127 ± 0.002	1.043
$\lambda = 0.64$	117.9 ± 0.8	19.5 ± 0.3	59.0 ± 0.5	0.137 ± 0.005	1.041
$\lambda = 0.65$	121.4 ± 0.2	18.3 ± 0.1	61.9 ± 0.2	0.132 ± 0.001	1.040
$\lambda = 0.66$	117.7 ± 0.2	17.4 ± 0.1	59.4 ± 0.1	0.135 ± 0.001	1.037
$\lambda = 0.68$	102.8 ± 0.2	16.3 ± 0.1	53.9 ± 0.1	0.140 ± 0.002	1.028
$\lambda = 0.70$	87.7 ± 0.2	16.0 ± 0.1	47.5 ± 0.1	0.148 ± 0.002	1.019
$\lambda = 1.00$	38.49 ± 0.07	10.85 ± 0.08	23.83 ± 0.02	0.192 ± 0.004	0.937

Table B.21: *Data of star polymers under various solvent conditions.* $f = 12$, $N = 721$.

$N = 1241$	$\langle {R_e}^2 \rangle$	$\langle {R_g}^2 \rangle_{\text{arms}}$	$\langle {R_g}^2 \rangle$	$\langle {R_h}^{-1} \rangle$	ϱ
$\lambda = 0.00$	538 ± 2	67.4 ± 0.8	256 ± 2	0.068 ± 0.001	1.080
$\lambda = 0.60$	263 ± 1	37.4 ± 0.5	133.8 ± 0.6	0.093 ± 0.001	1.077
$\lambda = 0.62$	228 ± 1	35.0 ± 0.4	114.9 ± 0.4	0.100 ± 0.002	1.071
$\lambda = 0.64$	209 ± 1	33.4 ± 0.3	106.7 ± 0.5	0.103 ± 0.001	1.065
$\lambda = 0.65$	197 ± 1	32.4 ± 0.2	99.0 ± 0.4	0.107 ± 0.002	1.062
$\lambda = 0.66$	161.1 ± 0.9	30.1 ± 0.3	77.6 ± 0.4	0.120 ± 0.003	1.038
$\lambda = 0.68$	148.7 ± 0.8	29.3 ± 0.3	76.0 ± 0.4	0.119 ± 0.002	1.037
$\lambda = 0.70$	144.0 ± 0.6	29.0 ± 0.3	61.0 ± 0.4	0.131 ± 0.002	1.021
$\lambda = 1.00$	54.3 ± 0.4	17.3 ± 0.1	34.0 ± 0.2	0.161 ± 0.002	0.941

Table B.22: *Data of star polymers under various solvent conditions.* $f = 12$, $N = 1241$.

$N = 451$	$\langle {R_e}^2 \rangle$	$\langle {R_g}^2 \rangle_{\text{arms}}$	$\langle {R_g}^2 \rangle$	$\langle {R_h}^{-1} \rangle$	ϱ
$\lambda = 0.00$	107 ± 1	12.5 ± 0.2	53.2 ± 0.8	0.137 ± 0.002	1.002
$\lambda = 0.65$	58.0 ± 0.5	7.84 ± 0.08	31.22 ± 0.07	0.177 ± 0.002	1.020

Table B.23: *Data of star polymers under various solvent conditions.* $f = 18$, $N = 451$.

$N = 901$	$\langle {R_e}^2 \rangle$	$\langle {R_g}^2 \rangle_{\text{arms}}$	$\langle {R_g}^2 \rangle$	$\langle {R_h}^{-1} \rangle$	ϱ
$\lambda = 0.00$	238 ± 3	28.6 ± 0.9	120 ± 2	0.093 ± 0.003	1.022
$\lambda = 0.65$	107 ± 10	16.3 ± 0.3	56.0 ± 0.4	0.135 ± 0.003	1.007

Table B.24: *Data of star polymers under various solvent conditions.* $f = 18$, $N = 901$.

$N = 1351$	$\langle {R_e}^2 \rangle$	$\langle {R_g}^2 \rangle_{\text{arms}}$	$\langle {R_g}^2 \rangle$	$\langle {R_h}^{-1} \rangle$	ϱ
$\lambda = 0.00$	404 ± 4	47.9 ± 0.6	200 ± 2	0.0730 ± 0.007	1.037
$\lambda = 0.65$	146 ± 1	25.8 ± 0.4	75.3 ± 0.3	0.118 ± 0.002	1.015

Table B.25: *Data of star polymers under various solvent conditions.* $f = 18$, $N = 1351$.

Table B.26: *Table of extrapolated shape-factors $sf_i^\star$ obtained in this work, compared with literature values. Our study covers the largest range of arm numbers f and all results were obtained by an ($N \to \infty$) extrapolation. The small deviations of data are probably due to the results in [229] not being extrapolated to infinite chain lengths.*

Reference	f							
	2	3	4	5	6	10	12	18
$sf_1^\star$	**good solvent**							
this work	0.7512	0.6751	0.6104	0.5728	0.5485	0.4822	0.4702	0.4292
Zifferer[a]	0.7487	0.6722	0.6177	−−	0.5522	0.4894	0.4714	−−
$sf_2^\star$								
this work	0.1868	0.2465	0.2772	0.2950	0.3044	0.3188	0.3220	0.3269
Zifferer[a]	0.1857	0.2460	0.2762	−−	0.3017	0.3180	0.3214	−−
$sf_3^\star$								
this work	0.06560	0.0821	0.1065	0.1517	0.1464	0.1988	0.2079	0.2455
Zifferer[a]	0.0655	0.0818	0.1061	−−	0.1467	0.1926	0.2071	−−
$sf_1^\star$	**θ-solvent**							
this work	0.7310	0.6641	0.6325	0.6067	0.5842	0.5149	0.5079	0.4587
Zifferer[a]	0.7239	0.6693	0.6283	−−	0.5731	0.5176	0.4993	−−
$sf_2^\star$								
this work	0.1922	0.2440	0.2797	0.2810	0.2874	0.3081	0.3143	0.3221
Zifferer[a]	0.1980	0.2311	0.2620	−−	0.2881	0.3072	0.3125	−−
$sf_3^\star$								
this work	0.0794	0.1052	0.1049	0.1207	0.1454	0.1748	0.1956	0.2236
Zifferer[a]	0.0781	0.0926	0.1097	−−	0.1388	0.1752	0.1882	−−

[a] [229]. MC simulation of stars of one single arm length $N_a = 480$ on a tetrahedral lattice.

G	N	$\langle {R_g}^2 \rangle$	$\langle {R_h}^{-1} \rangle$	ρ	g	W
1	28	5.578 ± 0.009	0.399 ± 0.002	0.9412	0.5278	9
2	64	11.94 ± 0.01	0.285 ± 0.001	0.9841	0.3797	117
3	136	20.908 ± 0.007	0.215 ± 0.0003	0.9848	0.2579	909
4	280	33.72 ± 0.05	0.167 ± 0.001	0.9715	0.1750	5661
5	568	52.63 ± 0.06	0.132 ± 0.006	0.9589	0.1142	31293
6	1144	79.58 ± 0.09	0.106 ± 0.006	0.9488	0.0756	160893
7	2296	116.9 ± 0.2	0.088 ± 0.006	0.9476	0.0326	788733

Table B.27: *Simulation data of regular dendrimers, ($\lambda = 0.0$).*

G	N	$\langle {R_g}^2 \rangle$	$\langle {R_h}^{-1} \rangle$	ρ	g	W
1	28	4.445 ± 0.008	0.437 ± 0.002	0.9215	0.6359	9
2	64	8.465 ± 0.008	0.334 ± 0.001	0.9703	0.4896	117
3	136	14.07 ± 0.01	0.260 ± 0.008	0.9789	0.3726	909
4	280	21.74 ± 0.05	0.209 ± 0.003	0.9726	0.2824	5661
5	568	32.71 ± 0.04	0.168 ± 0.009	0.9615	0.2184	31293
6	1144	48.99 ± 0.08	0.136 ± 0.009	0.9532	0.1958	160893
7	2296	75.0 ± 0.1	0.110 ± 0.007	0.9523	0.1679	788733

Table B.28: *Simulation data of regular dendrimers, ($\lambda = 0.65$).*

$\lambda = 0.0$	$G_{\text{max}} = 1$	$G_{\text{max}} = 2$	$G_{\text{max}} = 3$	$G_{\text{max}} = 4$
$G_{\text{sub}} = 0$	0.9458 ± 0.0002	0.9450 ± 0.0002	0.9456 ± 0.0002	0.9459 ± 0.0006
$G_{\text{sub}} = 1$	0.9435 ± 0.0002	0.9445 ± 0.0001	0.9446 ± 0.0006	0.9444 ± 0.0004
$G_{\text{sub}} = 2$	–	0.9437 ± 0.0001	0.94436 ± 0.00005	0.9445 ± 0.0002
$G_{\text{sub}} = 3$	–	–	0.94350 ± 0.00005	0.9446 ± 0.0001
$G_{\text{sub}} = 4$	–	–	–	0.9436 ± 0.0001

Table B.29: *Averaged squared bondlength ${l_b}^2$ of dendrimers in good solvent ($\lambda = 0.0$). The bondlengths of the monomers pertaining to each sub generation G_{sub} are displayed for generations 1 to 4.*

$\lambda = 0.0$	$G_{\text{max}} = 5$	$G_{\text{max}} = 6$	$G_{\text{max}} = 7$
$G_{\text{sub}} = 0$	0.9482 ± 0.0006	0.9535 ± 0.0008	0.9699 ± 0.0015
$G_{\text{sub}} = 1$	0.9455 ± 0.0003	0.9506 ± 0.0005	0.9575 ± 0.0009
$G_{\text{sub}} = 2$	0.9453 ± 0.0002	0.9469 ± 0.0004	0.9526 ± 0.0006
$G_{\text{sub}} = 3$	0.9447 ± 0.0001	0.9454 ± 0.0002	0.9484 ± 0.0004
$G_{\text{sub}} = 4$	0.9445 ± 0.0001	0.9452 ± 0.0002	0.9463 ± 0.0001
$G_{\text{sub}} = 5$	0.94333 ± 0.00008	0.9442 ± 0.0001	0.9444 ± 0.0002
$G_{\text{sub}} = 6$	–	0.9435 ± 0.0001	0.9442 ± 0.0001
$G_{\text{sub}} = 7$	–	–	0.9434 ± 0.0001

Table B.30: *Averaged squared bondlength ${l_b}^2$ of dendrimers in good solvent ($\lambda = 0.0$). The bondlengths of the monomers pertaining to each sub generation G_{sub} are displayed for generations 5 to 7.*

$\lambda = 0.65$	$G_{\text{max}} = 1$	$G_{\text{max}} = 2$	$G_{\text{max}} = 3$	$G_{\text{max}} = 4$
$G_{\text{sub}} = 0$	0.9425 ± 0.0003	0.94244 ± 0.0002	0.9424 ± 0.0002	0.9428 ± 0.0009
$G_{\text{sub}} = 1$	0.9424 ± 0.0001	0.94248 ± 0.00009	0.9422 ± 0.0001	0.9413 ± 0.0005
$G_{\text{sub}} = 2$	–	0.94233 ± 0.00005	0.9422 ± 0.0003	0.9421 ± 0.0002
$G_{\text{sub}} = 3$	–	–	0.94350 ± 0.00005	0.9446 ± 0.0001
$G_{\text{sub}} = 4$	–	–	–	0.9421 ± 0.0002

Table B.31: *Averaged squared bondlength ${l_b}^2$ of dendrimers in good solvent ($\lambda = 0.65$). The bondlengths of the monomers pertaining to each sub generation G_{sub} are displayed for generations 1 to 4.*

$\lambda = 0.65$	$G_{\text{max}} = 5$	$G_{\text{max}} = 6$	$G_{\text{max}} = 7$
$G_{\text{sub}} = 0$	0.9425 ± 0.0005	0.9443 ± 0.0009	0.949 ± 0.001
$G_{\text{sub}} = 1$	0.9415 ± 0.0003	0.9431 ± 0.0005	0.9441 ± 0.0008
$G_{\text{sub}} = 2$	0.9421 ± 0.0002	0.9418 ± 0.0003	0.9434 ± 0.0005
$G_{\text{sub}} = 3$	0.9421 ± 0.0002	0.9415 ± 0.0003	0.9425 ± 0.0002
$G_{\text{sub}} = 4$	0.9419 ± 0.0001	0.9415 ± 0.0003	0.9418 ± 0.0002
$G_{\text{sub}} = 5$	0.9416 ± 0.0004	0.9419 ± 0.0001	0.9421 ± 0.0002
$G_{\text{sub}} = 6$	–	0.9153 ± 0.0009	0.9418 ± 0.0001
$G_{\text{sub}} = 7$	–	–	0.9421 ± 0.0002

Table B.32: *Averaged squared bondlength ${l_b}^2$ of dendrimers in good solvent ($\lambda = 0.65$). The bondlengths of the monomers pertaining to each sub generation G_{sub} are displayed for generations 5 to 7.*

Topology	Quantity	$N = 101$	$N = 201$	$N = 401$	$N = 801$
10%	$\langle {R_e}^2 \rangle_{\text{backbone}}$	169 ± 2	400 ± 3	935 ± 11	2162 ± 18
	$\langle {R_e}^2 \rangle_{\text{arms}}$	72.2 ± 0.5	171.4 ± 0.8	397 ± 4	930 ± 13
	$\langle {R_g}^2 \rangle_{\text{back}}$	25.19 ± 0.13	59.8 ± 0.4	140.5 ± 0.8	327 ± 2
	$\langle {R_g}^2 \rangle_{\text{arms}}$	10.38 ± 0.08	24.78 ± 0.13	57.97 ± 0.08	136 ± 1
	$\langle {R_g}^2 \rangle_{\text{total}}$	50.5 ± 0.6	119.6 ± 0.6	275 ± 4	636 ± 12
	$\langle {R_h}^{-1} \rangle$	0.182 ± 0.001	0.125 ± 0.002	0.086 ± 0.001	0.058 ± 0.003
	g	0.902	0.922	0.919	0.935
	h	0.975	0.986	0.993	0.995
	g'	0.927	0.865	0.781	0.735
20%	$\langle {R_e}^2 \rangle_{\text{backbone}}$	166 ± 1	394 ± 2	897 ± 8	2146 ± 19
	$\langle {R_e}^2 \rangle_{\text{arms}}$	72.69 ± 0.09	173 ± 1	406 ± 3	922 ± 13
	$\langle {R_g}^2 \rangle_{\text{backbone}}$	25.17 ± 0.06	60.26 ± 0.06	139 ± 2	339 ± 5
	$\langle {R_g}^2 \rangle_{\text{arms}}$	10.41 ± 0.04	24.78 ± 0.04	58.5 ± 0.8	136.2 ± 0.8
	$\langle {R_g}^2 \rangle_{\text{total}}$	44.91 ± 0.07	105.7 ± 0.6	244 ± 2	572 ± 5
	$\langle {R_h}^{-1} \rangle$	0.186 ± 0.001	0.128 ± 0.002	0.088 ± 0.002	0.059 ± 0.002
	g	0.805	0.827	0.804	0.841
	h	0.953	0.962	0.972	0.978
	g'	0.958	0.891	0.803	0.754
40%	$\langle {R_e}^2 \rangle_{\text{backbone}}$	165.6 ± 0.8	391 ± 3	908 ± 12	2136 ± 19
	$\langle {R_e}^2 \rangle_{\text{arms}}$	73.7 ± 0.8	174 ± 1	414 ± 5	929 ± 15
	$\langle {R_g}^2 \rangle_{\text{backbone}}$	25.54 ± 0.08	60.4 ± 0.7	142 ± 1	337 ± 5
	$\langle {R_g}^2 \rangle_{\text{arms}}$	10.48 ± 0.07	24.88 ± 0.06	58.9 ± 0.8	136.5 ± 0.8
	$\langle {R_g}^2 \rangle_{\text{total}}$	35.9 ± 0.2	84.2 ± 0.4	199 ± 1	453 ± 5
	$\langle {R_h}^{-1} \rangle$	0.193 ± 0.001	0.132 ± 0.002	0.090 ± 0.001	0.061 ± 0.002
	g	0.643	0.659	0.655	0.666
	h	0.921	0.930	0.943	0.946
	g'	0.984	0.918	0.840	0.788
50%	$\langle {R_g}^2 \rangle$	33.18 ± 0.08	77.8 ± 0.5	182 ± 1	428 ± 5
	$\langle {R_g}^2 \rangle_{\text{arms}}$	10.65 ± 0.02	25.3 ± 0.1	59.9 ± 0.4	142.6 ± 2.7
	$\langle {R_h}^{-1} \rangle$	0.197 ± 0.0006	0.135 ± 0.001	0.092 ± 0.001	0.062 ± 0.001
	g	0.595	0.607	0.601	0.616
	h	0.9023	0.913	0.924	0.926
	g'	0.989	0.937	0.846	0.795

Table B.33: *Data of macromolecules of different topologies according to Figure 5.27 and Table 5.12 in Section 5.2.* $\lambda = 0.0$. *Values obtained by averaging over the backbone monomers and the monomers of side arms are displayed, as well as the calculated* g,h *and* g' *values. The* 50%*-systems correspond to stars with* $f = 4$.

Topology	Quantity	$N = 101$	$N = 201$	$N = 401$	$N = 801$
10%	$\langle {R_e}^2 \rangle_{\text{backbone}}$	86.5 ± 0.7	171 ± 2	326 ± 5	649 ± 8
	$\langle {R_e}^2 \rangle_{\text{arms}}$	42.0 ± 0.3	84.6 ± 0.4	166 ± 3	310 ± 7
	$\langle {R_g}^2 \rangle_{\text{back}}$	14.18 ± 0.07	28.51 ± 0.08	53.8 ± 0.8	109 ± 1
	$\langle {R_g}^2 \rangle_{\text{arms}}$	6.80 ± 0.05	13.97 ± 0.08	27.84 ± 0.08	54.1 ± 0.5
	$\langle {R_g}^2 \rangle_{\text{total}}$	26.06 ± 0.06	51.3 ± 0.8	98.5 ± 0.7	196 ± 2
	$\langle {R_h}^{-1} \rangle$	0.235 ± 0.001	0.175 ± 0.002	0.132 ± 0.001	0.098 ± 0.001
	g	0.924	0.913	0.880	0.875
	h	0.979	0.972	0.957	0.948
	g'	0.938	0.876	0.808	0.775
20%	$\langle {R_e}^2 \rangle_{\text{backbone}}$	86.1 ± 0.6	177 ± 1	357 ± 4	518 ± 8
	$\langle {R_e}^2 \rangle_{\text{arms}}$	42.09 ± 0.09	85.5 ± 0.9	168 ± 2	380 ± 7
	$\langle {R_g}^2 \rangle_{\text{backbone}}$	14.28 ± 0.06	29.26 ± 0.0	58.1 ± 0.6	78.7 ± 0.6
	$\langle {R_g}^2 \rangle_{\text{arms}}$	6.81 ± 0.04	14.05 ± 0.03	28.32 ± 0.08	56.1 ± 0.8
	$\langle {R_g}^2 \rangle_{\text{total}}$	23.39 ± 0.07	46.94 ± 0.09	94.2 ± 0.8	187 ± 2
	$\langle {R_h}^{-1} \rangle$	0.241 ± 0.001	0.178 ± 0.002	0.131 ± 0.001	0.107 ± 0.001
	g	0.829	0.835	0.832	0.835
	h	0.957	0.956	0.961	0.960
	g'	0.917	0.874	0.789	0.760
40%	$\langle {R_e}^2 \rangle_{\text{backbone}}$	88.3 ± 0.8	185 ± 3	333 ± 7	710 ± 12
	$\langle {R_e}^2 \rangle_{\text{arms}}$	742.2 ± 0.4	83.7 ± 0.5	172 ± 3	302 ± 11
	$\langle {R_g}^2 \rangle_{\text{backbone}}$	14.73 ± 0.06	30.3 ± 0.7	57.0 ± 0.3	112.5 ± 0.7
	$\langle {R_g}^2 \rangle_{\text{arms}}$	6.83 ± 0.05	13.83 ± 0.05	28.5 ± 0.7	53.3 ± 0.4
	$\langle {R_g}^2 \rangle_{\text{total}}$	19.92 ± 0.06	39.1 ± 0.7	78.7 ± 0.8	156 ± 1
	$\langle {R_h}^{-1} \rangle$	0.247 ± 0.001	0.184 ± 0.002	0.135 ± 0.001	0.100 ± 0.001
	g	0.693	0.696	0.695	0.696
	h	0.931	0.929	0.930	0.931
	g'	0.878	0.889	0.906	0.775
50%	$\langle {R_g}^2 \rangle$	43.1 ± 0.02	87.0 ± 0.1	170.9 ± 0.2	334 ± 1
	$\langle {R_g}^2 \rangle_{\text{arms}}$	6.88 ± 0.01	14.3 ± 0.1	28.6 ± 0.2	57.1 ± 0.4
	$\langle {R_h}^{-1} \rangle$	0.251 ± 0.000	0.186 ± 0.001	0.137 ± 0.001	0.101 ± 0.002
	g	0.658	0.649	0.639	0.631
	h	0.918	0.912	0.919	0.916
	g'	0.853	0.851	0.807	0.768

Table B.34: *Data of macromolecules of different topologies according to Figure 5.27 and Table 5.12 in Section 5.2.* $\lambda = 0.65$. *Values obtained by averaging over the backbone monomers and the monomers of side arms are displayed, as well as the calculated* g,h *and* g' *values. The* 50%*-systems correspond to stars with* $f = 4$.

Topology	Quantity	$N = 301$	$N = 601$	$N = 901$
side 2	$\langle {R_e}^2 \rangle_{\text{backbone}}$	862 ± 5	2013 ± 3	3436 ± 21
	$\langle {R_e}^2 \rangle_{\text{arms}}$	173 ± 3	408 ± 4	664 ± 7
	$\langle {R_g}^2 \rangle_{\text{back}}$	137 ± 2	325 ± 5	357 ± 4
	$\langle {R_g}^2 \rangle_{\text{arms}}$	24.76 ± 0.05	58.9 ± 0.6	96.2 ± 0.5
	$\langle {R_g}^2 \rangle_{\text{total}}$	153 ± 3	357 ± 6	582 ± 4
	$\langle {R_h}^{-1} \rangle$	0.105 ± 0.001	0.071 ± 0.001	0.561 ± 0.001
	g	0.725	0.733	0.734
	h	0.946	0.956	0.962
	g'	0.848	0.871	0.887
side 4	$\langle {R_e}^2 \rangle_{\text{backbone}}$	948 ± 5	2082 ± 15	3653 ± 26
	$\langle {R_e}^2 \rangle_{\text{arms}}$	73.8 ± 0.9	172 ± 1	284 ± 3
	$\langle {R_g}^2 \rangle_{\text{backbone}}$	146.6 ± 0.9	325 ± 4	557 ± 4
	$\langle {R_g}^2 \rangle_{\text{arms}}$	10.49 ± 0.05	24.72 ± 0.08	41.1 ± 0.8
	$\langle {R_g}^2 \rangle_{\text{total}}$	151.7 ± 0.9	356 ± 5	575 ± 6
	$\langle {R_h}^{-1} \rangle$	0.106 ± 0.001	0.072 ± 0.002	0.057 ± 0.002
	g	0.719	0.715	0.725
	h	0.920	0.929	0.930
	g'	0.817	0.821	0.844
H-molecule	$\langle {R_e}^2 \rangle_{\text{backbone}}$	922 ± 8	1994 ± 9	3378 ± 19
	$\langle {R_e}^2 \rangle_{\text{arms}}$	170 ± 4	402 ± 3	658 ± 5
	$\langle {R_g}^2 \rangle_{\text{backbone}}$	141 ± 2	316 ± 4	528 ± 5
	$\langle {R_g}^2 \rangle_{\text{arms}}$	24.56 ± 0.07	58.1 ± 0.8	96.0 ± 0.8
	$\langle {R_g}^2 \rangle_{\text{total}}$	166 ± 2	382 ± 4	625 ± 3
	$\langle {R_h}^{-1} \rangle$	0.104 ± 0.001	0.070 ± 0.002	0.556 ± 0.001
	g	0.787	0.785	0.788
	h	0.9567	0.962	0.969
	g'	0.875	0.889	0.910
side 10	$\langle {R_e}^2 \rangle_{\text{backbone}}$	1000 ± 9	2293 ± 13	3762 ± 20
	$\langle {R_e}^2 \rangle_{\text{arms}}$	22.59 ± 0.06	55.2 ± 0.6	92.3 ± 0.8
	$\langle {R_g}^2 \rangle_{\text{backbone}}$	155 ± 2	355 ± 5	581 ± 5
	$\langle {R_g}^2 \rangle_{\text{arms}}$	3.29 ± 0.04	7.86 ± 0.07	13.14 ± 0.06
	$\langle {R_g}^2 \rangle_{\text{total}}$	156 ± 2	359 ± 5	583 ± 5
	$\langle {R_h}^{-1} \rangle$	0.108 ± 0.001	0.073 ± 0.002	0.058 ± 0.002
	g	0.737	0.737	0.739
	h	0.934	0.940	0.945
	g'	0.779	0.797	0.806
stars, (f=3)	$\langle {R_g}^2 \rangle_{\text{total}}$	164 ± 1	374 ± 2	616 ± 8
	$\langle {R_g}^2 \rangle_{\text{arms}}$	58.8 ± 0.6	136.4 ± 0.7	224 ± 2
	$\langle {R_h}^{-1} \rangle$	0.102 ± 0.0006	0.070 ± 0.001	0.055 ± 0.001
	g	0.777	0.774	0.776
	h	0.967	0.975	0.977
	g'	0.906	0.920	0.937

Table B.35: *Data of macromolecules of different topologies according to Figure 5.26 and Table 5.11 in Section 5.2.* $\lambda = 0.0$. *Values obtained by averaging over the backbone monomers and the monomers of side arms are displayed, as well as the calculated* g,h *and* g' *values.*

Topology	Quantity	$N = 301$	$N = 601$	$N = 901$
side 2	$\langle {R_e}^2 \rangle_{\text{backbone}}$	327 ± 3	645 ± 4	837 ± 9
	$\langle {R_e}^2 \rangle_{\text{arms}}$	84.9 ± 0.7	163 ± 2	250 ± 3
	$\langle {R_g}^2 \rangle_{\text{back}}$	56.2 ± 20.6	103.8 ± 0.7	148.7 ± 0.8
	$\langle {R_g}^2 \rangle_{\text{arms}}$	14.00 ± 0.05	$28.28 \pm 0.0.8$	$43.36 \pm 0.0.8$
	$\langle {R_g}^2 \rangle_{\text{total}}$	62.3 ± 0.6	115 ± 1	163 ± 2
	$\langle {R_h}^{-1} \rangle$	0.153 ± 0.001	0.111 ± 0.001	0.100 ± 0.001
	g	0.723	0.717	0.708
	h	0.918	0.931	0.933
	g'	0.788	0.889	0.801
side 4	$\langle {R_e}^2 \rangle_{\text{backbone}}$	355 ± 4	674 ± 9	905 ± 10
	$\langle {R_e}^2 \rangle_{\text{arms}}$	42.4 ± 0.9	87.7 ± 0.5	127 ± 2
	$\langle {R_g}^2 \rangle_{\text{backbone}}$	60.0 ± 0.5	113.4 ± 0.6	158 ± 3
	$\langle {R_g}^2 \rangle_{\text{arms}}$	6.84 ± 0.06	14.26 ± 0.06	21.32 ± 0.06
	$\langle {R_g}^2 \rangle_{\text{total}}$	63.2 ± 0.8	119.2 ± 0.6	167 ± 2
	$\langle {R_h}^{-1} \rangle$	0.153 ± 0.001	0.114 ± 0.002	0.100 ± 0.002
	g	0.697	0.684	0.678
	h	0.876	0.876	0.879
	g'	0.718	0.668	0.665
H-molecule	$\langle {R_e}^2 \rangle_{\text{backbone}}$	363 ± 2	556 ± 5	856 ± 7
	$\langle {R_e}^2 \rangle_{\text{arms}}$	84.7 ± 0.8	176 ± 2	255 ± 3
	$\langle {R_g}^2 \rangle_{\text{backbone}}$	60.6 ± 0.4	106.1 ± 0.6	140 ± 1
	$\langle {R_g}^2 \rangle_{\text{arms}}$	13.99 ± 0.07	29.22 ± 0.07	42.3 ± 0.8
	$\langle {R_g}^2 \rangle_{\text{total}}$	70.4 ± 0.5	123 ± 1	181 ± 2
	$\langle {R_h}^{-1} \rangle$	0.148 ± 0.001	0.113 ± 0.002	0.097 ± 0.001
	g	0.798	0.799	0.796
	h	0.923	0.940	0.943
	g'	0.864	0.849	0.796
side 10	$\langle {R_e}^2 \rangle_{\text{backbone}}$	343 ± 2	542 ± 5	848 ± 9
	$\langle {R_e}^2 \rangle_{\text{arms}}$	15.81 ± 0.06	33.7 ± 0.6	51.9 ± 0.8
	$\langle {R_g}^2 \rangle_{\text{backbone}}$	57.8 ± 0.8	94.0 ± 0.5	138 ± 1
	$\langle {R_g}^2 \rangle_{\text{arms}}$	2.56 ± 0.03	5.411 ± 0.05	8.35 ± 0.06
	$\langle {R_g}^2 \rangle_{\text{total}}$	$60.0pm0.4$	97.5 ± 0.5	142 ± 1
	$\langle {R_h}^{-1} \rangle$	0.158 ± 0.001	0.123 ± 0.002	0.103 ± 0.001
	g	0.723	0.717	0.709
	h	0.904	0.915	0.918
	g'	0.783	0.810	0.803
stars, (f=3)	$\langle {R_g}^2 \rangle_{\text{total}}$	65.6 ± 0.1	126.5 ± 0.8	111 ± 1
	$\langle {R_g}^2 \rangle_{\text{arms}}$	28.3 ± 0.1	55.4 ± 0.5	68.7 ± 0.8
	$\langle {R_h}^{-1} \rangle$	0.154 ± 0.001	0.111 ± 0.001	0.109 ± 0.002
	g	0.734	0.735	0.726
	h	0.939	0.954	0.958
	g'	0.778	0.773	0.774

Table B.36: *Data of macromolecules of different topologies according to Figure 5.26 and Table 5.11 in Section 5.2.* $\lambda = 0.65$. *Values obtained by averaging over the backbone monomers and the monomers of side arms are displayed, as well as the calculated* g,h *and* g' *values.*

Appendix C

Rotation matrix of a vector

In a coordinate system with unit vectors $(\vec{e}_1, \vec{e}_2, \vec{e}_3)$ where $\vec{e}_3 \parallel \vec{v}$, $\vec{v}$ arbitrary, the expression for the rotation matrix M for a rotation of a vector $\vec{r}$ about the $\vec{e}_3$–axis with angle α is:

$$\mathcal{M} = \begin{pmatrix} \cos\alpha & -\sin\alpha & 0 \\ \sin\alpha & -\cos\alpha & 0 \\ 0 & 0 & 1 \end{pmatrix}.$$

Thus, for the expression of the spinned vector one yields:

$$\begin{aligned} \vec{r}' &= \vec{e}_1 \left[\cos\alpha \, (\vec{r}\vec{e}_1) - \sin\alpha \, (\vec{r}\vec{e}_2)\right] \\ &+ \vec{e}_2 \left[\cos\alpha \, (\vec{r}\vec{e}_2) + \sin\alpha \, (\vec{r}\vec{e}_1)\right] \\ &+ \vec{e}_3 (\vec{r}\vec{e}_3) \end{aligned}$$

The individual unit vectors $\vec{e}_i$ can be expressed in terms of $\vec{r}$ and $\vec{v}$:

$$\begin{aligned} \vec{e}_3 &= \frac{\vec{v}}{v} = \vec{v}_n \\ \vec{e}_2 &= \frac{\vec{v}_n \times \vec{r}}{\mid \vec{v}_n \times \vec{r} \mid} \\ \vec{e}_1 &= \frac{\vec{r} - \vec{v}_n(\vec{v}_n\vec{r})}{\mid \vec{r} - \vec{v}_n(\vec{v}_n\vec{r}) \mid}, \end{aligned}$$

with

$$\mid \vec{v}_n \times \vec{r} \mid \;=\; \mid \vec{r} - \vec{v}_n(\vec{v}_n\vec{r}) \mid = \sqrt{\vec{r}^2 - (\vec{v}_n\vec{r})^2}.$$

It follows:

$$\begin{aligned} \vec{e}_3\vec{r} &= \vec{v}_n\vec{r}, \\ \vec{e}_2\vec{r} &= 0, \\ \vec{e}_1\vec{r} &= \sqrt{\vec{r}^2 - (\vec{v}_n\vec{r})^2}, \\ (\vec{e}_1\vec{r})\vec{e}_1 &= \vec{r} - \vec{v}_n(\vec{v}_n\vec{r}), \\ (\vec{e}_1\vec{r})\vec{e}_2 &= \vec{v}_n \times \vec{r}. \end{aligned}$$

With these results one finally yields:

$$\begin{aligned}\vec{r}' &= \cos\alpha\,(\vec{r}\vec{e}_1)\;\vec{e}_1 + \sin\alpha\,(\vec{r}\vec{e}_1)\;\vec{e}_2 + (\vec{r}\vec{e}_3)\;\vec{e}_3 \\ &= \cos\alpha\,(\vec{r} - \vec{v}_n\,(\vec{v}_n\vec{r})) + \sin\alpha\,(\vec{v}_n \times \vec{r}) + \vec{v}_n\,(\vec{r}\vec{v}_n) \\ &= \vec{r}\cos\alpha + (\vec{v}_n \times \vec{r})\sin\alpha + \vec{v}_n(\vec{v}_n\vec{r})(1 - \cos\alpha)\end{aligned}$$

which corresponds to Eq. (3.13) on page 27.

Appendix D

The simulation code

One aim of this work was the development of a code for the simulation of polymer chains with variable topologies and molecular weights N. The code should be able to perform simulations of single isolated chains as well as of chains in a dense melt. Moreover, it should be designed in a style that allows for further changes without having to change the whole concept.

These objectives require a modular code design, as there are different functional units which crucially influence the performance of the code. A modular structure not only simplyfies the optimization of individual parts of the code, but also the exchanging of single modules during the test stage of development. The principal design of a simulation program, independent of the particular implementation, is sketched in Fig. D.1 on Page 168.

The individual parts of the code design are as follows:

- **Initialization:** The initialization routine. It initializes all independent parameters that characterize the respective physical system. The specific values are given by the initial conditions. This routine is done only once in a simulation and hence is not time critical.
- **Integration:** The integration routine. It contains the numerical part of the simulation. A particular implementation of the used algorithm for the integration of the equations of motion is included in this routine. It is the most time critical part of the whole simulation and requires special attention in particular when including long-range interactions, such as coulomb forces or when using very large systems. Virtually all efforts for code optimization deal with this particular part of the code.
- **Output:** The output routine. It stores the obtained simulation data on a hard disk medium to enable a later analyzing and grafic presentation of the results. The actual visualization is usually done with other commercial tools.

There is a hole host of languages of the third generation available for an implementation. However, in simulations *speed* is the most crucial criterion for the choice of a specific language. This immediately rules out Java, an object-oriented language, perfectly portable on any operating system, but usually not available on super computers. As the interpretation of byte code upon run time decreases the performance considerably, this language is not suitable for high performance simulations. C++, on the other hand, is available on most super computer facilities but has the disadvantage of lacking a standard. At present, there is only a provisional ANSI-standard which is not being abided by by all manufacturers. Because extensive use was made of dynamic memory allocation, C was used

Figure D.1: *Principal design of a simulation code.*

for an implementation of the model described in Chapter 3.4 and C++ for all others, not time critical tools.

The main code consists of approx. 15.000 lines of code [3] and is fully documented. Another approx. 4.000 lines pertain to the tool that contains all analyze routines for calculating static, dynamic or structural properties. Further 1.000 lines went into coding the tool that sets up the configuration files which contain all relevant simulation parameters and which are read upon starting the main simulation. Finally another approx. 1.000 lines are contained in the tool that prepares the data for being processed by commercial visualization tools such as xmol, insightII or VMD.

D.1 Code documentation

In the following, the different modules of the main simulation code are described in some more detail to elucidate the functionality of the code and to clarify how the modules are related to each other (see Fig. D.3 on Page 170 for a complete overview).

First of all, the different initialization routines parse the command-line arguments (**init_arguments)**, the parameters of the configuration file (**init_param.c**), check them for consistency (**init_paramCheck.c**), then allocate all needed memory (**init_allocation.c**) and finally calculate often used lemma variables that never change throughout the simulation such as the number of ghost cells or the size of sub-cells in each direction (**init_calculateConstants.c**).

The next module (**init.c**) sets up the polymer chains in the simulation box by means of a process that is described in detail in Section 3.3.2 on Page 32.

The properties of individual particles are stored in a *C-structure* that contains all topological information that is necessary for unambiguously identifying the individual particles, see Fig. D.2. The advantage of this topology structure is, that *any* desired topology can be accommodated in the simulation code without having to change anything in the main code. The parameters of the simulation are set appropriately by the configuration tool.

Due to possible singularities in the potential because of overlapping monomers one has to perform a *warmup procedure* (**warmup.c**) which gradually switches on the full excluded volume interaction.

[3] All figures including documentation.

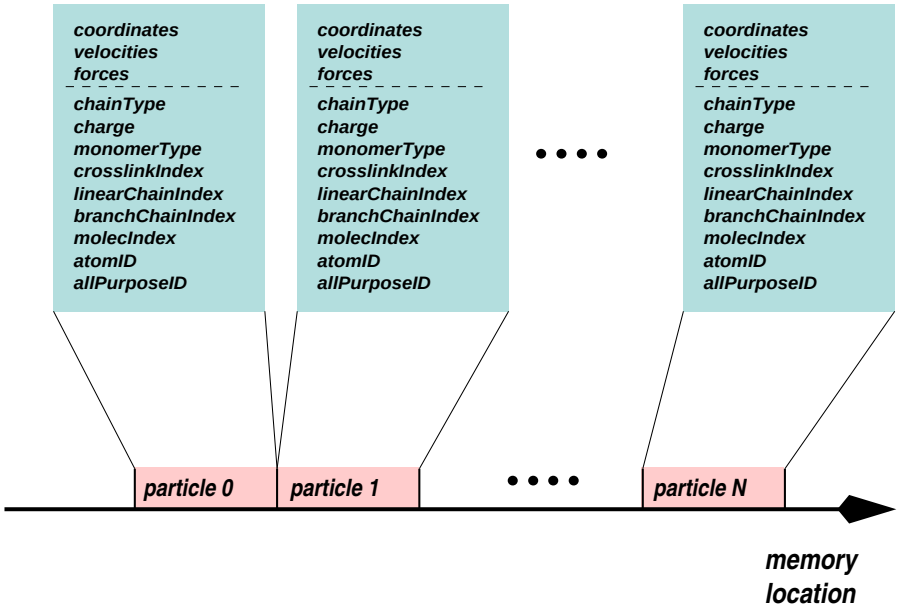

Figure D.2: *Members of the data structure that contains all information of the particles. The individual particle data are stored consequtively in computer memory and can be accessed by making use of the respective particle index.*

This warmup procedure is annotated in Section 3.3.2. After the particles are set in the simulation box, the structures to accommodate the neighbor-list tables (**verletTables.c**) and ghost particles (**ghosts.c**) are allocated and initialized.

The actual integration loop begins with calculating the forces (**forces.c**) on the particles according to the used potentials (**lennard_cosinus.c**), (**fene.c**). In addition to the actually used potentials, there is another module (**coulomb.c**) which contains an implementation of the *Ewald summation technique* [68], [128] and allows for the individual assignment of electric charges to the monomers.

The integrator is implemented in (**bd_verlet.c**). Pivot moves (**pivot.c**) can be used in addition to MD-steps. After the last integration step, but also *during* the simulation run, the system data are stored on hard disk for later analysis (**file_handling.c**).

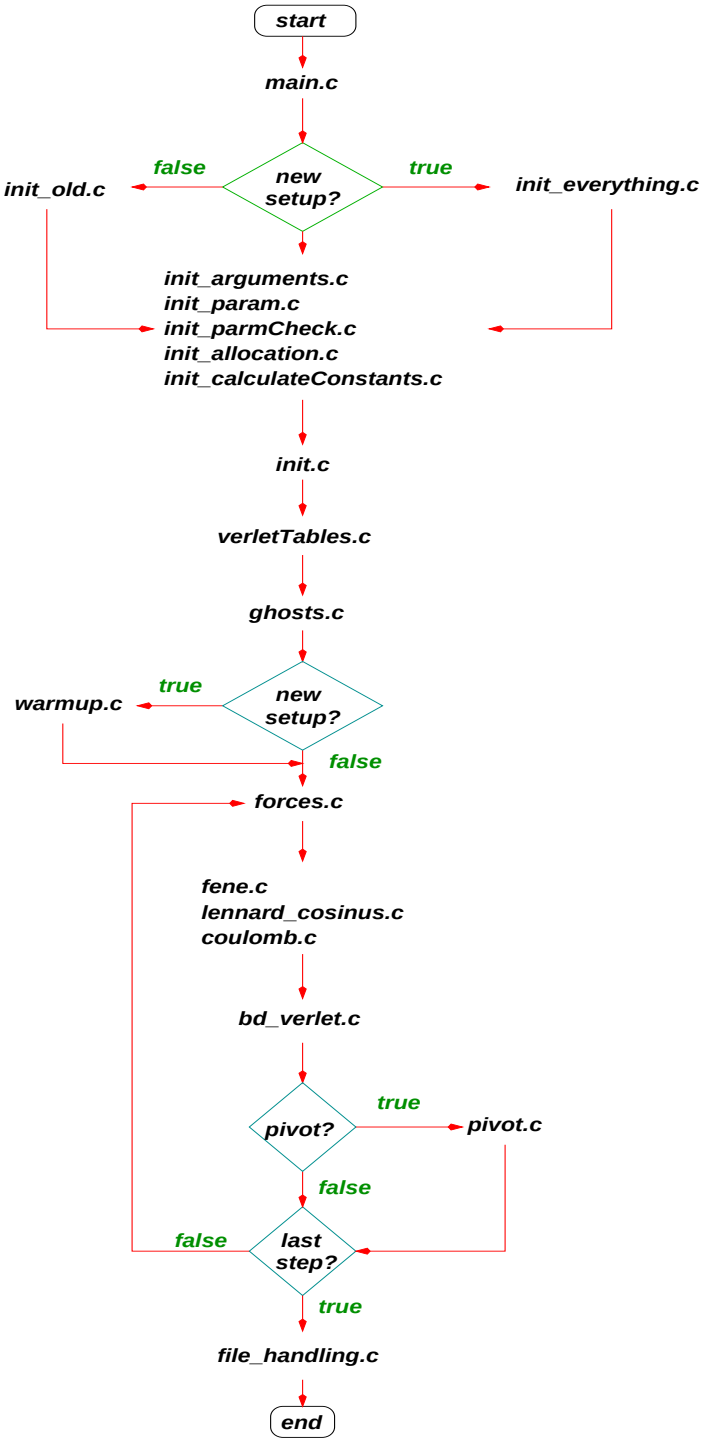

Figure D.3: *Float diagram displaying the order at which different modules of the main simulation code are called.*

As a summary, the most important features of the developed simulation code are as follows:

- Portability on many different architectures due to strict usage of ANSI-C.
- Suitability for simulations of single chains as well as of chains in a dense melt.
- Feasibility of simulations of branched chains, as well as of mixtures of different topologies.
- Good scalability of the code of approx. 380.000 particle updates per second.
- Full documentation.
- Easy adaptation to special needs due to a strict modular code-structure with well defined interfaces.

Appendix E

Derivation of the leading corrections to scaling for the hydrodynamic radius

The following simple derivation is proposed in [66].

In principle, the whole information about chain configurations is stored in the static structure factor $S(k)$ which is just the $t = 0$ value of $S(k, t)$. The approach we are taking here is to consider a very simple model function for $S(k)$, which should contain all the important physical features, scaling behavior as well as the finiteness of R_g and of a. $S(k)$ has the well–known properties [56]

- $S(k) \to N$ for $k \to 0$,
- $S(k) \to 1$ for $k \to \infty$ and
- $S(k) = Ak^{-1/\nu}$ in the scaling regime $R_g^{-1} \ll k \ll a^{-1}$. Here the prefactor A is independent of chain length.

Hence, we choose the following highly oversimplified function for $S(k)$:

$$S(k) = \begin{cases} N & 0 \le k \le 2\pi/R_0 \\ Ak^{-1/\nu} & 2\pi/R_0 \le k \le 2\pi/a \\ 1 & 2\pi/a \le k < \infty. \end{cases} \tag{E.1}$$

Here R_0 is some measure of the size of the chain which scales in the same way as the radius of gyration. Continuity of $S(k)$ requires

$$R_0 = aN^{\nu} \tag{E.2}$$

and

$$A = \left(\frac{a}{2\pi}\right)^{-1/\nu}. \tag{E.3}$$

In order to calculate the hydrodynamic radius from the structure factor, we integrate the relation

$$\frac{S(k)-1}{N} = \frac{1}{N^2}\sum_{i\neq j}\left\langle \frac{\sin(kr_{ij})}{kr_{ij}} \right\rangle \tag{E.4}$$

over k. In every term, the integration variable can be changed from k to $x = kr_{ij}$ and hence

$$\int_0^\infty dk \frac{S(k)-1}{N} = \frac{1}{N^2}\sum_{i\neq j}\left\langle \frac{1}{r_{ij}}\int_0^\infty dx \frac{\sin x}{x} \right\rangle = \frac{\pi}{2}\left\langle \frac{1}{R_h} \right\rangle . \tag{E.5}$$

Inserting our model function from above, one straightforwardly obtains

$$\left\langle \frac{1}{R_h} \right\rangle = \frac{4}{(1-\nu)a}\left(\frac{1}{N^\nu} - \frac{1}{N} \right) \tag{E.6}$$

or

$$N^{-\nu}\left\langle R_h^{-1} \right\rangle^{-1} = \frac{a}{4}(1-\nu)\left(1 - N^{\nu-1}\right)^{-1}, \tag{E.7}$$

giving the leading correction to scaling as

$$N^{-\nu}\left\langle R_h^{-1} \right\rangle^{-1} = \frac{a}{4}(1-\nu)(1 + N^{\nu-1}), \tag{E.8}$$

which is the functional form anticipated above (cf. Eq. 4.15) on Page 63.

Appendix F

Snapshots of the dendrimers

This appendix contains a series of representative snapshots of symmetric dendrimers taken from simulation runs. Snapshots of all simulated generations ($G = 1 - 7$) are displayed. The color code is such that monomers belonging to the spacers of endgroups are displayed in red whereas all other monomers are displayed in grey. The snapshots are ordered such that good solvent dendrimers are always displayed on the left side and corresponding snapshots in a θ-solvent are displayed on the right side for each generation.

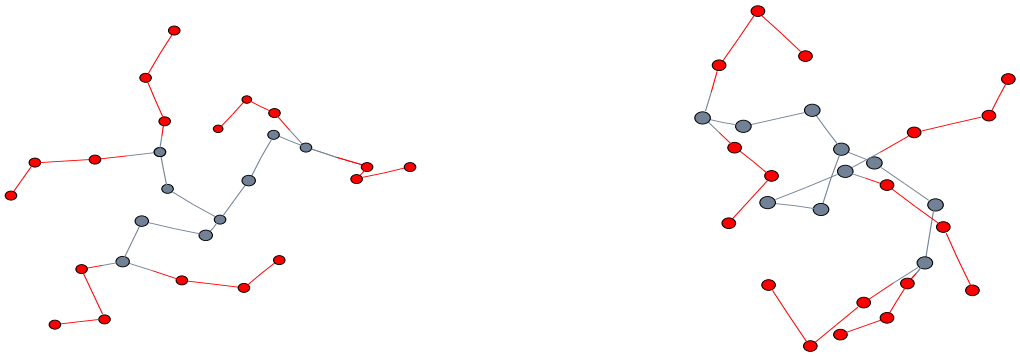

Figure F.1: *Snapshot of a regular dendrimer.* $G = 1$, $N = 28$.

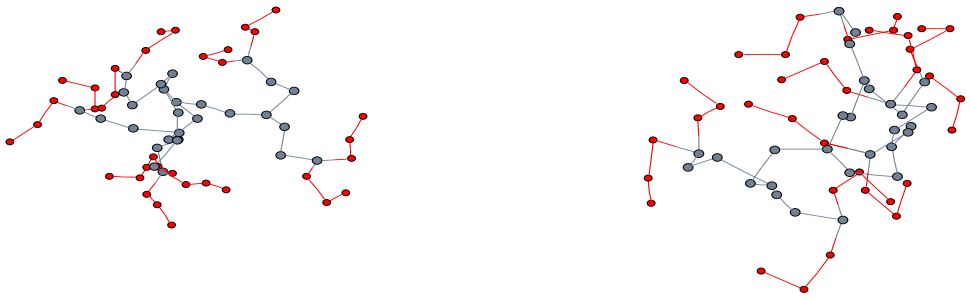

Figure F.2: *Snapshot of a regular dendrimer.* $G = 2$, $N = 64$.

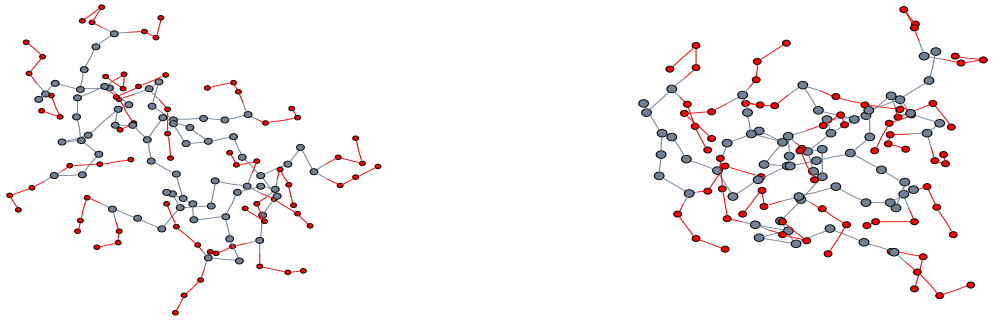

Figure F.3: *Snapshot of a regular dendrimer.* $G = 3$, $N = 136$.

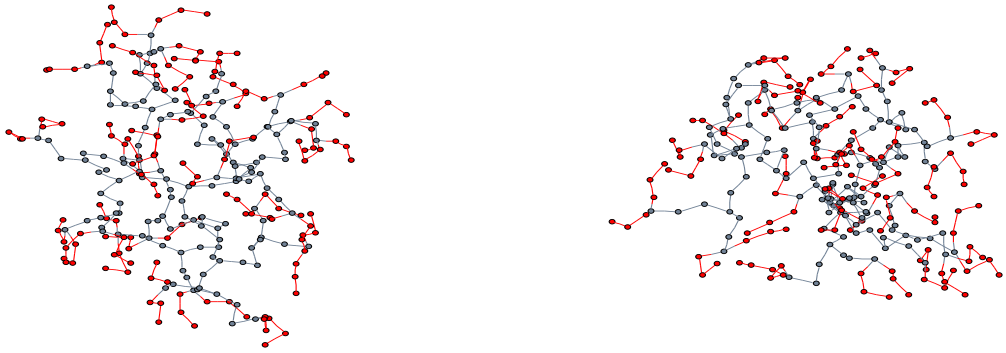

Figure F.4: *Snapshot of a regular dendrimer.* $G = 4$, $N = 280$.

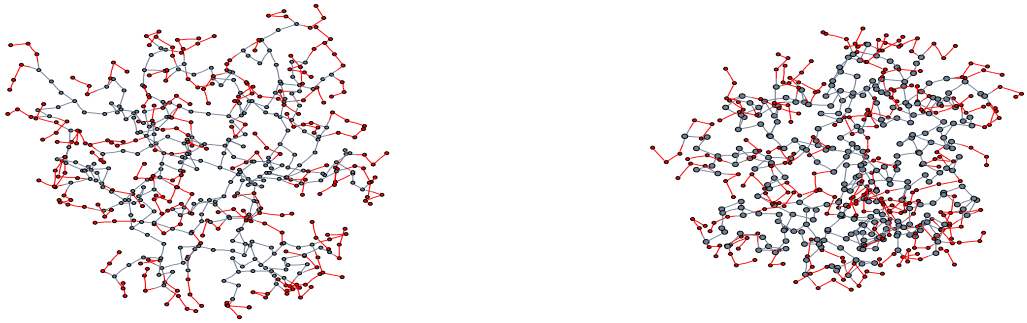

Figure F.5: *Snapshot of a regular dendrimer.* $G = 5$, $N = 567$.

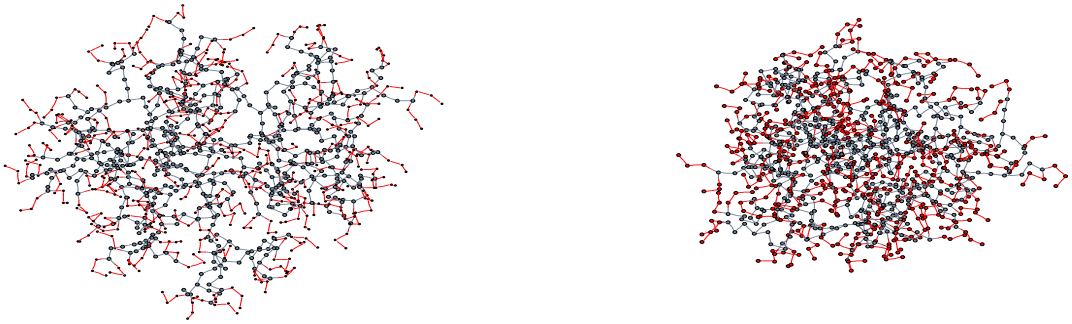

Figure F.6: *Snapshot of a regular dendrimer.* $G = 6$, $N = 1144$.

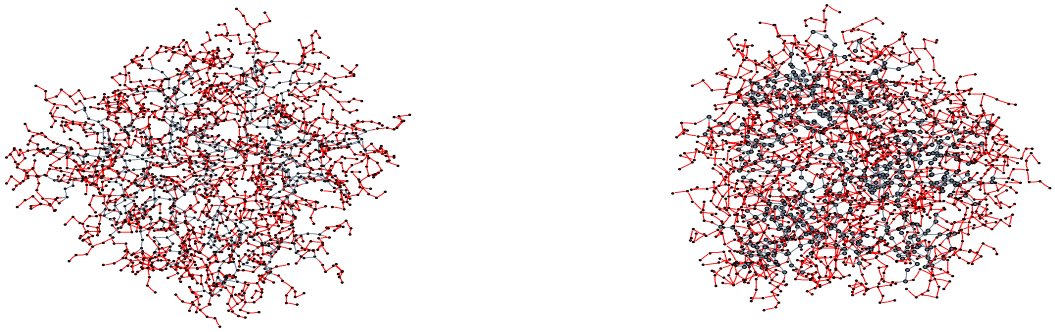

Figure F.7: *Snapshot of a regular dendrimer.* $G = 7$, $N = 2296$.

Bibliography

[1] **A. Z. Akcasu, C. C. Han:** *Molecular weight and temperature dependence of polymer dimensions in solution*.
Macromolecules **12**, (2), 276 (1979).

[2] **M. Adam, M. Delsanti:** *Light scattering by dilute solution of polystyrene in good solvent*.
J. Phys-Paris **37**, 1045 (1976).

[3] **D. J. Adams:** *Alternatives to the periodic cube in computer simulations*.
CCP5 Quarterly **10**, 30 (1983a).

[4] **A. Aharony, J. Feder:** *Fractals in physics – Essays in honor of B. B. Madelbrot*.
North Holland, Amsterdam (1990).

[5] **B. J. Alder, T. E. Wainwright:** *Phase transition for a hard sphere system*.
J. Chem. Phys. **27**, 1208 (1957).

[6] **B. J. Alder, T. E. Wainwright:** *Studies in Molecular Dynamics. I. General method*.
J. Chem. Phys. **31**, 459 (1959).

[7] **Z. Alexandrowicz:** *Monte Carlo of chains with excluded volume - A way to Evade sample attrition*.
J. Chem. Phys. **51**, 561 (1969).

[8] **M. P. Allen, D. J. Tildesley:** *Computer simulation of liquids*.
Oxford University Press (1991).

[9] **J. A. Aronovitz and D. R. Nelson:** *Universal features of polymer shapes*.
J. Phys-Paris **47**, 1445 (1986).

[10] **D. E. Axelson, W. C. Knapp:** *Size exclusion chromatography and low-angle laser light scattering. Application to the study of long chain-branched polyethylene*.
J. Appl. Polym. Sci. **25**, 119 (1980).

[11] **Matthias Ballauff:** *Topics in current chemistry*.
Springer Verlag Berlin Heidelberg, Vol. 212 (2001).

[12] **A. J. Barrett and D. L. Tremain:** *Lattice walk models of uniform star polymers with many arms*.
Macromolecules **20**, 1687 (1987).

[13] **J. Batoulis and K. Kremer:** *Thermodynamic properties of star polymers: Good solvents*.
Macromolecules **22**, 4277 (1989).

[14] **J. Batoulis:** *Monte-Carlo Simulationen von Sternpolymeren*.
PhD thesis, Mainz (1987).

[15] **B. J. Bauer, L. J. Fetters, W. W. Graessley, N. Hadjichristidis, G. F. Quack:** *Chain dimensions in dilute polymer-solutions - A light-scattering and viscometric study of multiarmed polyisoprene stars in good and theta-solvents*.
Macromolecules **22**, 2337 (1989).

[16] **A. Baumgärtner:** *Statics and dynamics of the freely jointed polymer chain with Lennard-Jones interaction*.
J. Chem. Phys. **72**, (2), 871 (1980).

[17] **A. Baumgärtner and K. Binder:** *Monte-Carlo studies on the freely jointed polymer chain with excluded volume interaction*.
J. Chem. Phys. **71**, (6), 2541 (1979).

[18] **A. Beldjenna, J. Rudnick, G. Gaspari:** *Shapes of random walks at order 1/D2*.
J. Phys. A **24**, (9), 2131 (1991).

[19] **T. W. Beneke, W. Schwippert:** *Datenanalyse und Präsentation mit Origin*.
Addison–Wesley Longman Inc. (1997).

[20] **B. J. Berne and R. Pecora:** *Dynamic light scattering*.
Wiley, New York (1976).

[21] **M. Bhatt, A. M. Jamieson and R. G. Petschek:** *Static and dynamic scaling relationships in the light scattering properties of polystyrenes in good solvents*.
Macromolecules **22**, 1374 (1989).

[22] **F. W. Billmeyer:** *The molecular structure of polyethylene. III. Determination of long chain branching*.
J. Amer. Chem. Soc. **75**, 6118 (1953).

[23] **K. Binder:** *Monte-Carlo methods in condensed matter physics*.
Springer Verlag Berlin (1992).

[24] **K. Binder:** *Monte-Carlo and Molecular Dynamics simulations in polymer science*.
Oxford University Press (1995).

[25] **K. Binder:** *Applications of Monte-Carlo methods to statistical physics*.
Reports on Progress in Physics, **60**, (5), 487 (1997).

[26] **K. Binder, D. W. Heermann:** *Monte-Carlo simulations in statistical physics*.
Springer Verlag Berlin, Heidelberg, New York, Tokyo, (1988).

[27] **R. B. Bird, H. C. Öttinger:** *Transport properties of polymeric liquids*.
Annu. Rev. Phys. Chem. **43**, 371 (1992).

[28] **T. M. Birshtein, E. B. Zhulina:** *Conformations of star-branched macromolecules*.
Polymer **25**, 1453 (1984).

[29] **T. M. Birshtein, S. V. Buldyres and A. M. Elyashevitch:** *Monte-Carlo simulation of the collapse transition of a two-dimensional polymer*.
Polymer **26**, 1814 (1985).

[30] **T. M. Birshtein, E. B. Zhulina, O. V. Borisov:** *Temperature concentration diagram for a solution of star-branched macromolecules*.
Polymer **27**, 1078 (1986).

[31] **J. J. Binney, N. J. Dowrick, A. J. Fisher and M. E: J. Newman:** *The theory of critical phenomena*.
Oxford University Press, (1992).

[32] **M. Bishop and J. P. J. Michels:** *Polymer shapes in three dimensions*.
J. Chem. Phys. **85**, (10), 5961 (1986).

[33] **M. Bishop and Saltiel:** .
J. Chem. Phys. **88**, 6594 (1988).

[34] **M. Bishop and J. H. R. Clarke:** *Brownian Dynamics study of the shape of star and linear polymers in different regimes*.
J. Chem. Phys. **90**, (11), 6647 (1989).

[35] **M. Bishop, W. Smith:** *Brownian Dynamics simulation of linear and star polymers*.
J. Chem. Phys. **95**, (5), 3804 (1991).

[36] **Marvin Bishop, J. H. R. Clarke, A. Rey and J. J. Freire:** *Shape of linear and star polymers with and without excluded volume*.
J. Chem. Phys. **94**, (5), 4009 (1991).

[37] **I. Bodnar, A. S. Silva, R. W. Deitcher, N. E. Weisman, Y. H. Kim, N. J. Wagner:** *Structure and rheology of hyperbranched and dendritic polymers. I. Modification and characterization of poly(propyleneimine) dendrimers with acetyl groups.* J. Polym. Sci. **38**, 857 (2000).

[38] **M. Bohdanecki, J. Kovar:** *Viscosity of polymer solutions*.
Elsevier, Amsterdam (1982).

[39] **D. Boris, M. Rubinstein:** *A self-consistent mean field model of a starburst dendrimer: Dense core vs. dense shell*.
Macromolecules **29**, 7951 (1996).

[40] **D. C. Bugada and A. Rudin:** *Sizes of long branches in low density polyethylenes*.
J. Appl. Polym. Sci. **33**, 87 (1987).

[41] **A. Bunde:** *Fractals in science*.
Springer Verlag, Heidelberg (1994).

[42] **W. Burchard:** *Static and dynamic light scattering from branched polymers and bio-polymers*.
Adv. Polym. Sci. **48**, 1 (1983).

[43] **W. Burchard, M. Schmidt and W. Stockmayer:** *Information on polydispersity and branching from combined quasi-elastic and integrated scattering.*.
Macromolecules **13**, 1265 (1980).

[44] **Bruns, W. Carl:** *Relations between averaged configurational properties of linear and starlike polymer models at the theta-temperature*.
Macromolecules **24**, (1), 209 (1991).

[45] **Bywater, S.:** *Preparation and properties of star branched polymers*.
Adv. Polym. Sci. **30**, 89 (1979).

[46] **J. W. Cannon, J. A. Aronovitz and P. Goldbart:** *Equilibrium distribution of shapes for linear and star macromolecules*.
J. Phys-Paris **1**, 629 (1991).

[47] **G. Cherbit:** *Non-integral dimensions and applications*.
John Wiley & Sons, New York (1991).

[48] **B.Chu, R. L. Xu, J. Zuo:** *Transition of polystyrene in cyclohexane from the theta to the collapsed state*.
Macromolecules **21**, (1), 273 (1988).

[49] **U. Dayal:** *High-temperature SEC copupled with MALLS detector for evaluating the end-use performance of LDPE*.
J. Appl. Polym. Sci. **53**, 1557 (1994).

[50] **M. Daoud, C. E. Williams:** *La juste argile*.
Les Editions de Physique, Paris 1995.

[51] **M. Daoud, G. Jannink:** *Temperature concentration diagram of polymer solutions*.
J. Phys-Paris **37**, 973 (1976).

[52] **M. Daoud, J. P. Cotton:** *Star shaped polymers: A model for the conformation and its concentration dependence*.
J. Phys-Paris **43**, 531 (1982).

[53] **G. P. de Gennes:** *Giant fluctuations and critical phenomena*.
Recherche **5**, (51), 1022 (1974).

[54] **G. P. de Gennes:** *Collapse of a polymer chain in poor solvents*.
J. Phys. Lett-Paris **36**, L55 (1975).

[55] **G. P. de Gennes:** *Collapse of a flexible polymer chain II*.
J. Phys. Lett-Paris **39**, L299 (1978).

[56] **P. G. de Gennes:** *Scaling concepts in polymer physics*.
Cornell University Press, Ithaca, London (1979).

[57] **P. G. de Gennes and H. Hervet:** *Statistics of starburst polymers*.
J. Phys-Paris **44** (9), L351 (1983).

[58] **H. W. Diehl:** *Universal shape ratios for open and closed random-walks – exact results for all dimensions*.
J. Phys. A **22**, (3), L87 (1989).

[59] **M. Doi, S. F. Edwards:** *The Theory of Polymer Dynamics*.
Clarendon Press, Oxford (1986).

[60] **C. Domb:** *Phase-transition in a polymer chain in dilute solutions*.
Polymer **15**, 259 (1974).

[61] **J. F. Douglas and K. F. Freed:** *Polymer contraction below the θ–point: A renormalization group description*.
Macromolecules **18**, 2445 (1985).

[62] **J. F. Douglas, J Roovers and K. F. Freed:** *Characterization of branching architectures through "universal" ratios of polymer solution properties*.
Macromolecules **23**, 2168 (1990).

[63] **B. Duplantier:** *Tricritical polymer chains in or below 3 dimensions*.
Europhys. Lett. **1**, (10), 491 (1986).

[64] **B. Duplantier:** *Direct or dimensional renormalizations of the tricritical polymer theory*.
J. Phys-Paris **47**, (5), 745 (1986).

[65] **B. Duplantier:** *Geometry of polymer chains near the theta-point and dimensional regularization*.
J. Chem. Phys. **86**, (7), 4233 (1987).

[66] **B. Dünweg, M. Steinhauser, D. Reith, K. Kremer:** *Corrections to scaling in the hydrodynamics of dilute polymer solutions*.
To be published in Macromolecules.

[67] **B. E. Eichinger:** *Shape distributions for Gaussian molecules*.
Macromolecules **18**, (2), 211 (1985).

[68] **P. Ewald:** *Die Berechnung optischer und elektrostatischer Gitterpotentiale*.
Ann. Phys. **64**, 253 (1921).

[69] **W. Feller:** *An introduction to probability theory and its applications*.
Wiley, New York (1950).

[70] **M. Fischer, F. Vögtle:** *Dendrimers: From design to application - A progress report*.
Angew. Chem. Intl. Ed. **38**, (7), 884 (1999).

[71] **M. Fixman:** *Radius of gyration of polymer chains*.
J. Chem. Phys. **36**, (2), 306 (1962).

[72] **P. J. Flory:** *Priciples of polymer chemistry*.
Cornell University Press, Ithaca, New York (1953).

[73] **P. J. Flory:** *Statistical mechanics of chain molecules*.
Wiley, New York (1969).

[74] **J. M. J. Fréchet, C. J. Hawker, I. Gitsov and J. W. Leon:** .
Macromol. Sci. Pure Appl. Chem. Soc. **A33**, 1399 (1990).

[75] **J. J. Freire, J. Pla, A. Rey and R. Prats:** *Monte-Carlo calculations for linear and star polymers with intramolecular interactions. 1. Dimensions*.
Macromolecules **19**, 452 (1969).

[76] **J. J. Freire, A. Rey, J.G. de la Torre:** *Monte-Carlo calculations for linear and star polymers with intramolecular interactions. 2. Nonpreaveraged study of hydrodynamic properties at the θ-state.*
Macromolecules **19**, 457 (1986).

[77] **F. Ganazzoli:** *Two- and three-body interactions in the θ-state: Linear and star polymers*.
Macromolecules **25**, 7357 (1992).

[78] **B. M. Gammel:** *Hurst's rescaled range statistical analysis for pseudorandom number generators used in physical simulations*.
Phys. Rev. E **58**, 2886 (1998).

[79] **G. Gaspari, J. Rudnick, A. Beldjenna:** *The shapes and sizes of 2-dimensional pressurized, self-intersecting rings, as models for 2-dimensional vesicles*.
J. Phys. A **26**, (1), 1 (1993).

[80] **C. W. Gear:** *Numerical initial value problems in ordinary differential equations*.
Prentice Hall, Englewood Cliffs, New Jersey (1971).

[81] **H. Gould, J. Tobochnik:** *An introduction to computer simulation methods*.
Addison Wesley, Reading, Massachusetts (1996).

[82] **P. Grassberger and R. Hegger:** *Simulations of three-dimensional θ-polymers*.
J. Chem. Phys. **102**, (17), 6881 (1994).

[83] **P. Grassberger:** *Pruned-enriched Rosenbluth method: Simulations of θ-polymers of chain length up to 1,000.000*.
Phys. Rev. E **56**, (3), 3682 (1996).

[84] **G. S. Grest, L. J. Fetters. J. S. Huang, D. Richter:** *Star polymers: Experiment, theory and simulation*.
Adv. Chem. Phys., Vol. XCIV **94**, 67 (1996).

[85] **G. S. Grest and K. Kremer:**
Molecular Dynamics simulation for polymers in the presence of a heat bath.
Phys. Rev. A **33**, 5 (1986).

[86] **G. S. Grest, K. Kremer und T. A. Witten:** *Structure of many-arm star polymers: A Molecular Dynamics simulation*.
Macromolecules **20**, 1376 (1986).

[87] **G. S. Grest, K. Kremer, S. T. Millner und T. A. Witten:** *Relaxation of self-entangled many-arm star polymers*.
Macromolecules **20**, 1965 (1987).

[88] **G. S. Grest and M. Murat:** *Structure of grafted polymeric brushes in solvents of varying quality: A Molecular Dynamics study*.
Macromolecules **26**, 3108 (1993).

[89] **A. Y. Grossberg and A. R. Khoklov:** *Statistical physics of macromolecules*.
American Institute of Physics, New York (1994).

[90] **W. F. van Gunsteren and H. J. C. Berendsen:** *Algorithms for Brownian Dynamics*.
Molec. Phys. **45**, 637 (1982).

[91] **W. F. van Gunsteren, E. Smith, R. Sperb, I. Tironi:** *A general reaction field method for Molecular Dynamics simulations*.
J. Chem. Phys. **102**, 5451 (1995).

[92] **I. Gutman, Y. N. Yeh, S. L. Lee, Y. L. Luo:** *Some recent results in the theory of the Wiener number*.
Ind. J. Chem. **32A**, 651 (1993).

[93] **J. Han and R. H. Boyd:** *Small-molecule penetrant diffusion in hydrocarbon polymers as studied by Molecular Dynamics simulation*.
Macromolecules **27**, 5365 (1994).

[94] **C. J. Hawker, J. M. J. Fréchet:** *Preparation of polymers with controlled molecular architecture - A new convergent approach to dendritic macromolecules*.
J. Am. Chem. Soc. **112**, 7638 (1990).

[95] **R. C. Hayward, W. W. Graessley:** *Excluded volume effects in polymer solutions. 1. Dilute solution properties of linear chains in good and θ–solvents*.
Macromolecules **32**, 3502 (1999).

[96] **L. J. Hobson, W. J. Feast:** *Dendritic solution viscosity behavior in core terminated hyperbranched poly(amidoamine)s*.
Chem. Commun. **21**, 2067 (1997).

[97] **R. W. Hockney and J. W. Eastwood:** *Computer simulation using particles*.
Mc Graw Hill, New York (1981).

[98] **B. Hoffmann:** *Albert Einstein*.
Zürich, p. 297 (1976).

[99] **W. G. Hoover:** *Molecular Dynamics*.
Springer Verlag, Berlin, New York (1986).

[100] **K. Huber, W. Burchard, S. Bantle, L. J. Fetters:** *Monte-Carlo calculations in comparison to neutron-scattering studies. 2. Global dimensions of 12-arm stars*.
Polymer **28**, 1990 (1987).

[101] **J. Han and R. H. Boyd:** *Small-molecule penetrant diffusion in hydrocarbon polymers as studied by Molecular Dynamics simulation*.
Macromolecules **27**, 5365 (1994).

[102] **J. H. Huang, W. H. Jiang, S. J. Han:** *A Monte-Carlo simulation on shape of grafted polymer chains*.
Chem. J. Chinese U. **21**, (4), 629 (2000).

[103] **K. Inoue:** *Functional dendrimers, hyperbranched and star polymers*.
Prog. Polym. Sci. **25**, 453, (2000).

[104] **R. A. Jackson, P. A. Small, K. S. Whiteley:** *Prediction of molecular-weight distributions in branched polymers*.
J. Polym. Sci. Pol. Chem. **11**, (8), 1781 (1973).

[105] **O. Jagodzinski, E. Eisenriegler, K. Kremer:** *Universal shape properties of open and closed polymer-chains-renormalization-group analysis and Monte-Carlo experiments*.
J. Phys. **2**, (12), 2243 (1992).

[106] **A. Jăvos (ed.):** *Simulation in research and development*.
North-Holland, Amsterdam (1984).

[107] **K. Kajiwara, W. Burchard:** *Computer experiments on branched chain molecules*.
Macromolecules **15**, 660 (1982).

[108] **I. G. Kaplan:** *Einführung in die Theorie der zwischenmolekularen Wechselwirkungen*.
Nauka, Moskau (1982).

[109] **D. E. Knuth:** *The art of computer programming, Vol. 2: Seminumerical algorithms*.
Addison-Wesley, Reading, MA (1981).

[110] **T. Konishi, T. Yoshizaki and H. Yamakawa:** *On the "universal constants" ϱ and Φ of flexible polymers*.
Macromolecules **24**, 5614, (1991).

[111] **O. Kratky and G. Porod:** *Röbtgenuntersuchungen gelöster Fadenmoleküle*.
Recl. Trav. Chim. Pay B **68**, (12), 1106 (1949).

[112] **K. W. Kratky and W. Schreiner:** *Computational techniques for spherical boundary conditions.*.
J. Comput. Phys. **47**, 313 (1982).

[113] **P. Kratochvil:** *Classical light scattering from polymer solutions*.
Elsevier (1987).

[114] **K. Kremer, A. Baumgärtner and K. Binder:** *Collapse transition and crossover scaling for self-avoiding walks on the diamond lattice*.
J. Phys. A **15**, 2879 (1981).

[115] **J. I. Kroschwitz (Executive Editor)** *Encyclopedia of Polymer Science and Engeneering*.
J. Wiley & Sons, New York 1987.

[116] **W.Kuhn:** *Die Gestalt eines langen Kettenmoleküls*.
Kolloid-Z. **68**, 2 (1934).

[117] **A. J. C. Ladd and D. Frenkel:** *Computer simulation studies of static and dynamical scaling in dilute solutions of excluded-volume polymers*.
Macromolecules **25**, 3435 (1992).

[118] **M. Lal:** *Monte Carlo computer simulation of chain molecules. I.*.
Mol. Phys. **17**, 57 (1969).

[119] **L. Landau, E. M. Lifschitz:** *Lehrbuch der Theoretischen Physik, Bd. V, Statistische Physik*.
Akademie Verlag, Berlin (1966).

[120] **N. Launay, A. M. Caminade, J. P. Majoral:** *Synthesis and reactivity of unusual phosphorus dendrimers. A useful divergent growth approach up to the seventh generation*.
J. Am. Chem. Soc. **117**, 3282 (1995).

[121] **D. Lecacheux, J. Lesec and C. Quivoron:** *High-temperature coupling of high-speed GPC with continuous viscometry. I. Long-chain branching in polyethylene*.
J. Appl. Polym. Sci. **27**, 4867 (1982).

[122] **D. Lecacheux, J. Lesec and C. Quivoron:** *Gel-permeation chromatography – problems caused by polydispersity in the application of the Benoits universal parameter*.
J. Liq. Chromatogr. **5**, (2) 217 (1982).

[123] **Y. U. Lee, S. S. Jang, W. H. Jo:** *Off-lattice Monte-Carlo simulation of hyperbranched polymers, 1. Polycondensation of AB(2) type monomers*.
Macromol. Theor. Sim. **9**, (4), 188 (2000).

[124] **R. L. Lescanec, M. Muthukumar:** *Configurational characteristics and scaling behavior of starburst molecules - A computational study*.
Macromolecules **23**, (8), 2280 (1990).

[125] **B. Li, N. Madras, A. D. Sokal:** *Critical exponents, hyperscaling, and universal amplitude ratios for 2-dimensional and 3-dimensional self-avoiding walks*.
J. Stat. Phys. **80**, 661 (1995).

[126] **I. M. Lifschitz, A. Y. Grosberg and A. R. Khoklov:** *Some problems of statistical physics of polymer chains with volume interaction*.
Rev. Mod. Phys. **50**, (3), 683 (1978).

[127] **L. Lue:** *Volumetric behavior of athermal dendritic polymers: Monta-Carlo simulation*.
Macromolecules **33**, 2266 (2000).

[128] **E. Madelung:** *Das elektrische Feld in Systemen von regelmässig angeordneten Punktladungen*.
Phys. Z. **19**, 524 (1918).

[129] **N. Madras, A. D. Sokal:** *The Pivot Algorithm – a highly efficient Monte-Carlo method for the self-avoiding walk*.
J. Stat. Phys. **50**, 109 (1988).

[130] **G. C. Maitland, M. Rigby, E. B. Smith, W. A. Wakeham:** *Intermolecular forces – their origin and determination*.
Clarendon Press, Oxford (1981)

[131] **I. Majid, Z. V. Djordjevic and H. E. Stanley:** *Conformation of linear polymers in three dimensions*.
Phys. Rev. Lett. **51**, 1282 (1983).

[132] **M. L. Mansfield and L. I. Klushin:** *Monte-Carlo studies of dendrimer macromolecules*.
Macromolecules **26**, 4262 (1993).

[133] **M. L. Mansfield:** *Dendron segregation in model dendrimers*.
Polymer **35**, 1827 (1994).

[134] **E. A. Di Marzio and C. M. Guttman:** *A simple treatment of the collapse transition in star molecules*.
J. Chem. Phys. **93**, 7004 (1989)

[135] **W. L. Mattice:** *Asymmetry of flexible chains, macrocycles and stars*.
Macromolecules **13**, 506 (1980).

[136] **W. L. Mattice and K. Sienicki:** *Extend of the correlation between the squared radius of gyration and squared end-to-end distance in random flight chains*.
J. Chem. Phys. **90**, (3), 1956 (1989).

[137] **D. A. McQuarrie:** *Statistical Mechanics*.
Harper & Row, New York, Evanston, San Francisco, London (1976).

[138] **H. Meirovitch and H. A. Lim:** *Comuter simulation study of the θ-point in three dimensions. I. Self-avoiding walks on a simple cubic lattice*.
J. Chem. Phys. **92**, (8), 5144 (1989).

[139] **N. Metropolis, A. W. Rosenbluth, A. H. Teller, E. Teller:** *Equation of state calculations by fast computing machines*.
J. Chem. Phys. **21**, 1087 (1953).

[140] **J. C. Meunier, R. van Leemput:** *Properties of branched star-polystyrene in diluted solution*.
Macromol. Chem. **156**, 121 (1972).

[141] **A. Milchev, W. Paul and K. Binder:** *Off-lattice Monte-Carlo simulation of dilute and concentrated polymer-solutions under theta-conditions*.
J. Chem. Phys. **99**, 4786 (1993).

[142] **T. M. Miller, E. W. Kwock, T. X. Neenan:** *Synthesis of 4 generations of monodisperse aryl ester dendrimers based on 1,3,5-benzenetricarboxylic Acid*.
Macromolecules **25**, 3143 (1992).

[143] **A. Miyake and K. F. Freed:** *Excluded volume in star polymers: Chain conformation space renormalization group*.
Macromolecules **16**, 1228 (1983).

[144] **A. Miyake and K. F. Freed:** *Internal chain conformation of star polymers*.
J. Chem. Phys. **17**, 678 (1997).

[145] **M. A. Moore:** *Theory of polymer coil-globule transition*.
J. Phys. A **10**, (2), 305 (1977).

[146] **M. Murat and G. S. Grest:** *Molecular Dynamics study of dendrimer molecules in solvents of varying quality*.
Macromolecules **29**, 1278 (1996).

[147] **M. Muthukumar and B. G. Nickel:** *Expansion of a polymer-chain with excluded volume interaction*.
J. Chem. Phys. **86**, (1), 460 (1987).

[148] **N. Nemoto, Y. Makita, Y. Tsunashima and M. Kurata:** *Dynamic light scattering studies of polymer solutions. 3. Translational Diffusion and internal motion of high-molecular weight polystyrenes in benzene at infinite dilution*.
Macromolecules **17**, 425 (1984).

[149] **G. R. Newkome, C. N. Moorfield, F. Vögtle:** *Dendritic molecules*.
VCH, Weinheim (1996).

[150] **I. Nezbeda, H. L. Vörtler:** *MC simulation results for a hard core model of carbon tetrachloride*.
Mol. Phys. **57**, 909 (1985).

[151] **S. Nosé:** *A unified formulation of the constant temperature Molecular Dynamics methods*.
J. Chem. Phys. **81**, 511 (1984).

[152] **S. Nosé:** *A Molecular Dynamics method for simulations in the canonical ensemble*.
Mol. Phys. **52**, (2), 255 (1984).

[153] **R. W. Numrich:** *Supercomputer applications*.
Plenum Press, NY, London (1984).

[154] **Y. Oono:** *Statistical physics of polymer solutions - conformation-space renormalization-group approach*.
Adv. Chem. Phys. **61**, 301 (1985).

[155] **I. H. Park, Q.-W. Wang and B. Chu et al.:** *Transition of linear polymer dimensions from θ to collapsed regime. 1. Polystyrene/Cyclohexane system*.
Macromolecules **20**, (8), 1965 (1987).

[156] **W. Paul, K. Binder, D. W. Heermann and K. Kremer:** *Crossover scaling in semidilute polymer solutions: A Monte-Carlo test*.
J. Phys. II **1**, 37 (1991).

[157] **W. H. Press et al.:** *Numerical recipes in C*.
Cambridge University Press, Cambridge, England (1992).

[158] **M. Pütz:** *Dynamik von Polymerschmelzen und Quellverhalten ungeordneter Netzwerke*.
PhD thesis, Mainz (1999).

[159] **A. Rahman:** *Correlations in the motion of atoms of liquid argon*.
Phys. Rev. **136A**, 405 (1964).

[160] **A. Rahman, F. H. Stillinger:** *Molecular Dynamics study of liquid water*.
Phys. Rev. **55**, 3336 (1971).

[161] **D. C. Rappaport:** *The art of molecular dynamics simulation*.
Cambridge University Press (1995).

[162] **F. Reif:** *Statistische Physik und Theorie der Wärme*.
Walter de Gruyter, Berlin (1988).

[163] **A. Rey, J. J. Freire:** *Monte-Carlo calculations for linear chains ans star ploymers with inttramolecular interactions. 3. Dimensions and hysrodynamic properties in good solvent conditions.*.
Macromolecules **20**, 342 (1987).

[164] **D. Richter:** *Star polymers: Experiment, theory and simulation*.
Advances in Chemical Physics. Volume XCIV. John Wiley & Sons Inc. (1996).

[165] **M. N. Rosenbluth, A. W. Rosenbluth:** *Monte-Carlo calculation of the average extension of melecular chains*.
J. Chem. Phys. **23**, 356 (1955).

[166] **J. Roovers, S. Bywater:** *Preparation and characterization of 4-branched star polystyrene*.
Macromolecules **5**, 384 (1972).

[167] **J. Roovers, S. Bywater:** *Preparation of 6-branched polystyrene - thermodynamic and hydrodynamic properties of 4-branched and 6-branched star polystyrenes*.
Macromolecules **7**, 384 (1974).

[168] **J. Roovers, P. Toporowski:** *Synthesis of high molecular-weight ring polystyrenes*.
Macromolecules **16**, 843 (1983).

[169] **J. Roovers, N. Hadjichristidis, L. J. Fetters:** *Analysis and dilute-solution properties of 12-arm-star and 18-arm-star polystyrenes*.
Macromolecules **16**, 214 (1983).

[170] **J. Roovers, P. Toporowski, J. Martin:** *Synthesis and characterization of multiarm star polybutadienes*.
Macromolecules **22**, 1897 (1989).

[171] **J. Roovers, L. L. Zhou, P. M. toporowski, M. van der Zwan, H. Iatrou and N. Hadjichristidis:** *Regular star polymers with* 64 *and* 128 *arms. Models for polymeric micelles*.
J. Chem. Phys. **26**, 4324 (1993).

[172] **J. Roovers (ed.):** *Advances in Polymer Science: Branched Polymers II*.
Adv. Polym. Sci. **143** (1999).

[173] **J. Rudnick, G. Gaspari:** *The asphericity of random walks*.
J. Phys. A **19**, (4), L191 (1986).

[174] **A. M. Rubio, J. J. Freire, M. Bishop and H. R. Clarke:** *Characterization of the theta-state and transition curves of off-lattice 3-dimensional chains*.
J Chem. Phys. **102**, (5), 2277 (1995).

[175] **I. C. Sanchez:** *Phase transition behavior of the isolated polymer chain*.
Macromolecules **12**, 980 (1979).

[176] **P. Senn:** *The computation of the distance matrix and the Wiener index for graphs of arbitrary complexity with weighted vertices and edges*.
Comput. Chem. **12**, 219 (1988).

[177] **L. Y. Shy, B. E. Eichinger:** *Large computer-simulations on elastic networks – small eigenvalues and eigenvalue spectra of the Kirchhoff-matrix*.
J. Chem. Phys. **90**, (9), 5179 (1989).

[178] **A. Sikorski and P. Romiszowski:** *Motion of star-branched vs linear polymer: A Monte-Carlo study*.
J. Chem. Phys. **104**, (21), 8703 (1996).

[179] **A. Sikorski and P. Romiszowski:** *Shape of star-branched polymers at various solvent conditions. A computer simulation study*.
J. Chem. Phys. **109**, (14), 6169 (1998).

[180] **P. A. Small:** *Effects of long branching on distribution of degree of polymerization*.
Polymer **14**, (10), 524 (1973).

[181] **R. P. Smith and E. M. Mortensen:** *Bond and molecular polarizability tensors. I. Mahtematical treatment of bond tensor additivity*.
J. Chem. Phys. **32**, (2), 502 (1960).

[182] **K. Sŏlc:** *Shape of a random-flight chain*.
J. Chem. Phys. **55**, (1), 335 (1971).

[183] **K. Sŏlc and W. H. Stockmayer:** *Shape of a random-flight chain*.
J. Chem. Phys. **54**, (6), 2756 (1970).

[184] **K. Sŏlc and W. H. Stockmayer:** *Statistical mechanics of random-flight chains. 4.Size and shape parameters of cyclic, star-like and comb-like chains*.
Macromolecules **6**, 378 (1973).

[185] **K. Sŏlc and W. H. Stockmayer:** *Ellipsoidal model of polymer coils and its applications*.
J. Chem. Phys. 7, 814 (1974).

[186] **C. C. Sorensen, J. Kovac:** *Role of attractive forces in the dynamics of polymer chains near the θ–point*.
Macromolecules **24**, (13), 3883 (1991).

[187] **D. Stauffer, A. Aharony:** *Introduction to Percolation Theory*.
Taylor & Francis, London, Washington (1991).

[188] **G. Strobel:** *The physics of polymers*.
Springer Verlag, Berlin, Heidelberg, New York (1996).

[189] **W. H. Stockmayer, M. Fixman:** *Dilute solutions of branched polymers*.
Ann. NY. Acad. Sci. 57 (4), 334 (53).

[190] **S. J. Su, J. Kovac:** *Concentration dependence of shape-fluctuations of uniform star polymers*.
J. Chem. Phys. **96**, (10), 3931 (1992).

[191] **S. T. Sun, I. Nishio, G. Swislow and T. Tanaka:** *Coil-globule phase-transition in a single polystyrene chain in cyclohexane*.
J. Chem. Phys. **73**, 5971 (1980).

[192] **S. F. Sun:** *Physical Chemistry of macromolecules*.
John Wiley & Suns, New York (1994).

[193] **W. C. Swope, H. C. Andersen, P. H. Behrens, K. R. Wilson:** *A computer simulation method for the calculation of equilibrium constants for the formation of physical clusters of molecules: application to small water clusters*.
J. Chem. Phys. **76**, 637 (1982).

[194] **P. Tackx and J. C. J. F. Tacx:** *Chain architecture of LPDE as a function of molar mass using size exclusion chromatography and multi-angle laser light scattering (SEC-MALLS)*.
Polymer **39**, (14), 3109 (1998).

[195] **G. Tanaka and W. L. Mattice:** *Chain collapse by lattice simulation*.
Macromol. Theory Simul. **5**, (3), 499 (1996).

[196] **D. N. Theodorou and U. W. Suter:** *Shape of unperturbed linear polymers: polypropylene*.
Macromolecules **18**, 1206 (1985).

[197] **D. A. Tomalia, D. Baker, J. Dewald, M. Hall, G. Kallos, S. Martin, J. Roeck, J. Ryder, J. P. Smith:** *A new class of polymers - starburst dendritic macromolecules*.
Polym. J. **17**, 117, (1985).

[198] **D. A. Tomalia, D. Baker, J. Dewald, M. Hall, G. Kallos, S. Martin, J. Roeck, J. Ryder, J. P. Smith:** *Dendritic macromolecules - synthesis of starburst dendrimers*.
Macromolecules **19**, 2466, (1986).

[199] **D. A. Tomalia, D. M. Hedstrand and L. R. Wilson:** *Encyclopedia of Polymer Science and Engeneering*.
Wiley, New York, p. 46 (1990).

[200] **A. Topp, B. J. Bauer, Ty. J. Prosa, R. Scahrrenberg and E. J. Amis:** *Size change of dendrimers in concentrated solution*.
Macromolecules **32**, 8923, (1999).

[201] **A. M. Torres, A. M. Rubio, J. J. Freire, M. Bishop, J. H. R. Clarke:** *Theta state and collapse of off-lattice chains in two dimensions*.
J. Chem. Phys. **10**, 100, 7754 (1994).

[202] **Y. Tsunashima, M. Hirata, N. Nemoto and M. Kurata:** *Dynamic light scattering studies of polymer solutions. 5. Universal behavior of highly swollen chains at infinite dilution observed for Polyisoprenes in Cyclohexane*.
Macromolecules **20**, 1992, (1987).

[203] **C. Vandermiers, P. Damman, M. Doisiëre:** *Static and quasielastic light scattering from solutions of poly(ethylene oxide) in methanol*.
Polymer **39**, (23), 5627 (1998).

[204] **V. I. Manousiouthakis and M. W. Deem:** *Strict detailed balance is unnecessary in Monte-Carlo simulation*.
J. Chem. Phys. **110**, 2753 (1999).

[205] **L. Verlet:** *Computer experiments on classical fluids. I. Thermodynamical properties of Lennard-Jones molecules*.
Phys. Rev. **159**, 98 (1967).

[206] **L. Verlet:** *Computer experiments on classical fluids. II. Equilibrium correlation functions*.
Phys. Rev. **165**, 201 (1968).

[207] **E. J. Wallace, D. M. A. Buzza, D. B. Adolf:** *Lattice Monte-Carlo simulation of dendrimers*.
Dept. of Physics & Astronomy, Univ. of Leeds, Leedsw LS2 9JT,
Private communication.

[208] **I. Webman, J. L. Lebowitz:** *A Monte-Carlo study of the collapse of a polymer chain*.
Macromolecules **14**, 5 (1981).

[209] **A. H. Widmann, G. R. Davies:** *Simulation of the intrinsic viscosity of hyperbranched polymers with varying topology. 1. Dendritic polymers built by sequential addition*.
Comp. and Theor. Polymer Science **8**, 191 (1998).

[210] **H. Wiener:** *Structural determination of paraffin boiling points*.
J. Am. Chem. Soc. **69**, 17 (1947).

[211] **J. D. Weeks, D. Chandler and H. C. Andersen:** *Role of repulsive forces in forming the equilibrium structure of simple liquids*.
J. Chem. Phys. **54**, 5237 (1971).

[212] **G. Wei and B. E. Eichinger:** *On shape asymmetry of Gaussian molecules*.
J. Chem. Phys. **93**, 1430 (1990).

[213] **G. Wei:** *Shapes and sizes of Gaussian macromolecules. 1. Stars and combs in two dimensions*.
Macromolecules **30**, 2125 (1997).

[214] **G. Wei:** *Shapes and sizes of Gaussian macromolecules. 2. Stars and combs in three dimensions*.
Macromolecules **30**, 2130 (1997).

[215] **G. Weill and J. des Cloizeaux:** *Dynamics of polymers in dilute solutions: an explanation of anomalous indices by cross-over effects*.
J. Phys. **40**, 99 (1979).

[216] **P. Welch, M. Muthukumar:** *Tuning the density profile of dendritic polyelectrolytes*.
Macromolecules **31**, 5892 (1998).

[217] **N. B. Wilding, M. Müller and K. Binder:** *Chain length dependence of the polymer-solvent critical point parameters*.
J. Chem. Phys. **105**, 2, (1996).

[218] **C. Williams, F. Brochard and H. L. Frisch:** *Polymer collapse*.
Annu. Rev. Phys. Chem. **32**, 433 (1981).

[219] **L. Willner, O. Jucknischke, D. Richter, J. Roovers, L. L. Zhou, P. M. Toporowski, L. J. Fetters, J. S. Huang, M. Y. Lin and N. Hadjichristidis:** *Structural investigation of star polymers in solution by small angle neutron scattering*.
Macromolecules **27**, 3821 (1994).

[220] **R. G. Winkler:** *Extended phase space isothermal Molecular Dynamics*.
Phys. Rev. A **45**, 2250 (1992).

[221] **L. V. Woodcock:** *Isothermal Molecular Dynamics calculations for liquid salts*.
Chem. Phys. Lett. **10**, 257 (1971).

[222] **S. G. Whittington, J. E. Lipson, M. K. Wilkinson, D. S. Gaunt:** *Lattice models of branched polymers - dimensions of uniform stars*.
Macromolecules **19**, 1241 (1986).

[223] **H. Yamakawa:** *Modern theory of polymer solutions*.
Harper & Row, New York (1971).

[224] **G. Zifferer:** *Monte-Carlo simulation of tetrahedral chains. 1. Very long (athermal) chains by pivot algorithm*.
Macromolecules **23**, 3166 (1990).

[225] **G. Zifferer:** *Monte-Carlo simulation of tetrahedral chains. 3. Star-shaped polymers by pivot algorithm*.
Macromol. Chem. **191**, 2717 (1990).

[226] **G. Zifferer:** *Size and shape of linear and star-branched polymers.*
Macromol. Chem. **192**, 1555 (1991).

[227] **G. Zifferer:** *Monte-Carlo simulation of tetrahedral chains. 5. The pivot algorithm for nonathermal linear and star-branched polymers*.
Macromol. Chem. **2**, 55 (1992).

[228] **G. Zifferer:** *Monte-Carlo simulation of thetrahedral chains. 6. Linear and star-branched polymers near to theta-conditions.*
Macromol. Chem. Theor. **2**, 319 (1993).

[229] **G. Zifferer:** *Shape assymetry of star-branched random walks with many arms*.
J. Chem. Phys. **102**, (9), 3720 (1994).

[230] **G. Zifferer:** *Monte-Carlo simulation of tetrahedral chains. 7. The shape of linear and star branched polymers near to theta-conditions*
Macromol. Theor. Simul. **3**, 163 (1994).

[231] **G. Zifferer:** *Shape distribution and correlation between size and shape of star-branched tetrahedral lattice chains in athermal and theta systems*.
J. Chem. Phys. **110**, (9), 4668 (1998).

[232] **G. Zifferer and O. F. Olaj:** *Shape assymetry of random walks and nonreversal random walks*.
J. Chem. Phys. **100**, (1), 663 (1994).

[233] **J. G. Zilliox:** *Morphological studies on diluted solutions of starlike polymers*.
Macromol. Chem. **156**, 121 (1972).

[234] **B. H. Zimm and W. H. Stockmayer:** *The dimensions of chain molecules containing branches and rings*.
J. Chem. Phys. **17**, (12), 1301 (1949).

List of Figures

Chapter 1

Chapter 2

Chapter 3

Chapter 4

Chapter 5

Appendix D

Appendix E

List of Tables

Chapter 2

Chapter 4

Chapter 5

Appendix A

Appendix B

Index